

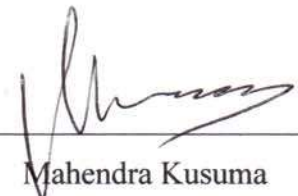
ANALYSIS OF TIME-LAPSE P-WAVE SEISMIC DATA
FROM RULISON FIELD, COLORADO

by
Mahendra A. Kusuma

A thesis submitted to the Faculty and the Board of Trustee of the Colorado School of Mines in partial fulfillment of the requirements for the degree of Master of Science (Geophysics).

Golden, Colorado

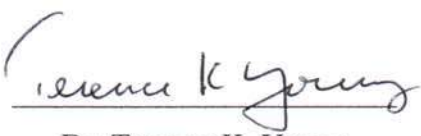
Date 11/14/2005

Signed: 
Mahendra Kusuma

Approved: 
Dr. Thomas L. Davis
Thesis Advisor

Golden, Colorado

Date Nov. 16, 2005


Dr. Terence K. Young
Professor and Head
Department of Geophysics

ABSTRACT

This study was conducted at Rulison field, Colorado as part of Reservoir Characterization Project (RCP) phase X. The focus of this research is to analyze the reservoir changes in this tight gas field using P-wave time-lapse seismic data. Rulison field has some unique reservoir characteristics. These characteristics are: very low permeability reservoir, complex sand channel geometry, and dominant secondary permeability (fracture network). These reservoir characteristics also affected the characteristics of Rulison P-wave seismic data. Some important characteristics of Rulison P-wave seismic data are low P-wave impedance contrast and discontinuous reflectivity within a thick reservoir interval.

Based on these unique characteristics, time-lapse data including three types of time-lapse attributes (time-shift, correlation coefficient and percent difference) and time-lapse inversion were used to analyze the data. Time-lapse analysis indicates that the time-shift attribute is a good indicator of average drainage performance over the reservoir interval. Inversion results have successfully delineated time-lapse anomalies inside the reservoir level. These two attributes (time-shift and inversion) were then used in the integrated analysis of Rulison field.

An integrated analysis of Rulison field was performed using P-wave time-lapse data and other field information. Based on this integrated analysis, the effects of faults and fractures on production were studied. Major NW-SE faults in this field formed boundaries between areas with high drainage performances. The occurrence of NE-SW or E-W faults in the reservoir increased fracture density in specific areas and increased drainage performance. The result of this study strongly supports the applicability of the Christie-Blick strike-slip model in this field as suggested by Jansen (2005). Integrated

interpretation results have suggested that this investigation area can be separated into 6 different areas. Each area has unique production characteristics. Some areas were interpreted to have dominant production intervals, while other areas were interpreted to have relatively equal production from many intervals within the well.

This study emphasized the value of time-lapse analysis in the tight gas field. Time-lapse analysis has been able to: detect the drainage areas; analyze the effects of faults and fractures on production; and detect the dominant production intervals. These results give a foundation for the reservoir characterization of this tight gas field.

TABLE OF CONTENTS

ABSTRACT	iii
LIST OF FIGURES	viii
LIST OF TABLES	xiv
LIST OF EQUATIONS	xv
ACKNOWLEDGEMENTS	xvi
Chapter 1. INTRODUCTION	1
1.1. Introduction.....	1
1.2. Research Objective	4
1.3. Hypothesis	4
1.4. Work Flow	4
1.5. Geology of Rulison Field.....	5
1.5.1. General Stratigraphy and Structure.....	9
1.5.2. Analysis of Petroleum System.....	16
1.6. Used Datasets.....	19
1.6.1. Time-lapse Seismic Datasets	19
1.6.1.1. 1996 Seismic Dataset.....	20
1.6.1.2. 2003 Seismic Dataset.....	20
1.6.2. Rock Properties and Well Data.....	24
1.6.2.1. Available Well Data.....	24
1.6.2.2. Well to Seismic Tie.....	27
1.6.3. Synthetic Seismic Datasets	32
1.6.4. Time-lapse Feasibility Study	35
1.6.5. Production History	35

Chapter 2. CROSS EQUALIZATION PROCESS	39
2.1. Introduction to the Cross Equalization Process	39
2.1.1. Reprocessing of Time-lapse Seismic Data	41
2.1.2. Cross Equalization of Time-lapse Seismic Data	41
2.2. Reprocessing of Rulison Time-lapse Seismic Data	43
2.3. Cross Equalization of Rulison Time-lapse Seismic Data	48
2.3.1. Time and Phase Matching.....	51
2.3.2. Spectral Balancing	57
2.3.3. Amplitude Matching	66
2.3.4. Time-variant Time Shifting	69
2.4. Summary of the Cross Equalization Process	75
Chapter 3. TIME-LAPSE SEISMIC ATTRIBUTES.....	79
3.1. Introduction to Time-lapse Seismic Attributes.....	79
3.1.1. Characteristic of Rulison Time-lapse Seismic Attributes	81
3.2. Application to Synthetic Time-lapse Datasets.....	85
3.2.1. Time Shifting Attributes	85
3.2.2. Correlation Coefficient	88
3.2.3. Percent Differences	89
3.3. Application to Rulison Time-lapse Datasets	91
3.3.1. Time Shifting Attributes	92
3.3.2. Correlation Coefficient	94
3.3.3. Percent Differences	102
3.4. Summary of the Time-lapse Attributes.....	107
Chapter 4. INVERSION OF TIME-LAPSE SEISMIC	109
4.1. Introduction to Time-lapse Seismic Inversion.....	109
4.1.1. General Seismic Inversion Methods	110

4.1.2. Time-lapse Seismic Inversion Methods.....	114
4.2. Application to Synthetic Time-lapse Datasets.....	116
4.2.1. Differences of Inversion	116
4.2.2. Inverse of Differences.....	123
4.3. Application to Rulison Time-lapse Datasets	128
4.3.1. Differences of Inversion	129
4.3.2. Inverse of Differences.....	138
4.4. Comparison of the Approaches.....	149
4.5. Summary of Time-lapse Seismic Inversion.....	152
Chapter 5. INTEGRATED INTERPRETATION OF TIME-LAPSE SEISMIC..	154
5.1. Integrated Interpretation	154
5.2. Production History	156
5.3. Structural Geology and Rock Properties Information	166
5.4. Integrated Analysis of Rulison Field	176
5.5. Summary of the Integrated Interpretation.....	183
Chapter 6. SUMMARIES, CONCLUSIONS AND RECOMENDATIONS	185
6.1. Summaries	185
6.2. Conclusions.....	186
6.2. Recommendations.....	187
REFERENCES.....	188

LIST OF FIGURES

Figure 1.1. Flowchart Rulison time-lapse analysis	6
Figure 1.2. Rulison Field Location (Williams Co.)	7
Figure 1.3.a. Geology map of the Piceance basin (Tyler et al., 1996).....	8
Figure 1.3.b. Structural cross section across Piceance basin (Tyler et al., 1996)	8
Figure 1.4. Stratigraphic column of the Upper Cretaceous in the Piceance basin (Hintze, 1988)	10
Figure 1.5. General fluvial deposition components (Reading, 1983)	11
Figure 1.6. General structural geology of Colorado (Sterner, 1995).....	13
Figure 1.7. Fault interpretation of the Piceance basin from seismic data (Jansen, 2005). 14	
Figure 1.8.a. Christie-Blick Model for strike slip fault (Christie-Blick and Biddle, 1985)	15
Figure 1.8.b. Interpreted faults of the Rulison field in Mid-Reservoir level (Jansen, 2005)	15
Figure 1.9. Gross sand thickness map of reservoir interval (Williams Co.).....	17
Figure 1.10. Rulison time-lapse seismic coverage area (Davis, 2004).....	21
Figure 1.11. Comparison of the CDP fold between two seismic surveys (Ansorger and Kendall, 2004).....	22
Figure 1.12.a. Vp/Vs ratio for lithology determination (Rojas, 2005)..	25
Figure 1.12.b. Vp/Vs ratio with fluid saturation (Rojas, 2005)	25
Figure 1.13. Correlation between pressure depletion and velocity increment (Rojas, 2005).....	26
Figure 1.14. Wells location and log information. P-wave log was generated from sonic log or dipole sonic log data (Williams Co.).....	28

Figure 1.15. Statistical relation between P-impedance and P-wave velocity based on available well information	29
Figure 1.16. Well-to-seismic tie procedure using log data from 4 available wells.	30
Figure 1.17. Extracted wavelet from well-to-seismic tie procedure	31
Figure 1.18. Log information from well Clough 19 that was used to generate the synthetic datasets	33
Figure 1.19. Synthetic time-lapse datasets.....	34
Figure 1.20. Result of Rulison time-lapse feasibility study (modified from: Johnston, 2005)	37
Figure 1.21. Estimate ultimate recovery (EUR) map (Williams Co.)	38
Figure 1.22. Cumulative gas production history 1996-2004 and the number of active wells	38
Figure 2.1.a. Offset coverage and azimuth coverage comparison between surveys. (Winarsky and Kendall, 2004).....	45
Figure 2.1.b. Sector divisions for seismic bins.(Winarsky and Kendall, 2004)	45
Figure 2.2. Rulison P-wave processing sequences (Winarsky and Kendall, 2004).....	46
Figure 2.3. Seismic trace from 1996 dataset and 2003 from inline 63 after reprocessed for time-lapse purpose.....	47
Figure 2.4. a. Amplitude differences between surveys.....	49
Figure 2.4.b. Amplitude envelope differences between surveys	49
Figure 2.5. NRMS value of the static window interval.	50
Figure 2.6. Cross-correlation plot of the trace in static window interval before and after time-shift correction from traces inline 63.	52
Figure 2.7. Distribution of time shift between time-lapse dataset on the static time window interval, before and after time-shift correction.	53
Figure 2.8. Comparison of NRMS values before and after time correction at static window interval.	55

Figure 2.9. Distribution of NRMS values and correlation coefficient values before and after time correction at static window interval.....	56
Figure 2.10. Amplitude envelope differences (inline 63) between the two data sets before and after time and phase correction	58
Figure 2.11. Comparison of NRMS values before and after phase correction at static window interval.	59
Figure 2.12. Distribution of NRMS values and correlation coefficient values before and after phase correction at static window interval.	60
Figure 2.13. The frequency spectrum of the seismic data	62
Figure 2.14. The frequency filter used in the spectral balancing process.....	62
Figure 2.15. Amplitude envelope differences between the two data sets before and after spetral balancing	63
Figure 2.16. Comparison of NRMS values before and after spectral balancing at static window interval.	64
Figure 2.17. Distribution of NRMS values and correlation coefficient values before and after spectral balancing at static window interval.	65
Figure 2.18. Comparison of average RMS amplitude in the static window interval between 2003 and 1996 seismic data.....	67
Figure 2.19. Amplitude envelope differences between the two data sets before and after amplitude balancing.....	68
Figure 2.20. NRMS values at static window interval before and after amplitude balancing.....	70
Figure 2.21. Distribution of NRMS values and correlation coefficient values before and after time correction at static window interval.	71
Figure 2.22. Time shift between 2003 and 1996 seismic data sets from horizon above the reservoir and below the reservoir.....	73
Figure 2.23. Amplitude envelope differences between the two data sets before and after time-variant time-shifting.....	74

Figure 2.24. Distribution of repeatability (NRMS) before and after cross equalization process.....	77
Figure 2.25. Distribution of NRMS values and correlation coefficient values before and after time correction at static window interval.	78
Figure 3.1. Schematic illustration of time shift attribute	83
Figure 3.2. Time-shift of the Cameo level from synthetic datasets.....	87
Figure 3.3. Cross correlation between monitor and base traces of the synthetic datasets.....	87
Figure 3.4. Comparison of percent difference (PD) and reflection strength (RS) attributes.....	90
Figure 3.5. Time shift for Cameo level indicates increase in velocity at the reservoir level.....	93
Figure 3.6. One-way travel time interval between UMV and Cameo for base and monitor data.....	95
Figure 3.7. Cumulative reservoir thickness	96
Figure 3.8. Distribution of average velocity inside reservoir interval for base and monitor data.....	97
Figure 3.9. Average velocity changes inside reservoir interval from time-shift attribute	98
Figure 3.10. Basemap for attributes analysis.....	100
Figure 3.11. Cross correlation attribute applied to Rulison time-lapse datasets.....	100
Figure 3.12. Time slice of correlation coefficient (CC) attribute at 1000 ms.....	101
Figure 3.13.a. Comparison between base amplitude before and after smoothing	103
Figure 3.13.b. Distribution of smoothed base amplitude at mid reservoir level.....	103
Figure 3.14. Comparison RS and PD attributes applied to Rulison time-lapse data.	104
Figure 3.15. Time slice of percent differences attribute at 1040 ms.....	105
Figure 3.16. PD attribute at the Cameo level (1230 ms).	106

Figure 4.1. Flowchart of time-lapse inversion approaches	115
Figure 4.2. Initial model for model base inversion (synthetic data).....	118
Figure 4.3. Correlation plot of inversion result (synthetic data).....	119
Figure 4.4. Inversion result for base and monitor data (synthetic data).	120
Figure 4.5. Impedance difference from DOI approach (synthetic data)	122
Figure 4.6. Distribution of AI value from inversion result using DOI and IOD approaches (synthetic data).....	124
Figure 4.7. Impedance difference from IOD approach (synthetic data).....	125
Figure 4.8. Comparison of velocity value (in percent velocity) between DOI and IOD approaches (synthetic data).....	127
Figure 4.9. Initial AI model for model base inversion.....	130
Figure 4.10. Cross validation for determining pre-whitening factor (λ).....	132
Figure 4.11. Correlation plot of inversion result for base and monitor data.....	134
Figure 4.12. Inversion result for base and monitor data.	135
Figure 4.13. Impedance difference value from DOI approach.	136
Figure 4.14. Impedance difference horizon slice at mid reservoir level.....	137
Figure 4.15. Impedance difference horizon slice from different inversion methods at the same level as Figure 4.14.	139
Figure 4.16. Analysis of inversion parameter for IOD approach.	140
Figure 4.17. QC on inversion result for IOD approach.	142
Figure 4.18. Distribution of AI differences value from inversion result using DOI and IOD approaches.....	142
Figure 4.19. Impedance difference value from IOD approach.	143
Figure 4.20. Impedance difference horizon slice at mid reservoir level.....	145
Figure 4.21. Impedance difference horizon slices from different inversion methods at the same level as Figure 4.20.	146
Figure 4.22. Velocity changes distribution after converted from time scale to depth ...	147
Figure 4.23. Velocity changes prediction from DOI and IOD inversions	148

Figure 5.1. Cumulative gas production from years 1996 to 2003 for all production intervals.....	157
Figure 5.2. Comparison between distribution of cumulative gas production (1996-2003) and time shifting attribute.	159
Figure 5.3. Comparison between distribution of cumulative gas production and velocity changes at upper Williams Fork reservoir level.....	161
Figure 5.4. Comparison between distribution of cumulative gas production (1996-2003) and velocity changes from inversion result at mid-lower Williams Fork reservoir level.	163
Figure 5.5. Comparison between distribution of cumulative gas production and velocity changes at lower William Fork reservoir level	165
Figure 5.6. Map of time shift attribute and interpreted faults (Jansen, 2005).....	168
Figure 5.7. Correlation between velocity changes and generalized fault distribution (Jansen, 2005) at upper Williams Fork reservoir level	169
Figure 5.8. Correlation between velocity changes and generalized fault distribution (Jansen, 2005) at mid-lower Williams Fork reservoir level	171
Figure 5.9. Correlation between velocity changes and generalized fault distribution (Jansen, 2005) at lower Williams Fork reservoir level	172
Figure 5.10. Correlation between velocity changes and faults distribution (Jansen, 2005) at Cameo level.....	173
Figure 5.11. Comparison between gross sand thickness map (Williams Co.) and time-shift attribute.....	175
Figure 5.12. Separation between areas based on integrated analysis.	179

LIST OF TABLES

Table 1.1. Acquisition parameters comparison between two seismic surveys	23
Table 4.1. General comparison between DOI and IOD approach.	150
Table 4.2. Comparison between DOI and IOD inversion on Rulison datasets.....	152
Table 5.1. Types of time-lapse anomaly.....	177
Table 5.2. Comparison between areas in the field.	180

LIST OF EQUATIONS

Equation 2.1. NRMS value (Kragh and Christie, 2002)	39
Equation 2.2. Cross equalization (Ross et al, 1996)	42
Equation 3.1. Percent differences attribute	84
Equation 3.2. Velocity changes	92
Equation 3.3. Velocity changes calculation	92
Equation 4.1. Basic seismic trace equation (Russell, 2005)	111
Equation 4.2. Least square optimization (Russell, 2005)	112
Equation 4.3. Statistical relation AI and Velocity	149

ACKNOWLEDGEMENTS

I would like to thanks to my advisor Dr. Tom Davis for giving me the opportunity to work with the Reservoir Characterization Project group. I really appreciate his support and consideration since my first day in this school through the completion of my study. I also would like to thank my thesis committee members: Dr. Bob Benson, Dr. Terry Young and Dr. Kasper Van Wijk for their discussion and input to this thesis.

It has been a wonderful time for me to work with the RCP students during this research. I would like to thank the RCP students: KJ, Eugenia, Lauri, Gaby, Shannon, Matt Silbernagel, Don, Mike, Firuz, Eldar, all past and present RCP students. Thank you all for the discussions, support and friendly environment.

I am really thankful to my parents, my brothers and all my family for supporting me during these years. Also, thanks to all the Indonesian students and Indonesian community in Golden for their help and the wonderful time together at Mines.

Finally, I would like to thanks to BP Migas and Caltex Pacific Indonesia for providing the financial support during my study. It has been indeed a great experience for me to pursue my Master degree at the Colorado School of Mines.

Chapter 1

INTRODUCTION

1.1. Introduction

Rulison field produces gas with low water production. As part of the Piceance basin, Rulison field is categorized as a tight gas field. The main characteristic is its low permeability and high reservoir heterogeneity (Kuuskraa and Brashear, 1978). The Piceance basin in general has a huge potential for gas production. Potential gas within the Piceance basin is estimated between 80 Tcf and 136 Tcf (Tyler et al., 1996).

The Reservoir Characterization Project (RCP) has been studying Rulison field as part of RCP phase X. The purpose of the Rulison field study is to improve seismic imaging of reservoir components to increase gas production from the tight gas formation. The research has involved geology, geophysics, petrophysics and reservoir engineering aspects of the Rulison field. Studies by other RCP researchers are listed below:

Petrophysics study	Burke, L., 2004, Anisotropy azimuth from RWF 332-21 cross dipole sonic log analysis, RCP Sponsor meeting, Fall 2004. Burke, L., 2005, Anisotropy from RWF 542-20 cross dipole sonic log analysis, RCP Sponsor meeting, Spring 2005. Rojas, E., 2004, Rock properties and Elastic wave logs, Rulison Field, RCP Sponsor Meeting, Fall 2004.
--------------------	--

	Rojas, E., 2005, Rock Physics of Tight Gas Sands for Seismic Reservoir Characterization, RCP Sponsor Meeting, Spring 2005. Rojas, E., 2005, Elastic rock properties of tight gas sandstones for reservoir characterization at Rulison Field Colorado, MS thesis, Colorado School of Mines.
Structural geology	Jansen, K., 2004, Fault and Fracture Interpretation Using P and Shear Seismic Data, RCP Sponsor meeting, Fall 2004. Jansen, K., 2005, Fault and Fracture Interpretation Using P and Shear Seismic data, RCP Sponsor meeting, Spring 2005. Jansen, K., 2005, Seismic Investigation of Wrench faulting and fracturing at Rulison Field, Colorado, MS Thesis, Colorado School of Mines.
Multicomponent Seismic	Rojas, E., 2004, Converted Wave Data Interpretation – Rulison Field, RCP Sponsor meeting, Fall 2004.
Petroleum engineering	Green, C.A., 2004, Hydraulic Fracture Modeling of massively stacked lenticular reservoirs with correlation to production, Rulison Field, Piceance Basin, Colorado, RCP Sponsor meeting, Fall 2004.

A time-lapse seismic study, that is the focus of this thesis, is an important part of the Rulison field study. Time-lapse seismic is a series of seismic data acquired in the same area after a certain time period for the purpose of analyzing changes in the reservoir. The seismic data used in this research is the P-wave time-lapse seismic

datasets. Time-lapse seismic is a useful tool to analyze the changes in the reservoir during production stages.

Rulison field reservoir consists of multiple-stacked channel sandstone bodies (Cole and Cummella, 2003). An important structural feature in this field is the presence of strike-slip faults (Jansen, 2005). These faults create highly fractured zones in the reservoir. From an engineering standpoint, this research is very challenging because the reservoir has very low permeability and the gas production is highly controlled by the secondary permeability (fracture network). The field has commingled production with no supporting data to indicate the contribution of each production interval. From a geophysical perspective, the seismic datasets used in this research also add some challenges. The seismic datasets used in this research consist of two 3-D seismic datasets acquired using different acquisition parameters. The difference in the acquisition parameters may generate noise in the time-lapse analysis. The reservoir interval has a low P-wave impedance contrast. The low P-wave impedance contrast and the thickness of the channels make it difficult to pick individual channels inside the reservoir.

In this challenging environment, time-lapse seismic data may give a significant contribution to more effective hydrocarbon exploitation. Some of the contributions are to understand more of the factors that control the gas movement and to determine the effective production area and production interval. In the low permeability reservoir, the biggest factor in the fluid movement is the fault and fracture network. The time-lapse analysis may help to understand more about the effects of faults and fractures on the gas production. The time-lapse analysis may also help to determine the effective production area and production interval. In the commingled production field, knowing the effective production interval could help the operator, Williams Production Company, to produce the field more effectively.

1.2. Research Objective

The objective of this research is to:

- a) Study the changes in amplitude and P-wave velocity during the time period 1996-2003 and its correlation with gas drainage in the tight gas sand reservoir
- b) Study the effective production area during the time period 1996 - 2003.
- c) Study the effect of faults and fractures on the hydrocarbon movement and depletion.

1.3. Hypothesis

In the tight gas sand reservoir, the most dominant reservoir property change is effective stress. There are two types of effective stress changes that may occur in this type of reservoir during the hydrocarbon production. The first type is the effective stress increase due to the decline of fluid pressure. The second type is the effective stress increase due to the fracture closure. Either mechanism, or both, could occur in this field during the production.

Hydrocarbon production is controlled by storage capacity of the sandstone bodies and the fracture network. By mapping time-lapse anomalies, I may be able to analyze the zones that are depleting and the mechanisms of depletion. Seismic inversion will help me to increase the resolution of thin beds and the detectability of these changes.

1.4. Work Flow

The Rulison time-lapse seismic study is separated into three stages. The first stage is the cross equalization stage. The cross equalization process is performed to reduce the noise of the time-lapse datasets due to the difference in data acquisition. The second stage

of the investigation is the seismic attribute and seismic inversion analysis. Seismic modeling using synthetic data is also performed to analyze the characteristic of the seismic attributes and the seismic inversion method. The last stage is the integrated interpretation. This process is performed by combining the time-lapse seismic anomaly with additional field information i.e. the production and pressure history, well data, structural geology information and rock properties data. The complete work flow is shown in Figure 1.1.

1.5. Geology of Rulison Field

Rulison field is located in the center of the Piceance basin, northwestern Colorado (Figure 1.2). The Piceance basin was created by the Laramide Orogeny from Late Cretaceous through Paleocene (McFall et al., 1986). This basin is an asymmetrical northwest-trending elongate basin. It is a part of the Rocky Mountain foreland and has gently dipping western and southwestern flanks and a sharply upturned eastern flank (Tremain and Tyler, 1997). The basin is bounded on the northwest part by the Douglas Creek Arch that separated it from the Uinta coal basin, Utah. The eastern part of the basin is bounded by the White River uplift (Figure 1.2).

The geology map of the Piceance basin (Figure 1.3.a) shows that the Upper Cretaceous Mesaverde group is exposed along the boundary of the basin. The Mesaverde Group is the focus of this study. Most of the hydrocarbon source, reservoir and trap in this area are contained in the Mesaverde Group. The geology map also indicates that the axis of the basin is approximately NW-SE. Rulison field is located near the deepest part of the basin (Tyler et al., 1996).

The structural cross section across the geology map (Figure 1.3.b) gives a more detailed depiction of stratigraphy and structure of the Piceance basin. The upper Cretaceous sediment consists of Mancos Shale, Iles and Williams Fork Formations. This

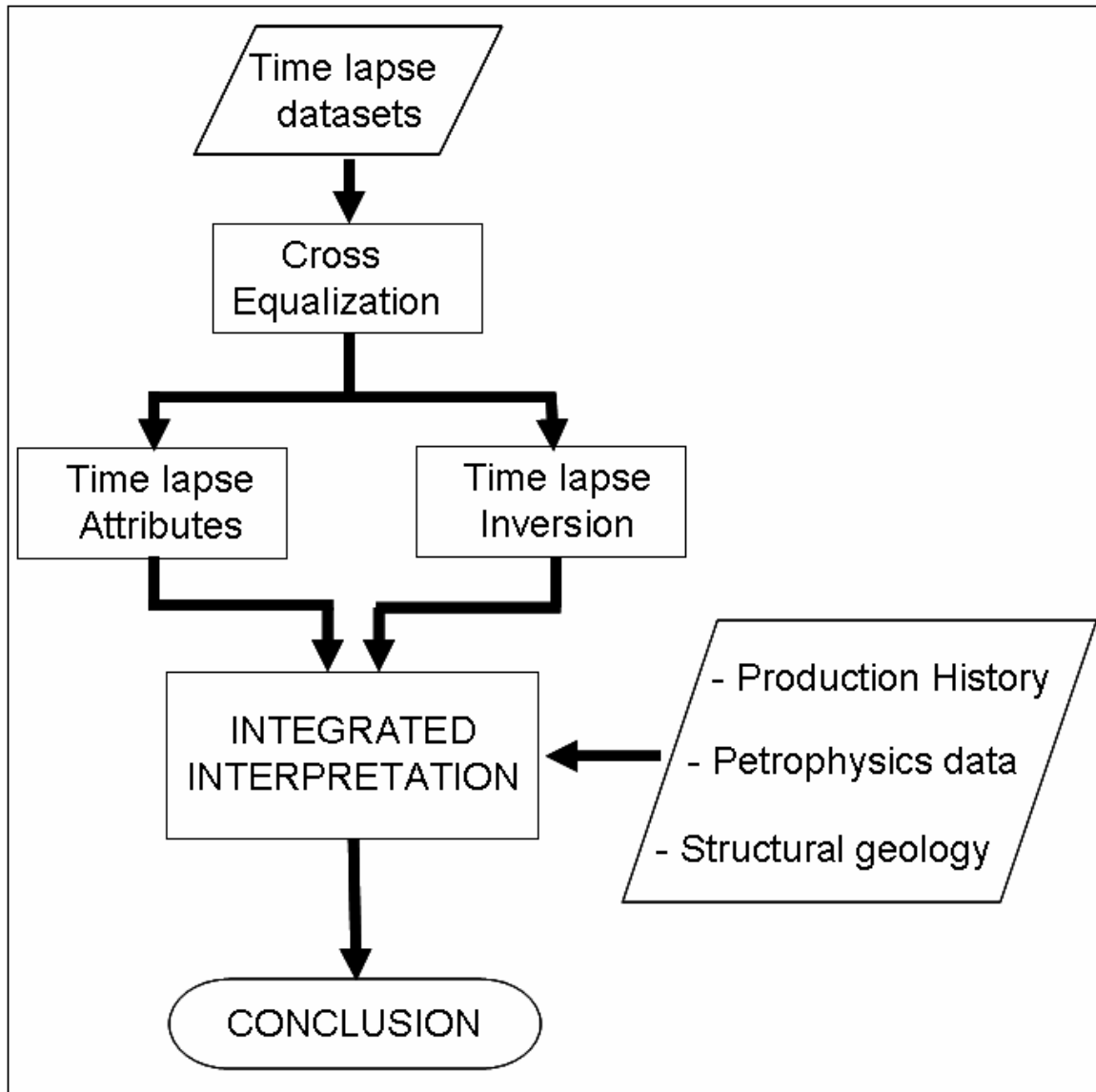


Figure 1.1. Flowchart Rulison time-lapse analysis.

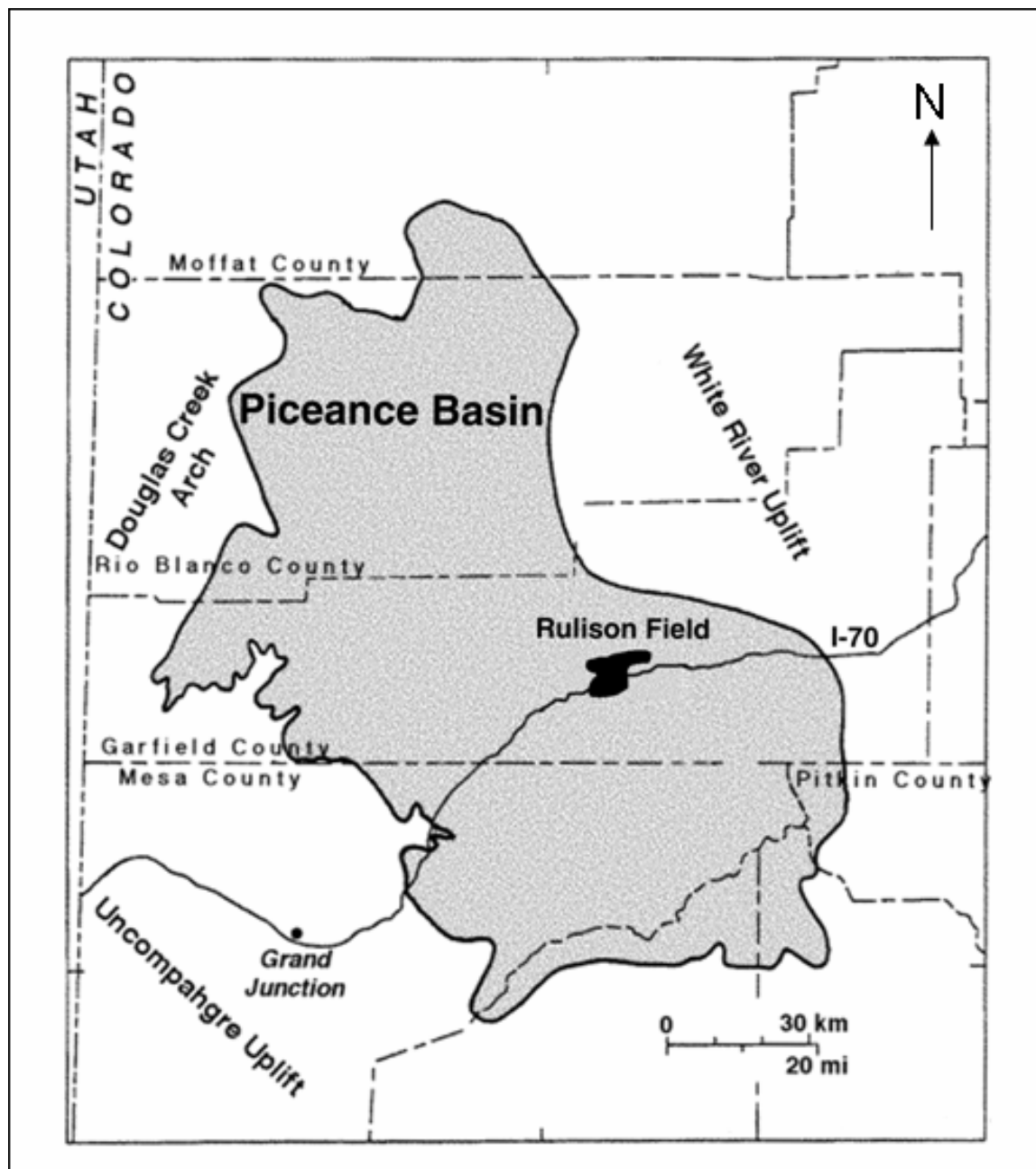


Figure 1.2. Rulison field location (Courtesy: Williams Production Co.).

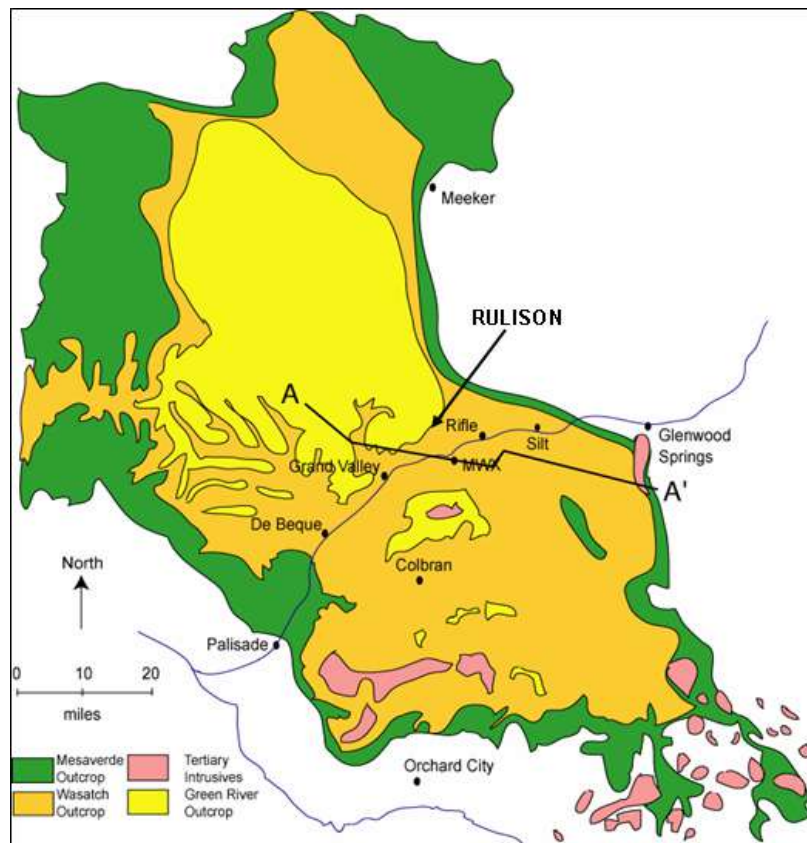


Figure 1.3.a. Geology map of the Piceance basin (Tyler et al., 1996).

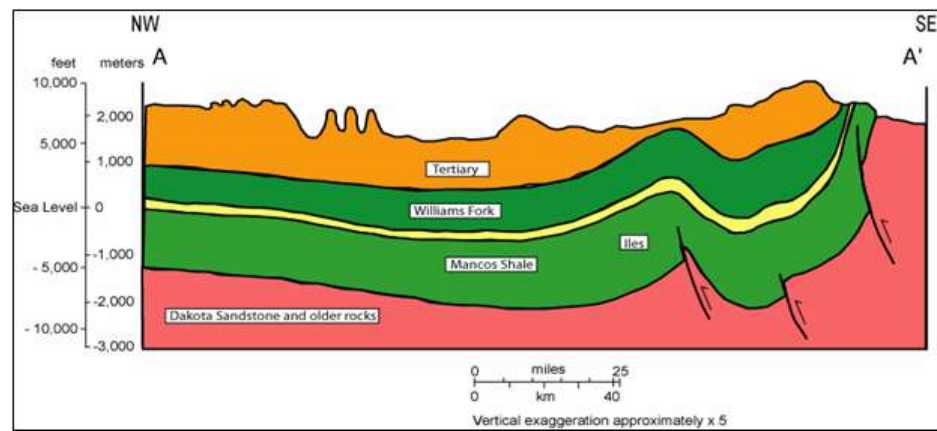


Figure 1.3.b. Structural cross section across Piceance basin trending NW-SE
(Tyler et al., 1996).

sediment package is very thick in cross section. It reaches almost 10,000 ft in thickness. This Upper Cretaceous sediment is overlain by younger tertiary sediments with about 5,000 ft of thickness in cross section. The Mancos Shale and Williams Fork Formations are separated by coal layers. These coal sediments were deposited during the Late Cretaceous era in a transitional coastal plain environment (Tyler et al., 1996).

1.5.1. General Stratigraphy and Structure

Figure 1.4 shows the stratigraphic column of the Upper Cretaceous in the Piceance basin. This stratigraphic column indicates the changes in the sedimentation environment of the Upper Cretaceous sediment. The Mesaverde Group is underlain by the Mancos Shale and overlain by the Lower Tertiary Fort Union and Wasatch Formations. The Mancos Shale was deposited in a marine environment. The Mesaverde and the overlying Fort Union and Wasatch Formations, on the other hand, were deposited mainly in deltaic to fluvial environments (marine to non-marine transitional environments) (Hintze, 1988).

In the Piceance basin, most of coal deposits are contained within the Iles and William Fork Formations of the Mesaverde Group (McFall et al., 1986). The coal sediments were deposited in marine transitional, brackish, interdistributary marshes and freshwater deltaic swamps (Collins, 1976 *in* McFall et al., 1986). The depth of this coal sediments vary from outcrops to more than 12,000 ft in the deepest part of the basin (Tyler et al., 1996).

The Iles and William Fork Formations composed of sandstone and shale sediments (McFall et al., 1986; Johnson, 1989). The Iles Formation was deposited in a deltaic environment and separated from the William Fork Formations by a thick coal layer, the Cameo coal deposit. The Upper Williams Fork Formation is characterized principally as a meandering fluvial system (Blakey, 2004). Most of the fluvial sandstones

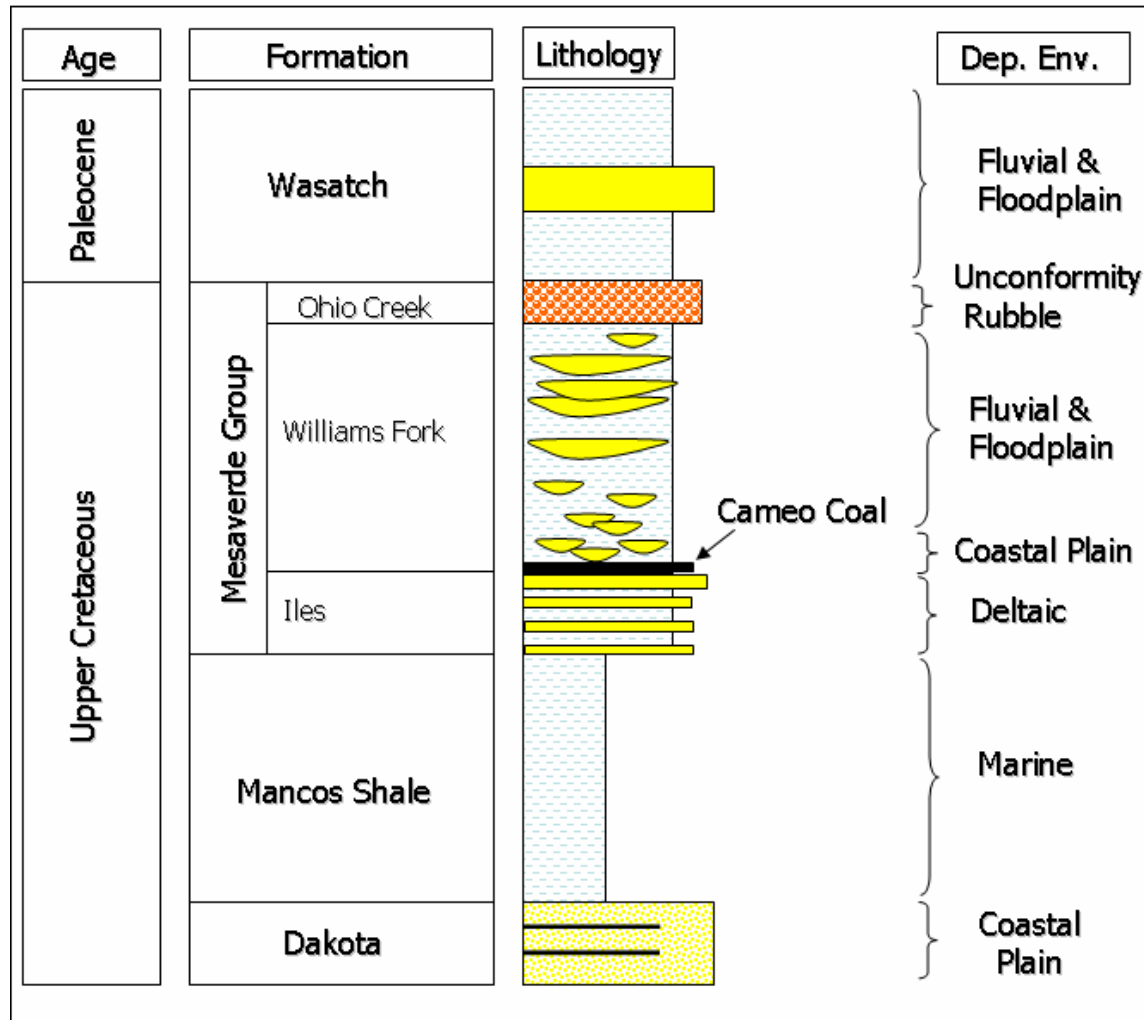


Figure 1.4. Stratigraphic column of the Upper Cretaceous in the Piceance basin.

(Hintze, 1988)

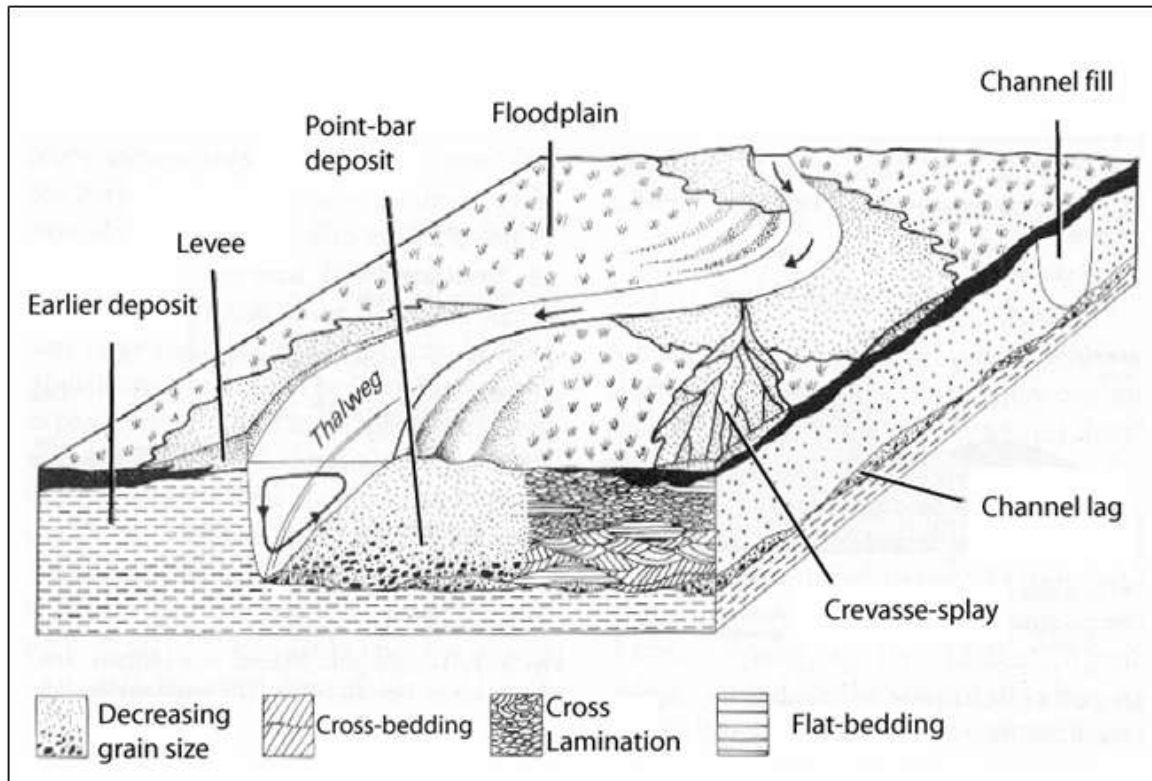


Figure 1.5. General fluvial deposition components (Reading, 1983).

were deposited as point bars during the lateral migration of rivers (Figure 1.5). The point bar units are stacked and they formed composite meander-belt sandstone reservoirs. The average thickness of the sand body is about 9 ft while the average width is 526 ft (Cole and Cummela, 2003). The Lower Williams Fork was deposited during the Campanian Stage of the Cretaceous Period in a coastal-plain environment with meandering streams, swamps, and floodplains. These deposits mostly consist of isolated sandstones (e.g. point-bar sand bodies) encased in floodplain mudstones and coals (Blakey, 2004). The overlying Fort Union and Wasatch Formations consist of fluvial sandstones and shale.

The major fold structure of the Piceance basin is the Grand Hogback Monocline. This structure was formed as the White River Uplift was uplifted and thrust westward during the Laramide Orogeny in Late Cretaceous through Eocene time (McFall et al., 1986). Broad folds, such as the Crystal Creek and Rangley Syncline, trend northwest to southeast and generally parallel the axis of the basin. Intrusions occur mostly in the southeastern part of the basin. A buried laccolith intrusion also occurs under a coal basin anticline along the southeast margin of the basin (Collins, 1976).

The geomorphology of Colorado (Figure 1.6) shows general NW-SE trending structural features. These NW-SE structural features are a result of the structural process during the Laramide Orogeny. Most of the structural features in the Piceance basin also follow this general NW-SE trend. A previous study on the structural geology (Jansen, 2005) showed that a general NW-SE trend also occurs on most of the faults in Rulison field (Figure 1.7). This study also showed the appearance of strike-slip faults in the reservoir level.

Some characteristics of the strike-slip faults are wrench faults exhibiting, fault splay, and minimum vertical movement of the fault (Jansen, 2005). Most of the faults in this area splay out in the reservoir level from the Cameo coal layer to the UMV shale. There are only a few faults that can be identified above the reservoir level. These strike-slip faults generate step over faults in between (Figure 1.8.a). Jansen (2005) suggested the use of the Cristie-Blick model (Figure 1.8.b) to explain fault networks in Rulison field.

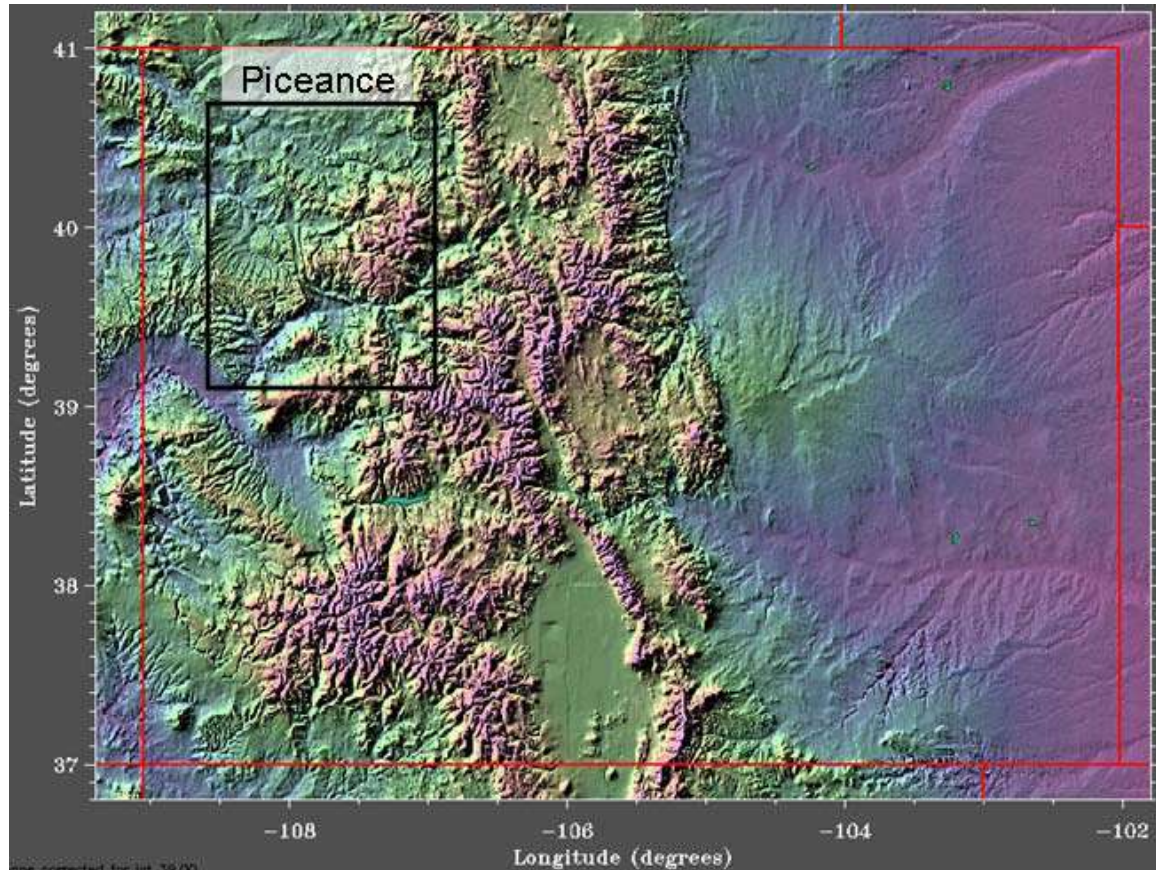


Figure 1.6. General structural geology of Colorado (Sterner, 1995).

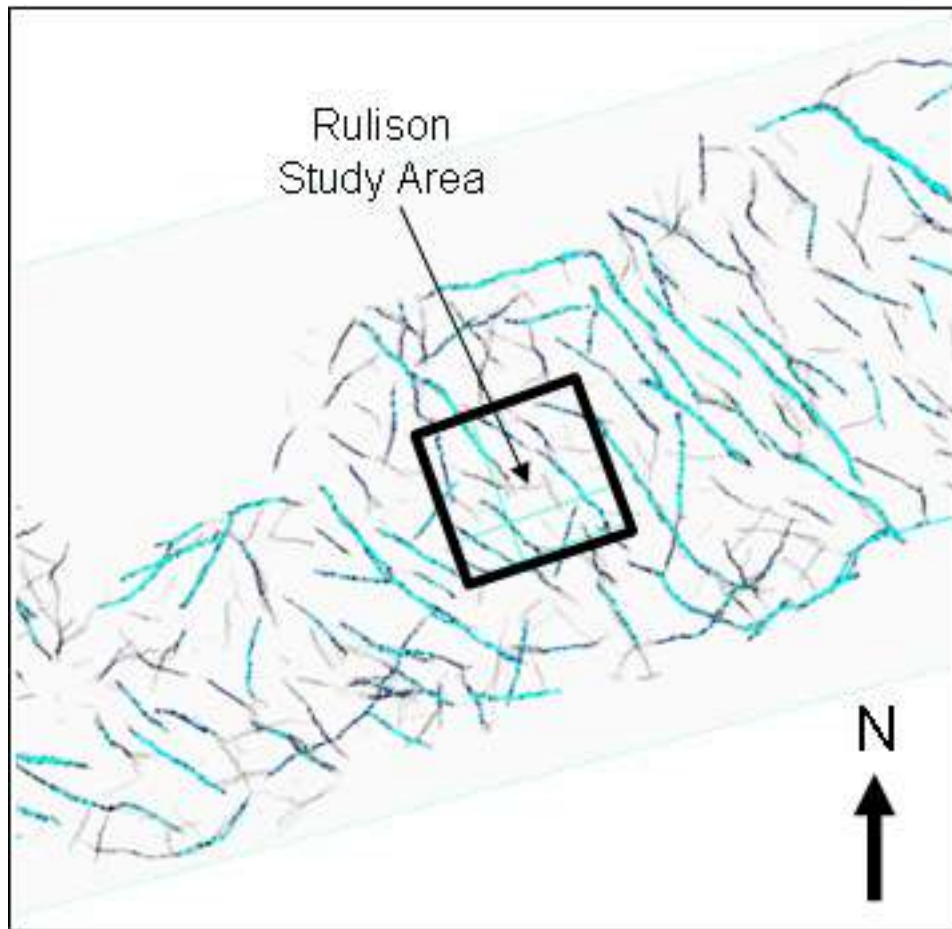


Figure 1.7. Fault interpretation of the Piceance basin from seismic data at Cameo level (Modified from : Jansen, 2005).

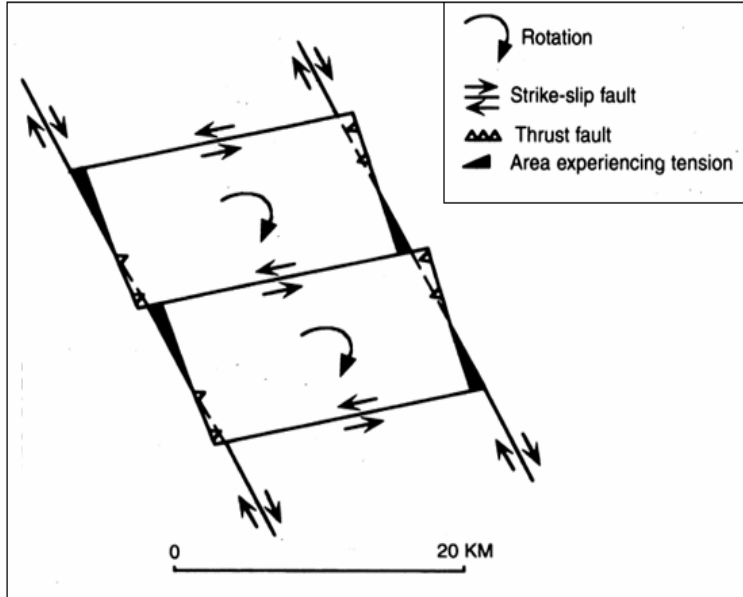


Figure 1.8.a Christie-Blick Model for strike-slip fault.
(Christie-Blick and Biddle, 1985)

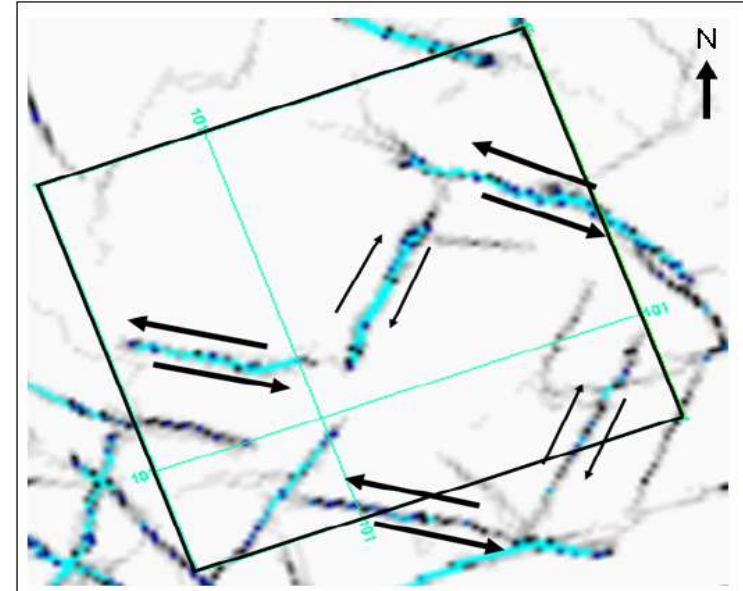


Figure 1.8.b. Interpreted faults of the Rulison field in
Mid-Reservoir level.
(Jansen, 2005)

The rotated blocks and step over faults generate highly fractured areas. These highly fractured areas mostly occur in the edge of rotated blocks. In Rulison field, the major strike-slip faults are the NW-SE trending faults, while the NE-SW trending faults are the stepover faults generated by the main faults (Figure 1.8.a) (Jansen, 2005).

A study on the fracture orientations within the reservoir was conducted by Burke (2005). This study was performed based on the cross dipole sonic logs in well RWF 542-20 and RWF 332-21. The result of this study indicates the presence of two fracture trends, that is a NW-SE and a NE-SW trend. The NW-SE trend is more dominant than the NE trend. This study also suggests that most of the fractures occur in the sandstones (Burke, 2005).

The depiction of gross sandstone in the Williams Fork Formation is shown in Figure 1.9. This map was generated based on the gamma ray cutoff from available well information (Williams Co.). Analysis of this figure indicates that there are only small variations of gross sand thickness inside the Williams Fork reservoir level (from 500 to 780 ft). These values indicate a relatively similar sand content inside the reservoir across the investigation area.

1.5.2. Analysis of Petroleum System

Magoon (1988) suggested the definition of petroleum system: “A petroleum system is a classification scheme identifying all the essential geologic elements and processes necessary for the creation of a family of petroleum accumulation in a sedimentary basin”. The main elements of this petroleum system are the source rock, reservoir rock, seal, migration and traps. Magoon and Dow (1994) also suggested that the geographic extent of a petroleum system includes the pod of active source rock and the locations of all petroleum shows, seeps and accumulation that originated from that pod.

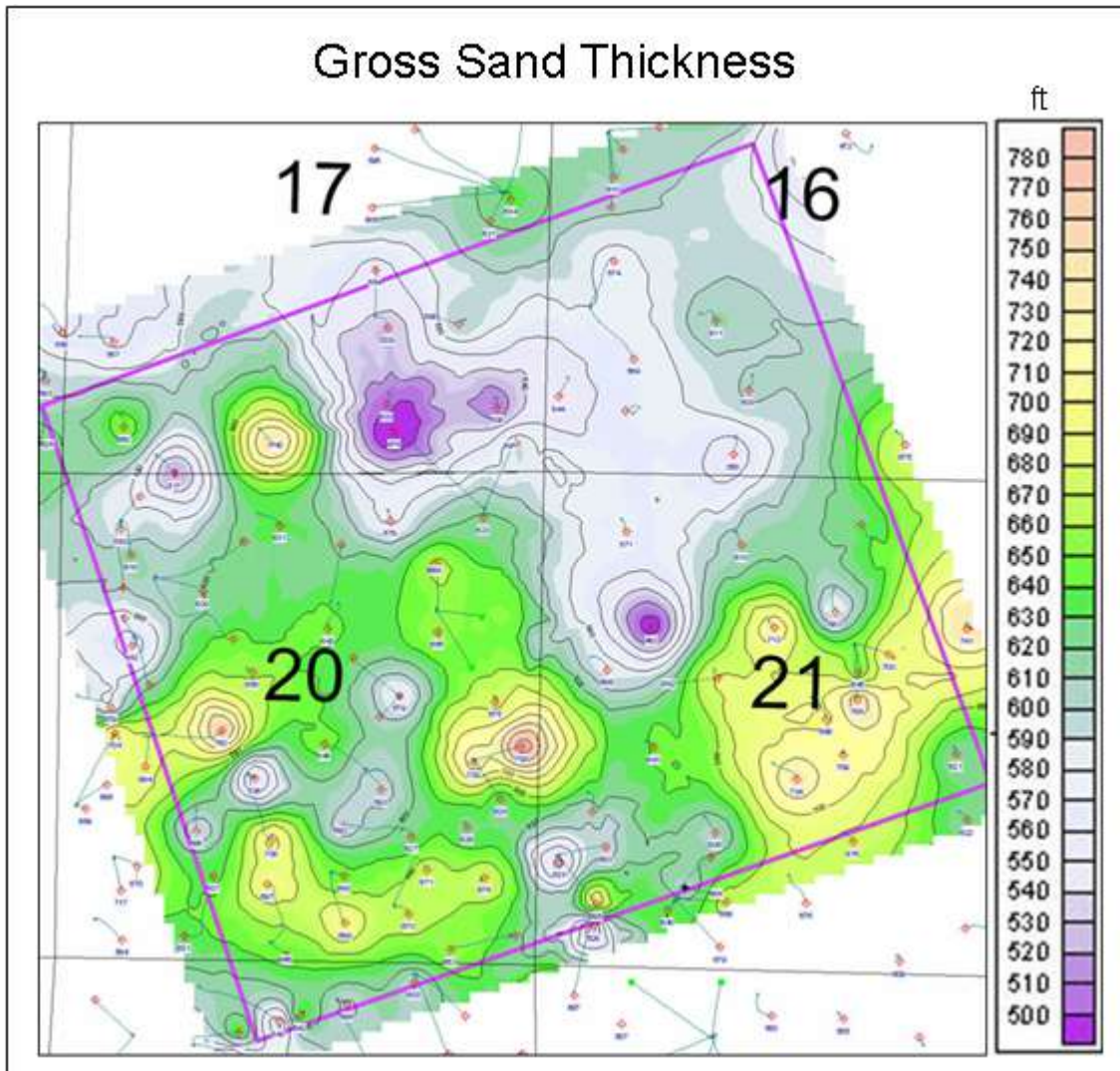


Figure 1.9. Gross sand thickness map of reservoir interval.

(Williams Production Company)

The term “total petroleum system” was introduced by Magoon and Schmoker (2000) to include undiscovered petroleum occurrences that may exist outside the mapped petroleum system. The geographic extent of the total petroleum system includes the petroleum system as well as areas where geologic evidence indicates possible existence of petroleum accumulation (Magoon and Schmoker, 2000).

The first important element of the petroleum system is the existence of the hydrocarbon source rock. Possible hydrocarbon source rocks in Piceance basin comes from the Mancos; the Lower Williams Fork; and Iles Formations (Johnson and Rice, 1990; Lilis et al., 2003). In the Rulison field, the gas source rock mostly comes from the coal deposits in the Lower Williams Fork and Iles Formations.

The reservoir rock in the Piceance basin is assumed to be mostly the fluvial channel sand bodies in the Mesaverde Formation. The sand bodies in this formation formed stacked channel sandstones. The thickness of individual channel bodies average 9 ft, which is well below temporal seismic resolution. This reservoir has very low permeability ranges from 5 μD to 80 μD . Due to its permeability, the Piceance basin is characterized as a tight gas basin. Therefore, secondary permeability through the fracture network is very important for gas exploitation. Due to these facts, the study on the natural fractures is the highest priority exploration goal in this area (Kuuskraa et al, 1997).

Another important element of the petroleum system is the seal. In Rulison field, there are several shale layers with good sealing properties overlying the reservoir (Williams Fork Formation). A previous study of structural geology (Jansen, 2005) indicates that fault and fracture networks within the reservoir level have very little affect on these shale layers. This result underlines the good quality of these shale layers as seals to prevent the gas to migrate vertically. Some shale deposits in the reservoir level (Williams Fork Formation) also act as seals to prevent gas to migrate laterally.

The migration path from source rock to reservoir rock is an important part of the petroleum system. In Rulison field, the main migration pathways from the source rock (Cameo coal) to the reservoir rock (Williams Fork) are the existing fault and fracture

networks. The existence of strike-slip faults, step-over faults and their associated fracture networks may generate good migration pathways.

The last element of the petroleum system is the trap. The trap is the most important part of the system. Generally, a hydrocarbon trap can be categorized into a structural trap, a stratigraphic trap or a combination trap (Landes, 1951). Some examples of structural traps include the anticline trap and fault trap. The stratigraphic trap is the hydrocarbon trap formed by deposition or erosion of the reservoir rock. Some examples of the stratigraphic traps are the erosional truncation trap, channel sand trap, and sequence boundary trap. A combination trap is formed by a combination of the structural geology and stratigraphy features. The hydrocarbon trap in the Rulison field is a diagenetic and hydrodynamic trap.

1.6. Used Datasets

This research focuses on the analysis of reservoir changes during the period 1996 to 2003, based on the time-lapse seismic data. Some additional datasets are used with the time-lapse seismic datasets to generate more understanding of the reservoir changes during this period. The additional datasets include the well data, rock properties information, structural geology information, production history and pressure history.

1.6.1. Time-Lapse Seismic Datasets

The time-lapse analysis is an analysis performed on two or more datasets that was acquired in the same area after a certain time period. The seismic datasets used in this research consists of two seismic data i.e. 1996 seismic data and 2003 seismic data. The 1996 seismic data was acquired before intensive development of the field. These data

have a larger coverage. The 2003 seismic survey was acquired by RCP using multi component seismic. For the purpose of this research only the P-wave are analyzed. Figure 1.10 shows the boundary of the 1996 survey and the 2003 survey. The time-lapse analysis is performed on the overlap area.

1.6.1.1. 1996 Seismic Dataset

The 1996 seismic dataset was acquired by the Department of Energy (DOE). This survey was performed using a source interval of 220 ft and receiver interval of 220 ft. The source is a vibroseis with frequency range from 12 Hz to 96 Hz. The maximum far offset of this seismic data is 16,722 ft. The acquisition parameters are listed in table 1.1. Since the 1996 survey had a higher coverage area, the CDP fold of each bin is low (Figure 1.11). The average CDP fold for this dataset is 100 to 200.

1.6.1.2. 2003 Seismic Dataset

The 2003 seismic dataset was acquired by RCP. This survey is a high resolution survey with source interval of 110 ft and receiver interval of 110 ft. The range of frequencies used in this survey is also broader than the early survey i.e. 5 Hz to 125 Hz. The 2003 survey has higher CDP fold (Figure 1.11), especially in the middle of the survey area where it reaches about 700 CDP fold for each bin. Compared to the 1996 survey, the 2003 seismic data has shorter maximum far offsets (10,905 ft) but has more data in the near offset range. Table 1.1 shows the complete details of the acquisition parameters.

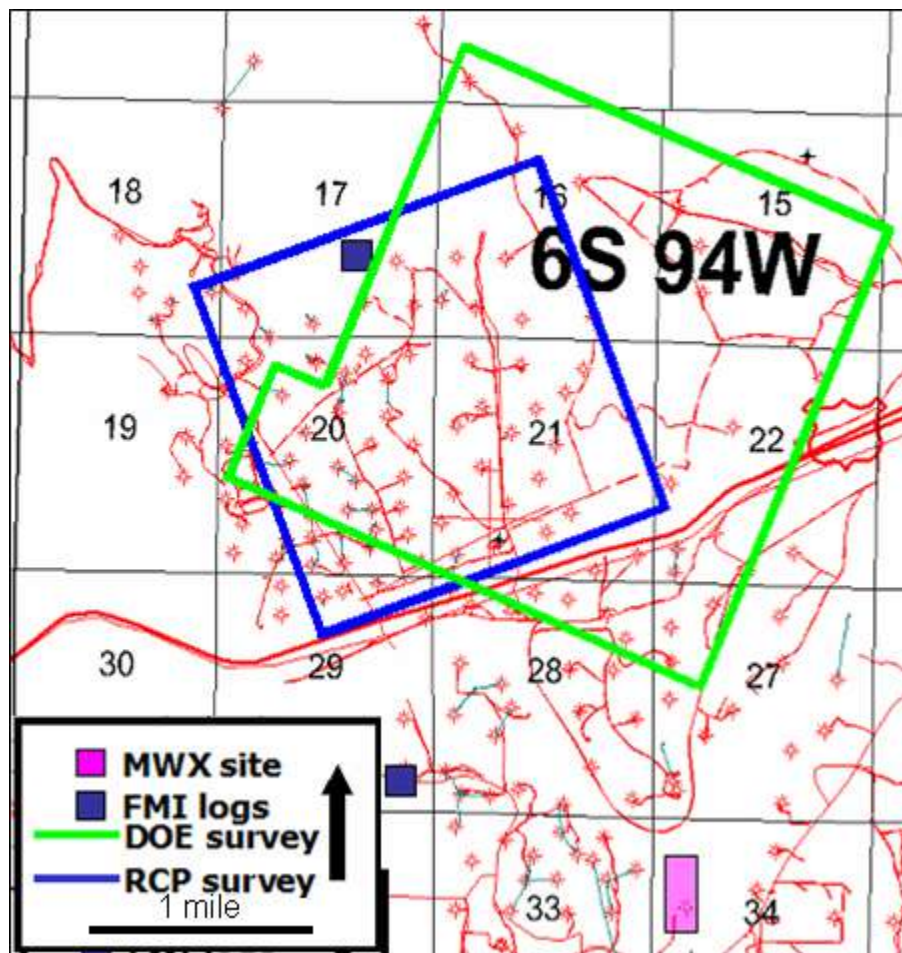


Figure 1.10. Rulison time-lapse seismic coverage area.

(Davis, 2004)

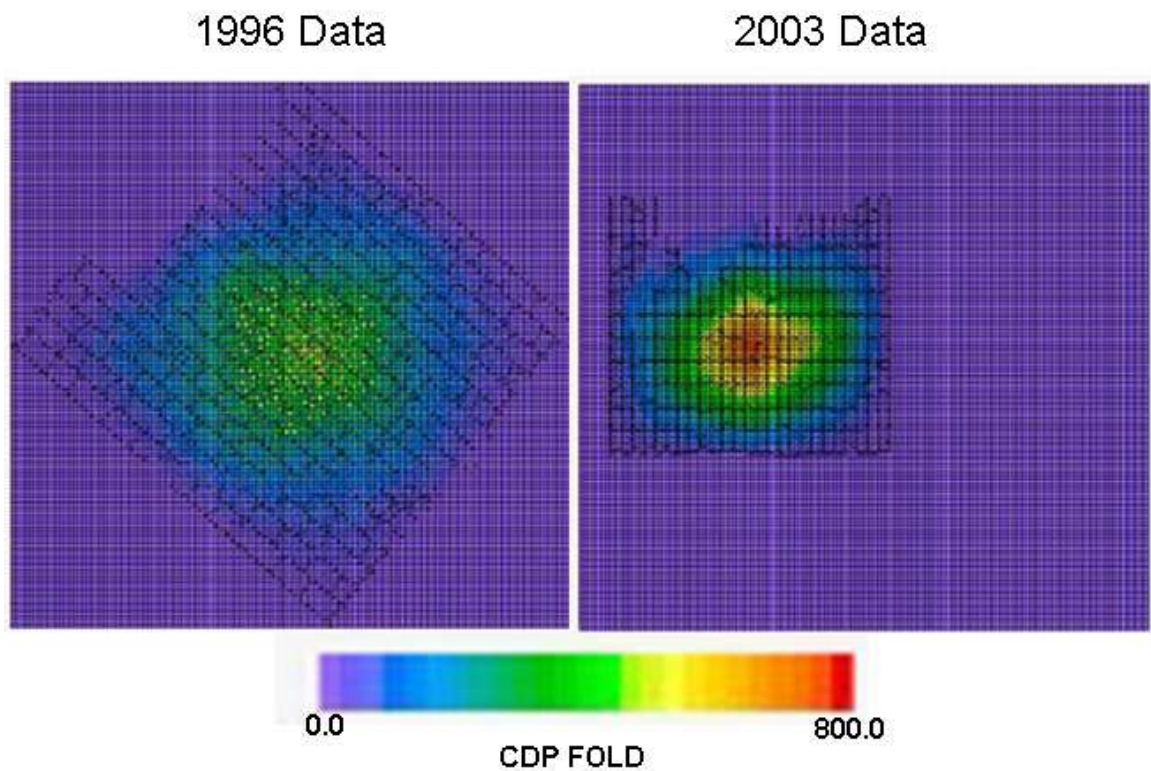


Figure 1.11. Comparison of the CDP fold between two seismic surveys.
(Ansorger and Kendall, 2004)

Parameters	1996 Survey	2003 Survey
Source Interval	220 ft	110 ft
Receiver Interval	220 ft	110 ft
Source	AHV-II Vibrator	AHV-4 and VIBPRO 3X
Sweep	12 to 96 Hz. for 16 sec.	5 to 125 Hz. for 10 sec.
Receiver	Geospace 20X	I/O Vector Seis
Survey Layout	Brick	Orthogonal
Max. Offset	16,722 ft	10,905 ft
Original Processing		
3D Azimuth	290 ⁰	250 ⁰
Bin size	110 ft x 110 ft	55 ft x 55 ft

Table 1.1. Acquisition parameters comparison between two seismic surveys.
 (Ansorger and Kendall, 2004)

1.6.2. Rock Properties and Well Data

The study of Rulison field rock properties has been conducted by many researchers over the years. The latest research has been conducted by Rojas (2005) to analyze the rock properties (porosity, permeability, gas saturation) and its relation with the seismic parameters (V_p and V_s). The result of this study is that the V_p/V_s ratio can be used to identify sand/shale ratio (Figure 1.12.a). This study also shows that the V_p/V_s ratio can also be used to detect the changes in the gas saturation (Figure 1.12.b).

The analysis of the reservoir rock properties is focused on the porosity, density, and permeability values of the sediment within the reservoir level. Shale and sand sediments within the reservoir have overlapping porosity values (Rojas, 2005). Porosity of these sediments ranges from 5% to 25%. The density of shale on the other hand is a little bit higher on average than the sandstone deposits. The shale density is about 2.7 g/cc while the sandstone is about 2.65 g/cc. Thus, it is very difficult to separate the sandstone and shale in the reservoir based on porosity and density values. The reservoir has a very low primary permeability (5 μD to 80 μD). Fractures in the reservoir increase the total permeability.

A study of rock properties by Rojas (2005) also shows the correlation between pressure depletion and velocity (Figure 1.13). A result of this study indicates that there are significant P-wave velocity changes during the primary depletion regime. A pressure depletion of 2000 psi in the primary depletion regime can increase P-wave velocity by about 10% (Figure 1.13).

1.6.2.1. Available Well Data

In this research, rock property information is gathered from 74 wells. Some of the rock property information include gamma ray, density, resistivity (induction log),

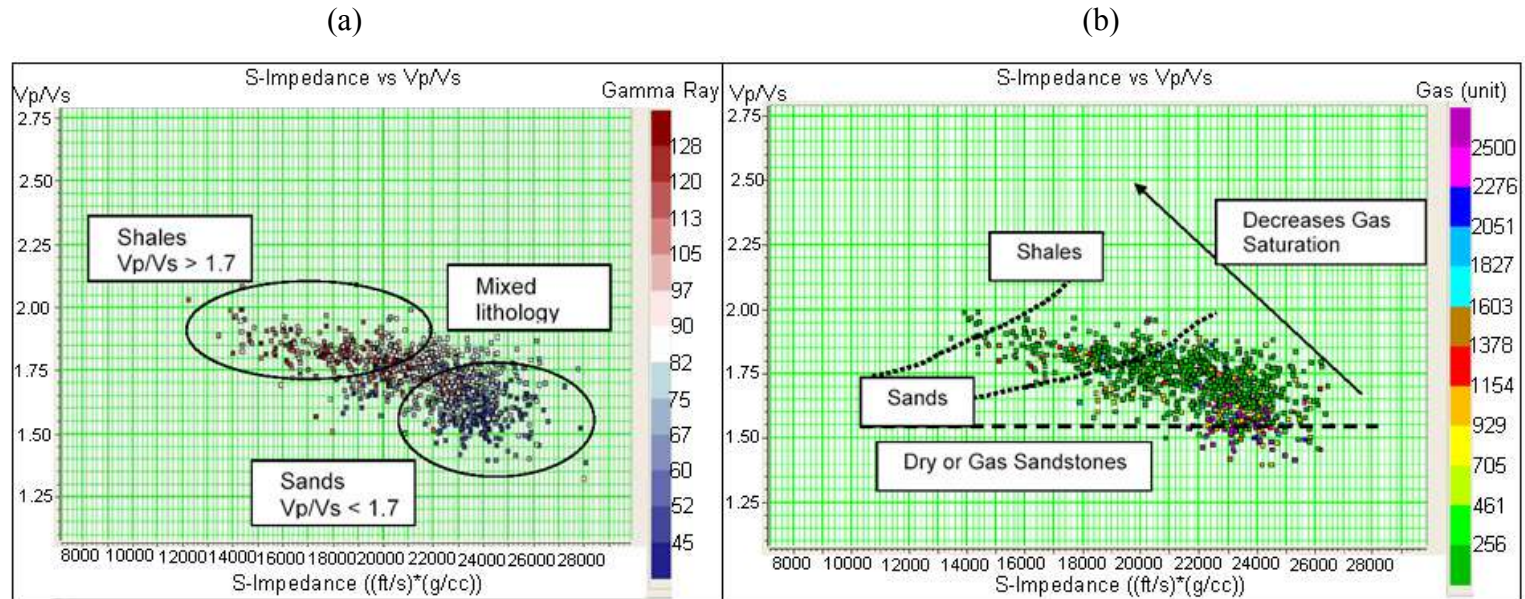


Figure 1.12. (a) Vp/Vs ratio for lithology determination. (b) Vp/Vs ratio with fluid saturation.

(Rojas, 2005)

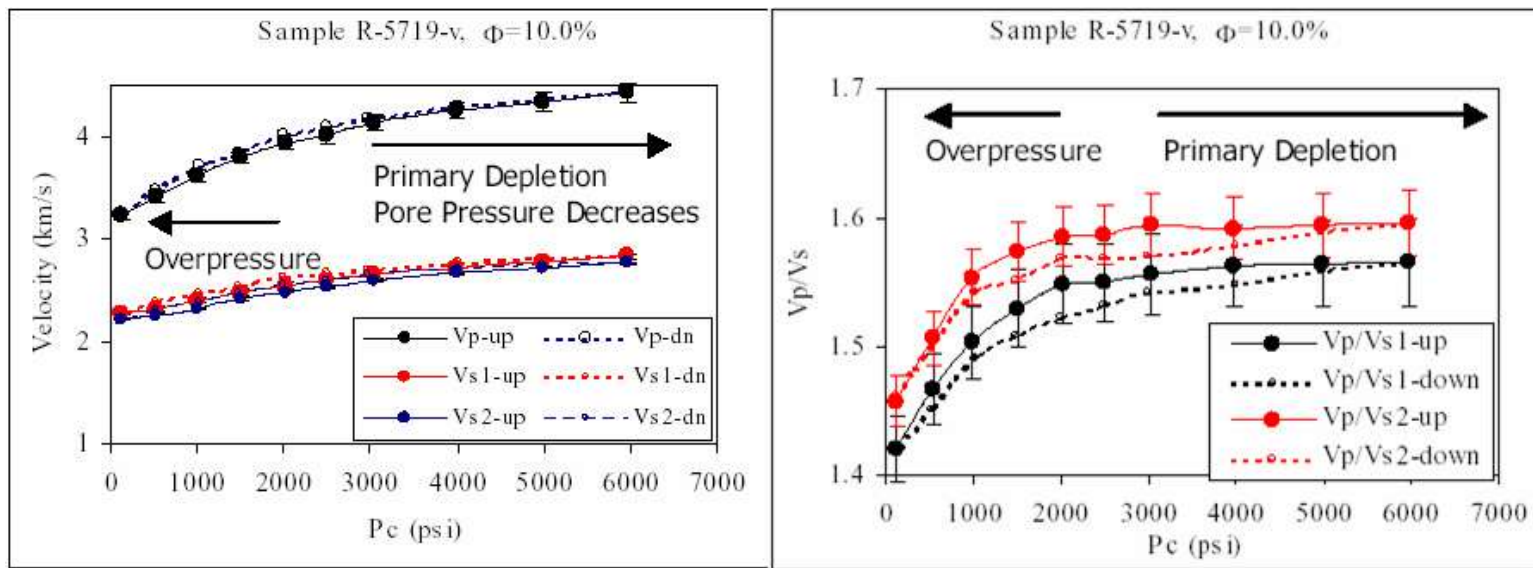


Figure 1.13. Correlation between pressure depletion and velocity increment.

(Rojas, 2005)

neutron porosity and P-wave velocity. Among the 74 wells, there are 6 wells with P-wave velocity data (Figure 1.14). These wells are the Clough 19, RWF 332-21, RMV 68-21, RWF, RMV 94-21H and RWF 524-20.

Based on log information from these wells, a statistical relation between rock properties is extracted. The most important statistical relation in this study is the relation between velocity and acoustic impedance (Figure 1.15). This relation between velocity and impedance is used in this study to convert from impedance model to a velocity model.

Most of the velocity logs are generated from sonic travel-times. There are 2 wells in this area that have dipole sonic log data i.e. RWF 332-21 and RWF 524-20. The dipole sonic log data has been analyzed by Burke (2005) to determine fracture orientations.

1.6.2.2. Well to Seismic Tie

The well-to-seismic tie process is performed to correlate the log data (depth domain) with the seismic traces (time domain). The seismic traces used in this process are the 1996 seismic datasets. This process is performed by generating a seismic wavelet to match the seismic traces with the log information. The well to seismic tie process in Rulison field is performed using 4 out of 6 available wells in this area. Those wells are the Clough 19, RWF 332-21, RWF and RMV 68-21. Other wells with available log information are well RMV 94-21 and RWF 524-20. These wells are not used in this study because they are located near the edge or outside the survey area (i.e. RMV 94-21 and RWF 524-20). Figure 1.14 shows the location of all wells.

Figure 1.16 shows the result of the well-to-seismic tie of those 4 wells. This result indicates a good correlation between synthetic traces and the seismic data. The result of the extracted wavelet from this process is shown in Figure 1.17. This wavelet has a

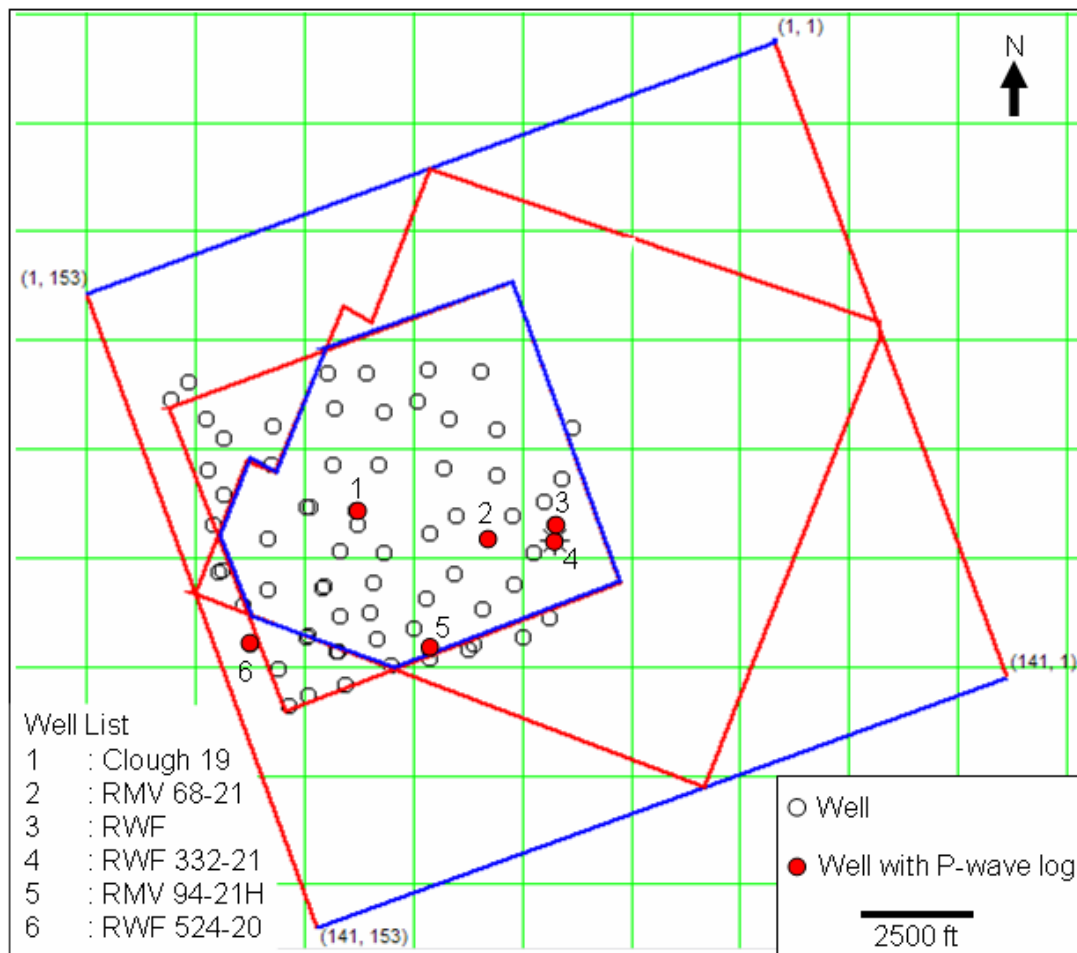


Figure 1.14. Wells location and log information. P-wave log was generated from sonic log or dipole sonic log data (Courtesy: Williams Co.).

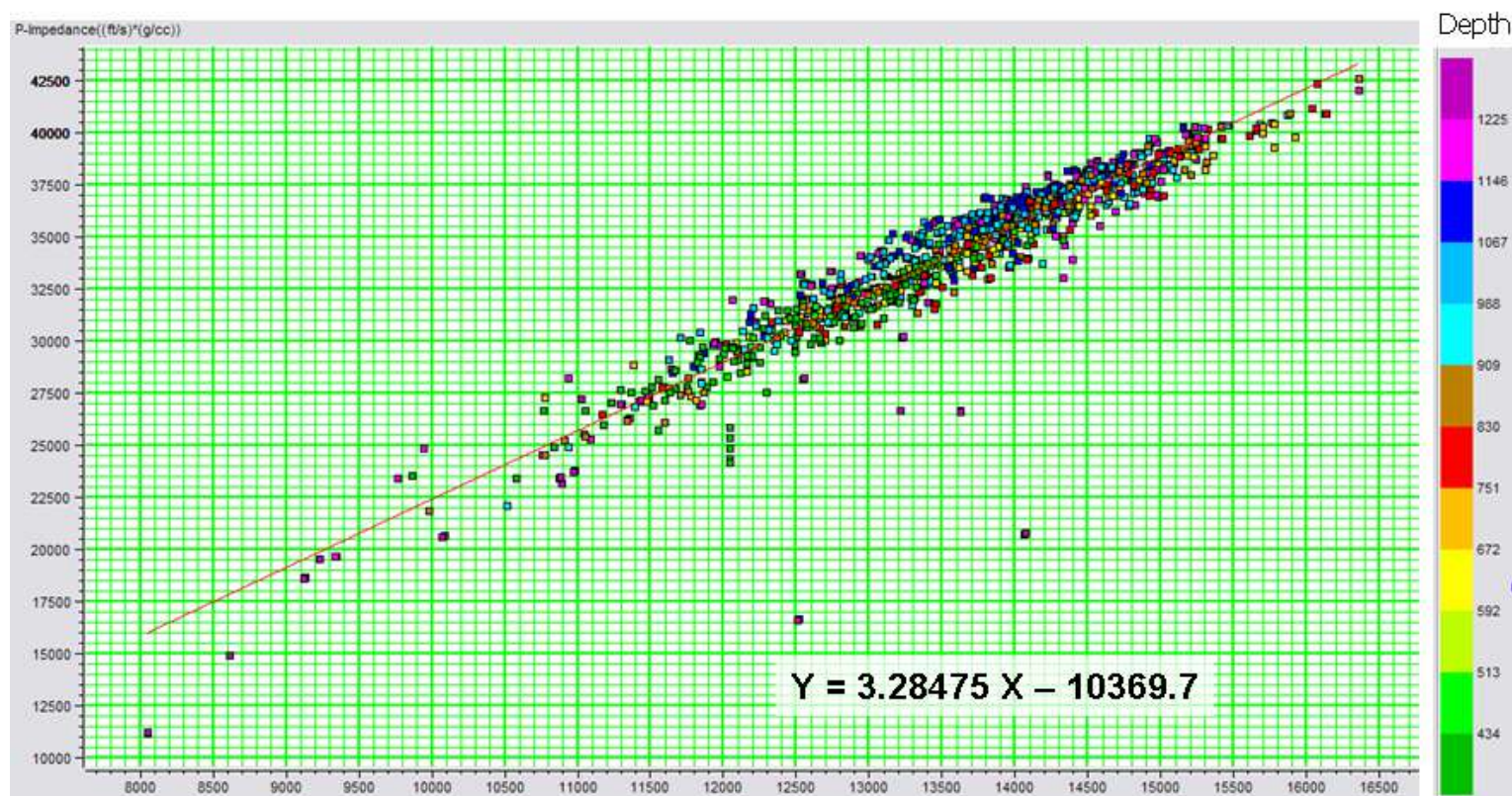


Figure 1.15. Statistical relation between P-impedance and P-wave velocity based on available well information.

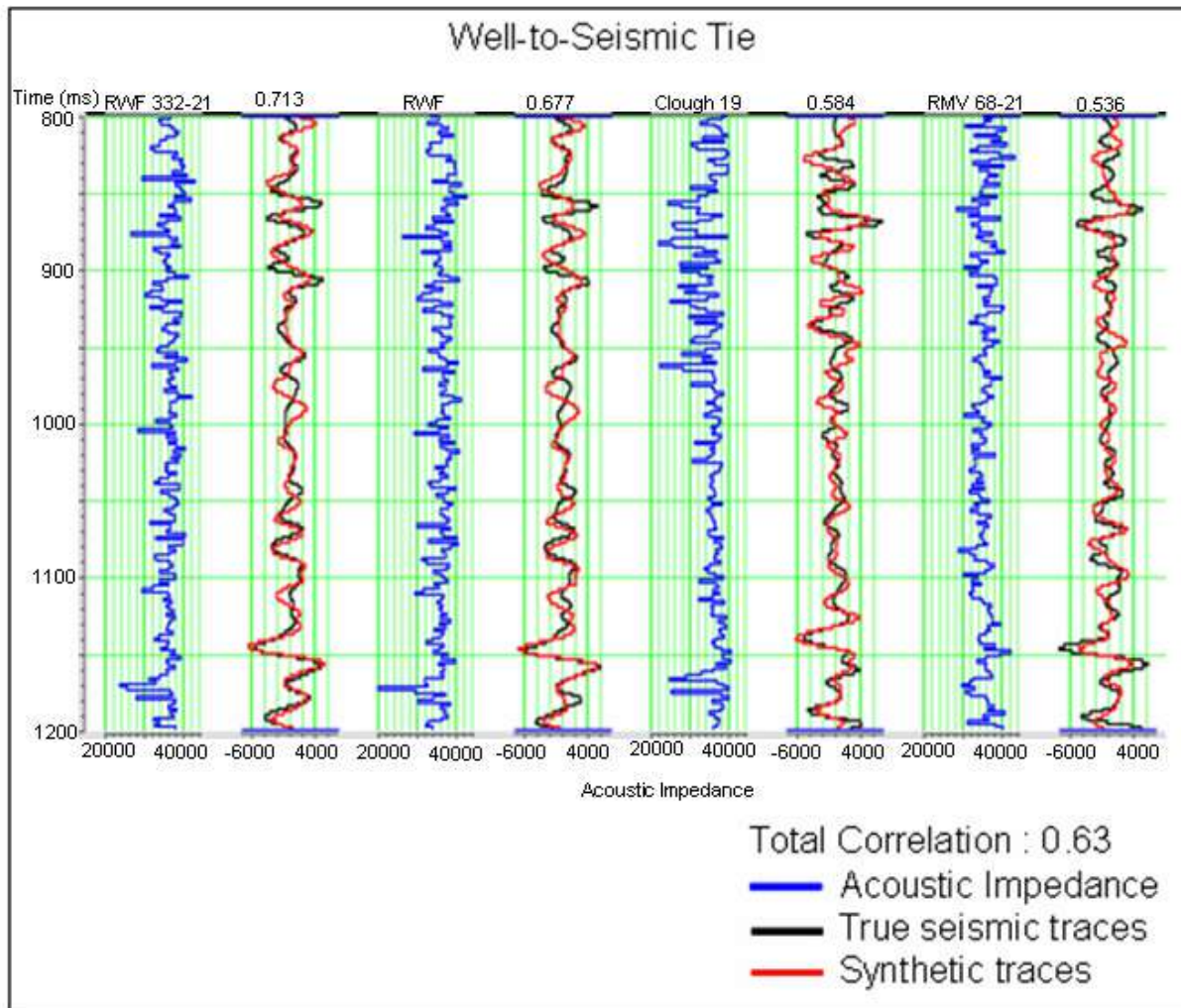


Figure 1.16. Well-to-seismic tie procedure using log data from 4 available wells.

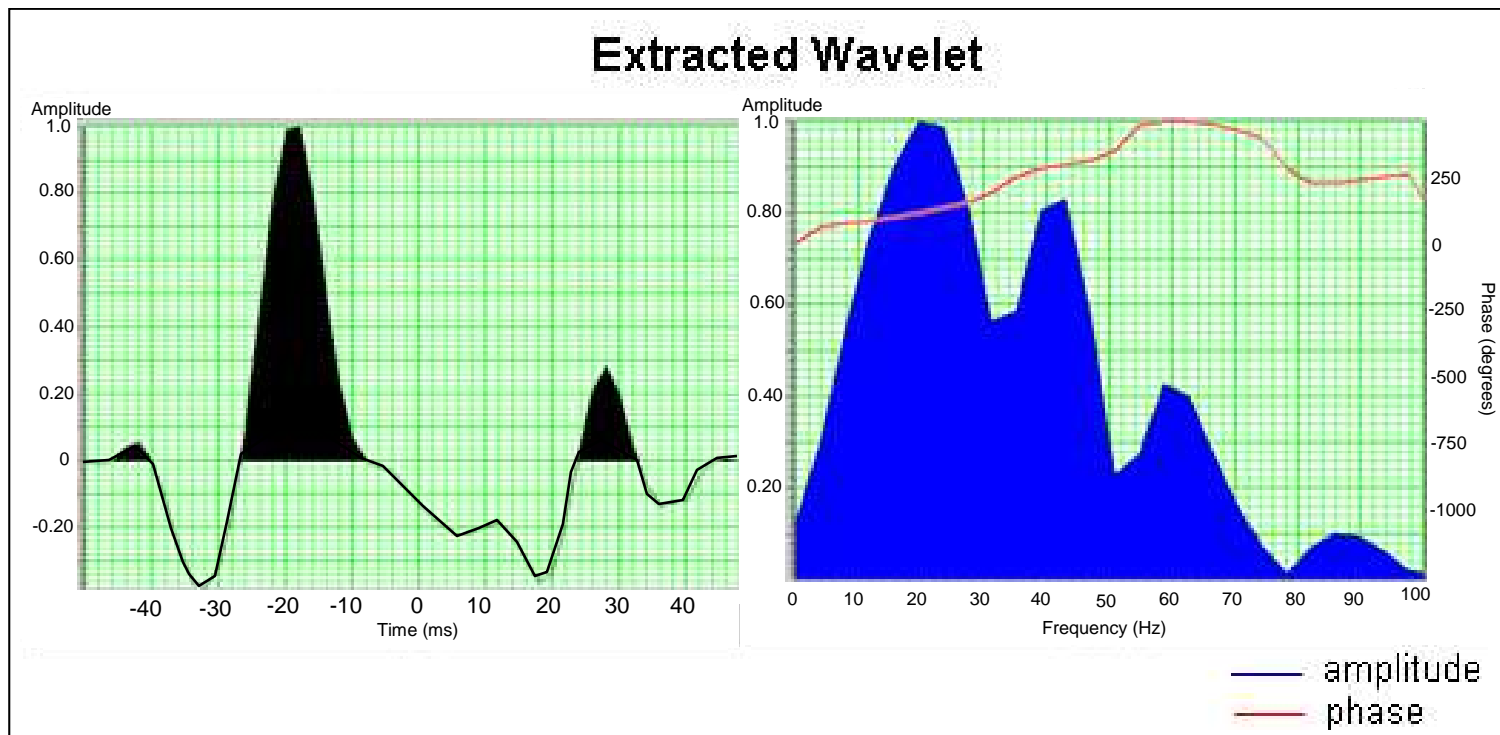


Figure 1.17. Extracted wavelet from well-to-seismic tie procedure.

general phase -8 degree and -20 ms time shift from zero time. This wavelet has most of its frequency spectrum between 10 Hz to 70 Hz.

1.6.3. Synthetic Seismic Datasets

A synthetic time-lapse dataset is simulated to understand the reliability, sensitivity, and error estimation of the time-lapse attributes and the time-lapse inversion method. To better represent the Rulison field time-lapse datasets, synthetic time-lapse datasets are generated using a wavelet extracted from field datasets and log data from a representative well.

Log information from the well Clough 19 is used to generate these synthetic datasets. This well is chosen because it has complete log information to generate synthetic datasets (density logs and velocity logs) and it also has log information from the deeper interval (Cameo level). The log information is up-scaled using a 15 ft block size (Figure 1.18). The objective of the up-scaling process is to generate smoothed synthetic data. Synthetic seismic traces are then generated from the RC log and the extracted wavelet. A 0.5 ms sampling interval is used in the forward modeling of the synthetic traces. This sampling interval is designed to image the log data that has 15 ft smoothing interval. To match with the field data, the synthetic traces are then re-sampled at 2 ms sampling interval. Additional random noise is also added to the synthetic data. The random noise level is 10% of the maximum trace amplitude to represent the noise level in the field data.

Synthetic data are generated with an additional time-lapse anomaly. This anomaly is started from 5900 ft (1010 ms). This anomaly inside the dataset have two main parameters i.e. velocity and thickness (Figure 1.18). The velocity of the anomaly vary from 10% (90% decrease in velocity) up to 190% (90% increase in velocity). The thickness of the anomaly also vary from 0 ft (no anomaly) up to 200 ft. Figure 1.19

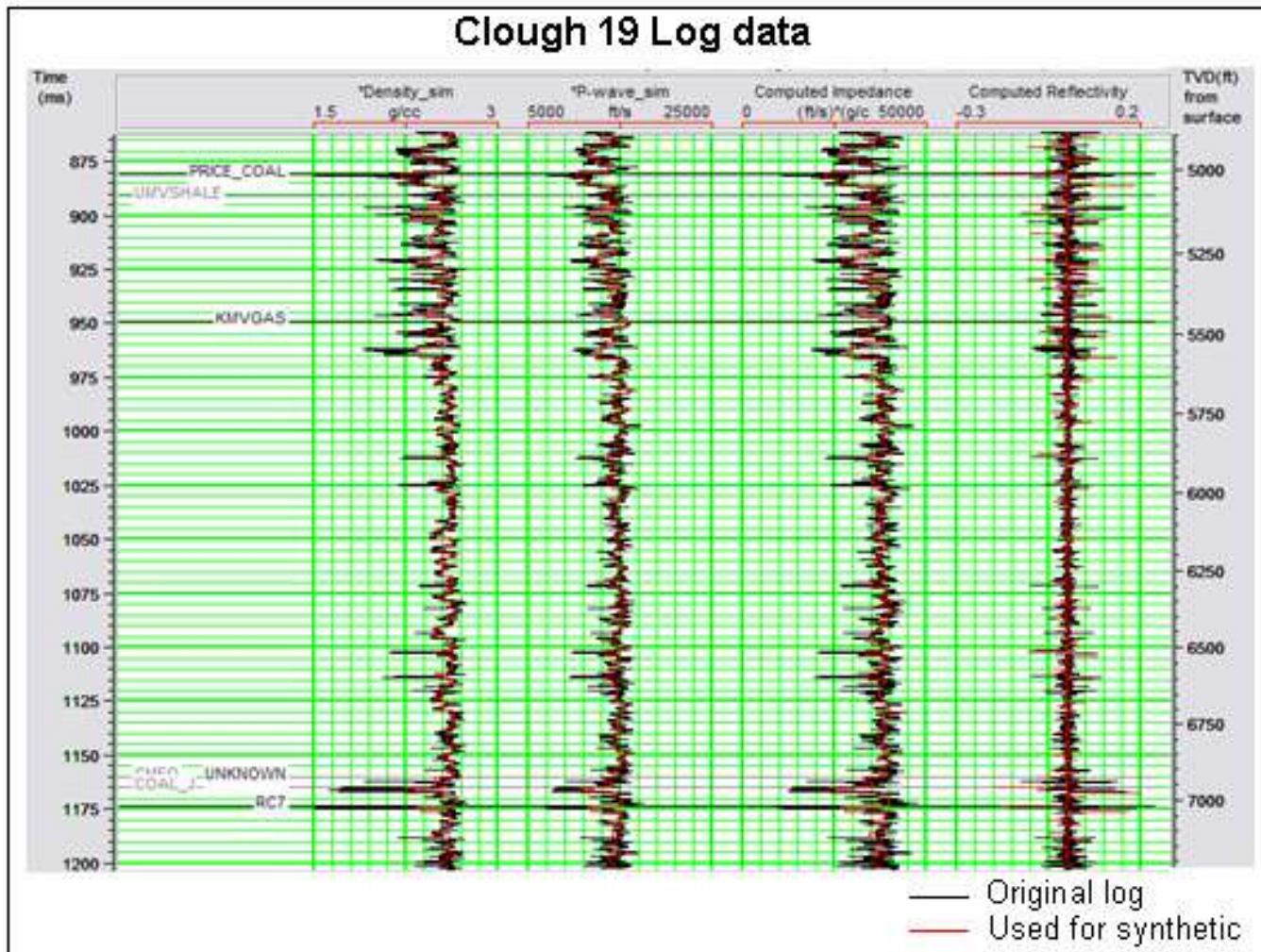


Figure 1.18. Log information from well Clough 19 that was used to generate the synthetic datasets.

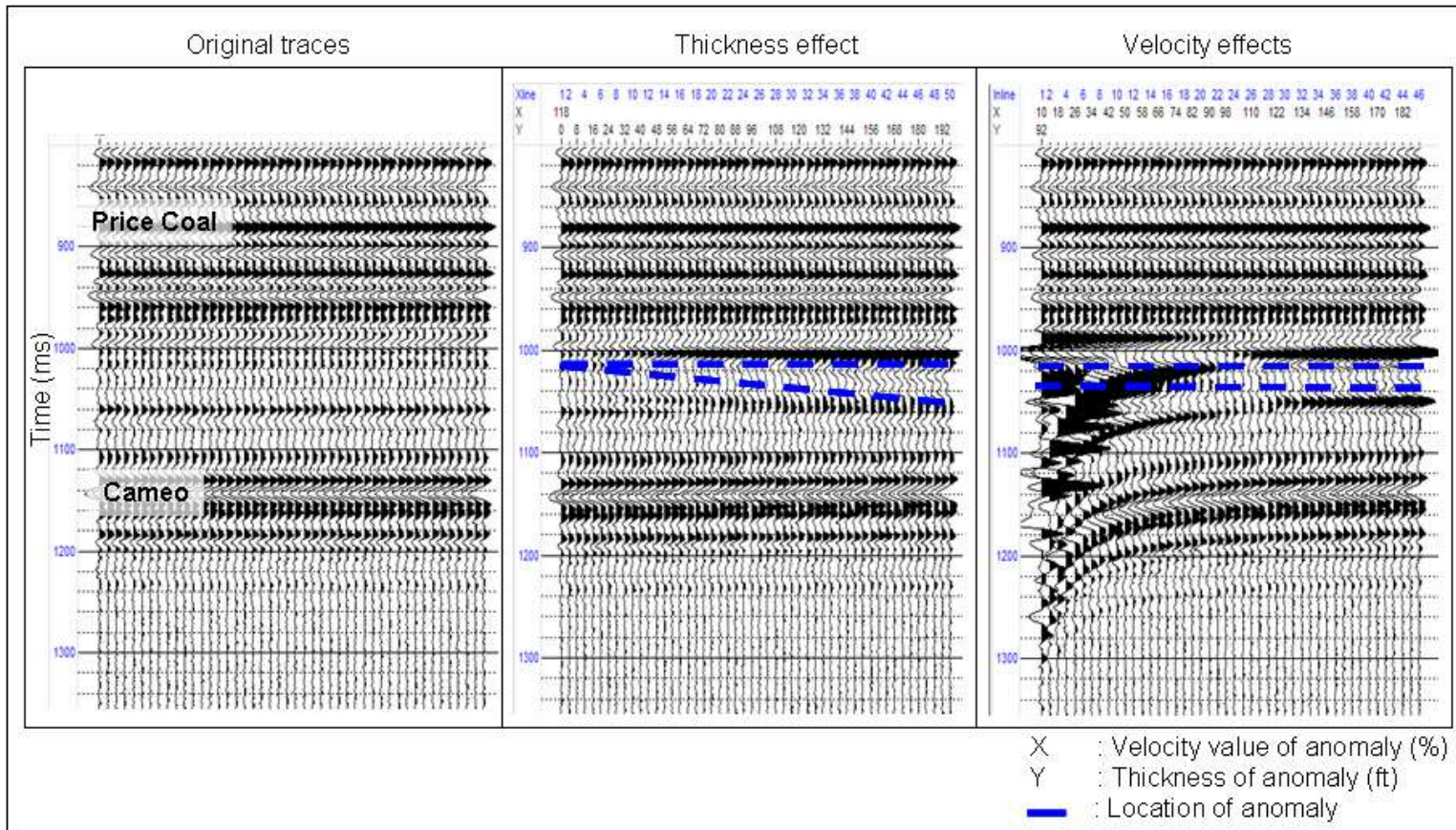


Figure 1.19. Synthetic time-lapse datasets. (Note: Velocity 100% means no velocity changes, Velocity 120% means there is a 20% increase in velocity.)

shows the synthetic traces with the time-lapse anomaly. The figure “thickness effect” shows synthetic traces with different values of thickness within the anomaly for velocity of 118% (18% increase in velocity). The figure “velocity effect” shows synthetic traces with different values of velocity within the anomaly for thickness of 92 ft.

1.6.4. Time-lapse Feasibility Study

A time-lapse feasibility study is performed to predict the time-lapse seismic response during reservoir changes. This simulation was conducted by Johnston (2005), in conjunction with the author, using average values of reservoir properties. Figure 1.20 shows the result of this simulation. The result of this simulation shows that pressure depletion of about 2000 psi can increase impedance changes by about 10% and increase reflectivity values by about 112%. This high percent increment of reflectivity is mostly due to the fact that the base reflectivity has very low values.

Based on this information, a time shift between base and monitor traces is calculated. This time shift value indicates a time lag between traces for a reflector below the reservoir interval. A time shift value predicted from this simulation is about -5 ms two-way time. The minus sign in this value indicates velocity pull up.

1.6.5. Production History

The analysis of the production history is based on the 74 wells in the area. Most of the wells were drilled and produced after 1996. Some of the wells have already produced before the first survey (1996). Based on the EUR map (Figure 1.21), the best produced well is the Clough 19 with EUR value 3.39 BCF. The Clough 19 has been

producing before 1996. Total gas produced from Clough 19 from 1996 to 2003 is 1.28 BCF.

Analysis of cumulative production history (Figure 1.22) shows that the time period 1996 – 2003 was an extensive production period. The number of active wells increased significantly from 23 in 1996 to 74 in 2003. Cumulative yearly gas production also increased significantly during the period 1996 to 2001. The yearly production in this area decreased after 2002, but is being ramped back up in the recent year by infill drilling.

Time Lapse Feasibility Velocity Worksheet

Basin

Piceance

Field

Rulison

Reservoir

William Fork

Enter Vp and Density from Gassmann

	Saturation	Dist.	Vp	Vs	Density	P-wave Impedance	Impedance Change %	Reflectivity Change %	Travel Time, ms	Sw	So	Sg	Sum
Base		U	3879	2295	2.444	9480.28				40	0	60	100
Depleted		U	4313	2568	2.439	10519.41	10.961	-112.34	-5.34	40	0	60	100

Top seal

4000	2200	2.6	10400.00
------	------	-----	----------

Base seal

4000	2200	2.6	10400.00
------	------	-----	----------

Reservoir gross thickness, m

515
10
20

Reservoir porosity, %

Reservoir net-to-gross, %

U = Uniform saturation distribution

P = Patchy saturation distribution

Swirr

40
na
na
na
na

Srow

Srog

Sgcritical

Enter 1 if P<Pb

Reference Information

Reservoir temperature

80
4420
na
4026
2280
2.48

Reservoir pressure

80
2200
na
4360
2550

Solution GOR

Water sand P velocity

Water sand S velocity

Water sand density

Oil API

Gas Gravity

Brine salinity, ppm

Injection salinity

na
0.6285
25000
na

Notes:

Figure 1.20. Result of Rulison time-lapse feasibility study (modified from: Johnston, 2005). Note: Velocity (Vp,Vs) in m/s; density in g/cc; Saturation (Sw,So,St) in percent. Pressure in psi. (Johnston, 2005).

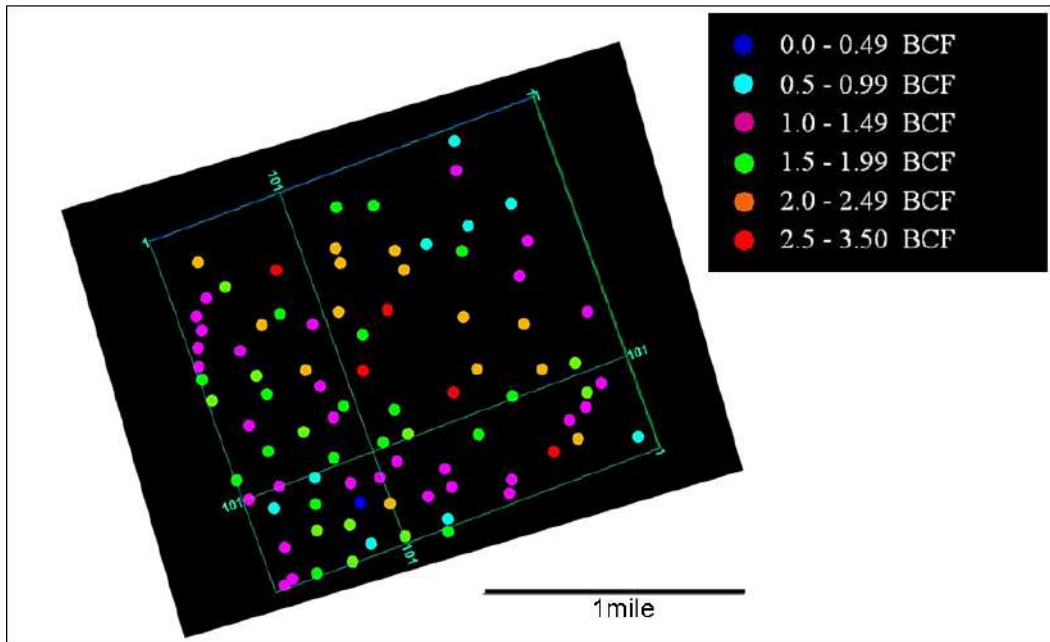


Figure 1.21. Estimate ultimate recovery (EUR) map (Williams Co.).

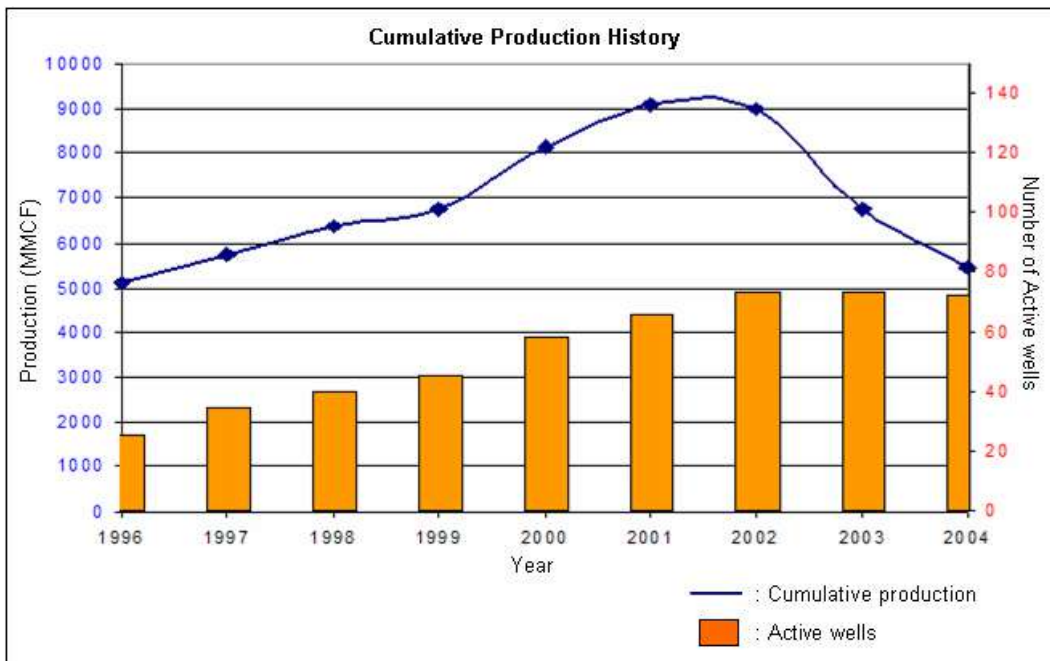


Figure 1.22. Cumulative gas production history 1996-2004 and the number of active wells.

Chapter 2

CROSS EQUALIZATION PROCESS

2.1. Introduction to the Cross Equalization Process

The success of the 4D seismic monitoring depends on the ability to analyze small changes of the seismic traces due to changes in the reservoir. The ability to produce repeatable traces is essential to differentiate small reservoir changes from the noises (Calvert, 2005). The cause of the non-repeatable noise may occur during data acquisition (Rickett and Lumley, 2001), for example the different in acquisition geometries (grid orientation, bin sizes, offset azimuths); different source waveforms or shooting direction; different receivers; positioning errors for source and receiver locations; different acquisition equipment; and changing near-surface conditions (weather, ambient noise). Other sources of noise are the different seismic processing flows and parameters (Rickett and Lumley, 2001; Ross et al, 1996). In seismic processing, the use of different processing parameters may generate additional noise for time-lapse analysis especially the different stacking velocities, different amplitude recovery equation and different migration techniques.

The trace repeatability can be analyzed quantitatively using the normalized root mean square (NRMS) differences (Kragh and Christie, 2002). The NRMS value varies between 0 and 2. The zero value indicates a perfect repeatable datasets, while value 2 indicates 180° phase rotation. The NRMS can be calculated from equation 2.1.

(Kragh et al, 2002)

Where :

- $\text{rms}(T_n)$: root mean square value of trace-n
- T_{1t} : Seismic trace from survey-1 for t time interval
- NRMS : normalized rms value in fraction

The best approach, as suggested by Calvert (2005), is to use well repeated seismic datasets for the time-lapse analysis. But even in the best case with a well repeated and similar acquisition parameter and processing flow, the presence of non-repeatable elements is real (Herawati, 2002; Rickett and Lumley, 2001). This analysis led to the importance of equalizing the time-lapse seismic traces to suppress these non-repeatable elements.

Rulison time-lapse seismic data used in this research consists of two seismic datasets acquired with different acquisition parameters. More detail on the acquisition parameters is explained in the previous chapter (Chapter 1.6.1.). The first seismic dataset, 1996 survey, was acquired prior to intensive gas production. The second dataset, 2003 survey, was acquired after 8 years of production with higher seismic resolution.

The type of seismic datasets used in this research is the type of seismic datasets available in most fields. Most of the hydrocarbon field has seismic datasets acquired before the production started and some seismic datasets acquired after a certain time period of hydrocarbon production. The ability to use the “old” dataset for 4D analyses will be very useful to give an indication of what is happening in the reservoir during the time of production.

To reduce the effect of the difference in seismic acquisition parameters, the approaches used in this research are the reprocessing of the seismic datasets followed by cross equalization of the post stack data. Reprocessing the seismic datasets was performed by Veritas in Calgary using similar processing flows and parameters to avoid adding more non-repeatable or non-comparable elements to the time-lapse analysis. The

post stack data as a result of this seismic reprocessing was then cross equalized to reduce the non-repeatable elements from the seismic acquisition.

2.1.1. Reprocessing of Time-lapse Seismic Data

In order to reduce noise in the time-lapse analysis, the seismic datasets should always be processed from pre-stack data in a consistent manner (Rickett and Lumley, 2001). For the Rulison time-lapse seismic datasets that have different acquisition geometries, the first important aspect of the reprocessing is the survey re-sampling to a common grid. The survey re-sampling is important to compensate for differences in geometries and acquisition parameters. After this process, the seismic datasets would have consistent bin parameters (bin size, azimuth coverage, offset coverage).

For time-lapse purposes, each of the seismic processing steps should be done consistently for each survey. The use of consistent processing parameters (velocity, static correction, dynamic correction) is an important part of this time-lapse processing. Previous research shows that the use of inconsistent processing parameter may lead to pitfalls in time-lapse analysis (Rickett and Lumley, 2001).

2.1.2. Cross Equalization of Time-lapse Seismic Data

Cross equalization (Ross et al, 1996) is a processing sequence applied on time-lapse seismic data with an objective to remove the differences in the data that are not related to reservoir changes. This process is performed in the post stack domain by correcting the monitor traces to match the base survey seismic traces. The correction is performed with respect to time, amplitude, magnitude, and phase (Ross et al, 1996).

$$t_{XEQ} = t^* f(S_{corr}, RMS_{corr}, M_{corr}, P_{corr}) \dots \quad \text{(Eq.2.2)}$$

(Ross et al, 1996)

Where :

- | | |
|----------------------------|------------------------------------|
| t_{XEQ} | : Traces after cross equalization |
| t | : Traces before cross equalization |
| S_{corr} | : Time correction |
| RMS_{corr} | : Amplitude balancing |
| M_{corr} | : Magnitude/spectral correction |
| P_{corr} | : Phase correction |

The filter to equalize the two time-lapse seismic datasets is estimated in the static portion of the data and then applied for the dynamic portion of the data (Duranti, 2001). In this static time window, no rock properties changes are expected. The effectiveness of the cross equalization process can be analyzed from the amplitude differences in the static portion of the data.

To analyze the amplitude differences of the static window and the effectiveness of cross-correlation process, an amplitude envelope of the differences is used. Amplitude envelope or reflection strength is a robust, smoothed, polarity-independent measure of the energy in the trace at a given time (www.edge.ou.edu). The amplitude envelope of the static window indicates the amount of energy from non-repeatable elements of the time-lapse dataset.

The first important correction in cross equalization process is the time correction (S_{corr}). This correction is performed especially to compensate for the different ground conditions between two surveys. When there is a difference in weather condition or soil condition between surveys, the near surface velocity will change. The change in the near surface velocity can generate a global time shift in the seismic traces. The time correction (S_{corr}) is performed to correct the time shift and reduce the effect of the different ground conditions (Rickett and Lumley, 2001; Duranti, 2001).

The second part of the cross equalization is amplitude balancing (RMS_{corr}). The amplitude balancing is performed to scale the data to the same amplitude or energy level (Rickett and Lumley, 2001). This correction is important to compensate for an alteration in the amplitude or energy level between surveys. The difference in the amplitude or energy level may occur due to the different in the source generated wavelet, the different in geophone responses, and difference in ground condition that absorbed the energy.

Another important correction in the cross equalization process is spectral balancing (M_{corr}). This process is performed to equalize the energy spectrum of time-lapse seismic datasets. The difference in the amplitude spectrum between time-lapse surveys is mostly caused by different bandwidth of the source generated wavelet (Rickett and Lumley, 2001).

The difference in the source generated wavelet between surveys can also generate a phase shift between traces. The occurrence of the phase shift in the time-lapse seismic datasets can generate an error in the analysis. Ross (1996) showed that only a small phase mismatch (15^0) could generate an amplitude difference error of 20%. The phase correction (P_{corr}) is performed to correct for this phase lag.

2.2. Reprocessing of Rulison Time-lapse Seismic Data

The Rulison time-lapse seismic datasets consists of the 1996 seismic data and 2003 seismic data. Both seismic datasets were acquired using different acquisition parameters. A complete detail of acquisition parameters is explained in chapter 1 (table 1.1). To reduce the differences in acquisition parameters, both seismic volumes were reprocessed with similar processing parameters. The seismic processing of these datasets was performed by Veritas Geosciences.

The first important parameter difference is the different offset coverage from both volumes. In general, the Rulison 1996 and 2003 seismic volumes have a different offset

coverage. The 2003 data has more traces in the near offset while the 1996 data has more traces in the far offset (Benson, 2005, pers. comm.). Other important acquisition parameter difference is the difference in azimuth coverage. The Rulison 2003 seismic data covers more azimuths than the 1996 seismic data in most parts of the area.

To reduce the effect of these differences (offset coverage and azimuth coverage), a re-binning process was performed. The re-binning process includes the process to choose the stacked traces for each bin. Since both volumes has a different natural bin size (table 1.1). The bin size was set to be 110 ft x 110 ft for both seismic volumes. To achieve a comparable offset coverage, the 2003 dataset was truncated in the near offset traces while the 1996 data was truncated in the far offset traces (Benson, 2005, pers. comm..).

Due to the acquisition parameters, some of the seismic bins do not have enough traces to cover all offset in the defined offset range. Some seismic bins also do not have enough traces to cover all azimuths. This situation can be illustrated in Figure 2.1.a. To generate bins with similar offset and azimuth coverage, a bin sharing procedure was applied to the datasets. The bin sharing process (Ansorger and Kendall, 2004) was performed by dividing each bin into sectors (Figure 2.1.b). Each part of the sector azimuth and offset should have a trace to represent it. If some specific sectors do not have a trace to represent it, the trace is borrowed from a nearby bin for the same azimuth and offset. After the bin sharing procedure, each bin in both volumes had similar azimuth and offset coverage (Ansorger and Kendall, 2004).

Other seismic processing procedures were performed using similar parameters for both datasets. The complete processing flow for this datasets is shown in Figure 2.2. The static corrections (refraction, residual and trim) were performed independently for each volume but with the same parameters (Ansorger and Kendall, 2004). All other processing parameters i.e. spherical divergence, deconvolution, and velocity model were identical in both volumes. After all the processing procedures were applied, the traces were then

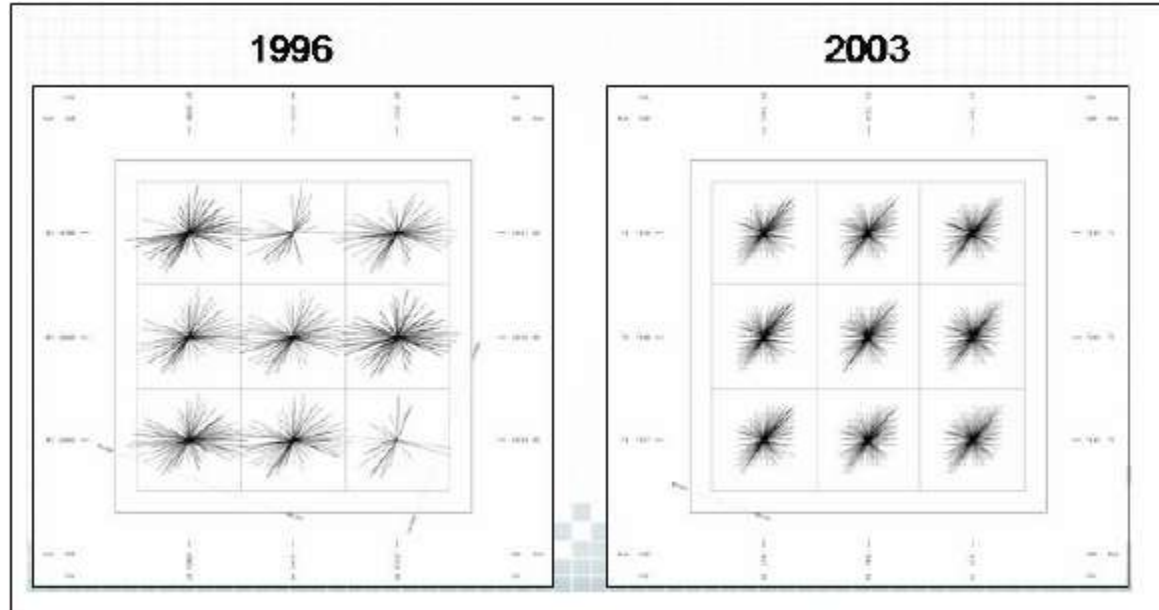


Figure 2.1.a. Offset coverage and azimuth coverage comparison between surveys.
(Winarsky and Kendall, 2004)

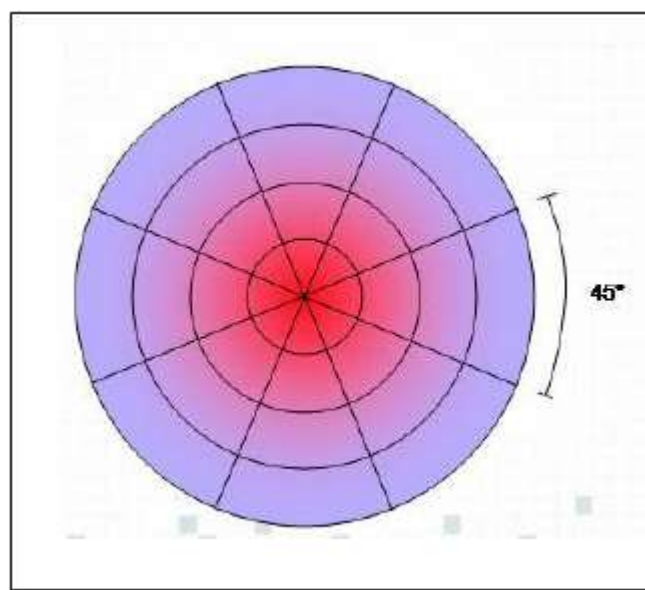


Figure 2.1.b. Sector divisions for seismic bins (Winarsky and Kendall, 2004).

Rulison P-Wave Processing Sequences

- Tilt Correction for Vectorseis phone applied in Field
- Demultiplex/Geometry/First Break Picks
- Refraction Tomography Statics
- Manual Trace Edits/ Amplitude Recovery – T2
- Surface Consistent Amplitude Equalization and Deconvolution
- Velocity Analysis (Preliminary)
- Surface Consistent Statics (Preliminary)
- Velocity Analysis (Final)
- Surface Consistent Statics (Final)
- First Break Mutes
- Trim Statics
- Amplitude Equalization – Mean Scaling
- Stack
- Noise Attenuation (FXY Deconvolution)
- Migration – Kirchhoff
- Filter – 5/10-100/110Hz 0-1600 ms, 5/10-80/95Hz 1600-2800 ms
- Amplitude Equalization – Mean Scaling



Figure 2.2. Rulison P-wave processing sequences.

(Winarsky and Kendall, 2004)

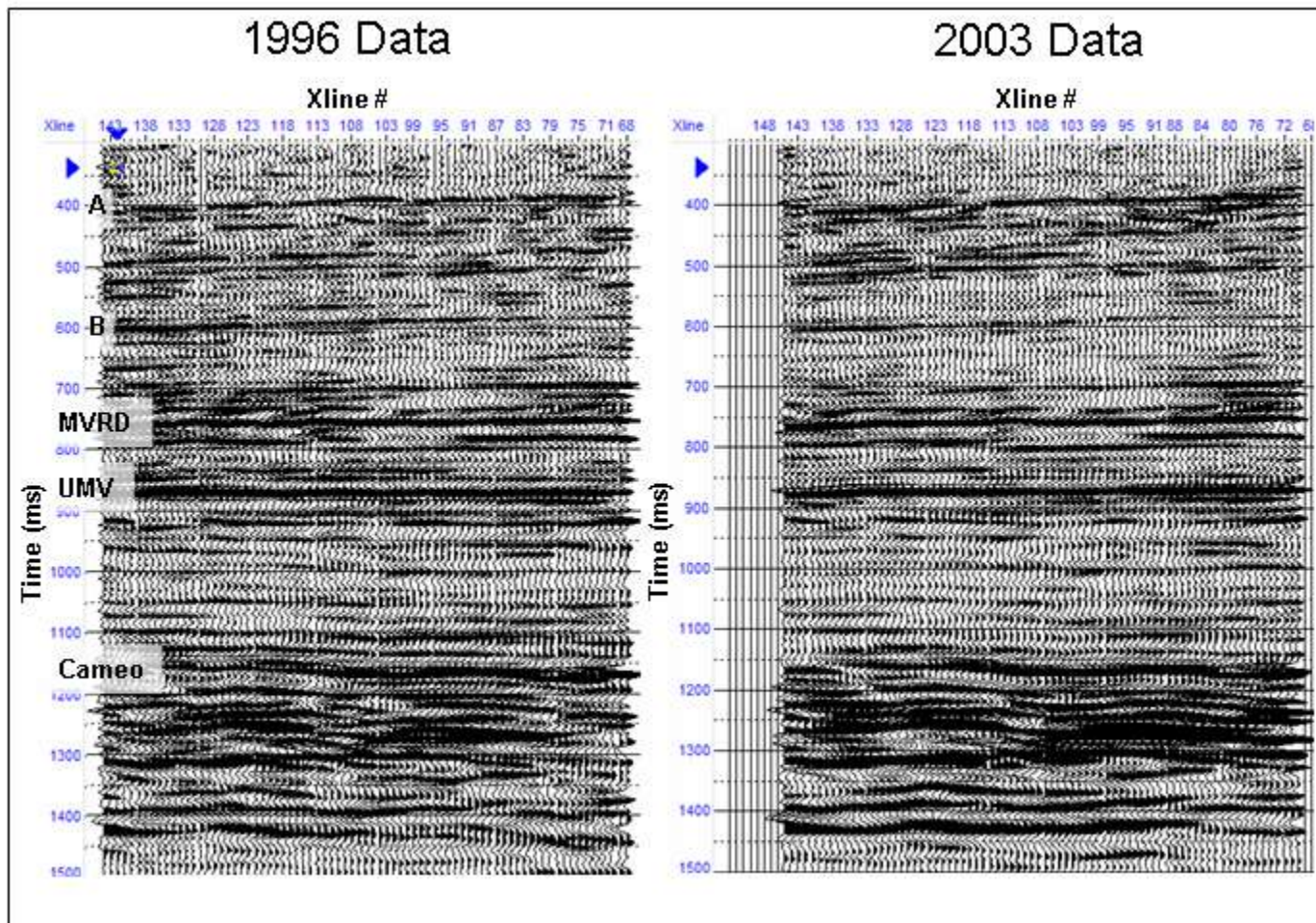


Figure 2.3. Seismic sections from 1996 dataset and 2003 from inline 63 after processing with time-lapse workflow.

stacked and migrated in the new bin geometry (Ansorger and Kendall, 2004). The resultant seismic sections are shown in Figure 2.3.

2.3. Cross Equalization of Rulison Time-lapse Seismic Data

During the period 1996 – 2003, most of the hydrocarbons produced in Rulison field were predicted to come from the Williams Fork Formation (see explanation in chapter 1.5.). The major producing interval ranges from the UMV shale to Cameo (Figure 2.3). Some wells in this area also produced from the Cameo coal interval. But, there are no hydrocarbons produced from above the UMV shale horizon. Based on this information, the author defined the static window interval from 300 – 800 ms which is above the interpreted UMV shale horizon. The amplitude difference appearing in this static window interval is mostly caused by the non-repeatable elements of the acquisition process.

In this static window interval there are some horizons that can be identified such as horizons A and B (Figure 2.3). These horizons are consistently defined in both datasets and have strong amplitudes. The cross equalization process can be analyzed by determining how well this process can equalize these horizons.

The amplitude differences between both datasets (Figure 2.4.a) indicate the existence of high amplitude differences in the static window interval. Most of the amplitude differences appear in the western part of the overlap area. The amplitude envelope differences (Figure 2.4.b) give a quantitative measurement of the amount of energy left in the static window interval. For further analysis of the cross equalization process, the amplitude envelope differences are used.

The distribution of NRMS value on this time-lapse datasets (Figure 2.5) is generated to analyze the repeatability of the seismic traces. NRMS values are calculated using equation 2.1. High NRMS values indicate low trace repeatability. The NRMS distribution indicates low trace repeatability especially in the southwestern

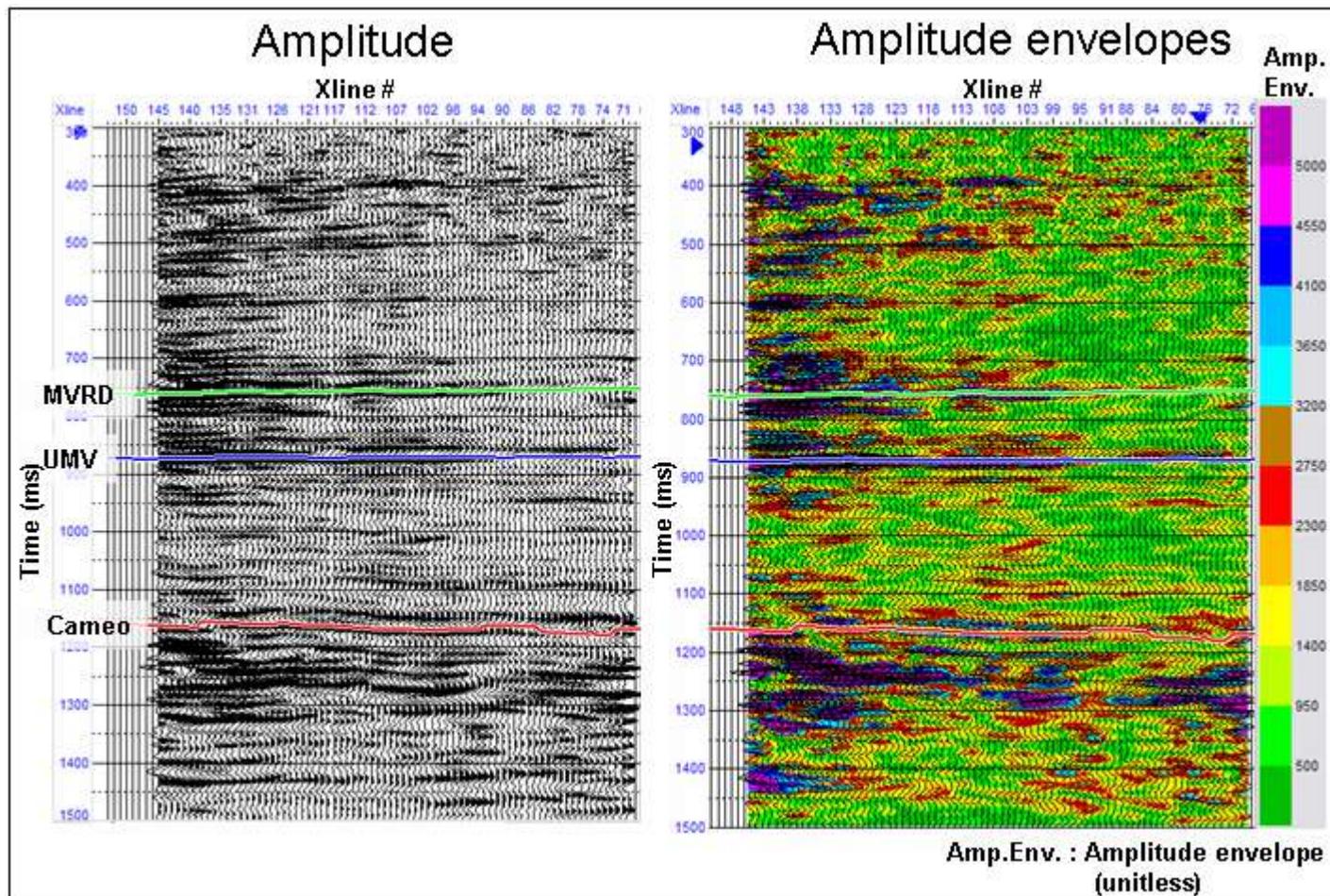


Figure 2.4. (a) Amplitude differences between surveys. (b) Amplitude envelope differences between surveys from inline 63.

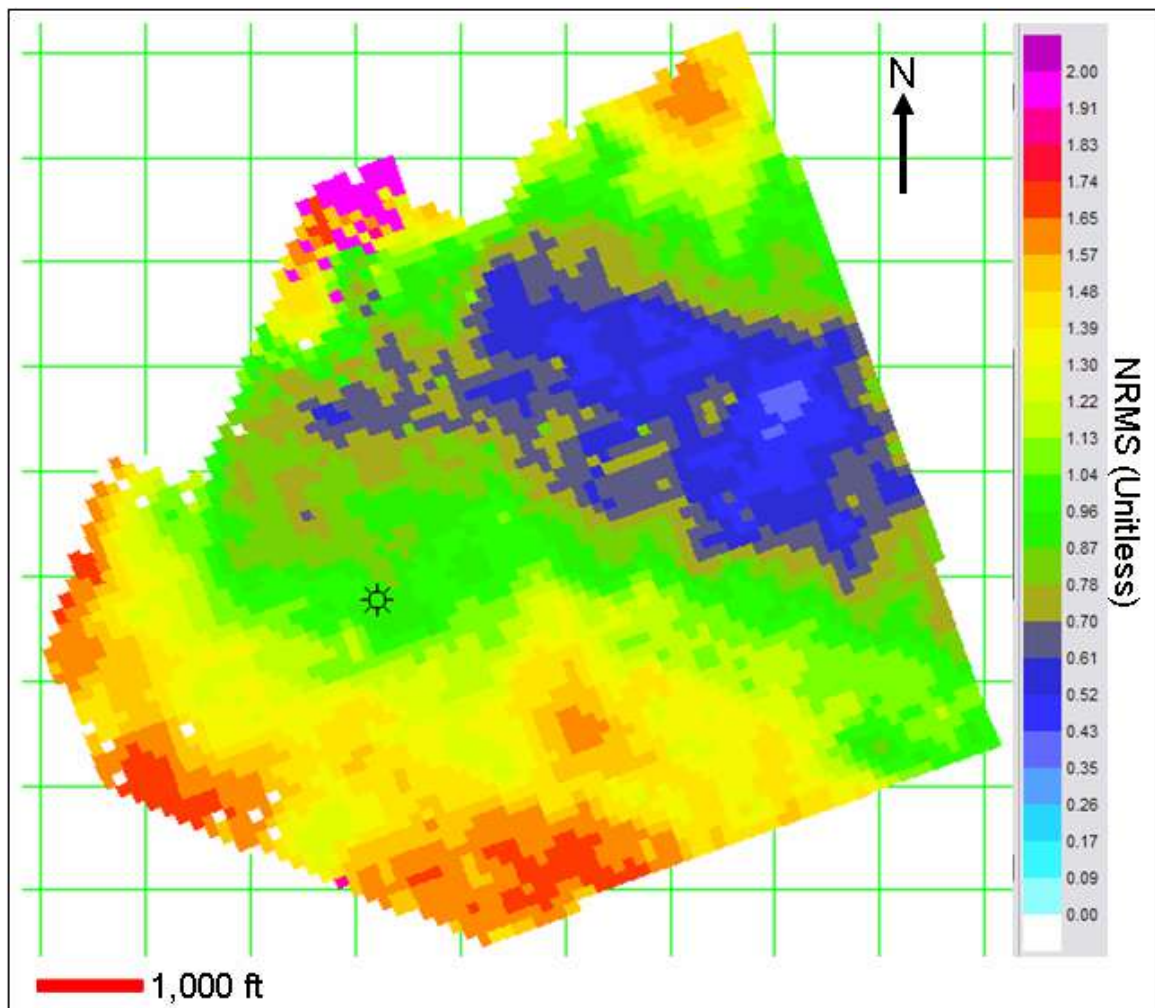


Figure 2.5. NRMS value of the static window interval before post-stack cross equalization process.

part. The trace repeatability is much lower near the edge of the surveys. The edge area has much lower fold coverage that causes a higher non-repeatable noise content.

Based on the analysis of the amplitude envelope differences and the distribution of NRMS value, the author determines that these seismic datasets need to be cross equalized to reduce the non-repeatable noise in the data. The cross equalization process is performed on these post stack seismic data. The correction includes correction for time and phase matching, spectral balancing, amplitude balancing and time-variant time shifting correction.

2.3.1. Time and Phase Matching

The first process of cross equalization is the time and phase matching (S_{corr} and P_{corr}). As explained in the previous section, the time and phase differences may occur due to different ground conditions and different source generated wavelet between surveys. For the Rulison time-lapse datasets, a different seismic source is a dominant factor affecting time and phase differences. Ground conditions might have also changed significantly.

The seismic surveys (1996 and 2003 survey) were conducted with different seismic sources. The first seismic survey was conducted using AHV-II vibrator with frequency ranges 16 – 96 Hz while the second survey used AHV-4 and VIBPRO 3X with frequency ranges 5 – 125 Hz (Ansorger and Kendall, 2004). The differences in seismic source and frequency ranges of the source between surveys had generated a different source wavelet in the time-lapse volumes.

Cross-correlation between both seismic datasets is generated to measure any time lag between traces. The cross correlation result (Figure 2.6) shows the appearances of global time shift between both datasets. It is indicated by the shift of the highest amplitude of the cross correlation from the zero time. The distribution of the time shift

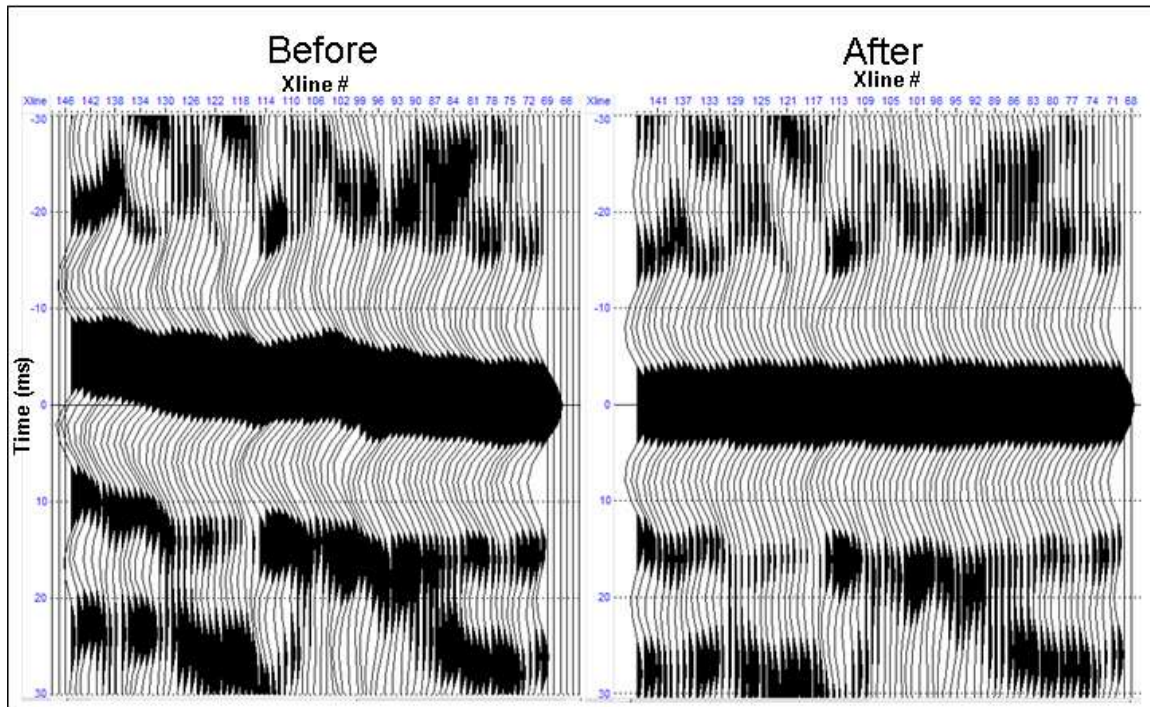


Figure 2.6. Cross-correlation plot of the trace in static window interval before and after time-shift correction from traces inline 63.

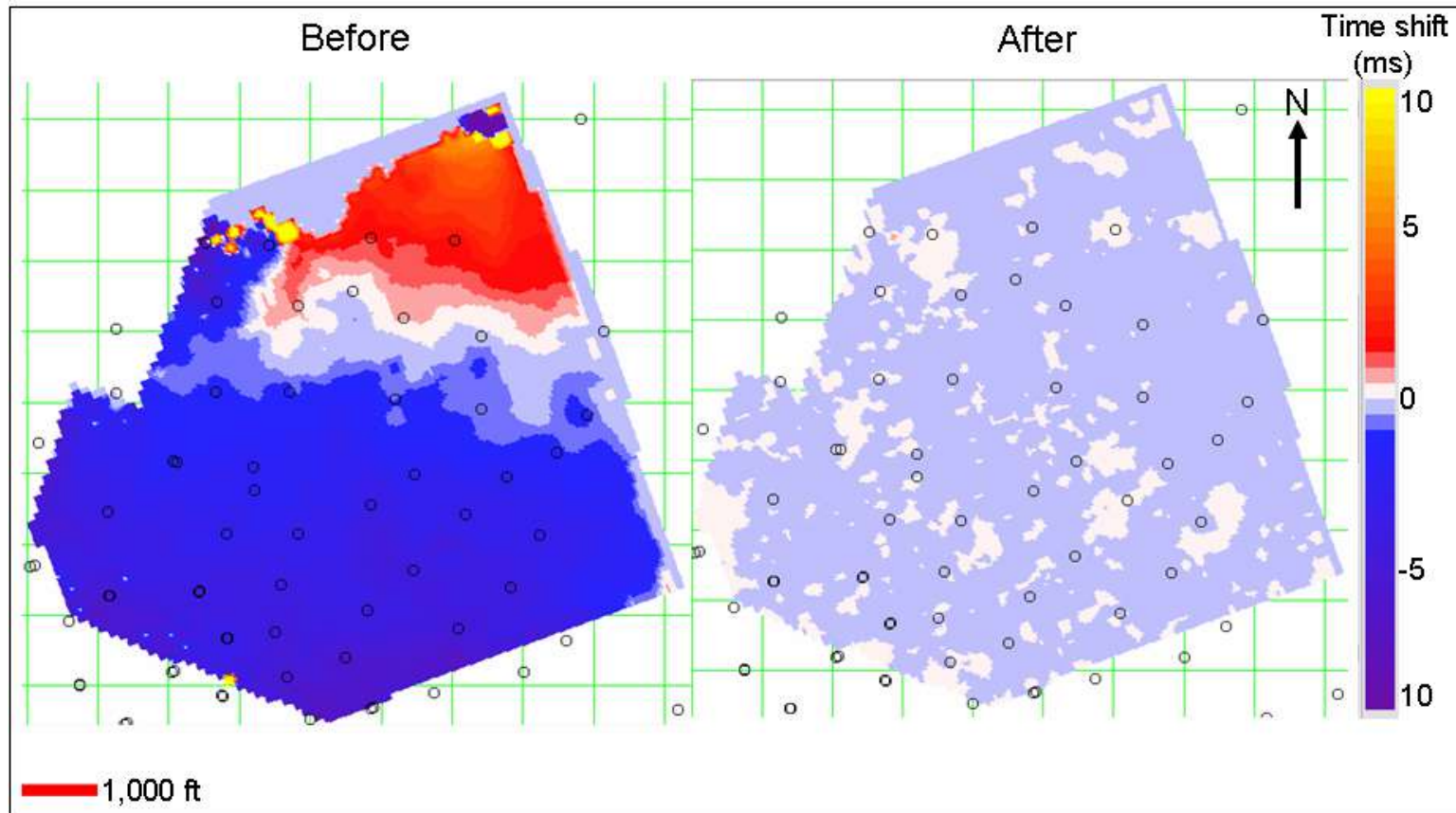


Figure 2.7. Distribution of time shift between the time-lapse datasets over the static time window interval, before and after time-shift correction.

between datasets on the static window interval (Figure 2.7) shows a general negative time lag in the southern part of the area and a positive time lag in the northern part of the area. The negative time lag indicates that the second survey (2003 survey) has a relatively lower near surface velocity than the initial survey (1996 survey). The positive time lag indicates otherwise.

The highest time lag of about 8 ms appears in the northern part of the area. The northern part of the area has rough topography and less bin coverage compared with other part of the area. The rough topography affects the repeatability of the seismic traces and generates a high global time shift.

The time correction is performed on the seismic datasets to reduce the time lag. The phase matching is also performed simultaneously to correct for smaller phase shifting. The filter for time correction and phase matching is estimated in the static time window interval (300-800 ms) on a trace-by-trace basis. The correction for the entire volumes is performed based on this filter.

The plot of the cross correlation between the two datasets (Figure 2.6) indicates that the time correction and phase matching has successfully reduced the time lag between the surveys. It is indicated by the distribution of the highest amplitude in the zero times after the correction is applied. Figure 2.7 shows that most of the time lag has been reduced to less then 0.5 ms, which is less then the seismic sampling interval (2 ms). The time lag left after the correction has a random pattern.

Analysis is performed to compare NRMS value between time-lapse data before and after time shift correction. Figure 2.8 shows distribution of average NRMS value for static window interval. This figure (Figure 2.8) indicates a large reduction in NRMS value of time-lapse data after time shift correction. Analysis is also conducted using the distribution of NRMS value and correlation coefficient before and after the correction (Figure 2.9). Correlation coefficient in this figure (Figure 2.9) indicates the maximum correlation value over static interval. Figure 2.9 shows that time shift

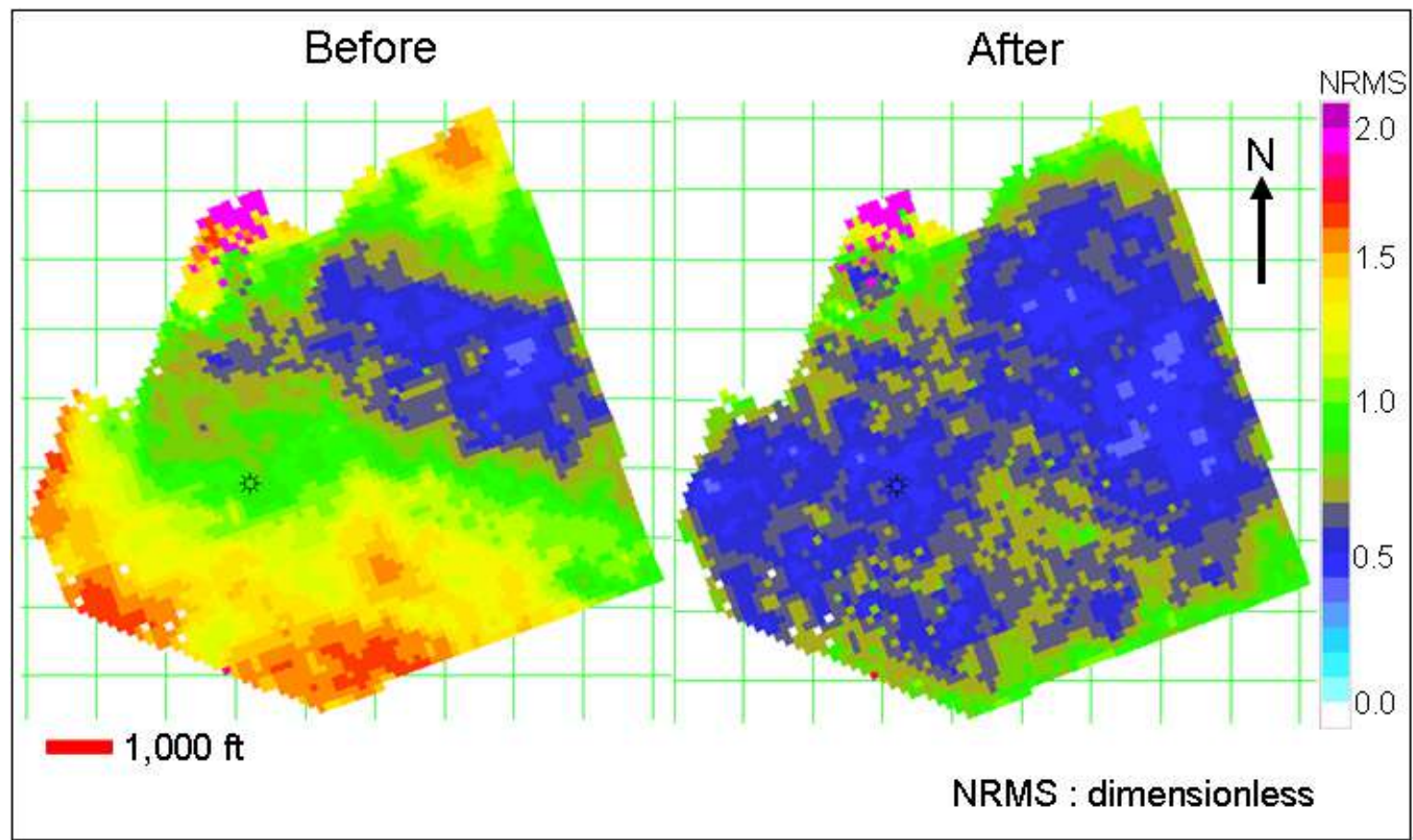


Figure 2.8. Comparison of NRMS values before and after time correction at static window interval.

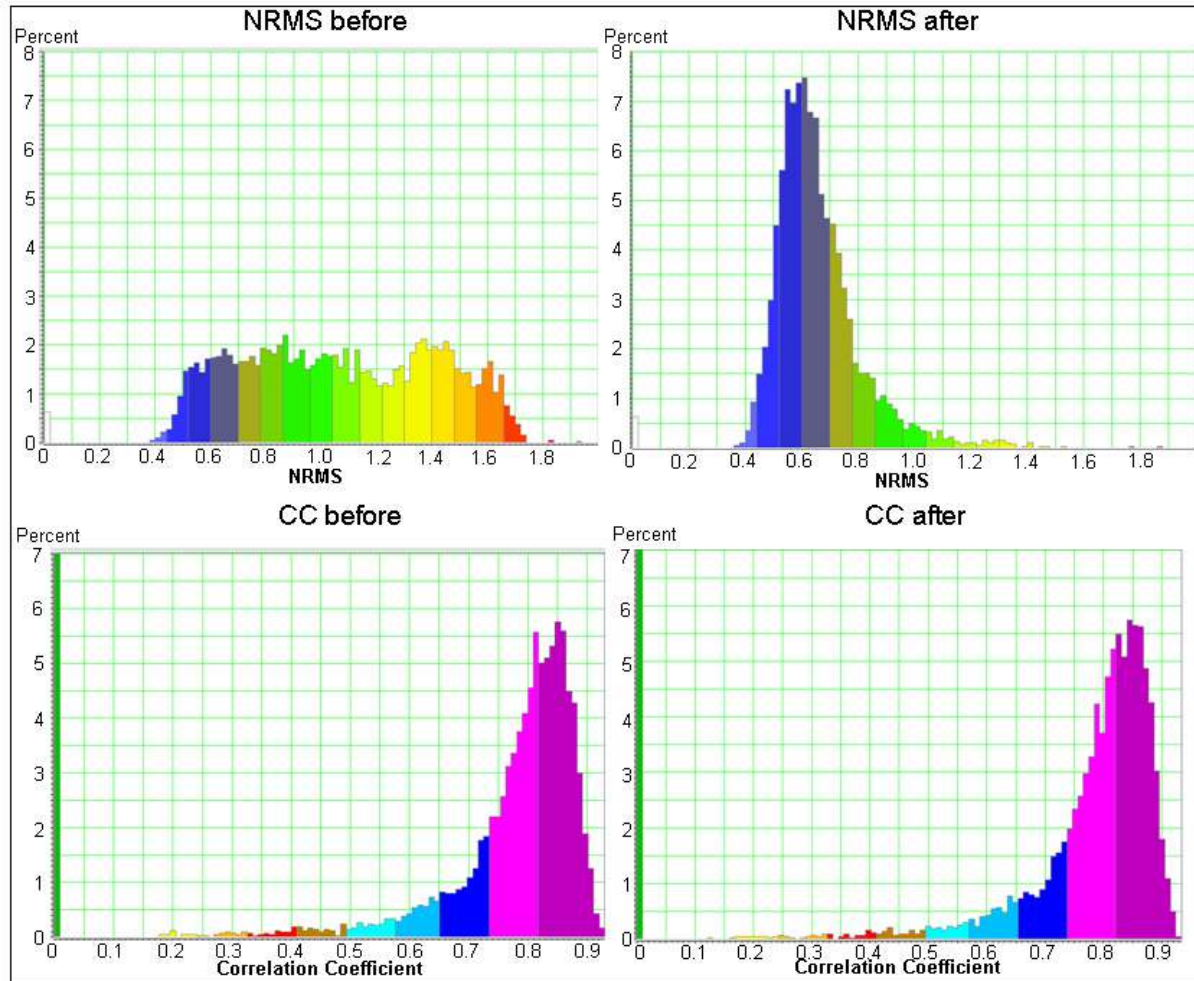


Figure 2.9. Distribution of NRMS values and correlation coefficient values before and after time correction at static window interval.

correction has successfully reduced NRMS value from an average of 1.0 to 0.6. This reduction indicates the improvement of repeatability between seismic traces.

To analyze the effect of time shift correction on the time-lapse data, the amplitude envelope differences are generated (Figure 2.10). The amplitude envelope differences show a high reduction of the amplitude on the static window after the time correction. A high reduction of amplitude and high reduction of NRMS value gives an indication that the time correction has successfully equalized both datasets in term of time equalization.

The phase matching is also performed to correct for phase shift between seismic data. Figure 2.11 shows the distribution of average NRMS value before and after phase shift correction. There are slight improvements of NRMS value that can be identified especially in the middle of area. Distribution of NRMS value and correlation coefficient is also analyzed (Figure 2.12). This figure (Figure 2.12) shows an improvement in NRMS value. This improvement can be identified by the reduction in high NRMS value and increase in low NRMS value. A slight increase in correlation coefficient can also be detected in this figure (Figure 2.12). The decrease in NRMS value and increase in correlation coefficient indicates that phase correction has successfully increased the repeatability of time-lapse data.

2.3.2. Spectral Balancing

A second important part of the cross equalization process is spectral balancing (M_{corr}). The differences in frequency spectrum of seismic traces between surveys can occur due to a difference in the source generated wavelet, difference in receiver type and ground condition (section 2.1.2. Cross equalization of time-lapse seismic data). These conditions appear during Rulison time-lapse surveys.

To analyze the differences in frequency spectrum between the two seismic volumes, global frequency spectrum of the seismic traces from the 300 -1500 ms time

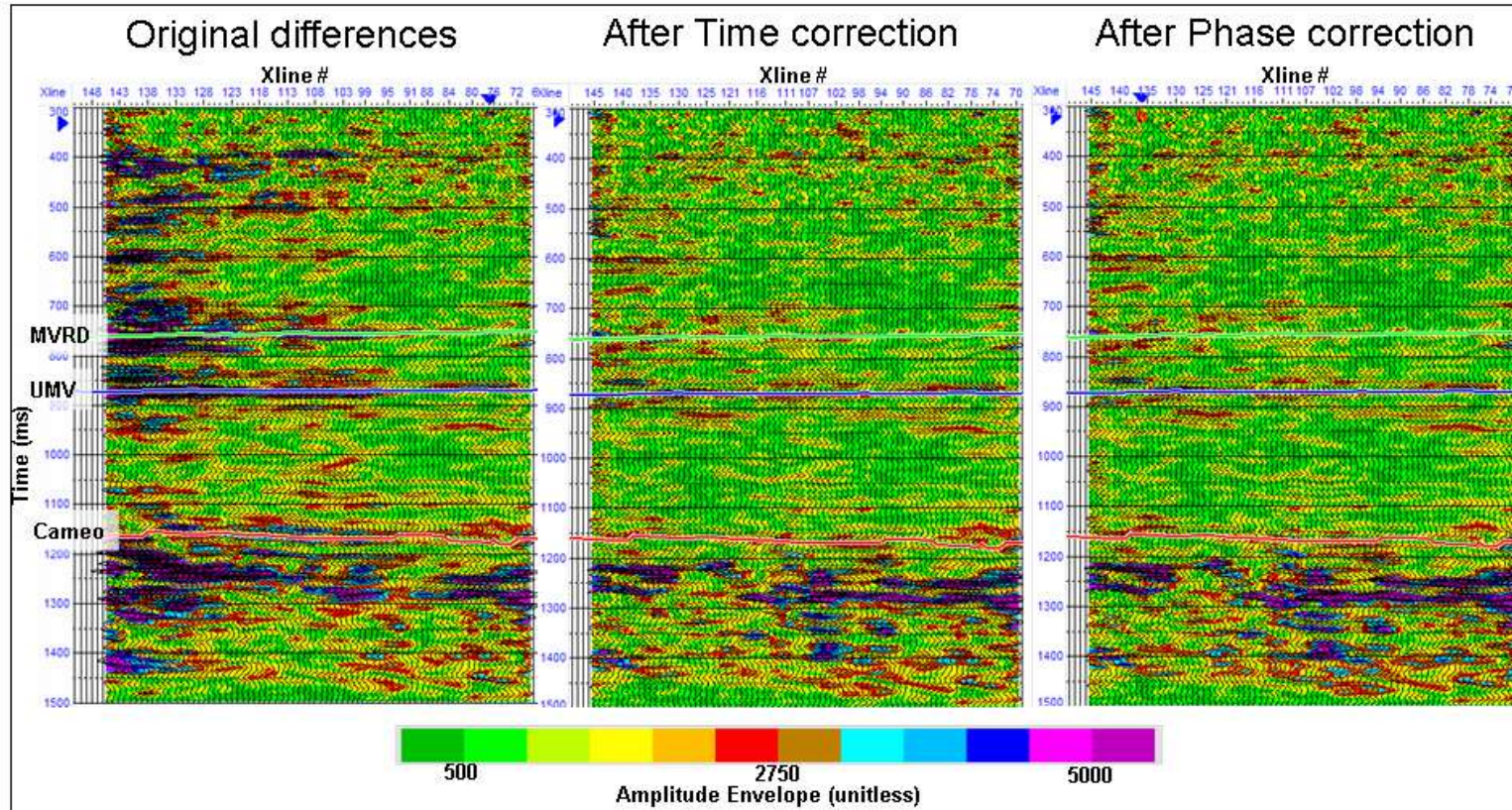


Figure 2.10. Amplitude envelope differences (inline 63) between the two data sets before and after time and phase correction.

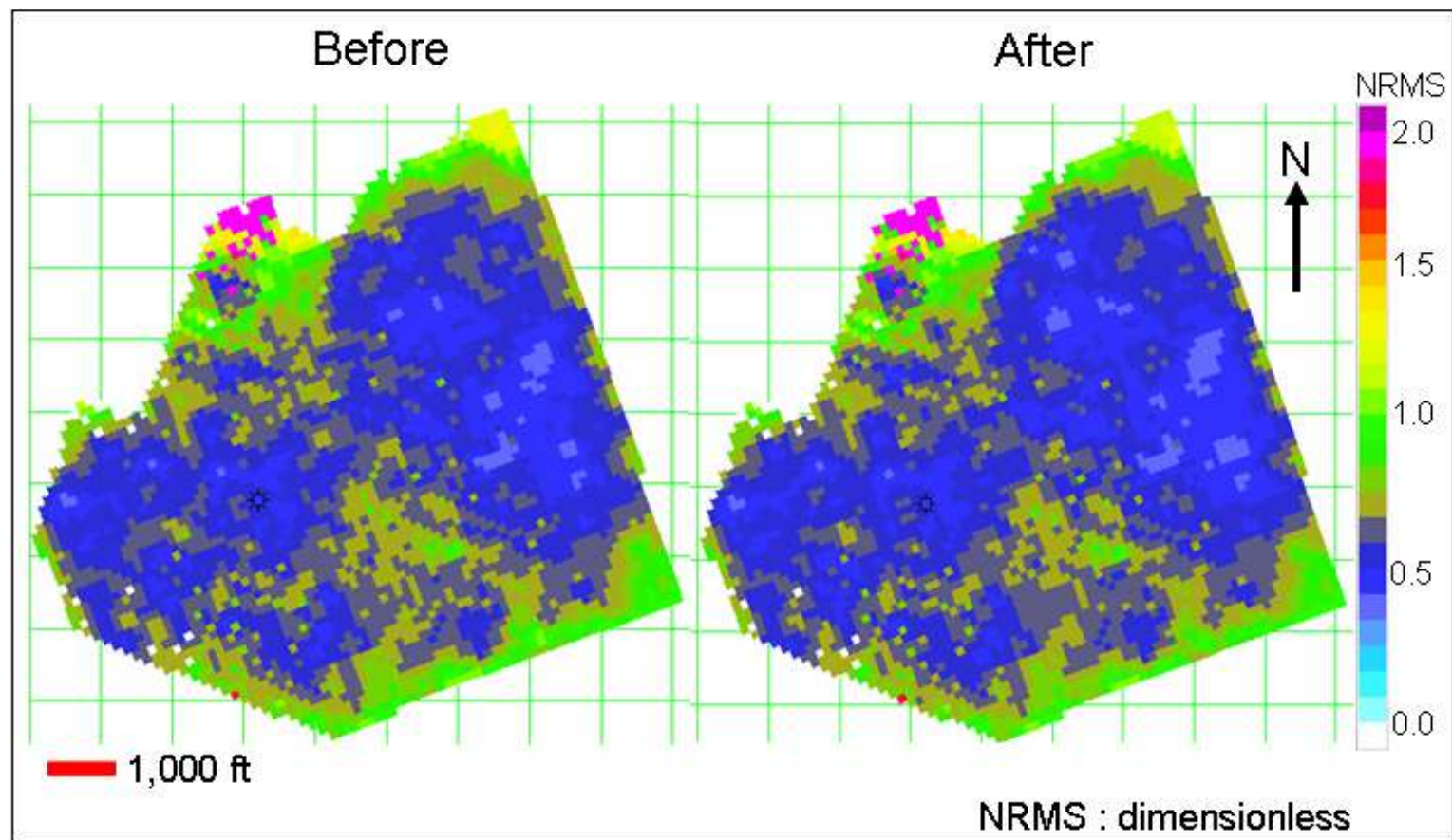


Figure 2.11. Comparison of NRMS values before and after phase correction over the static window interval.

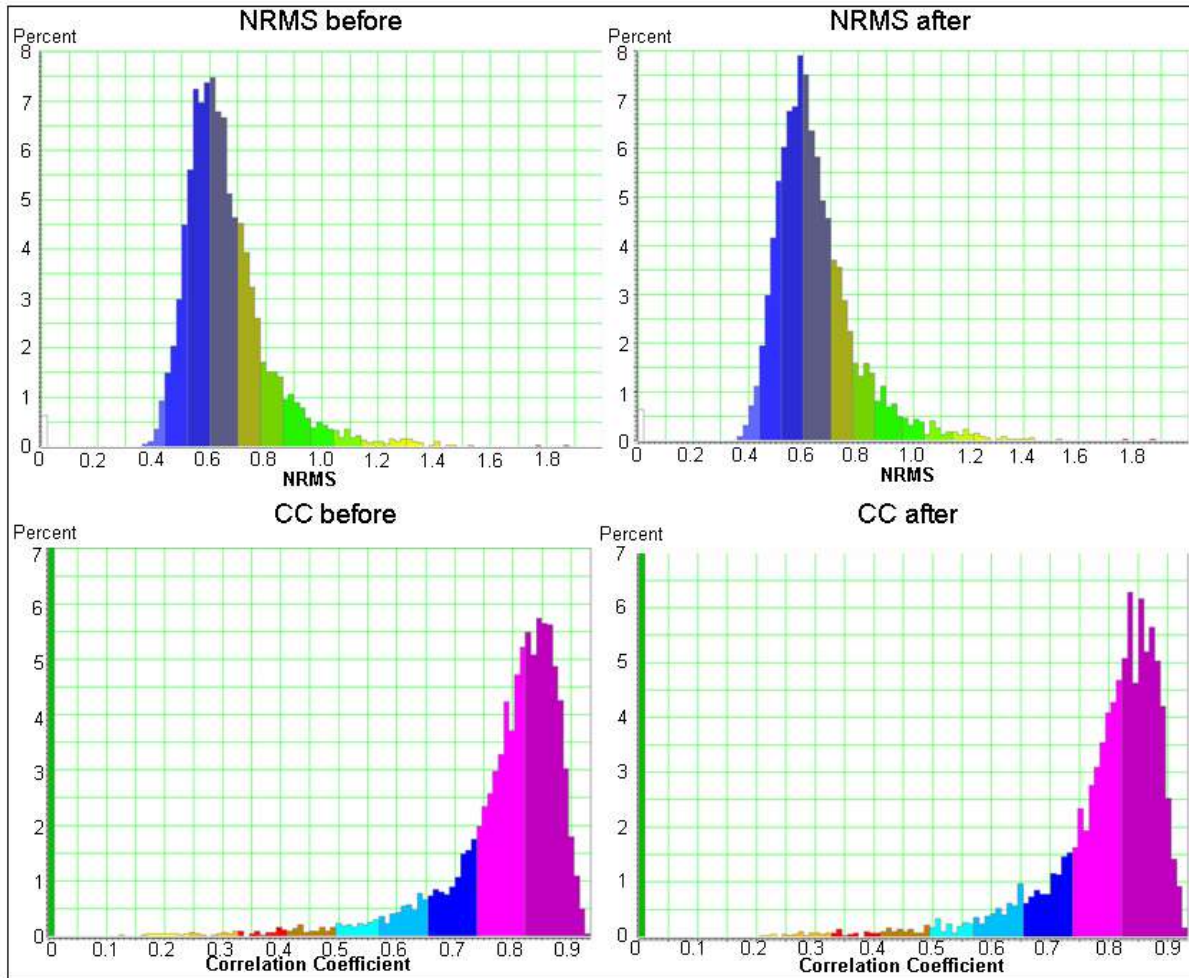


Figure 2.12. Distribution of NRMS values and correlation coefficient values before and after phase correction at static window interval.

window is calculated. The frequency spectrum of the datasets (Figure 2.13) indicates that both volumes have a similar spectrum frequency content in the low frequency region. In the high frequency region, the monitor data (2003 survey) has higher amplitude than the base data (1996 survey).

The spectral balancing process is performed by equalizing the frequency spectrum of the monitor data to the base data using a frequency filter operator. Since the monitor data has relatively higher frequency content, the process to match with the lower frequency data can significantly reduce high frequency noise. The filter operator (shaping filter) is designed using only the seismic traces that have a minimum correlation coefficient of 0.6. This trace limitation can avoid the use of traces with high non-repeatable elements in the filter operator. Figure 2.14 represents the shaping filter used for spectral balancing of both volumes.

After the spectral balancing process, the frequency of both seismic volumes has a more comparable frequency spectrum as shown in Figure 2.13. The spectral balancing process also affects the amplitude differences of the static time window (Figure 2.15). This process has helped to reduce more of the energy left in the static time window caused by the non-repeatable element of time-lapse especially around time 400 ms.

Analysis of NRMS value is then performed to analyze the effect of spectral balancing in trace repeatability. Figure 2.16 shows distribution of average NRMS value for the static window interval. There are significant reductions in NRMS values that can be identified in the western part of the area. Analysis is also conducted using the distribution of NRMS value and correlation coefficient before and after the correction (Figure 2.17). There are significant increases in low NRMS values identified in Figure 2.17. The distribution of correlation coefficient also shows significant increases. These two factors strongly indicate an improvement of repeatability between seismic traces after a spectral balancing correction.

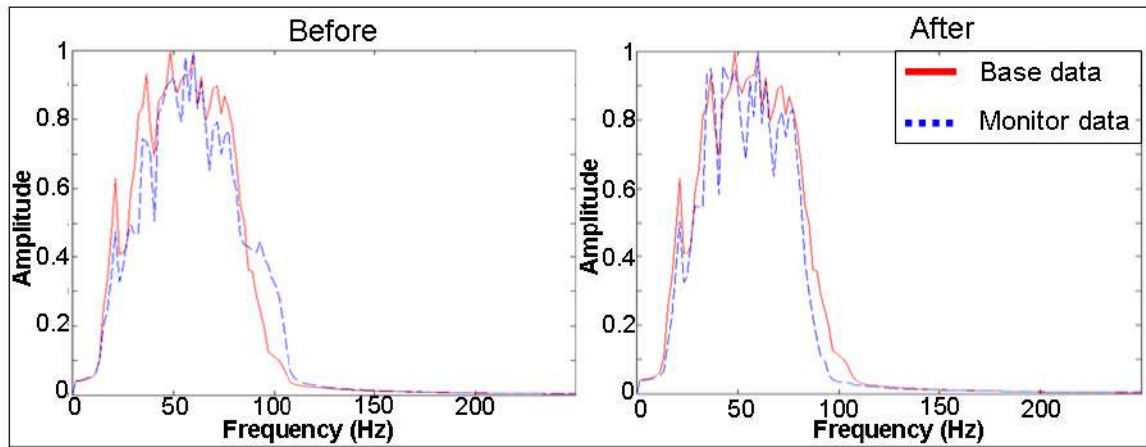


Figure 2.13. The frequency spectrum of the seismic data before and after spectral balance correction.

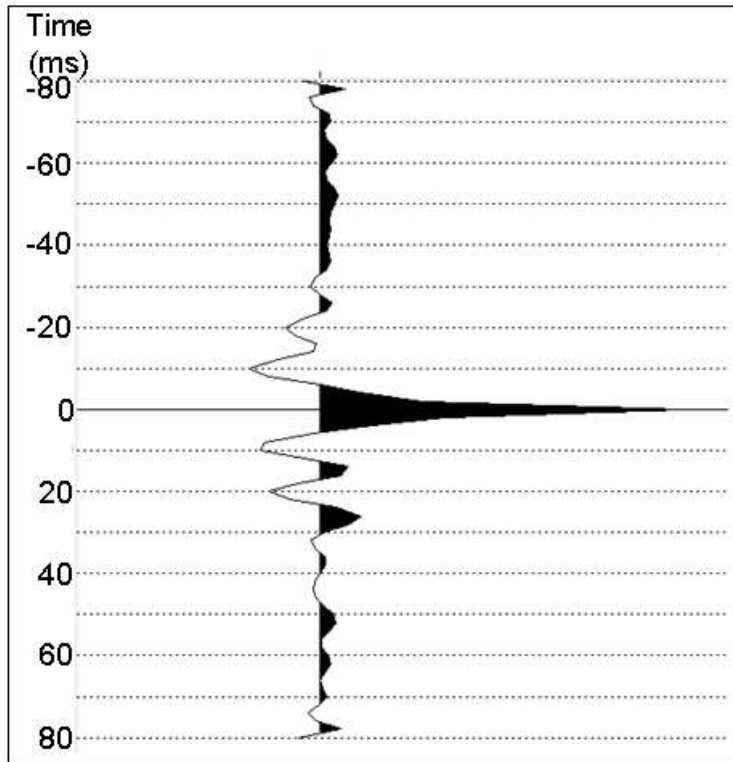


Figure 2.14. The frequency filter used in the spectral balancing process.

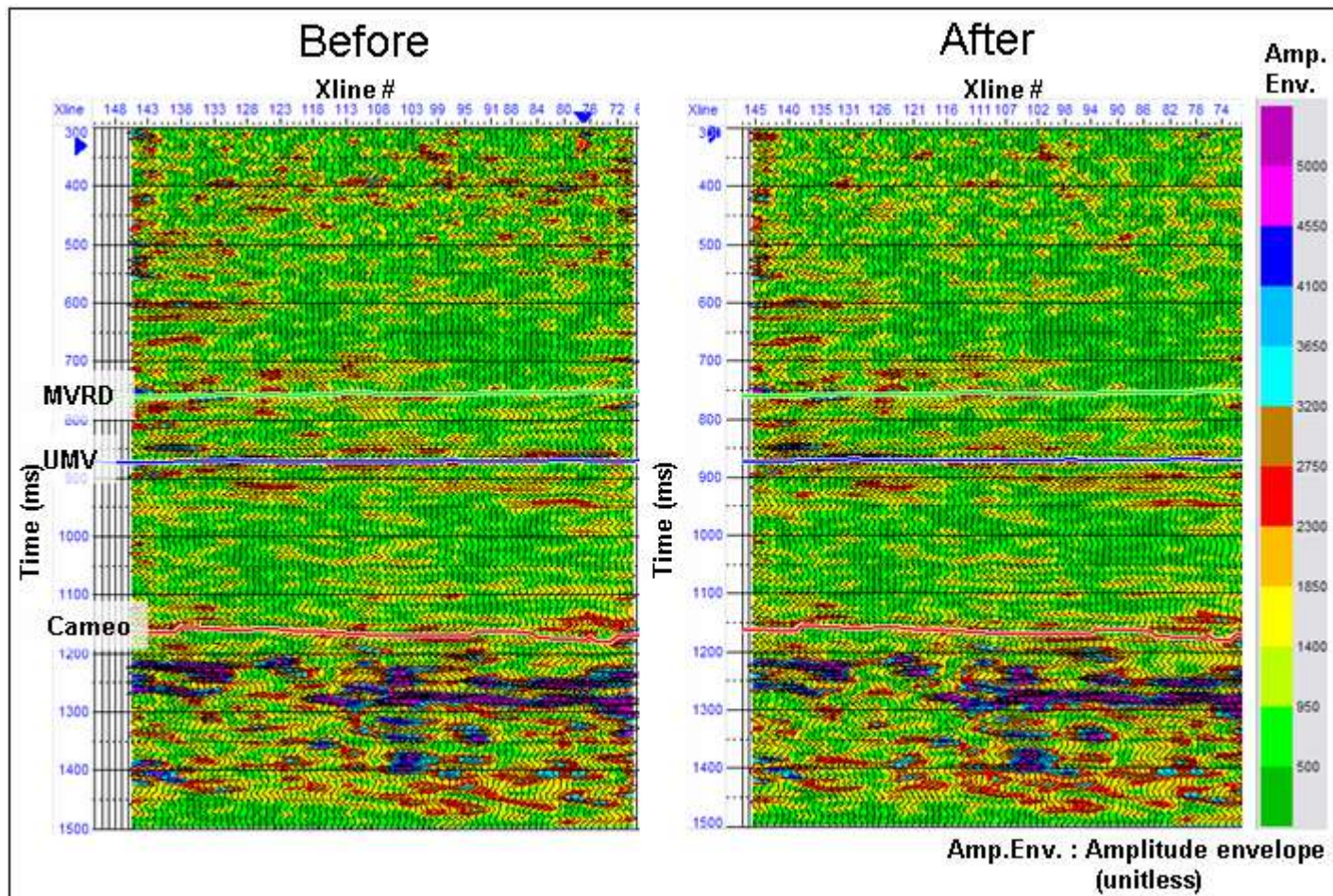


Figure 2.15. Amplitude envelope differences between the two data sets before and after spectral balancing from inline 63.

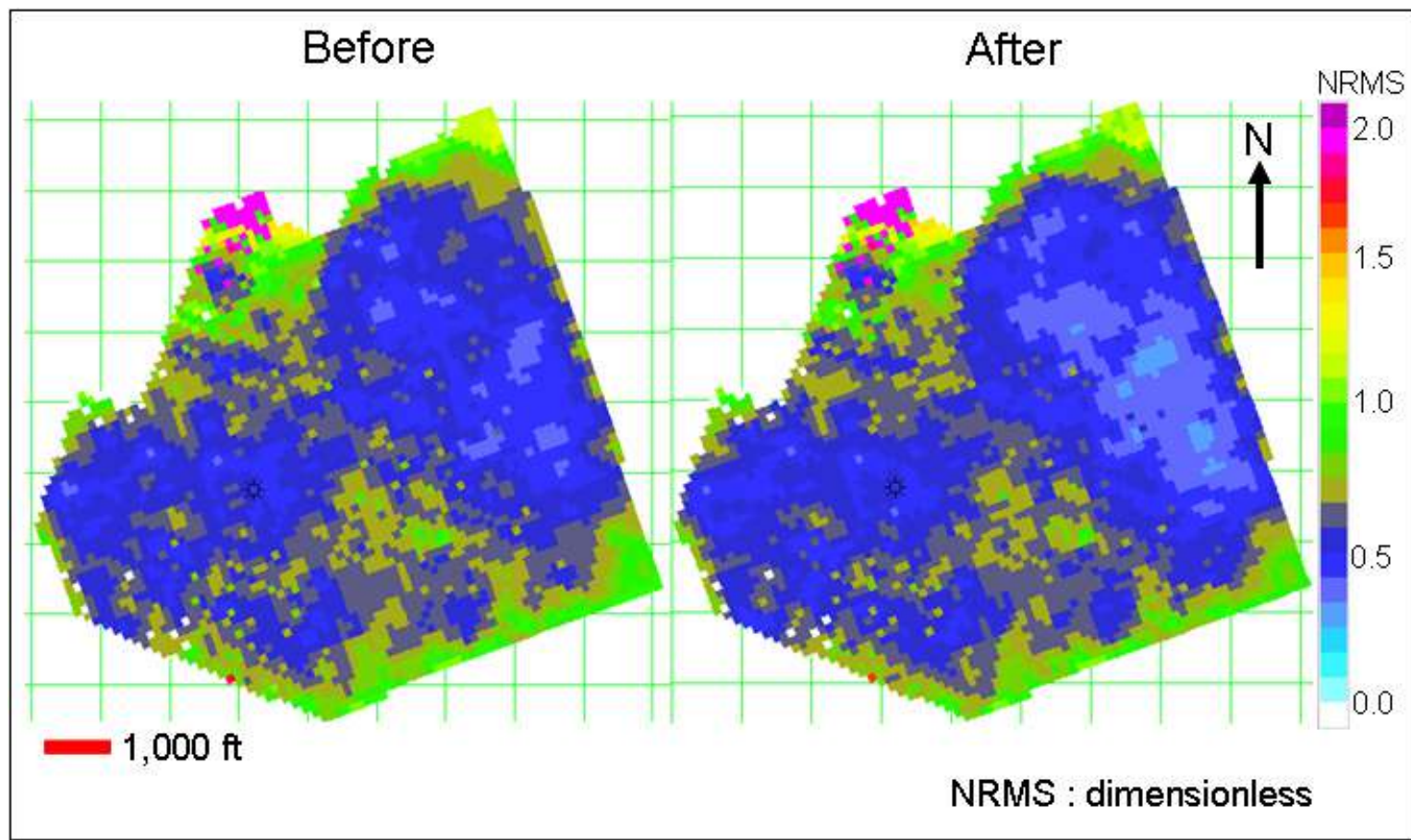


Figure 2.16. Comparison of NRMS values before and after spectral balancing at static window interval.

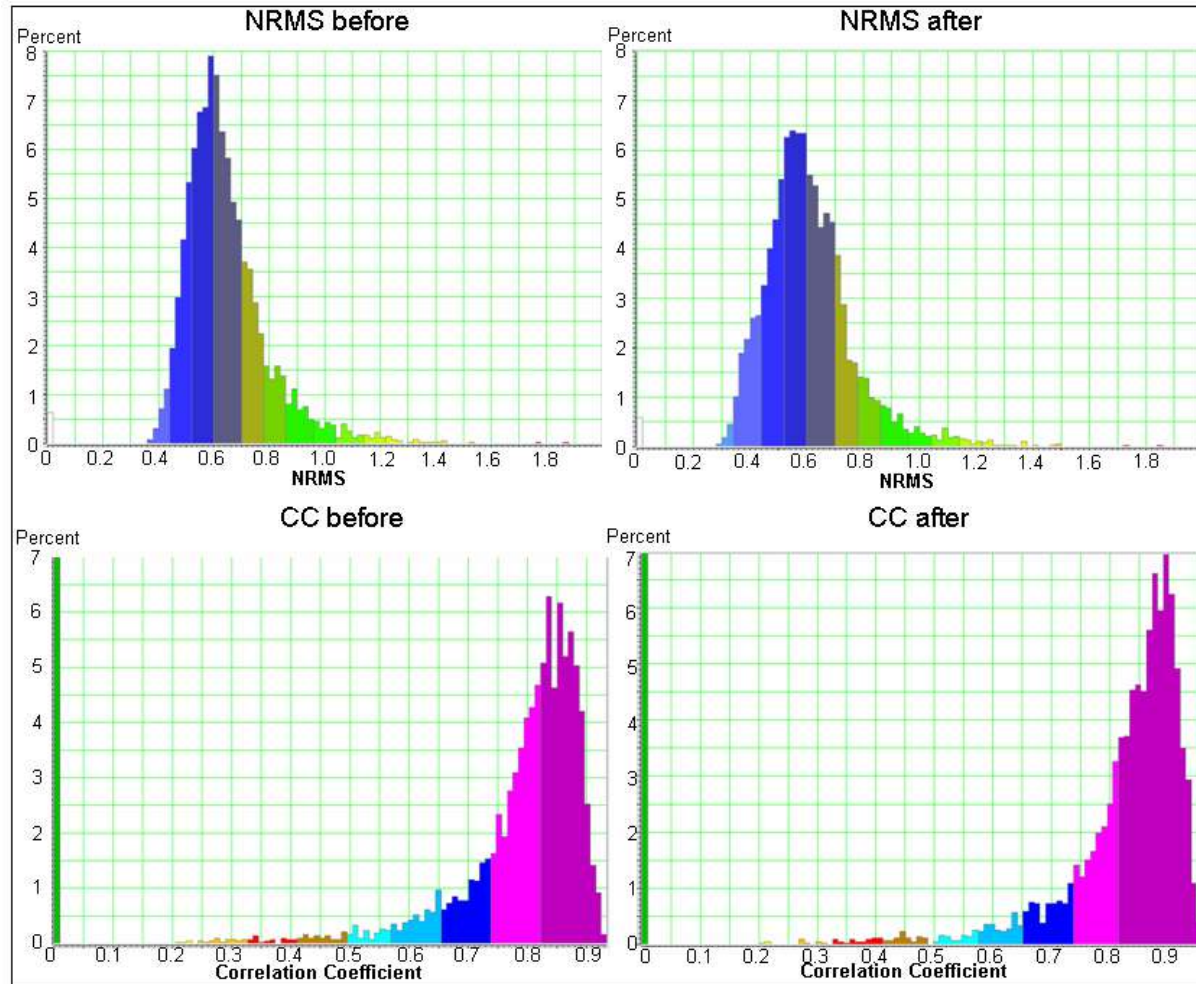


Figure 2.17. Distribution of NRMS values and correlation coefficient values before and after spectral balancing over the static window interval.

2.3.3. Amplitude Matching

The amplitude matching is a process to match the energy level between surveys. The amplitude matching is an important process to equalize the seismic traces between surveys especially if the survey is conducted using different types of sources, different types of geophones and different ground conditions.

The Rulison time-lapse seismic surveys were conducted using different types of sources and receiver. The global amplitude level of the Rulison time-lapse data might differ for each survey. To analyze the differences in the amplitude level between the time-lapse datasets, the average amplitude comparison is calculated. The average amplitude comparison is generated by dividing the average RMS amplitude of the 2003 data compare with the average amplitude of the 1996 data for the static window interval (300-800 ms). The distribution of average amplitude comparison (Figure 2.18) indicates that most of the western region of the area has a high amplitude comparison value. In some areas the value reaches 1.4-1.5. This value indicates that in this area, the monitor data (2003 dataset) has a higher average amplitude level then the base data (1996 dataset).

Based on the distribution of the average amplitude comparison, the amplitude level of the monitor data is then corrected to match the amplitude level of the base data. The correction is performed on a trace-by-trace basis for the entire window interval (300-1500 ms). After the correction was applied, the average amplitude level of both seismic data becomes more similar. Figure 2.18 shows improvement in average amplitude comparison between seismic datasets after amplitude balancing process.

Figure 2.19 shows the amplitude envelope differences between the time-lapse data before and after the amplitude matching. In general, there is not much improvement of the amplitude differences of the static window interval after correction. Some slight improvement of the amplitude differences reduction occurs in parts of the investigation

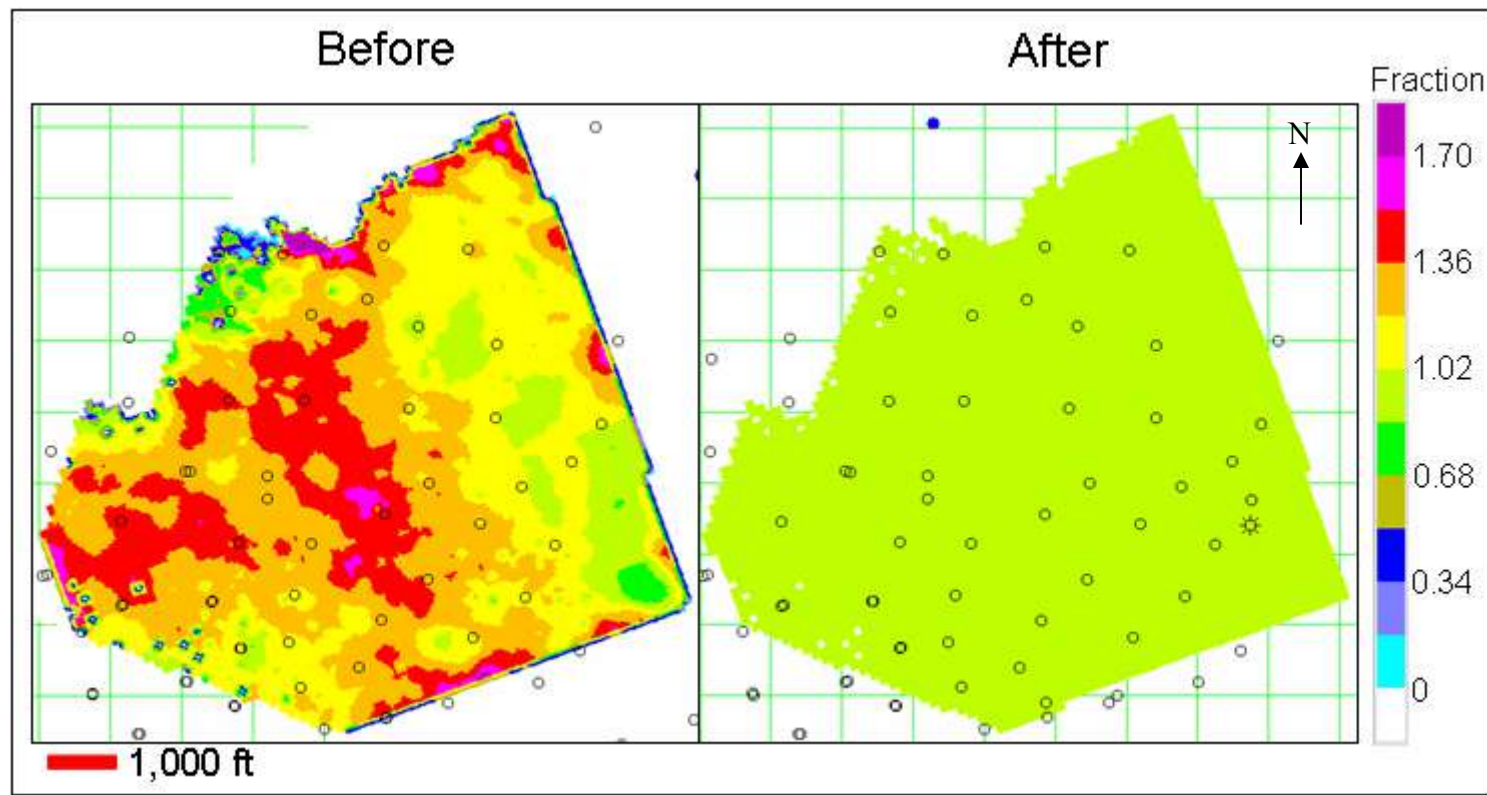


Figure 2.18. Comparison of average RMS amplitudes in the static window interval between 2003 and 1996 seismic data. This value is ratio between average RMS amplitude of 2003 and 1996 data. The distribution was calculated for time-lapse data before and after amplitude correction.

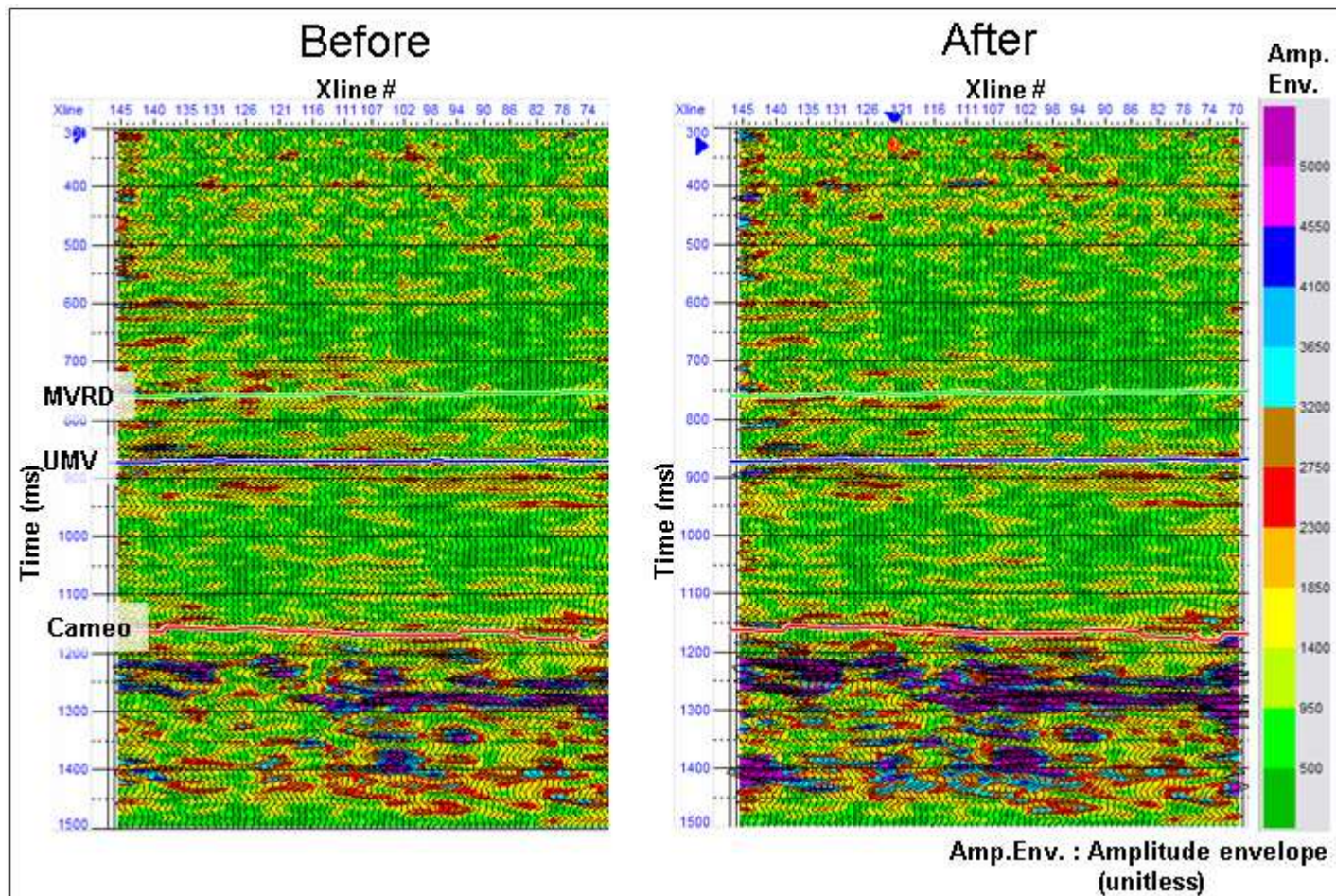


Figure 2.19. Amplitude envelope differences between the two data sets before and after amplitude balancing from inline 63.

area. In Figure 2.18, some slight improvement can be identified around 700 ms. In the upper region (around 400 ms), some increase in amplitude differences can be detected. The increase in amplitude difference of the static windows gives some doubt to the effectiveness of the amplitude balancing process.

To better study the effectiveness of amplitude balancing process, distribution of average NRMS value before and after correction is analyzed (Figure 2.20). Figure 2.20 shows that amplitude balancing process has significantly reduced NRMS value especially in the middle of the area. Distribution of NRMS value and correlation coefficient is also analyzed (Figure 2.21). Figure 2.21 shows an improvement in NRMS value. This improvement can be identified by the reduction in high NRMS value and increase in low NRMS value. The decrease in NRMS value and increase in correlation coefficient indicates that amplitude balancing has increased the repeatability of time-lapse data. Although amplitude balancing process has increased amplitude differences of certain areas, this process has successfully decreased non-repeatable elements in general.

2.3.4. Time-variant Time Shifting

Another type of correction that was performed in this time-lapse dataset is the time-variant time shifting. The time-variant time shifting is a time correction for any time lag in the seismic traces between surveys that appears due to the velocity changes in the reservoir level. When there are some velocity changes caused by reservoir changes, the seismic traces below the reservoir will be time shifted.

This type of time shift is important information to analyze the changes at the reservoir level. The approach that the author used for this research is by separating this time shift information from the amplitude changes information. The advantages of separating the time shift and amplitude changes are the ability to generate acoustic

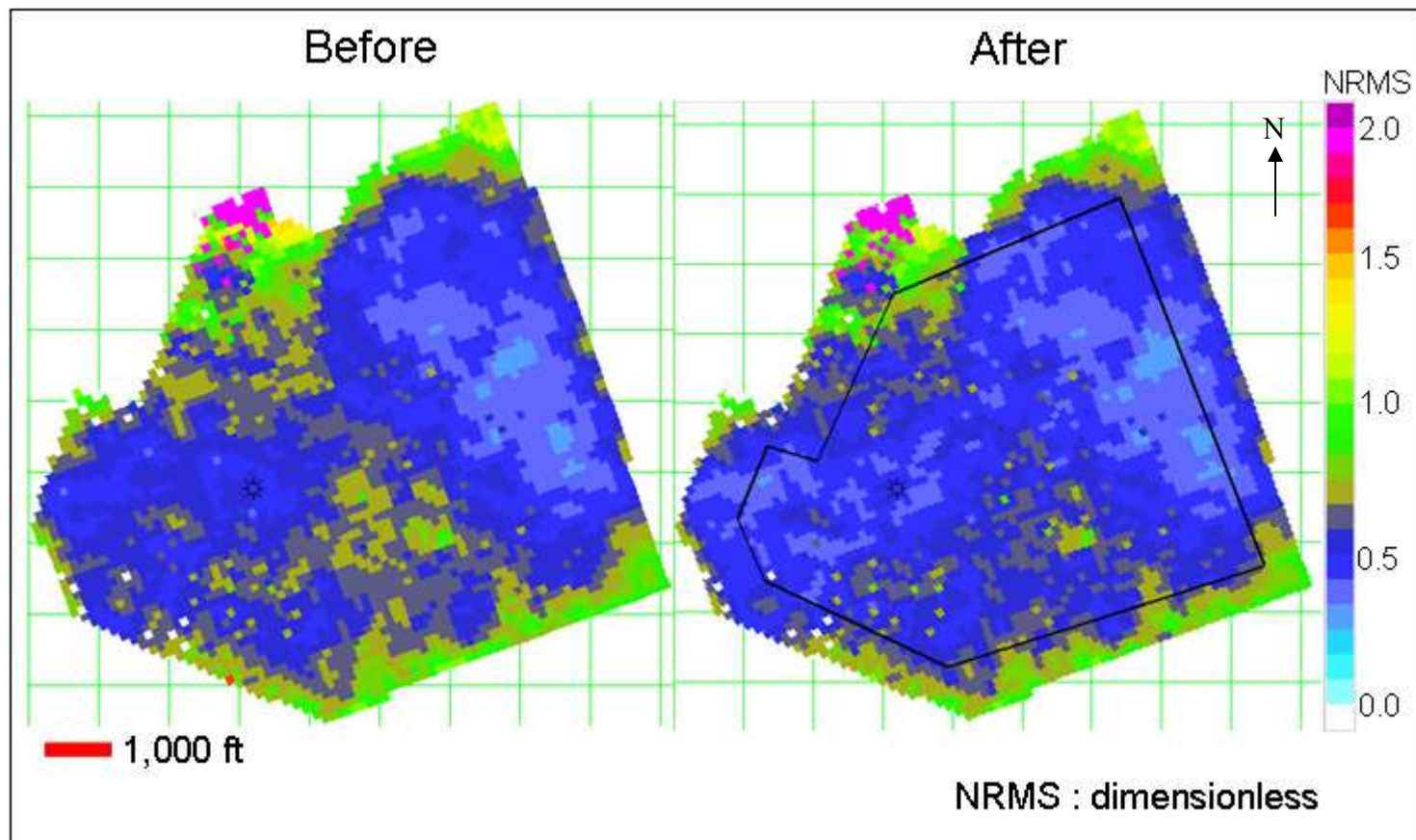


Figure 2.20. NRMS values at static window interval before and after amplitude balancing.

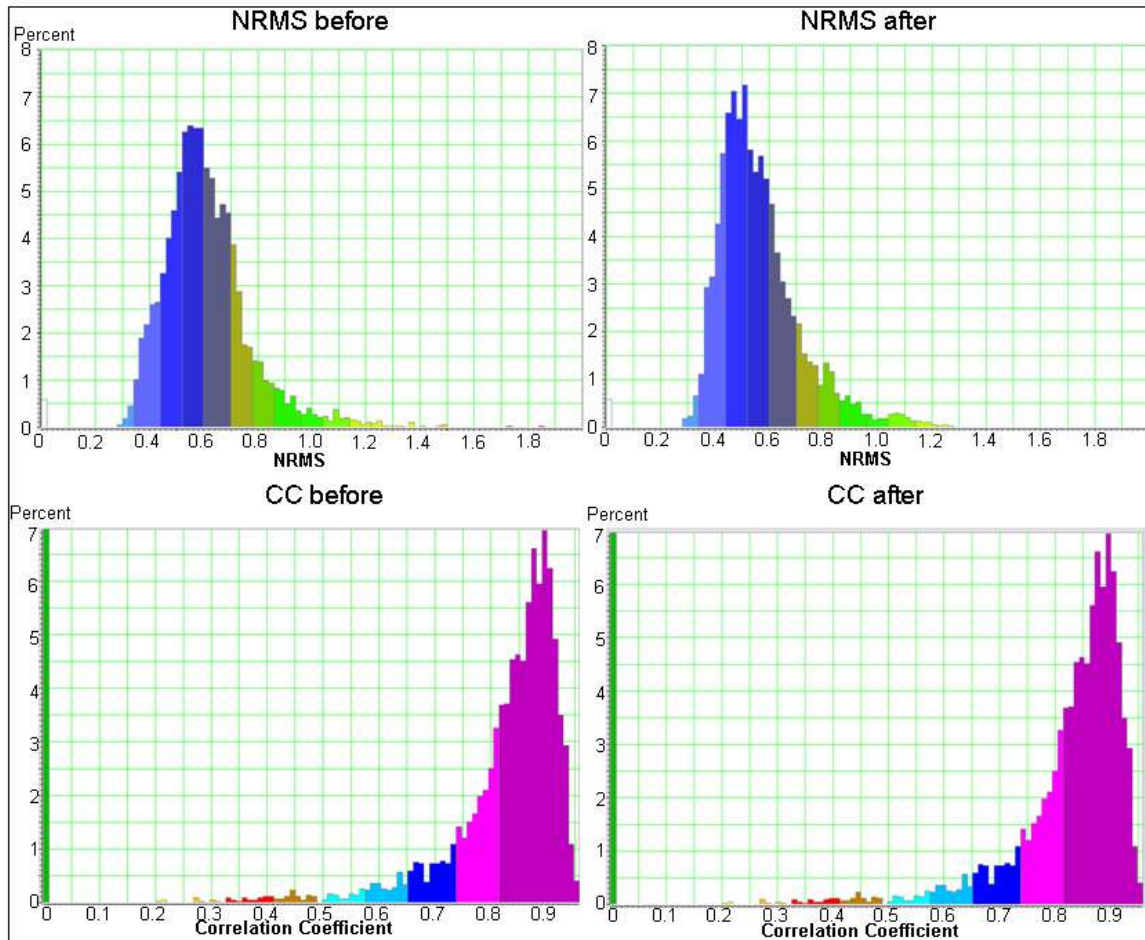


Figure 2.21. Distribution of NRMS values and correlation coefficient values before and after time correction at static window interval.

impedance differences. By separating the two types of information, the author has been able to generate the inversion of the differences from amplitude data and compare it with the time shift information. If the information is not separated, *fake* amplitude differences can appear below the reservoir level as a result of reservoir changes.

To analyze the appearances of time-variant-time shift in the Rulison time-lapse data, time lag from horizons above and below the reservoir is generated (Figure 2.22). This figure shows that after the cross equalization process on the static window interval, there is only a small time lag that still exists above the reservoir. The time lag below the reservoir on other hand is still high after the previous cross-correlation process. This analysis implies that velocity-changes within the reservoir interval generated the time shift at the Cameo level. In some parts of the area especially near the edge of the survey, the time shift reaches -15 ms. This high time shift could be the result of high noise levels at the edge of the overlapping survey grids.

The correction of the time shift is then performed to separate the amplitude change information from the time lag information. The time-variant-time shift operator is calculated from the analysis of 4 different horizons above and below the reservoir interval. These horizons are MVRD, UMV shale, Cameo top and Cameo B (Figure 2.23). Using the time lag information from these horizons, the seismic traces are then time-equalized. This correction process is performed in trace-by-trace bases.

Figure 2.23 shows the amplitude differences between seismic volumes before and after the time-variant time shift correction. This figure indicates no significant changes of the amplitude differences at the static window interval and the reservoir interval after the correction. On other hand, the amplitude differences of the Cameo interval changes significantly after the correction. This analysis implies that before the correction is applied, the amplitude difference at the Cameo interval is affected by the velocity changes at the reservoir level.

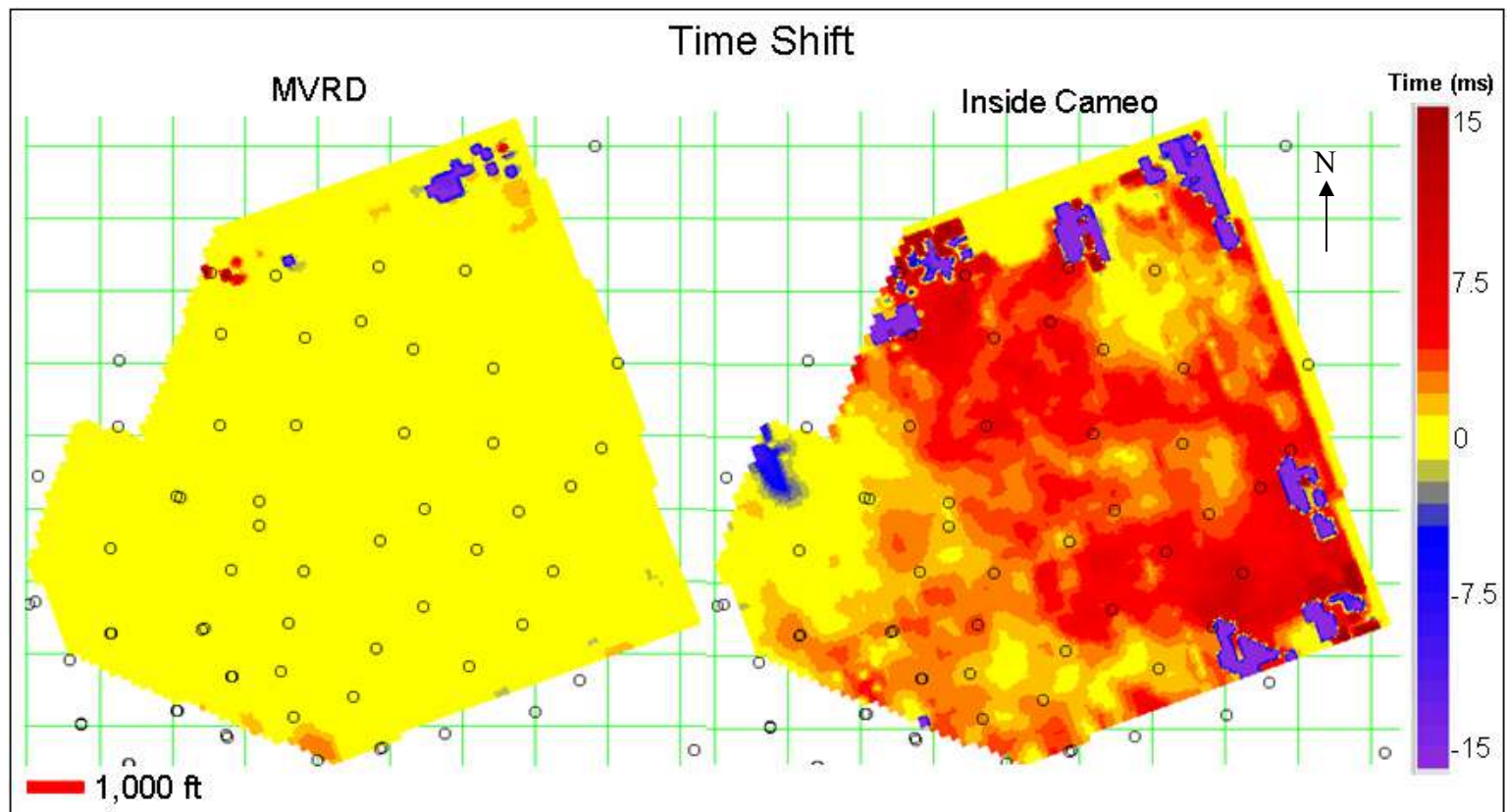


Figure 2.22. Time shift between 2003 and 1996 seismic data set from horizon above the reservoir (MVRD horizon) and below reservoir (Inside Cameo).

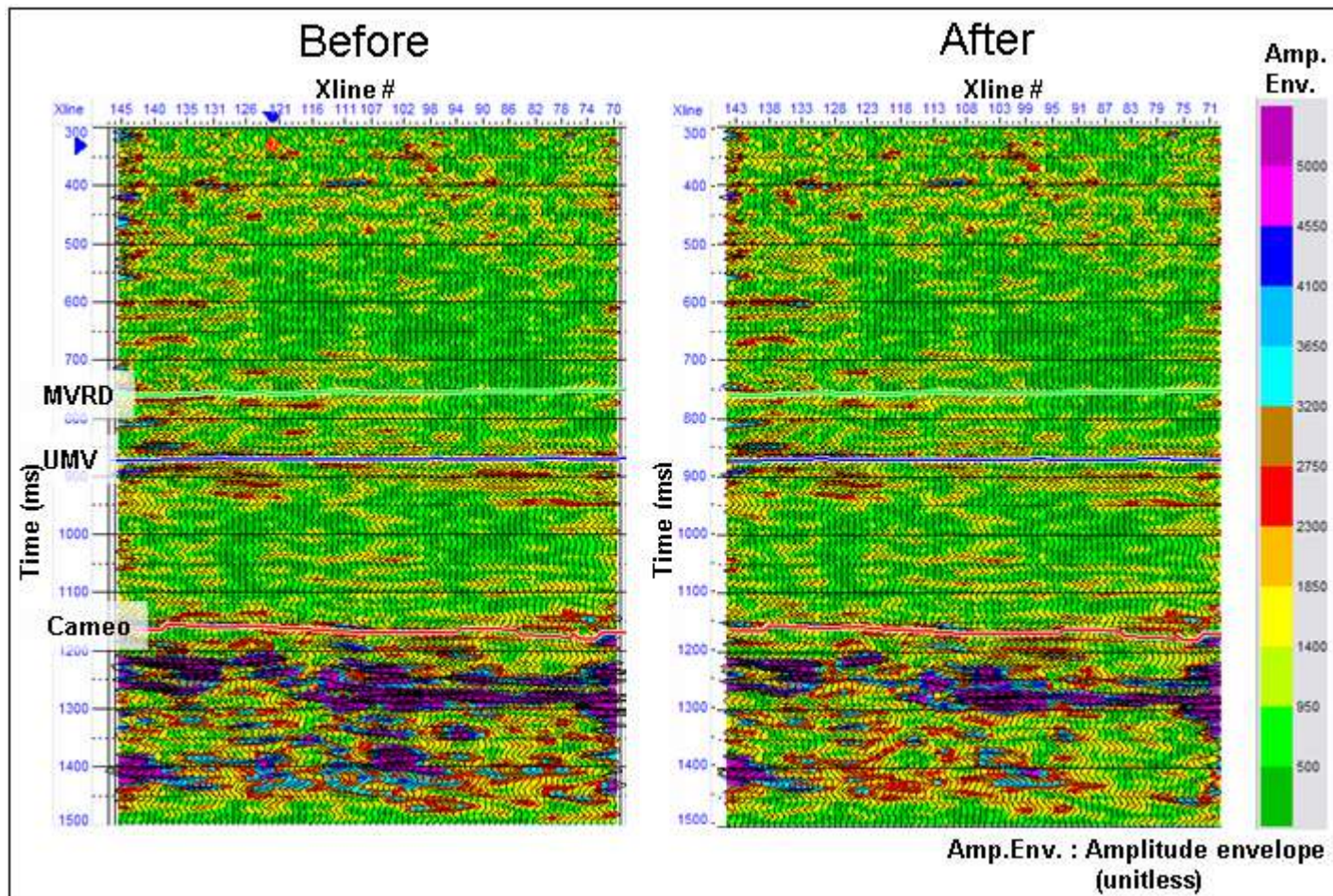


Figure 2.23. Amplitude envelope differences between the two data sets before and after time-variant time-shifting from inline 63.

The time lag information is then used separately as one of the time-lapse attributes to analyze the Rulison datasets. More information on the time-lag as a time-lapse attribute and its contribution on the Rulison time-lapse analysis will be explained in chapter 3. The amplitude differences after time variant correction will also be used as the main data input for the time-lapse analysis.

2.4. Summary of the Cross Equalization Process

The Rulison 1996-2003 time-lapse seismic datasets consist of two seismic volumes from two surveys with different acquisition parameter. To reduce the effect of different acquisition parameters and other non-repeatable elements of the surveys, both datasets is reprocessed and cross equalized. The reprocessing of both volumes includes the bin sharing procedure to equalize the traces used in the stacking process. The reprocessing of Rulison time-lapse datasets was performed by Veritas Geosciences. The cross equalization process is performed to equalize the time, phase, frequency and amplitude of both seismic volumes. The cross equalization parameter is extracted from the static time window interval (300 – 800 ms) and applied for the whole interval (300-1500 ms).

The cross equalization process has successfully reduced the non-repeatable elements of the two surveys. Figure 2.24 indicates the NRMS value for the static window before and after the cross equalization process. A high improvement of the trace repeatability after the cross equalization is shown in Figure 2.24. This improvement is indicated by the reduction of the NRMS value after the cross equalization process. In the southern part of the area the NRMS value is reduced from 1.6 to 0.5. Figure 2.24 shows that NRMS value in the edge area is still significantly high. High NRMS value in this area is mainly caused by high noise level in the edge of surveys. This edge area is then excluded for further time-lapse analysis. Figure 2.24 shows the area of investigation that

is used for further analysis. Analysis of the distribution of NRMS value and correlation coefficient (Figure 2.25) also shows a general reduction of NRMS value and an increase correlation value after the cross equalization process.

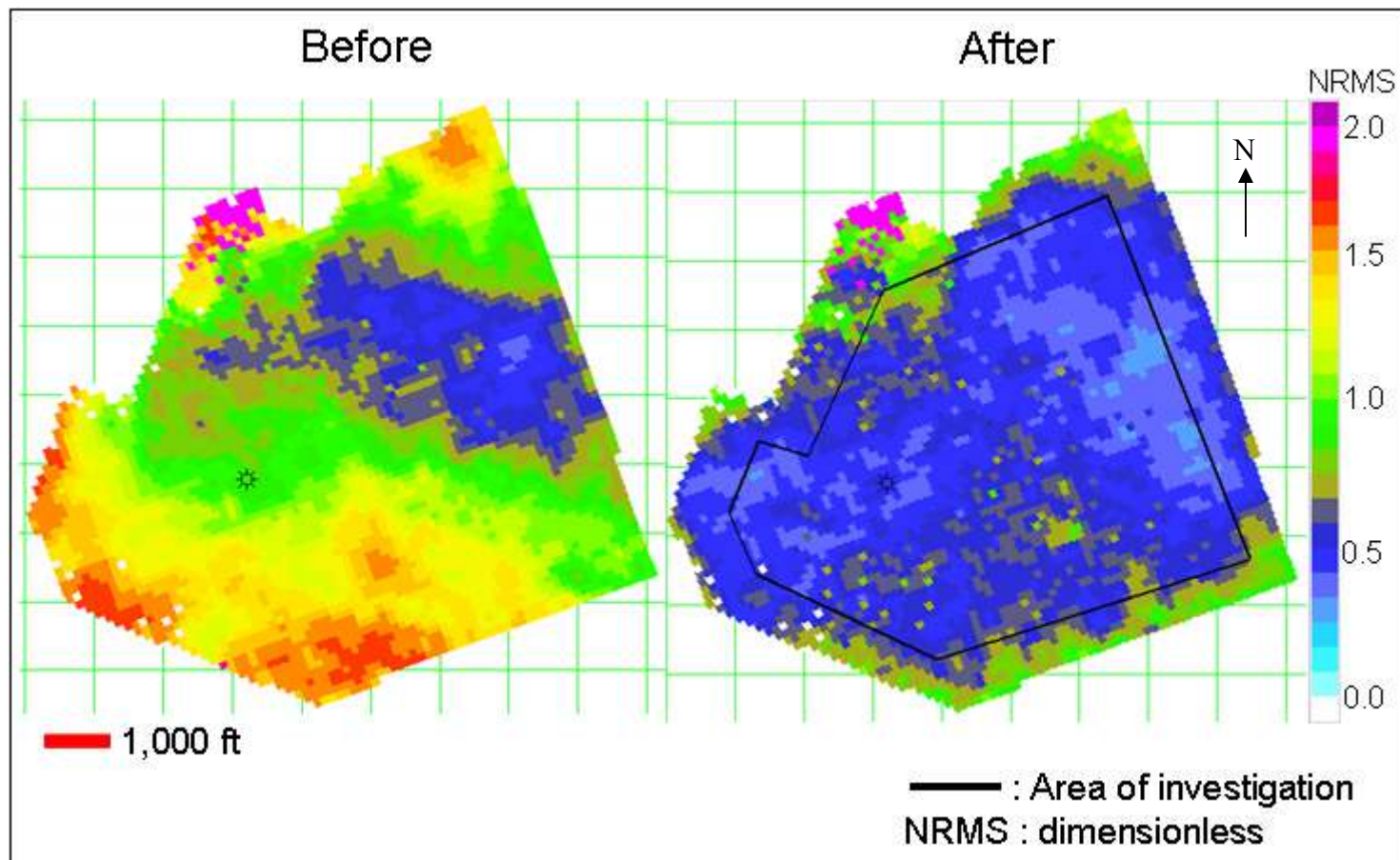


Figure 2.24. Distribution of repeatability (NRMS) before and after cross equalization process.

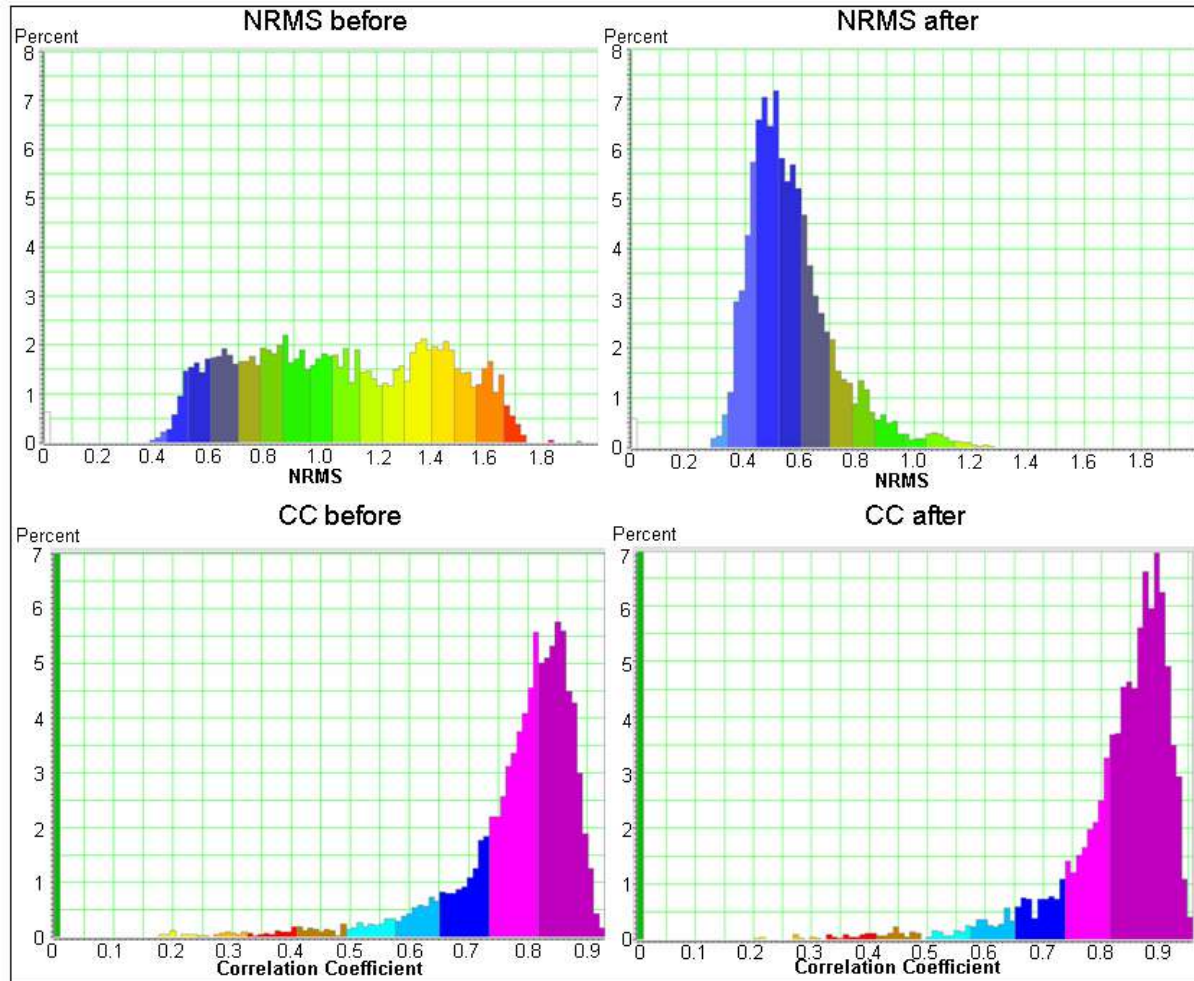


Figure 2.25. Distribution of NRMS values and correlation coefficient values before and after time correction at static window interval.

Chapter 3

TIME-LAPSE SEISMIC ATTRIBUTES

3.1. Introduction to Time-lapse Seismic Attributes

Taner (2001) suggested the definition of seismic attributes: “Seismic attributes are all the information obtained from seismic data, either by direct measurement or by logical or experience based reasoning”. The objectives of the seismic attributes are to provide detailed information to interpret the structural, stratigraphic and lithological parameters from the seismic data. Among the well-established seismic attributes are the reflection strength and mean frequency attributes (Balch, 1971; Taner et al, 1979).

The reflection strength attribute is derived from seismic amplitude, while the mean frequency attribute is derived from the frequency component of the seismic datasets. Seismic amplitude content is an important factor to determine the physical parameters, such as acoustic impedance, reflection coefficients, velocities, and absorption. The frequency and phase component are the important factors to determine the shape of reflectors, and their geometrical configurations (Taner, 2001).

Brown (1996) introduced two main classifications of seismic attributes. The first classification is based on the domain of the attributes i.e. pre-stack attributes and post-stack attributes. The pre-stack attributes will have azimuth and offset related information. This information is directly related with the fluid content and fractures within the formation (Taner, 2001). Some examples of pre-stack attributes are AVO and azimuthal variation attributes. The post-stack attributes, on the other hand, will have no azimuth and offset related information due to the stacking process. These attributes will help to analyze the huge volume of seismic data and perform general analysis of the field (Taner,

2001). Some post-stack attributes are reflection strength, edge, and spectral decomposition. The second attribute classification (Brown, 1996) is based on the basic information used in the attributes. In this classification, there are 4 types of attributes i.e. time based attributes, amplitude based attributes, frequency based attributes, and attenuation based attributes. Some examples of the time based attributes include: trend, edge, and semblance; amplitude based attributes include: AVO, reflection strength, and total energy; frequency based attributes include: response frequency, spectral bandwidth and RMS instantaneous frequency; attenuation based attributes include: instantaneous Q factor (Brown, 1996).

Application of the seismic attributes in the time-lapse datasets has been introduced by many researchers (Galikeev, 2004; Vasco et al., 2004; Landro and Stammeijer, 2004). The attributes of the time-lapse seismic data has a unique characteristic that separates it from the attributes of the static seismic data. The unique characteristic is that the time-lapse attribute focuses on the changes in attributes values on traces between surveys. In many cases, the individual trace attributes are not used to analyze the data, only the changes of the attributes.

Previous studies have shown the use of different types of time-lapse attributes for time-lapse analysis. Some of those studies will be mentioned in this paragraph. The first example is the use of spectral decomposition for time-lapse analysis by Galikeev (2004). Spectral decomposition was performed to analyze the amplitude spectrum over small windows of seismic data (Galikeev, 2004). In the static seismic data, this attribute is used especially to image stratigraphic features such as incised valleys, channels and deltaic deposits (Partyka et al., 1997; Peyton et al., 1998). Application of frequency decomposition to dynamic data (Galikeev, 2004) indicates the ability to analyze the fluid movement in the reservoir level. Another attribute used in time-lapse analysis is 3-D semblance (Galikeev, 2004). 3-D semblance is the measurement of the likeliness of traces in 3 dimensions. Application of the 3D semblance on the time-lapse analysis was implemented by Galikeev (2004) to image fluid movement. Vasco et al. (2004) shows the

use of the time-lapse amplitude changes to analyze the reservoir flow properties. Landro and Stammeijer (2004) have used the amplitude differences and travel time shift to analyze the changes in velocity and compaction from the time-lapse datasets. Another important case study is monitoring steam flood injection using the time-lapse by Jenkins et al.(1997).

3.1.1. Characteristic of Rulison Time-lapse Seismic Attributes

The Rulison time-lapse seismic data have unique characteristics due to the geologic setting of the area. Time-lapse seismic attributes applied to these datasets have been designed with consideration to these unique characteristics. As previously explained in chapter 1, the Rulison field consist of complex geological features i.e. complex stacked channel bodies, high gas content in the reservoir level, highly fractured areas, and very low permeability reservoir. These features have affected the characteristics of the time-lapse seismic data in Rulison field. There are two main characteristics of Rulison time-lapse seismic data i.e. the low impedance contrast and the discontinuous reflectivity within the reservoir.

The first unique characteristic of the Rulison time-lapse seismic datasets is the low impedance contrast within the reservoir. The low impedance contrast has generated low seismic amplitude response at the reservoir level (Mesaverde). Below the reservoir level, the Cameo has high amplitudes due to the coal layers within. This amplitude contrast has affected the time-lapse analysis especially if the analysis is based on the absolute amplitude value. Velocity changes at the reservoir level have a smaller effect on the amplitude difference values compared with velocity changes at the Cameo level. The time-lapse seismic attributes applied to these datasets is designed to help the analysis of this low amplitude anomaly at the reservoir level.

Another characteristic of the Rulison time-lapse seismic dataset is the discontinuous reflectivity within the reservoir interval. Since the reservoir consists of multiple stacked channel sand bodies and complex channel geometries with thickness below seismic resolution (detail explanation in Chapter 1), it is difficult to pick individual reservoir horizons. This characteristic has made horizon-based analysis difficult, if not impossible. In this research, the author uses volume-based analysis instead of the horizon-based analysis. To analyze the distribution of the anomalies, the author uses time slice analysis to replace the horizon slice analysis.

Based on these unique characteristics of the Rulison time-lapse datasets, the author uses three types of time-lapse attributes for this research i.e. time shifting attributes, correlation coefficient, and amplitude percent differences. These attributes are generated to add more quantitative and qualitative information to interpret the time-lapse anomalies within the reservoir.

The time shifting attribute is a seismic attribute based on the time lag between similar traces in different surveys. This attribute is similar to the analysis of pull-down anomalies by Jenkins et al. (1997). Figure 3.1 shows the schematic illustration of the time shifting attributes. This figure shows the changes in the horizon position in the time domain due to the appearance of the velocity changes within the reservoir level. The difference between the horizon position before and after the appearance of velocity changes is expressed by the time shifting (Δt). By analyzing the time shift of the horizon below the reservoir, the velocity changes within the reservoir level can be analyzed. One of the requirements of this time shifting analysis is that there is no time shift on the horizon above the reservoir. The appearances of the time shift above the reservoir level will affect the time shift for the horizon below the reservoir. For this research, the author uses the cross equalization process to eliminate the time shift at the horizon above the reservoir.

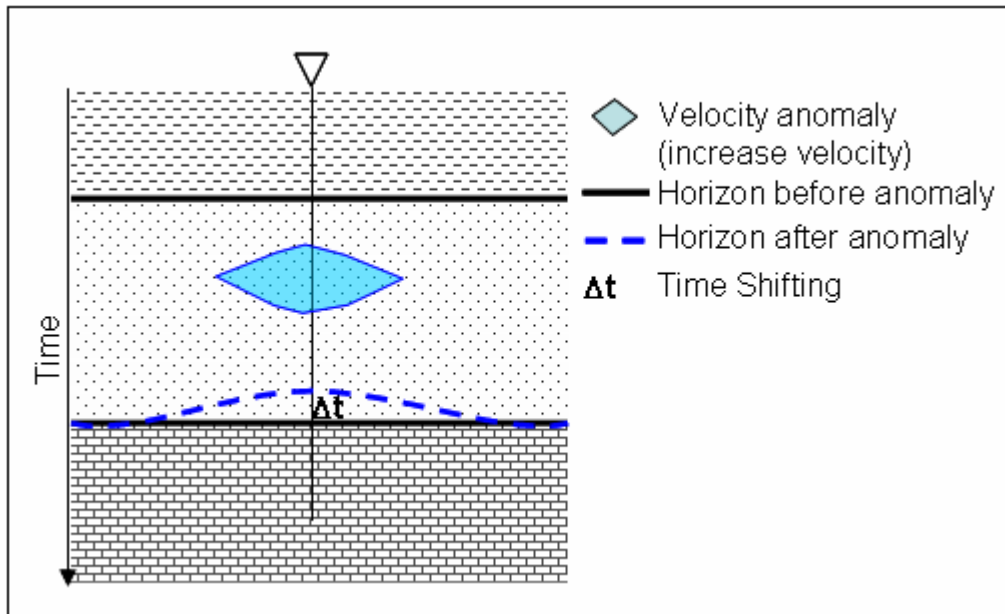


Figure 3.1. Schematic illustration of time-shift attribute.

To calculate the time shift between traces, the author uses cross correlation procedures. Cross correlation is a measure of similarity between two signals (Wikipedia Online, 2005). The cross correlation is a function of the relative time between the signals. The results of the cross correlation between traces are the correlation coefficient and the time shift (Hampson Russell, 1999). The correlation coefficient is the value of similarity between traces and ranges between 0 and 1. Correlation coefficient value of 1 indicates absolute similar traces while value of 0 indicates 90 degree phase differences. The time shift value is the value of the time lag that the traces need to achieve highest correlation value. The calculation of cross correlation in this research is performed using Hampson-Russell software. A negative time shift indicates that the base volume has been shifted upwards (lower time) relative to the monitor volume and vice versa (Hampson Russell, 2004).

The second attribute used in the Rulison time-lapse seismic analysis is the correlation coefficient. The correlation coefficient value is an indication of the amplitude changes. This correlation coefficient is more sensitive to the amplitude changes especially in the low amplitude region, because it detects the relative changes of the amplitude. The application of this attribute to the Rulison time-lapse seismic datasets will help to focus the low amplitude anomaly at the reservoir level.

The third attribute used in this research is the amplitude percent differences. This attribute is also designed to help the analysis of the low-amplitude anomalies within the reservoir. This attribute is generated by calculating the relative percent amplitude differences to the original amplitude (equation 3.1.).

$$Amp. P.D. (\%) = \frac{RS[(Amp_{II} - Amp_{I})]}{RS[Amp_I^{Smooth}]} * 100\% \quad \dots \dots \dots \text{(Eq.3.1)}$$

Where:

Amp.P.D : Amplitude percent differences (%)

Amp. 1 : Amplitude of first survey (base survey) (unitless)

Amp. II : Amplitude of second survey (monitor survey) (unitless)

RS[..] : Reflection strength attributes (unitless)

The calculation of this attribute is generated by dividing the reflection strength of the amplitude differences with the reflection strength of the smoothed-amplitude base survey. By using the reflection strength attribute in this calculation, the author will only focus on the amount of the energy from the amplitude differences and not the phase changes. The smoothed-amplitude from the base survey is used to avoid using the percent difference attribute to pick up any small amplitude anomaly that originally exists in the base data.

3.2. Application to Synthetic Time-lapse Datasets

The time-lapse attributes are applied to synthetic time-lapse datasets to study the reliability, sensitivity, and error estimation of the attributes. The synthetic datasets used in this modeling are extracted from field seismic data information. Detailed explanation on the synthetic datasets is discussed in chapter 1. These datasets are generated with all important components of the field data i.e. noise, wavelet extracted from field data and log representation of all horizons.

As previously explained in chapter 1, the synthetic dataset consists of the time-lapse anomaly with thickness changes (inline) and velocity value changes (crossline). The application of time-lapse attributes to these datasets can help to understand the characteristic of each attribute to detect time-lapse anomalies with certain thickness and velocity values. The most important thing in this study is to analyze the sensitivity of each attribute for detecting an anomaly with low velocity values and small thickness. Characteristics of the attributes to detect an anomaly with high velocity values and large thickness are also analyzed. Another important application is to analyze the ability of time-lapse attributes to detect the position of the anomaly.

The synthetic study will help the application of time-lapse attributes for the field datasets. The characteristic of each attribute especially dealing with low velocity value and small thickness will provide guidance in interpreting the Rulison time-lapse attributes.

3.2.1. Time Shifting Attributes

To detect the time-lapse anomaly at the synthetic datasets, time shifting attributes are calculated at the Cameo level. Figure 3.2 shows time shift at the Cameo level. As

previously explained in chapter 3.1.1 Rulison time-lapse attributes, positive time shift value indicates that the original traces have been shifted downward (higher in time) relative to the simulated traces and vice versa. The time shift at Cameo level (Figure 3.2.) indicates that positive time shift value increases proportionally with the increase of velocity. The negative time shift value, on the other hand, decreases proportionally with the decrease of velocity. The thickness of time-lapse anomaly also affects the time shift value. In the area of high decrease of velocity with high thickness (left upper corner of the figure), the time shifting attributes starts to pick random values of time shift even a positive time shift. This random value indicates that the time shifting attributes started to correlate the noise instead of trace data. Another possible explanation of the random value is that the time shifting correlated some horizons with the shifted version of the horizons above it. This phenomenon is not observed on the velocity increase section. But, there is a possibility that this phenomenon also happens when the velocity is highly increased with very large thickness.

Analysis of the time shift attributes applied to the synthetic data illustrates several important points to understand the characteristic of these attributes. These characteristics are mentioned below.

1. Time-shift attribute is a sensitive indication of time-lapse anomaly inside reservoir interval.
2. The value of time shift is proportional to the velocity change and the thickness of anomaly.
3. It is difficult to determine the value of velocity changes and thickness from time shift attributes. But, the time shift attributes can be useful to determine the ranges of possible velocity values and thickness.

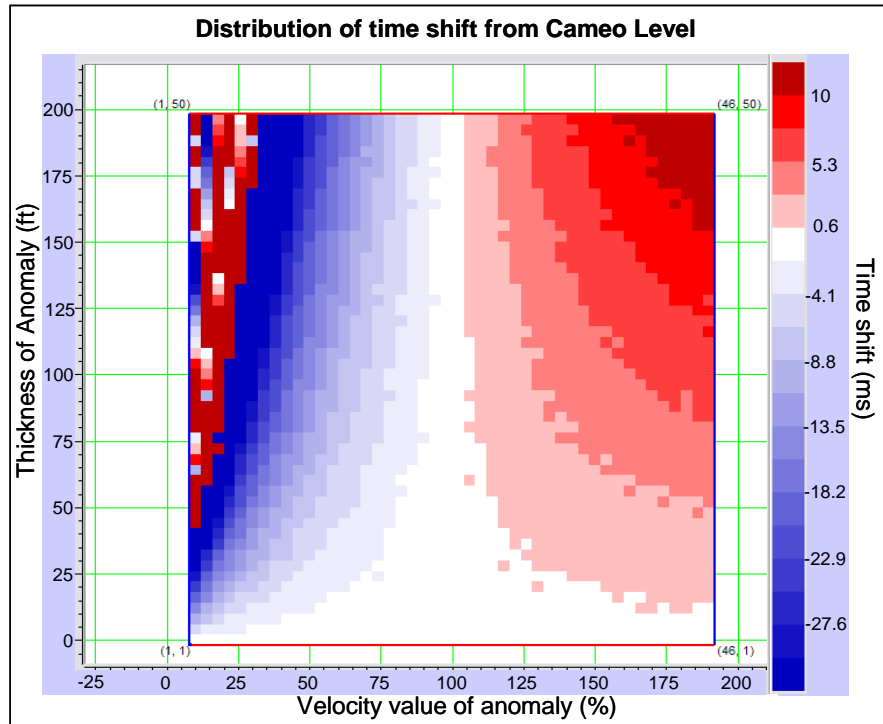


Figure 3.2. Time-shift of the Cameo level from synthetic datasets.

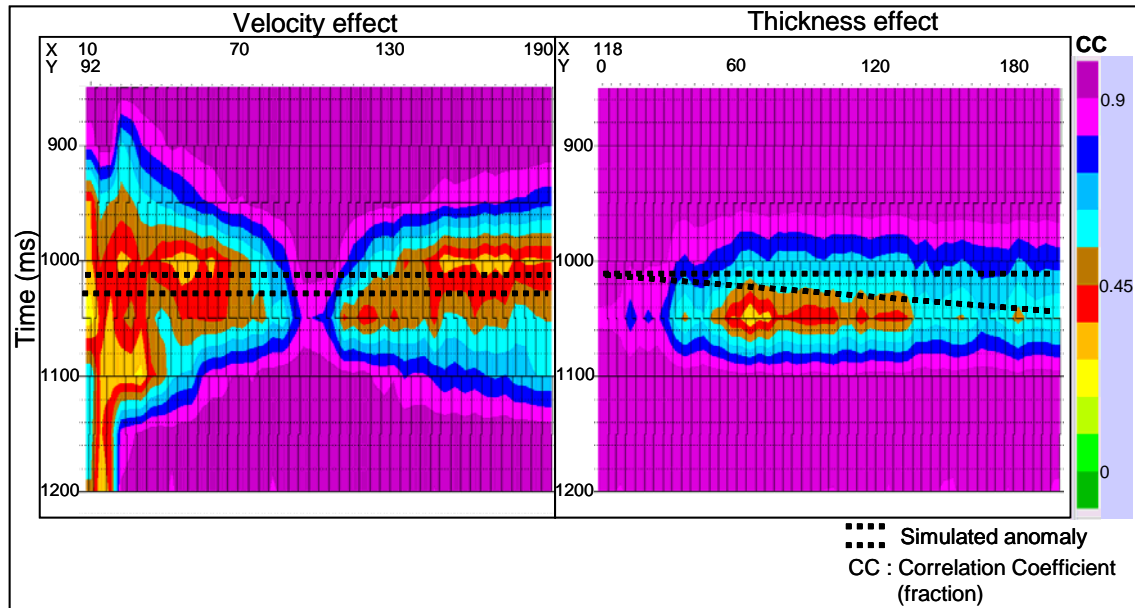


Figure 3.3. Cross correlation between monitor and base traces of the synthetic datasets.

3.2.2. Correlation Coefficient

The correlation coefficient (CC) attributes are also generated for the synthetic datasets. The CC attributes are calculated using the synthetic datasets after the time-variant time shift correction. This correction is applied to the datasets to reduce the time shift at the horizons below the reservoir (detail explanation in chapter 2.3.4. Time variant time shifting). These attributes are calculated using a time window 100 ms with time interval 50 ms. Using these parameters, CC attributes are calculated for the synthetic data volumes to detect areas with low trace similarity (CC value).

Figure 3.3 shows the distribution of CC attributes for synthetic data with different velocity values and different thickness values. The velocity effect on the CC attributes can be analyzed on these datasets. For positive velocity changes, a small increase in velocity can be easily detected using the CC attributes. As shown in Figure 3.3, a velocity increase of less than 10% can highly decrease the CC value to 0.5. For the negative velocity changes, a small decrease in velocity can also be detected using CC attributes but with slightly less contrast. An analysis on this synthetic data indicates that a 10% velocity decrease can decrease the CC value to 0.6. This CC value can still be detected in the dataset but with less contrast than the positive velocity changes.

Another application of the CC attributes on the synthetic data is to analyze the effect of the thickness changes on the attributes. The thickness effect analysis indicates that the CC value started to detect anomalies even with only small thickness (Figure 3.3). After 60 ft of thickness, the CC value is not sensitive anymore to the increase of thickness. Figure 3.3 also indicates that the CC attributes can be a good indication of relative position of the anomaly within the reservoir level.

The application of the CC attributes on the synthetic data has helped the author to analyze some important characteristics of this attribute. Those characteristics are explained below.

1. The CC attribute is a sensitive indicator of velocity changes.

2. An anomaly with very small thickness can alter the CC anomaly value and position, but after certain thickness value (60 ft), the CC anomaly is not affected anymore by thickness changes.
3. The CC attribute is a good indicator of the relative position of the anomaly.

3.2.3. Percent Differences

The percent differences (PD) attribute is generated for the synthetic datasets to study the attribute characteristics. The PD attribute is calculated using equation 3.1. The datasets used in this calculation is the synthetic dataset after time-variant time shifting correction. For the PD calculation, the original traces are smoothed using a 50 ms time window interval.

To analyze the characteristic of the PD attribute, the PD attribute is compared with the plain reflection strength (RS) attributes (Figure 3.4). The RS attributes are calculated from the amplitude differences between simulated data and the original data. Figure 3.4 shows that the both attributes (PD and RS attribute) can image the anomaly near the true location. Comparison between Figure 3.4.c and 3.4.d indicates that PD attribute has been able to image the anomaly with higher contrast. The study of the RS and PD attributes also indicates that these attributes can detect small velocity changes when the anomaly has thickness more than a certain value (in this specific case 40 ft). Figure 3.4.a and 3.4.b shows that the RS and PD attributes are able to detect a small velocity increase (less than 10%) for anomaly with 92 ft of thickness. The analysis of Figure 3.4.b and 3.4.c shows that the anomaly can only be detected when it reaches a certain thickness (in this case 40 ft). These figures also show that both attributes had failed to determine the thickness of time-lapse anomaly.

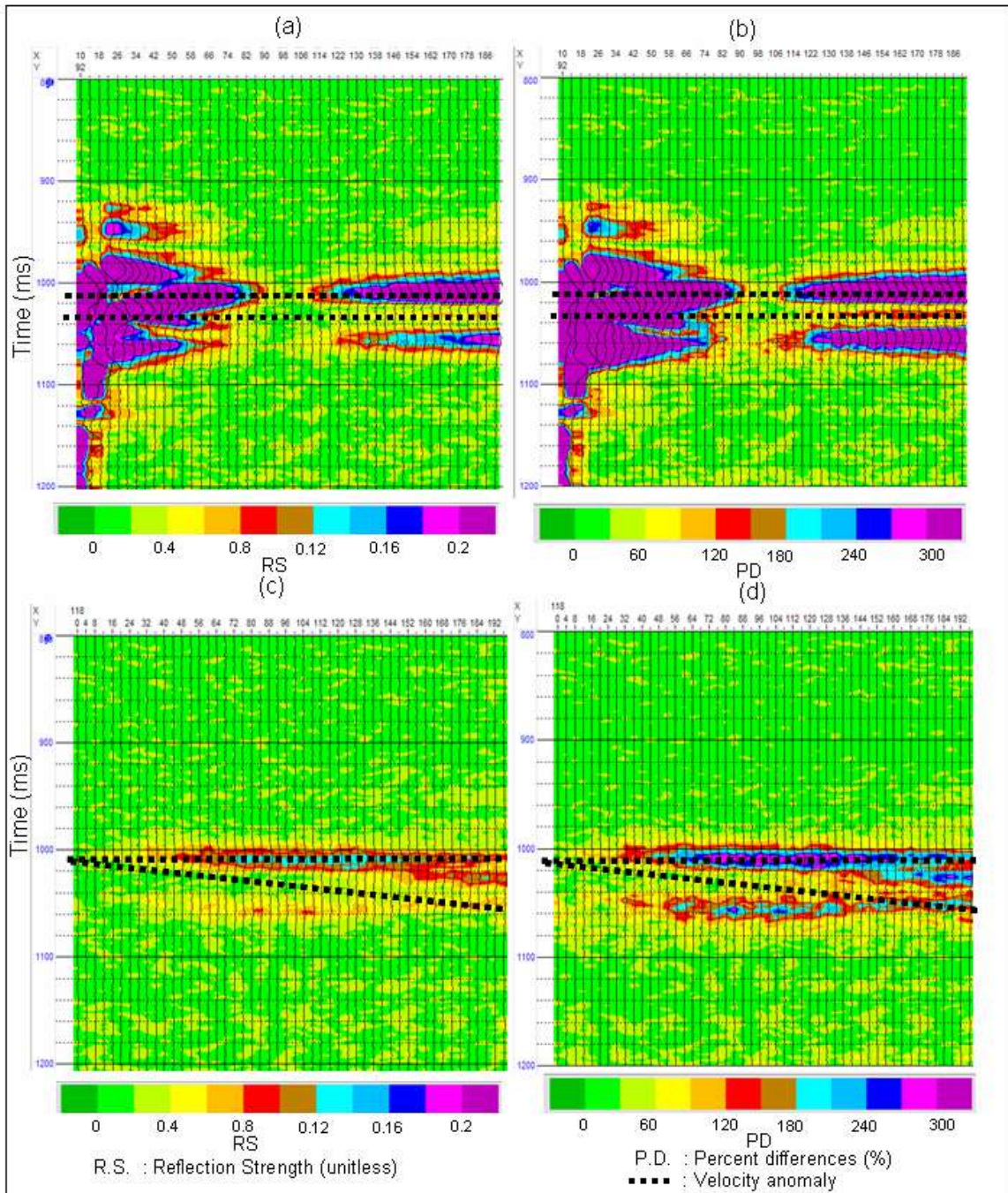


Figure 3.4. Comparison of percent difference (PD) and reflection strength (RS) attributes.

(a) RS for velocity effect simulation. (b) PD for velocity effect simulation.

(c) RS for thickness effect simulation. (d) PD for thickness effect simulation.

The analysis of the PD attributes on synthetic data gives more understanding on the characteristic of PD attributes. Those characteristics are explained below.

1. The PD attributes can focus the amplitude anomaly at the true anomaly location.
2. The PD attributes can detect small positive velocity changes if the anomalies have thicknesses more than a certain value (in this case 40 ft).
3. The PD attributes fail to determine the thickness of time-lapse anomaly.

3.3. Application to Rulison Time-lapse Datasets

Time-lapse seismic attributes are applied to the Rulison time-lapse datasets to extract important information about time-lapse anomaly in Rulison field. The field datasets used in this analysis are the seismic datasets after cross equalization process (chapter 2) with an exception of the time shift attributes. For the time shift attributes, the datasets used in the analysis are the datasets before the time-variant time shifting correction.

Each time-lapse attribute is generated for the Rulison time-lapse datasets. The analysis of the attributes is also performed for the volumes with the exception of the edge area. As previously explained in chapter 2, the edge area has low trace repeatability, even after the cross equalization process, due to the low trace coverage in this part of the field. Due to this fact, the edge area is excluded from the attribute analysis.

The analysis of the Rulison time-lapse attributes consists of several analysis steps. These steps are developed based on the analysis result of the synthetic data. The first analysis step is the time shifting attribute analysis. This attribute helps to detect a general trend of velocity changes (decrease or increase) and also to determine a general area in which the velocity changes occurs. The second attribute used is the correlation coefficient (CC). This CC attribute is used to identify the detail location and shape of the time-lapse anomaly. The last step of the analysis is the percent differences (PD) attribute analysis.

The PD attribute is used to describe more detail on the position of the anomaly. This attribute is also used in conjunction with the CC attributes to understand more about the distribution/shape of the anomalies.

3.3.1. Time Shifting Attributes

The time shifting attribute is generated on the Rulison time-lapse datasets before time-variant time shifting correction. The most important point in the application of this attribute is the absence of time lag for the horizon above the reservoir. As previously described in chapter 2 (2.3.4. Time variant time shifting), the cross correlation process has successfully reduced any time lag for the horizon above the reservoir to almost zero time lag. This fact implies that the time shift analysis for horizon below the reservoir will be a good indicator of velocity changes at the reservoir level.

The time shifting attribute is calculated using a cross correlation process for the Cameo level with time window of 150 ms. The calculated time shifting attribute is shown in Figure 3.5. This figure indicates a dominant positive time shift in most of the area. This result indicates that an increase in velocity (positive velocity) will dominate the time-lapse anomaly at the reservoir level. Figure 3.5 also shows that most of the time shift appears in the middle to western part of the area. This fact indicates that most of the time-lapse anomalies will appear in the middle to western part of the area.

Based on time shift attribute, average velocity changes over reservoir interval is calculated. The calculation of average velocity changes is based on equation 3.2 and 3.3.

$$\Delta V = V_2 - V_1 \dots \text{.....(Eq. 3.2.)}$$

$$\Delta V = \frac{L}{T_2} - \frac{L}{T_1} \quad \dots \quad (\text{Eq. 3.3.})$$

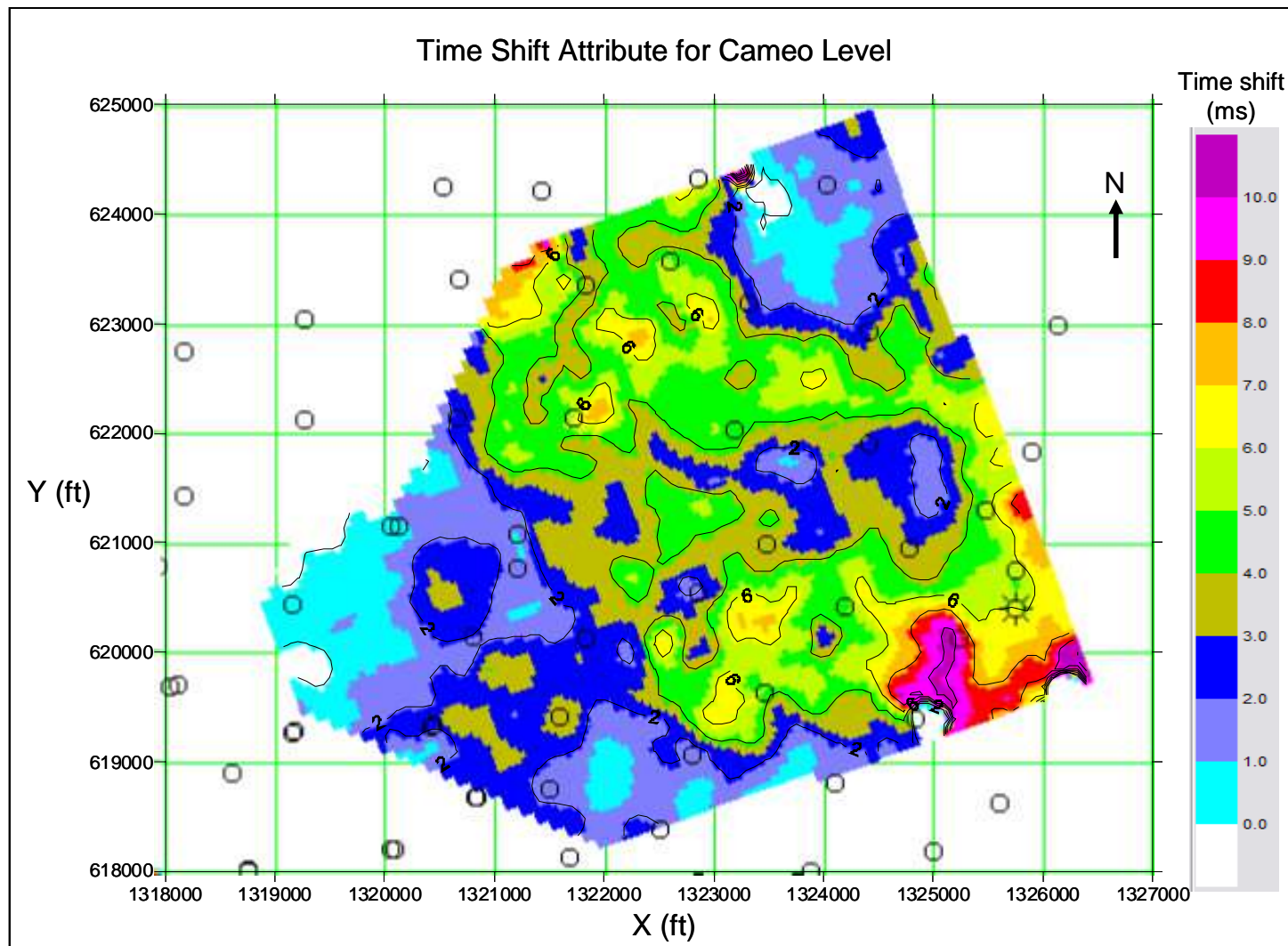


Figure 3.5. Time shift for Cameo level indicates increase in velocity at the reservoir level.

Where:

- ΔV : Average velocity changes (ft/s)
- V_1 : Average velocity of base data (ft/s)
- L : Reservoir thickness (ft)
- T_1 : Reservoir time interval of base data (s)
- T_2 : Reservoir time interval of monitor data (s)

To calculate velocity changes, three input parameters are needed i.e. reservoir time interval of base data (T_1), reservoir time interval of monitor data (T_2) and reservoir thickness (L). Figure 3.6 shows time interval between UMV and Cameo horizon. This one-way time interval is calculated based on interpreted UMV and Cameo horizon of the base data. Reservoir time interval of monitor data is calculated based on reservoir time interval of base data and time shift attribute (Figure 3.6). Another input in velocity change calculation is reservoir thickness. Figure 3.7 shows distribution of reservoir thickness. This map is generated using depth conversion of UMV and Cameo horizon after well-to-seismic tie process. The depth conversion process is discussed in chapter 4. Using these three input parameters, average velocity distribution is generated (Figure 3.8). Figure 3.8 shows average velocity distribution of base data and monitor data. Analysis on Figure 3.8 indicates increase of average velocity in some part of the area. To better delineate velocity anomalies, velocity change distribution is calculated (Figure 3.9). Analysis on this map (Figure 3.9) indicates high velocity changes especially in the middle of investigation area. Velocity changes in this region are about 300 to 500 ft/s.

3.3.2. Correlation Coefficient

The correlation coefficient attribute (CC) is the second attribute used in the Rulison time-lapse attributes analysis. This attribute is calculated from the Rulison time-lapse dataset after the cross equalization process. The CC attribute is generated by

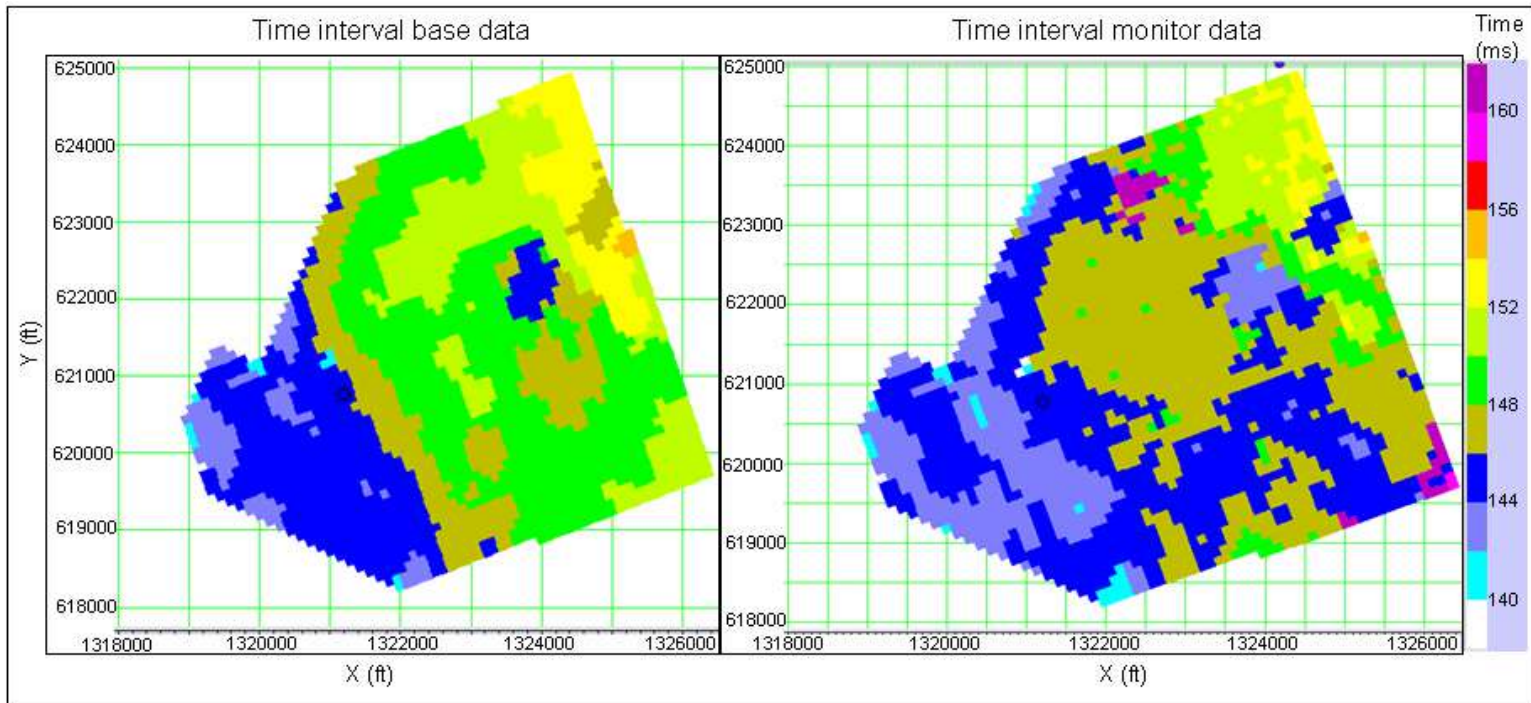


Figure 3.6. One-way travel time interval between UMV and Cameo for base and monitor data. Time interval of base data was calculated based on time differences between interpreted UMV and Cameo horizon. Time interval of monitor data was calculated based on time interval of base data and time shift attribute.

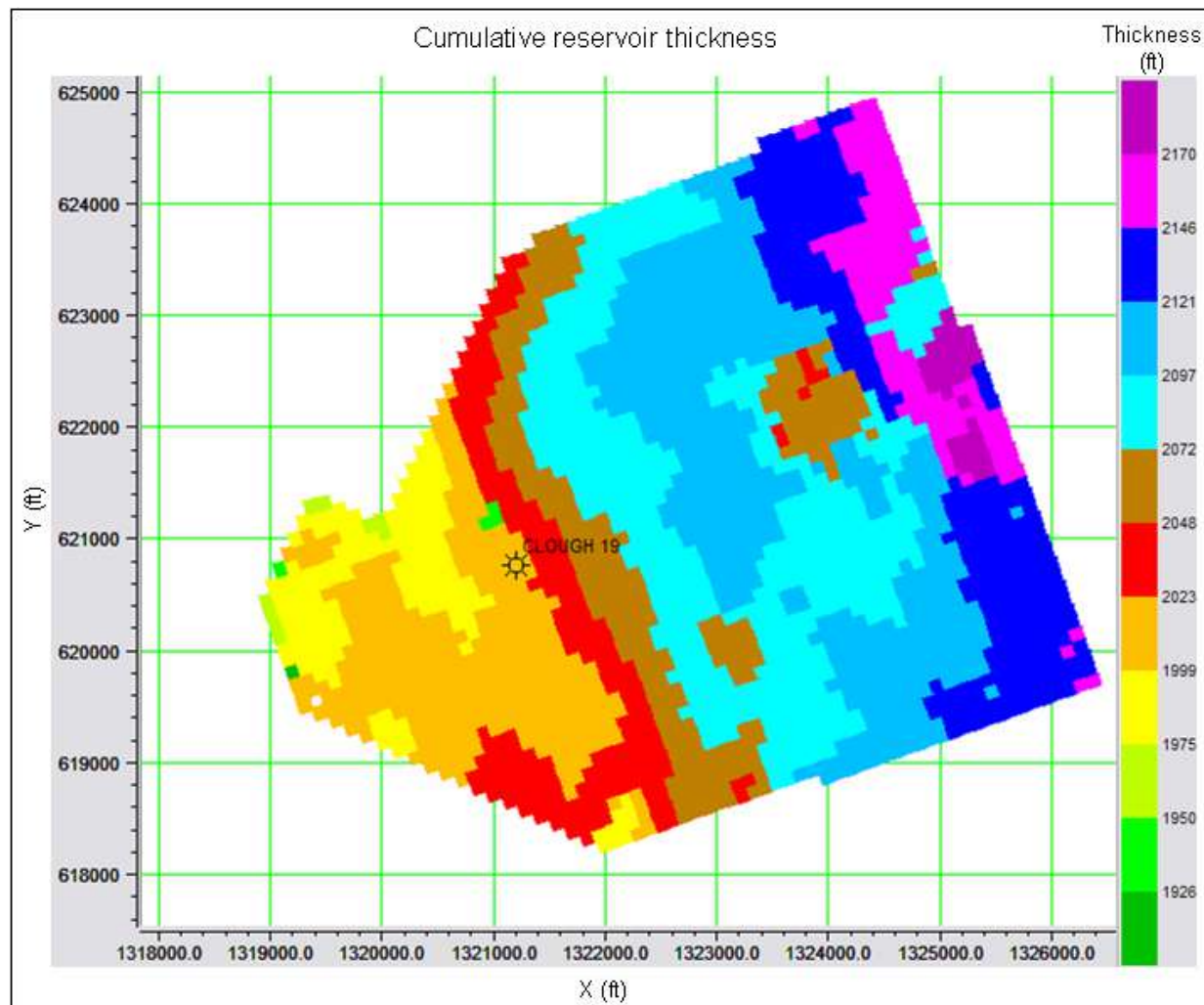


Figure 3.7. Cumulative reservoir thickness. This value was extracted from depth-converted UMV and Cameo horizon.

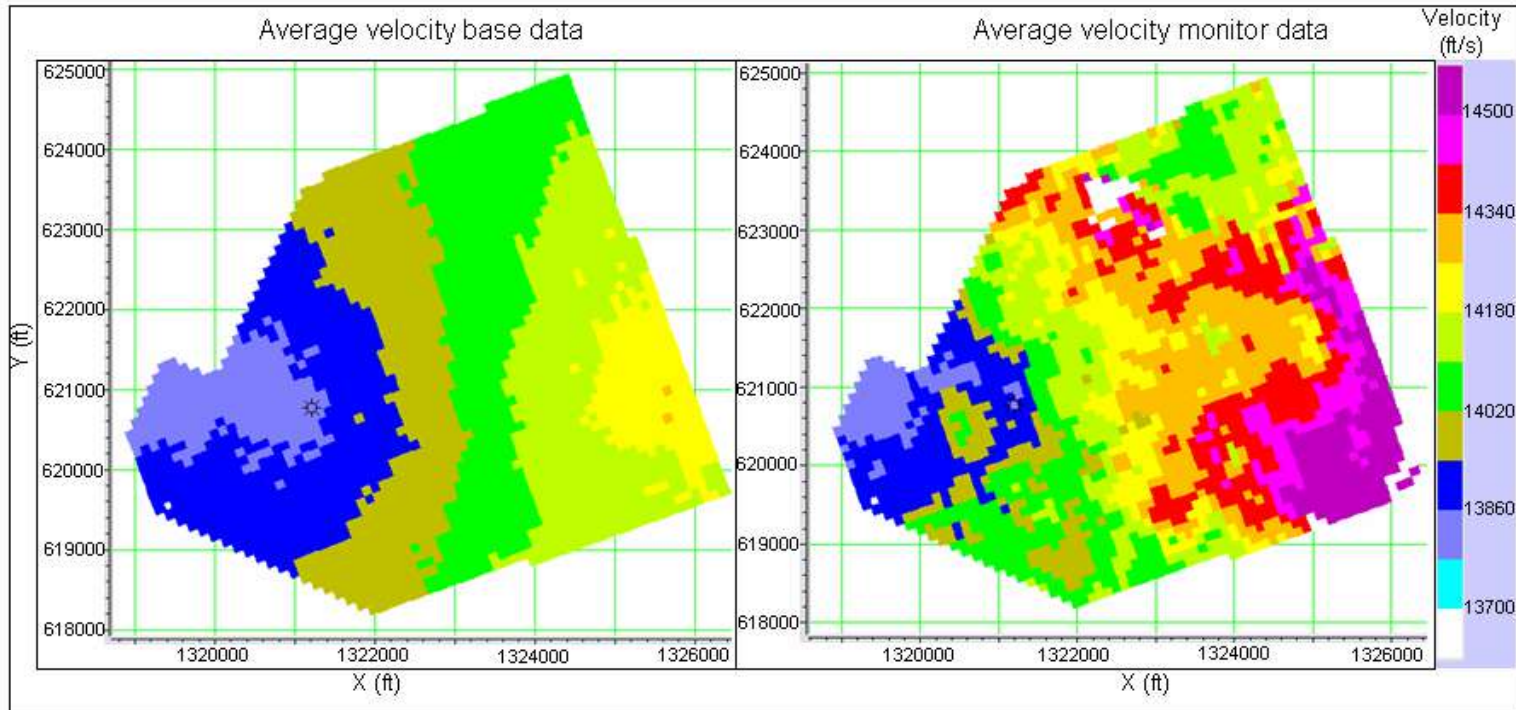


Figure 3.8. Distribution of average velocity inside reservoir interval for base and monitor data. Velocity of base data was extracted from inversion result (chapter 4). Velocity of monitor data was calculated from velocity of base data and time shift information.

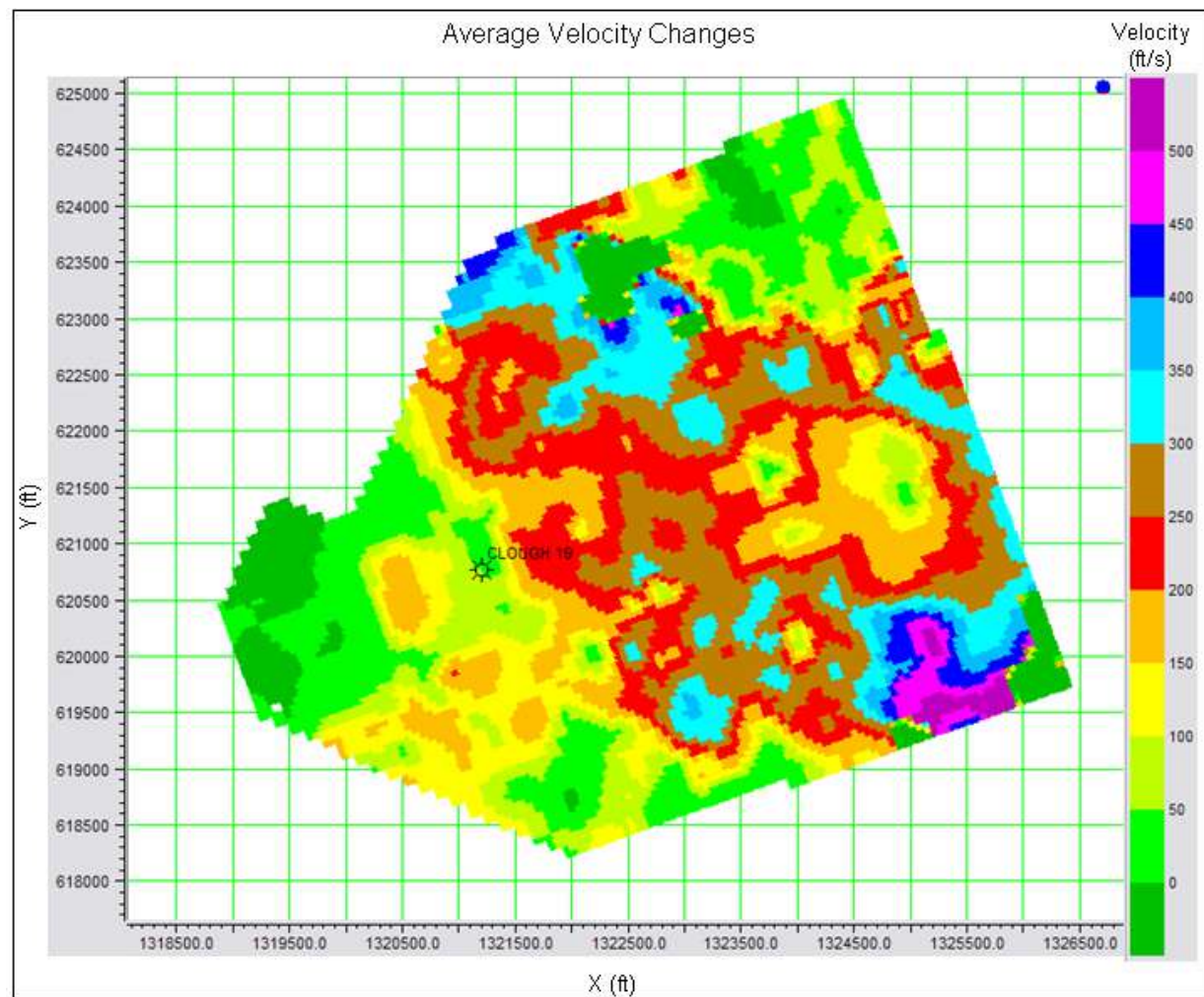


Figure 3.9. Average velocity changes inside reservoir interval. This velocity changes was calculated using information of time shift attribute.

calculating the CC value from cross correlation process of traces from different surveys. This process is applied to the Rulison datasets using a time window 100 ms and time interval 50 ms. Different correlation windows are also applied (50 ms and 150 ms) with no significant differences in the result.

To analyze the CC attribute, inline slice and cross-line slice across the seismic volumes are used (Figure 3.10). These two 2D slices are chosen because they intersect one of the largest producing wells (well Clough 19). Both 2D slices are shown in Figure 3.11. This figure also shows the relative position of well Clough 19 and its gamma-ray log information.

An analysis of the CC attribute in these 2D slices indicates CC anomalies at the reservoir level especially in the 950-1050 ms time interval (Figure 3.11). Some CC anomalies also appear near the edge of the data. The anomaly near the edge is interpreted as the result of higher noise area at the edge of the data. The CC attributes also indicates that there is no strong anomalies at the Cameo level except in the edge of the area.

To understand the distribution of this CC anomaly, a time slice of the CC attribute is generated (Figure 3.12). This time slice is created at 1000 ms using a 100 ms time window. Figure 3.12 shows the distribution of the CC anomaly around well Clough 19. The CC value at this anomaly ranges from 0.75 to 0.8. The CC anomaly forms an almost “O” shape with a higher CC value at the center (almost 0.9). Low CC values are also found at the edge of the area. The CC values at the edge of the area reach as low as 0.5. This fact strengthens the argument that the appearance of noise at the edge area strongly affects the CC attributes.

The appearance of the CC anomaly in this part of the field is supported by the time shifting attribute. In previous analysis, the time shifting attribute suggested that the time-lapse anomaly appears mostly in the middle to western part of the area. The combination of these two attributes strongly suggests that the anomaly around well Clough 19 is a real time-lapse anomaly.

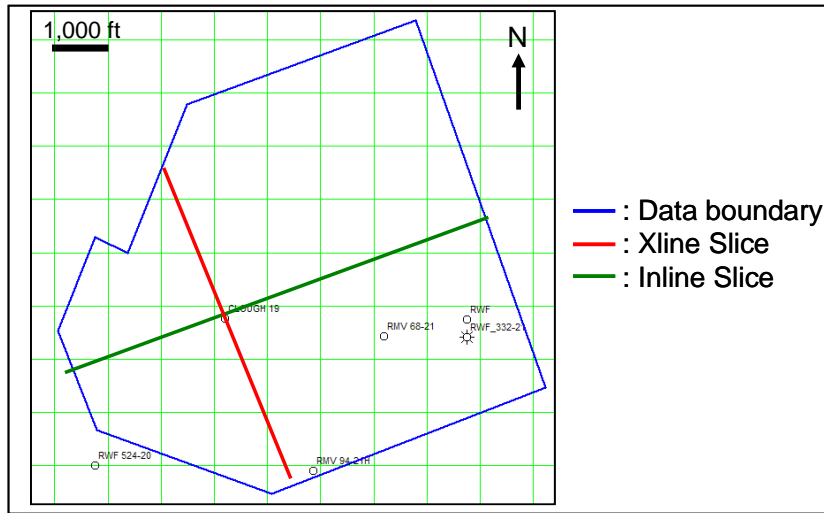


Figure 3.10. Basemap for attribute analysis.

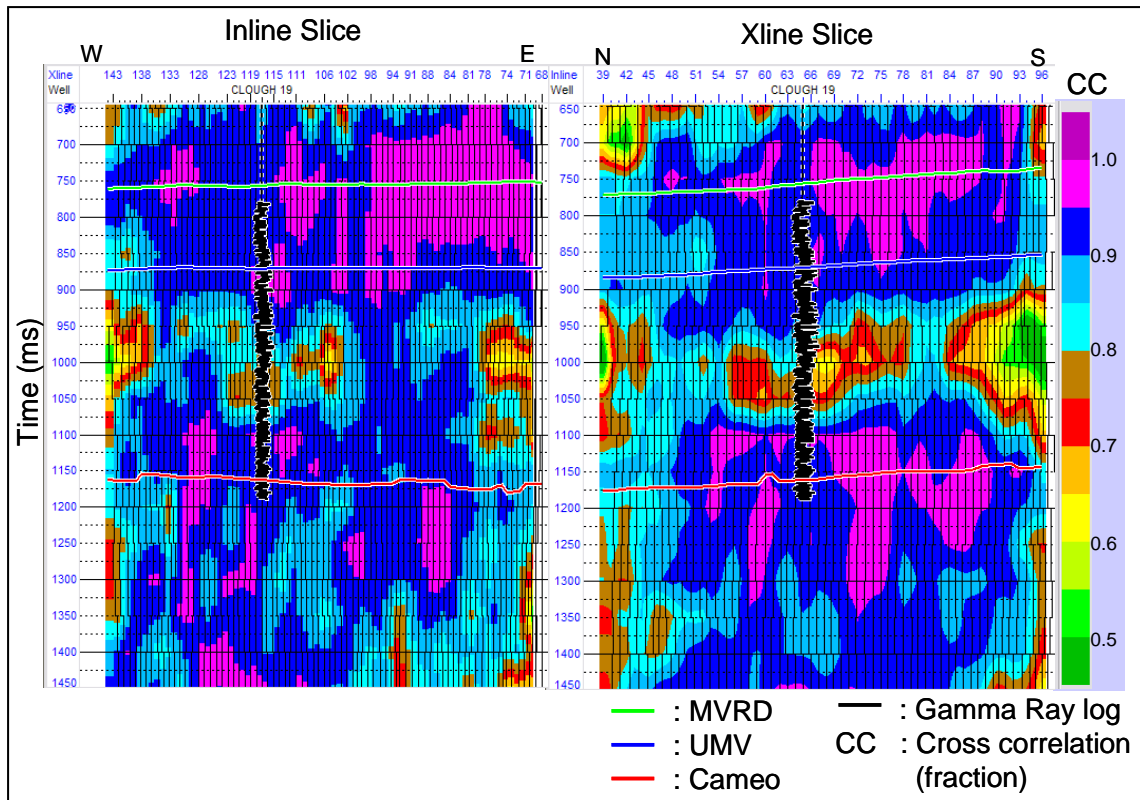


Figure 3.11. Cross correlation attribute applied to Rulison time-lapse datasets.

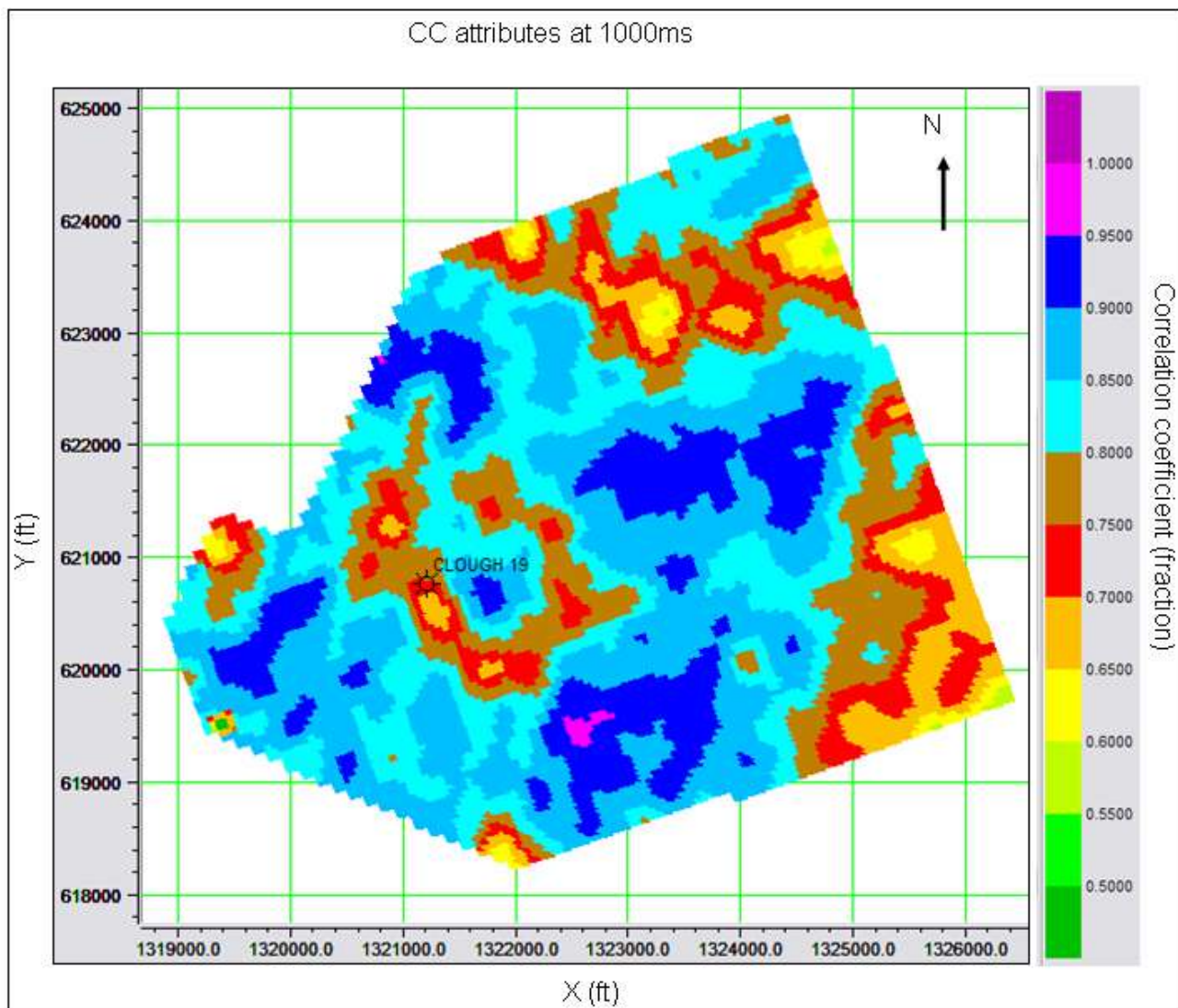


Figure 3.12. Time slice of correlation coefficient (CC) attribute at 1000 ms.

3.3.3. Percent Differences

The last attribute applied on the Rulison time-lapse analysis is the percent difference (PD) attribute. This attribute is generated from Rulison time-lapse data after the cross equalization process using equation 3.1. For the calculation purpose, the amplitude of the base data (1996 datasets) is smoothed. The smoothing process is applied vertically using a 30 ms block time window and horizontally with 5 x 5 traces window. Figure 3.13 shows the amplitude of the base data after the smoothing process.

Inline and cross-line slices are used for the analysis of the PD attributes. These 2D slices are located in the same location with the 2D lines used in CC attributes analysis which is intersecting well Clough 19. Figure 3.14 shows the PD attributes on the selected 2D slices and its comparable reflection strength (RS) attributes. Analysis on these 2D slices indicates the appearance of a PD anomaly around well Clough 19 especially at 1040 ms. The RS attribute does not clearly pick up this amplitude anomaly. A possible cause of this phenomenon is the low magnitude of the amplitude anomaly. The PD attribute has significantly increased the contrast between this low magnitude anomaly and its surrounding area. Some PD anomalies also occur at the Cameo level. Both of the attributes (PD and RS) picks up these anomalies clearly. The RS attributes picks up more anomalies at the Cameo level than the PD attribute.

To analyze the distribution of the PD anomalies at the reservoir level, the time slice is generated at 1040 ms. This time slice (Figure 3.15) shows the distribution of a PD anomaly, west of well Clough 19. Some other PD anomalies are also found along the edge of the data, but it is interpreted to be the result of edge effect. The time slice is also generated to analyze the distribution of the anomaly at the Cameo level. Figure 3.16 shows the time slice at 1230 ms. This figure shows that the PD anomaly is distributed near Clough 19 well at 1040 ms.

Analysis is performed on these anomalies using all other information i.e. synthetic data result, time shift attributes and CC attributes. The anomaly picked up by

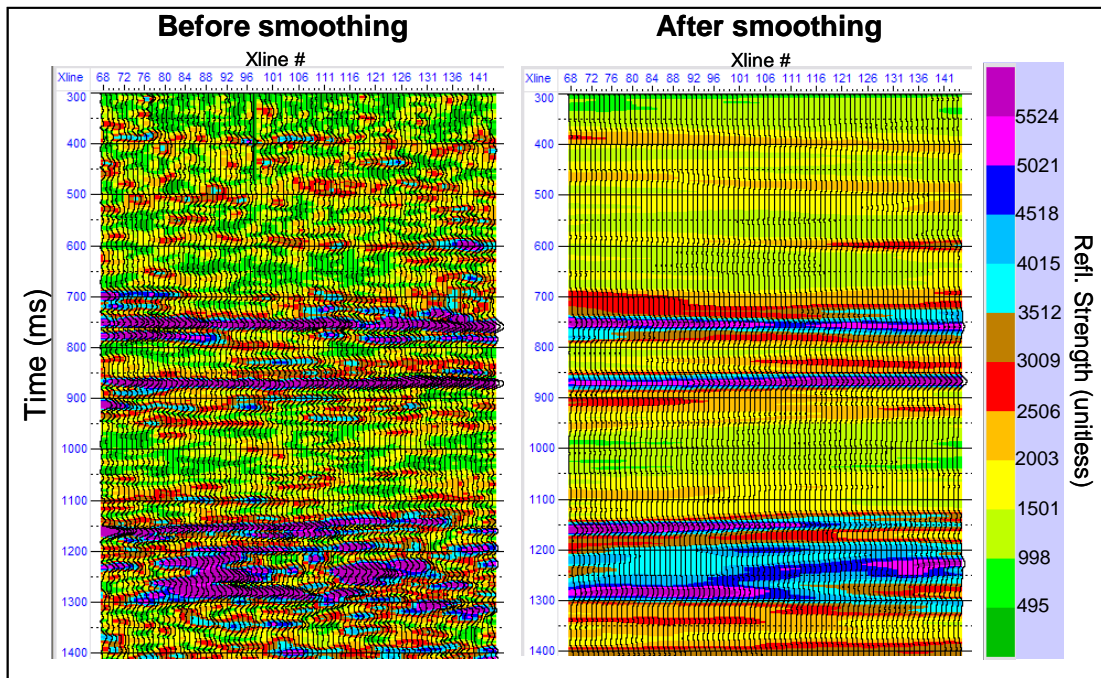


Figure 3.13.a. Comparison between base amplitude before and after smoothing.

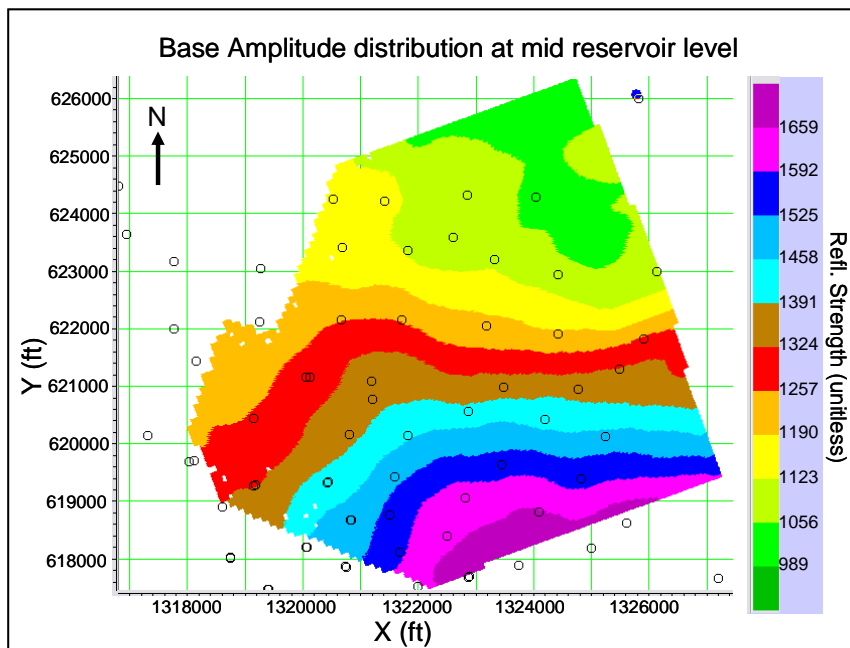


Figure 3.13.b. Distribution of smoothed base amplitude at mid reservoir level (1040 ms).

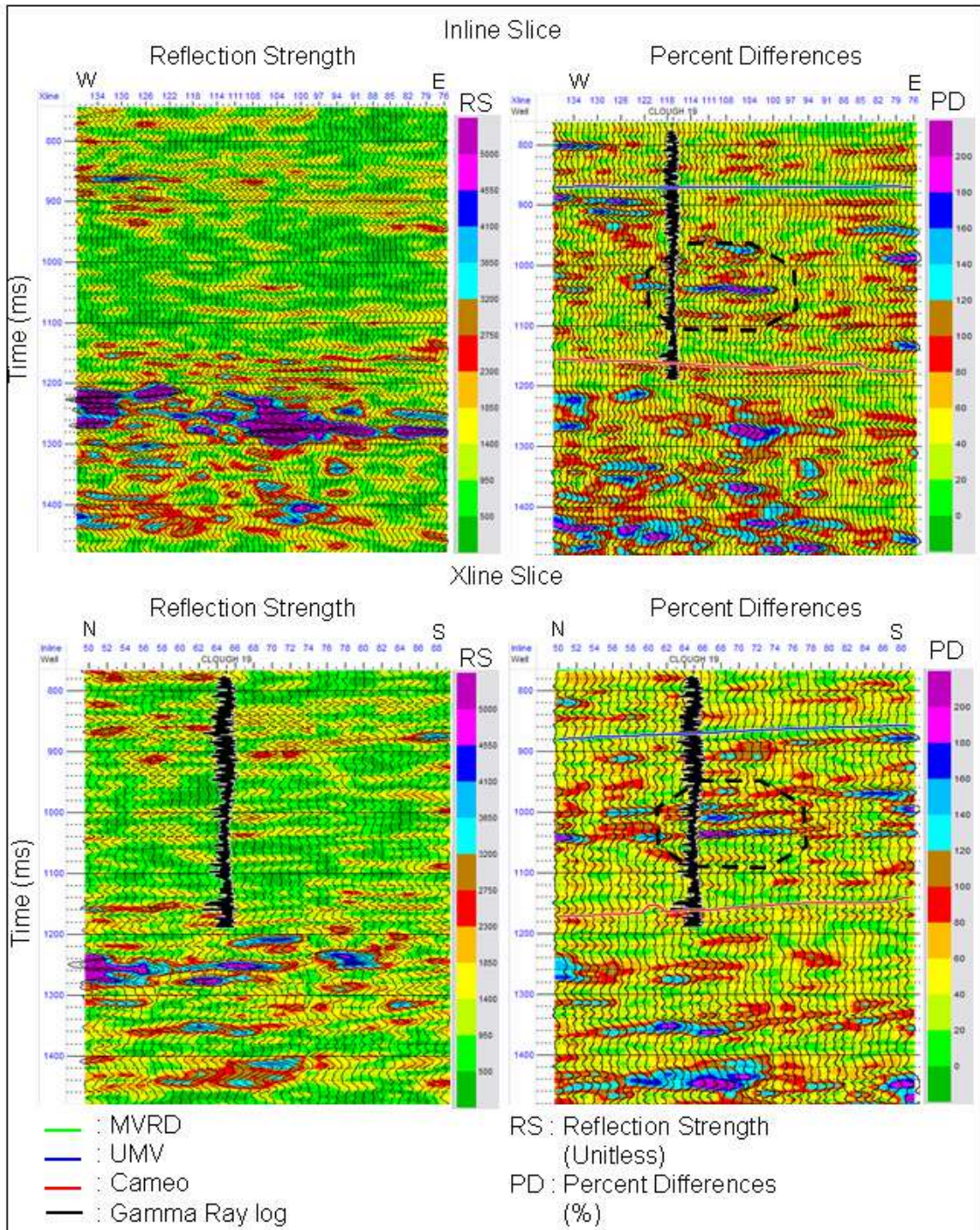


Figure 3.14. Comparison RS and PD attributes applied to Rulison time-lapse data.

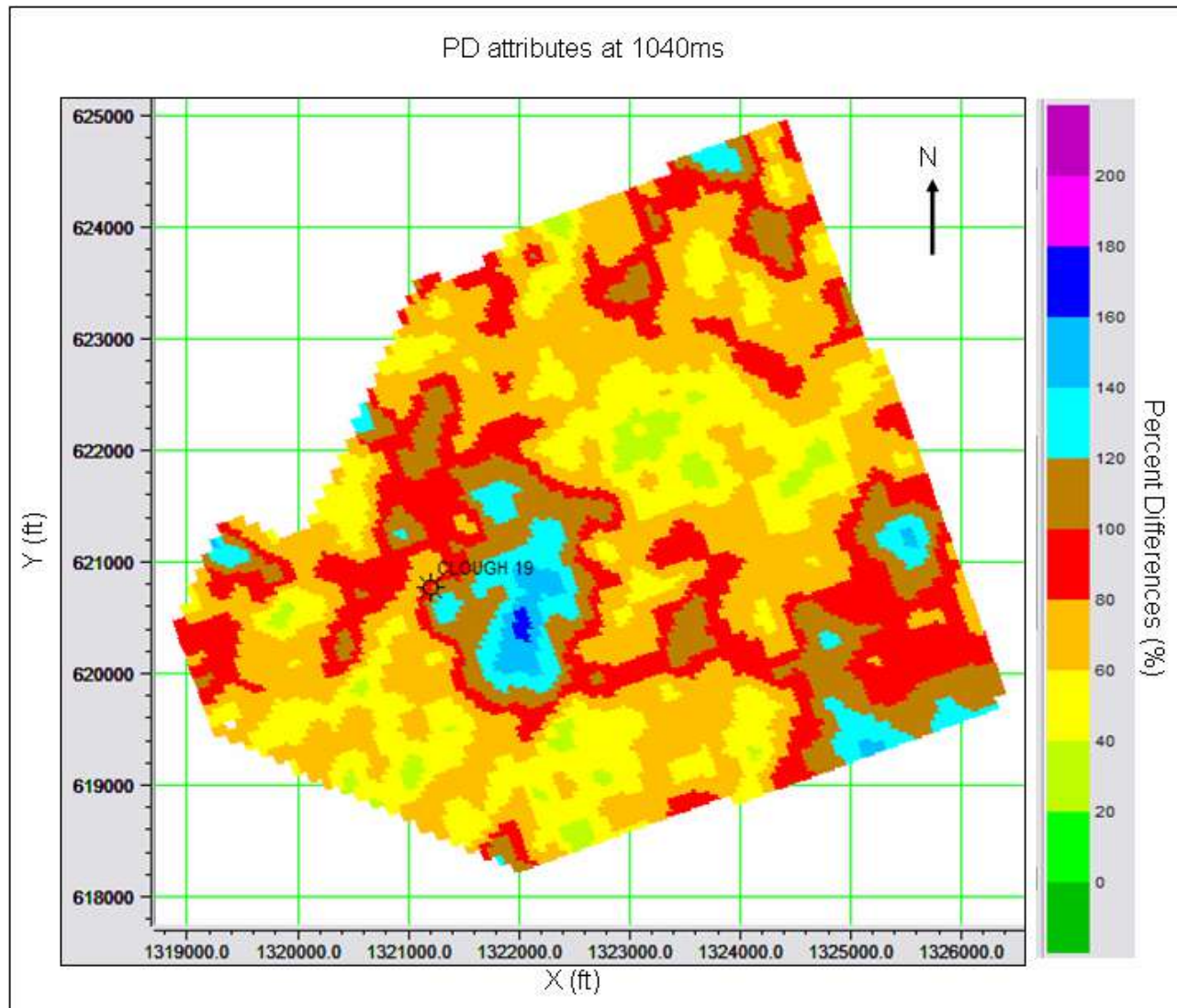


Figure 3.15. Time slice of percent differences attribute at 1040 ms.

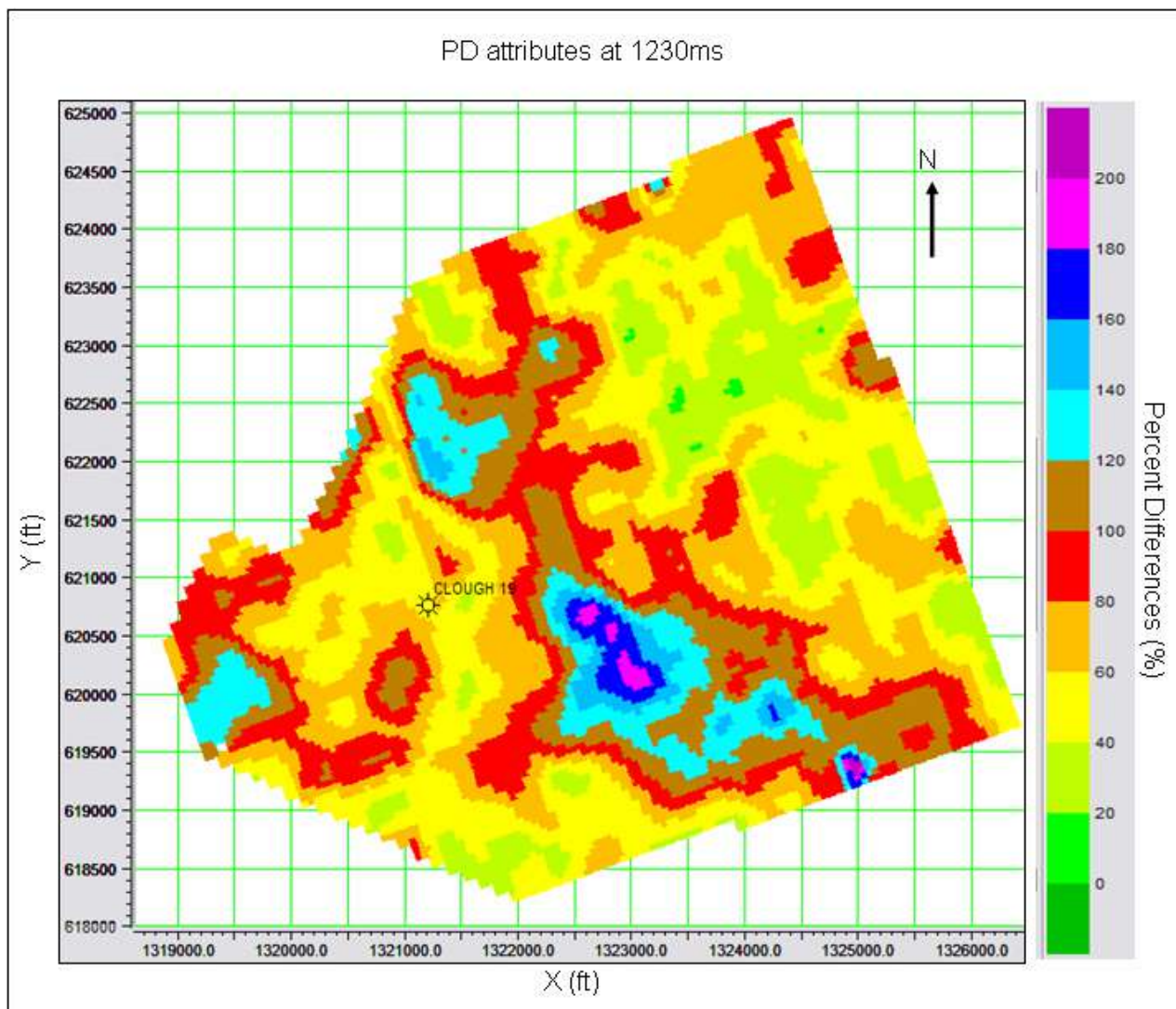


Figure 3.16. PD attribute at the Cameo level (1230 ms).

PD attribute at the reservoir level is located near the well Clough 19. This anomaly is strongly supported by the CC attribute and time shift attribute. Both attributes indicate a strong time-lapse anomaly near well Clough 19. The CC attribute also picks up the anomaly at the level of 950-1050 ms. This fact strongly supports the anomaly at the 1040 ms level. The distribution of the anomaly at this level also indicates a similar area with the CC anomaly. Analysis is also performed for the anomaly at the Cameo level. The synthetic data result suggests that the PD attributes highly reduce the effect of the velocity anomaly at the reservoir level for the horizon below reservoir. The appearance of a PD anomaly below the reservoir strongly suggests the existence of the time-lapse anomaly at the Cameo level. Some wells in this field have active perforation intervals in the Cameo level, including well Clough 19.

3.4. Summary of the Time-lapse Attributes

The Rulison time-lapse seismic datasets has some unique seismic characteristics i.e. low acoustic impedance contrast and discontinuous reflectivity within the thick reservoir interval. Based on these unique characteristics, three time-lapse attributes are chosen and applied to this datasets to analyze the time-lapse anomaly. Those attributes are time shift, correlation coefficient (CC) and percent differences (PD).

These attributes are then applied to the synthetic data to study the reliability, sensitivity, and error estimation of the attributes. The synthetic study has brought more knowledge on the characteristics of each attribute. Based on this synthetic study, the time-lapse attributes are then applied to the Rulison time-lapse datasets.

Time-lapse attribute analysis is performed on the cross equalized Rulison datasets. The time-lapse attributes analysis using a combination of the three seismic attributes has successfully detected time-lapse anomalies within the reservoir. An analysis of the time shifting attributes suggests that these anomalies are velocity-increase

anomalies. One of the largest time-lapse anomalies is detected around well Clough 19. The time-lapse analysis also indicates time-lapse anomalies within the Cameo interval.

Chapter 4

INVERSION OF TIME-LAPSE SEISMIC

4.1. Introduction to Time-lapse Seismic Inversion

Seismic inversion is a process of extracting the underlying geology information using seismic data (Russell, 2005). This process is performed by extracting acoustic impedance volumes from seismic traces. The acoustic impedance values are determined by rock properties (lithology, porosity, pressure, temperature etc) and fluid properties (fluid content, water saturation etc) within the formation. By generating impedance volumes and establishing their correlation with the rock and/or fluid properties, the distribution of the properties within the formation can be calculated. Seismic inversion can also reduce tuning in seismic data and increase the bandwidth (Lorenzen, 2000; Herawati, 2002). By removing the wavelet, the inversion process can reduce the tuning in the data. The seismic inversion can also increase the bandwidth of the data by including the low frequency information (Herawati, 2002).

Seismic inversion has been widely used in exploration especially to analyze rock and fluid properties distribution. Many case studies indicate the ability of seismic inversion to predict these properties (Madiba, 2003; Mukerji et al, 2001). Seismic inversion can also be used to analyze structure e.g. fracture zones (Vasco et al., 1996; Karaman and Carpenter, 1997).

There are many seismic inversion methods used in the industry. Three methods are discussed and used in this study. Those methods are Model Based inversion, sparse-spike inversion and colored inversion. The main differences among these three methods are approaches used to solve the inversion problem. In Model Based inversion, the

inversion is performed by iteratively updating an initial impedance model to produce more comparable synthetic traces. Sparse-spike inversion, on the other hand, is performed by updating the reflection coefficient (RC) series from an initial model to generate better-match synthetic traces. The colored inversion is a modern derivative of bandlimited inversion (Russell, 2005). This inversion is performed by matching the amplitude spectrum of seismic traces with impedance spectrum of the well data. More explanation on these inversion methods will be given in chapter 4.1.1.

Time-lapse seismic inversion has a unique characteristic that separates it from static seismic inversion. In time-lapse seismic inversion, the main goal is to calculate the impedance changes between datasets. In many cases, the impedance distribution for each dataset is not the main focus of the analysis, but detection of the change is. Most of the inversion methods applied in static seismic data can also be applied in time-lapse cases.

There are two different approaches that have been used by many researchers to solve the time-lapse inversion problem. The first approach is Differences of Inversion (DOI) approaches. DOI is a conventional approach to address the time-lapse inversion problems by calculating impedance models in static sense (Galikeev, 2002). This approach is performed by inverting each dataset separately and then combining them to generate an impedance difference model. The second approach is Inverse of Differences (IOD) approaches. IOD is an emerging technique in time-lapse analysis that has been introduced recently by many researchers (Sarkar et al., 2003; Galikeev, 2004; among others). This technique is performed using dynamic approaches by inverting amplitude differences between datasets to directly calculate the impedance difference model.

4.1.1. General Seismic Inversion Methods

Seismic inversion is performed by calculating an impedance model from measured seismic traces. The convolutional model for seismic traces (Yilmaz, 1987;

Yilmaz, 2001; Russell, 2005; among others) describes seismic traces as a result of convolution process between wavelet and RC series, with some additional uncorrelated and/or correlated noise. This relation is described in equation 4.1 (Russell, 2005). Inversion of the seismic data is performed to extract reflectivity series (R) and its derivative (Impedance) from the seismic traces (T).

$$T = W * R + Noise \dots \dots \dots \text{(Eq. 4.1)}$$

(Russell, 2005)

Where :

T : Seismic trace

W : Wavelet

R : Reflectivity series

In general, some assumptions need be made in order to solve this P-wave inversion problem. These assumptions are (Russell, 2005; Herawati, 2000):

- a) 1-D Earth
- b) No AVO effect
- c) Transmission loss and geometric spreading is ignored
- d) Frequency dependent absorption is ignored
- e) Wavelet (W) is not time-varying
- f) Wavelet (W) is known
- g) Noise is random and uncorrelated with the signal

One of the important assumptions is that the wavelet is known. There are several methods to predict the wavelet signature. The first method is by direct measurement of the wavelet signature. This method is usually applied to marine data by putting a hydrophone near the seismic source. This hydrophone then records wavelet signatures from seismic source. But in reality, the seismic wavelet is time-varying/depth-varying. For inversion of deep seismic data, this recorded wavelet needs to be corrected. The second method is well-to-seismic tie. This method is used in this research. This method is

performed by generating a wavelet to match between calculated seismic traces from well log data and measured seismic traces around the well. Using this method, the extracted wavelet is already corrected for time-variation/depth variation.

Solving the reflectivity series (R) which satisfies equation 4.1 is a non-linear problem (Russell, 2005). The common approach to address this problem is by using Least Square optimization. In this study, seismic inversion is performed using STRATA from Hampson-Russell Software. In this software package, inversion is done using iterative Least Square techniques. Equation 4.2 shows the objective function of the Least Square optimization for the seismic inversion (Russell, 2005). Pre-whitening factor λ is a regularization parameter. This parameter λ determines the trade-off between the data misfit and a model or data structure penalty term (Scales et al., 1997).

$$L = (M^T \cdot M + \lambda \cdot I)^{-1} \cdot M^T \cdot T \quad \dots \dots \dots \text{(Eq. 4.2.)}$$

(Russell, 2005)

Where:

L : Impedance model

M : Forward matrix

I : Identity matrix

λ : Pre-whitening factor

T : Seismic traces

As previously mentioned, there are three seismic inversion methods used in this study. The first inversion method is Model Based inversion. This method is performed by introducing an initial impedance model as an input to the inversion process. The initial model is then updated using least square optimization to achieve synthetic seismic traces that match within a certain level with measured seismic traces. In this inversion, a pre-whitening factor λ determines how well the model fit the data without matching the noise. One of the main issues in this inversion method is that the inversion result can be very dependent on the initial model (Russell, 2005). In order to generate a representative

initial model, the model is derived from the available well data in the area. The model base can also be performed using a stochastic inversion method. This inversion is performed by generating equiprobable impedance traces from the initial model (Robinson, 2001). Synthetic seismic traces are then generated based on these impedance models. The best match impedance model is selected for the inversion result.

The second inversion method is Sparse Spike inversion. This method is based on assumptions that the earth is represented by a series of parallel layer and the reflectivity function is characterized by the sparse and isolated spikes (Russell, 2005). Based on these assumptions, the optimum impedance profile is obtained by iteratively adding the reflectivity spikes from the initial model. This inversion method tends to focus more on the larger spikes and consists less detail when compared with Model Based method. On the other hand, this method is less dependent on the initial model compared to the Model Based inversion.

The third inversion method is Colored inversion. This inversion method is performed by matching the amplitude spectrum of seismic data with impedance spectrum of well data. A single spectrum operator is extracted from available well information and seismic traces around the wells. This spectrum operator is then applied to the entire seismic volume to transform it directly into the inversion result. Using this kind of approach, the inversion result has very little dependence on the initial model (Russell, 2005). The disadvantage of this method is that it produces a relative impedance value. In the case of time-lapse inversion, this relative impedance value can be useful to analyze impedance changes.

4.1.2. Time-lapse Seismic Inversion Methods

Seismic inversion is applied in time-lapse datasets with the main goal of extracting impedance differences/changes between time-lapse surveys. As previously mentioned, there are two different approaches that have been used to solve this time-lapse inversion problem. Those approaches are Differences of Inversion (DOI) and Inverse of Differences (IOD). Figure 4.1 shows the flow chart of both methods.

Differences of Inversion (DOI) is a conventional approach to solve the time-lapse inversion problem. The DOI approach is performed by inverting each dataset separately to generate a set of impedance models. Impedance changes are then calculated by taking the differences between impedance models of monitor surveys and the base surveys. To generate a set of comparable impedance models from each dataset, all inversion processes are performed using the same inversion parameters (initial model, pre-whitening factor, wavelet etc). Previous case studies by Herawati, 2000 and Galikeev, 2002 shows that seismic inversion with DOI approach has been successfully used to analyze time-lapse data.

The second approach for time-lapse inversion is Inverse of Differences (IOD). This approach is performed by calculating amplitude differences between seismic traces from monitor and baseline surveys. These amplitude differences are then used as an input in the seismic inversion process to calculate an impedance difference model. Galikeev (2004) has studied the implementation of this IOD approach and the comparison between IOD approach and conventional (DOI) approach. In this study, Galikeev (2004) has emphasized some of the advantages of IOD approaches compare to conventional (DOI) approach. Those advantages are (Galikeev, 2004):

- a) The processing time is done much faster using IOD approach than DOI approach since inversion is performed in lesser volumes.
- b) IOD result has lesser noise. Noise, in this case, is defined as the anomalies outside the reservoir level.

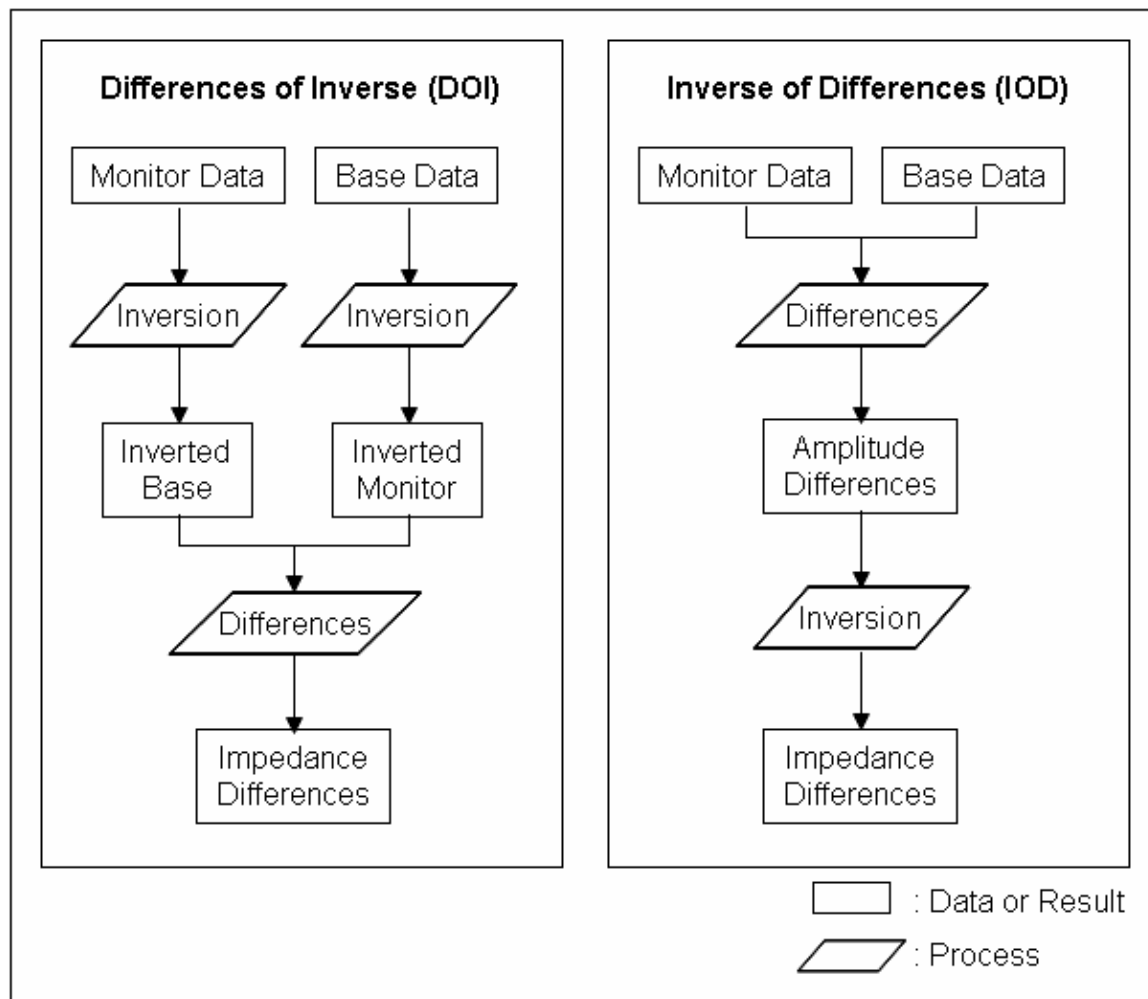


Figure 4.1. Flowchart of time-lapse inversion approaches.

(modified from: Galikeev, 2004; Sarkar et al., 2003)

4.2. Application to Synthetic Time-lapse Datasets

Application of seismic inversion to synthetic time-lapse datasets is performed to study reliability, sensitivity, and error estimation of the inversion process. Inversion of synthetic time-lapse data is also performed to analyze the difference between the DOI and IOD approaches. The synthetic time-lapse datasets used in this study are extracted from field seismic data information. More explanation on the synthetic time-lapse datasets is contained in chapter 1 (1.6.3. Synthetic seismic datasets). The synthetic datasets are simulated using all important components of field data i.e. noise, wavelet extracted from field data and well log information.

As previously explained in chapter 1, the synthetic datasets was generated from a simulated impedance model with additional time-lapse anomalies. The time-lapse anomalies were simulated with different thickness values (inline) and different velocity values (crossline). An inversion process is then applied to this datasets to predict the time-lapse anomaly. The application of different inversion approaches to these datasets can help to understand the characteristic of each inversion method to detect the time-lapse anomaly with certain thickness and velocity values.

Analysis of this synthetic study will help the application of time-lapse inversion for Rulison field datasets. Comparison between DOI and IOD result from this synthetic study can help in inversion process of field data. Study on the sensitivity of each inversion to detect time-lapse anomalies will provide guidance to interpret the inversion of the field data.

4.2.1. Differences of Inversion

The first time-lapse inversion approach used for this synthetic dataset is Differences of Inversion (DOI). Inversion using DOI approach is performed by inverting

individual seismic datasets separately. In this study, a constrained Model Based inversion technique is used in the inversion process.

The inversion process begins with an initial impedance model. This impedance model (Figure 4.2) is generated from simulation-input-well datasets (Clough 19). This impedance model is then used as an initial model in the inversion process of both base and monitor data. The second input of the inversion process is the seismic wavelet. The wavelet used in this inversion process is taken from field-data-extracted wavelet (Chapter 1.6.2.2. Well to seismic tie). This wavelet was also previously used to simulate the synthetic time-lapse datasets. To produce a comparable inversion result, each inversion is performed using the same inversion parameters i.e. initial impedance model, wavelet, pre-whitening factor and number of iteration.

Figure 4.3 shows the result of seismic inversion for both base and monitor data. This inversion result is set to have seismic traces correlated within a 10% noise level by modifying inversion parameters especially pre-whitening factor. The parameters used in this inversion are: 10% pre-whitening factor (λ); 5 maximum iterations; and 25% impedance constraint. In this figure (Figure 4.3), a comparison is presented between the inversion result of base data and monitor data with high velocity increase (60%). This comparison shows that the inversion process can still match traces well in the presence of high-velocity anomaly. There are significant differences between the impedance model of base data and monitor data around 1020 ms. The impedance model of monitor data has a higher value in this level than base data.

Analysis is also performed on the distribution of inversion result throughout the entire seismic volume (Figure 4.4). This analysis indicates that the impedance model for both base and monitor data has a similar value distribution except in the level around 1010-1060 ms. To understand better this anomaly, a difference between the base

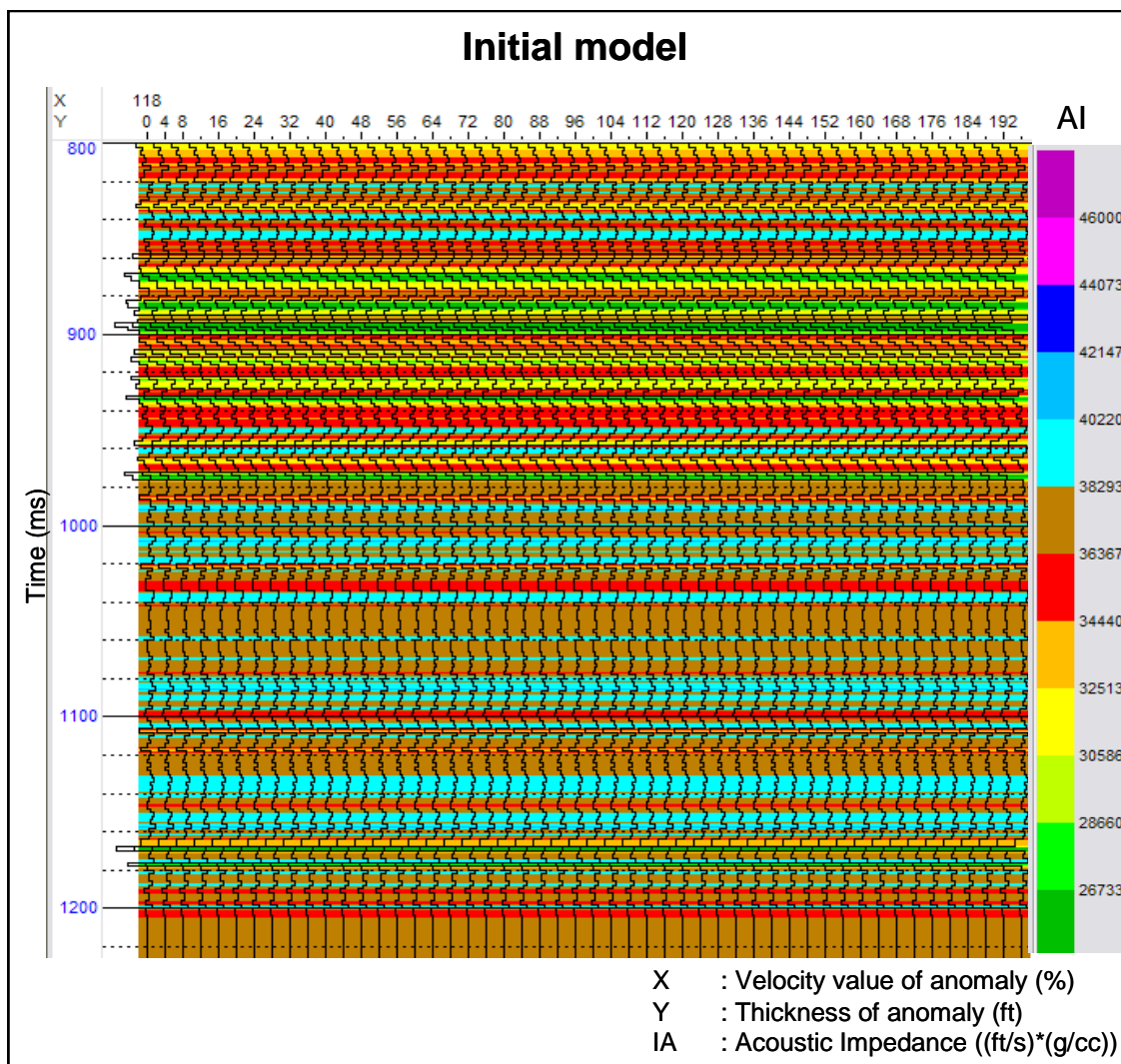


Figure 4.2. Initial model for model base inversion.

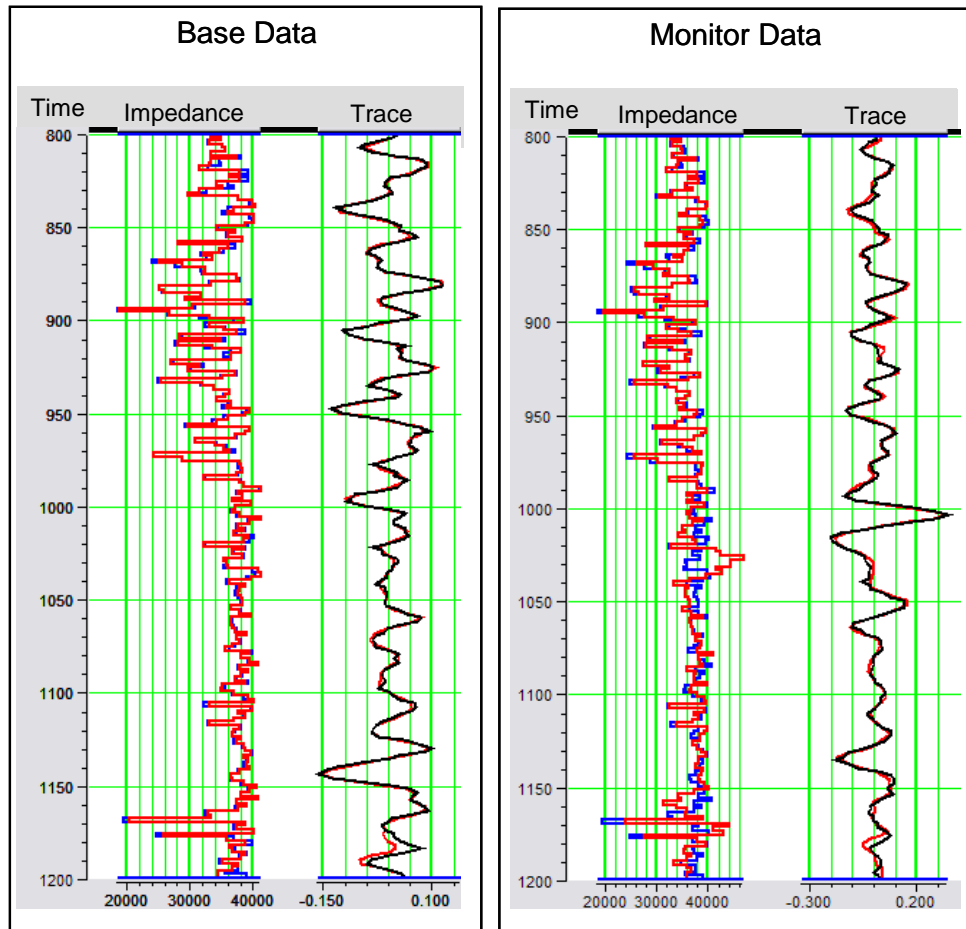


Figure 4.3. Correlation plot of inversion result. Left figure is a plot of impedance and synthetic correlation for base data. Right figure shows the plot of correlation for monitor data from traces with time-lapse anomaly (velocity increase : 60%; thickness: 160 ft).

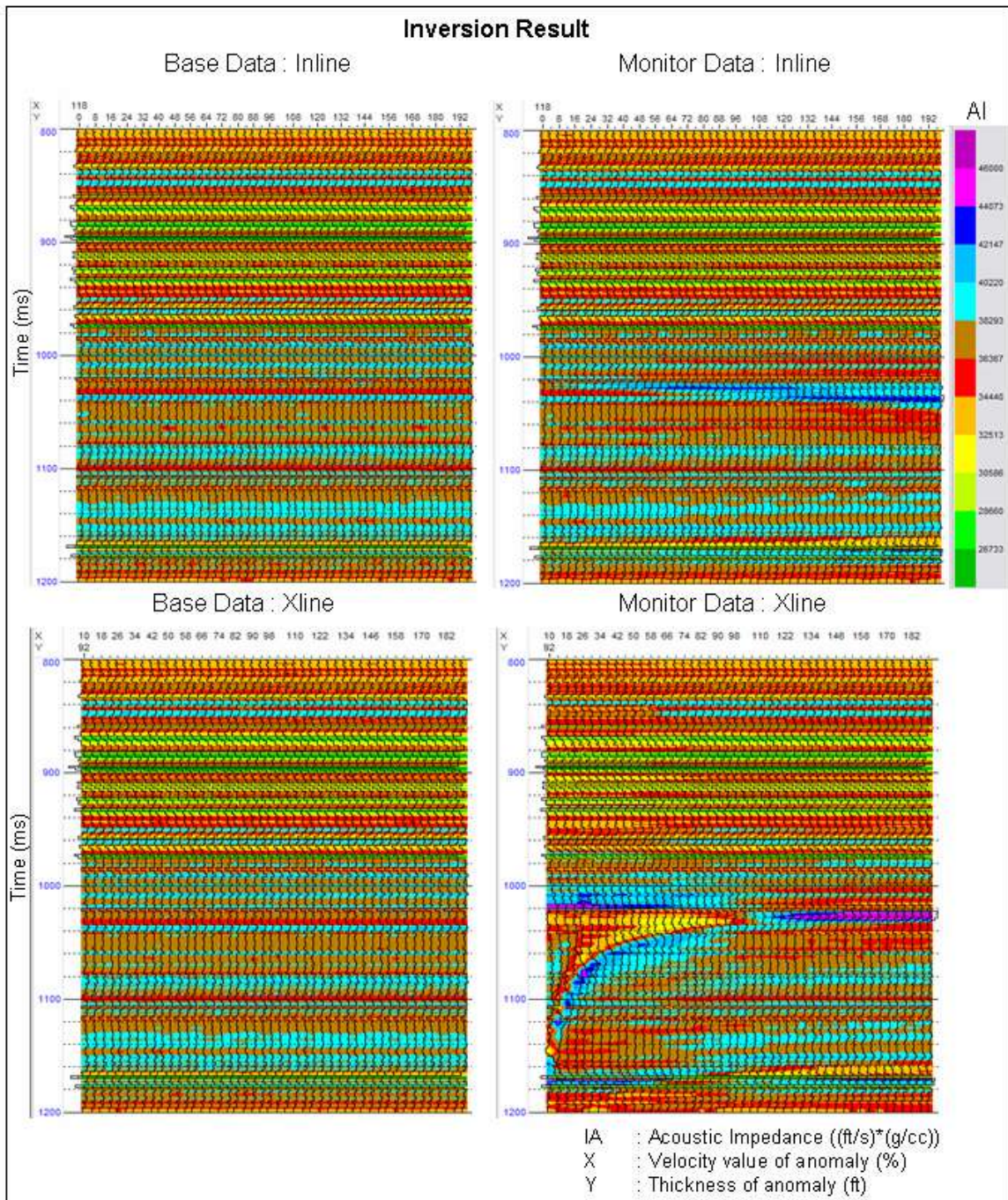


Figure 4.4. Inversion result for base and monitor data (Synthetic datasets).

Inline indicates thickness variation. Cross line indicates velocity variation.

impedance model and monitor impedance model is generated (Figure 4.5). In this figure (Figure 4.5), the anomaly is better defined. The location of this anomaly matches with the location of the simulated time-lapse anomaly. Some impedance differences are also detected outside the area of original anomaly especially at deeper level (around 1160 ms). These differences are considered to be noise. Further analysis on Figure 4.5.inline shows that this DOI inversion result has been able to detect the thickness of simulated time-lapse anomaly with a good approximation. Figure crossline (Figure 4.5) also shows that this inversion result has been able to detect velocity anomaly changes from negative changes in the left area to positive changes at right area. This figure also shows that when velocity value (X) is less than 42 (58% decrease in velocity), the inversion result has failed to detect the time-lapse anomaly in the true position. Possible explanation of this phenomenon is that the seismic traces have been shifted down far from original traces (more than 40 ms) because of very-low velocity anomaly (see Figure 1.16). Because of this high time shift, cross correlation process (time shift correction) tends to correlate traces signature with nearest possible match signature. This process generates time shift to incorrect signatures. Random time-shift values at low velocity anomaly (Figure 3.6) also support this analysis. There is a possibility that this phenomenon could occur at a very high velocity anomaly based on this analysis.

Application of DOI inversion on synthetic data has helped the author to analyze some important characteristic of this approach. Some of those characteristics are:

- a) DOI inversion has successfully detected the time-lapse anomalies.
- b) DOI inversion result has been able to detect the thickness of time-lapse anomalies.
- c) Noise occurs in DOI inversion result especially at the deeper time level (around 1160 ms).
- d) Inversion result has failed to recover the position of time-lapse anomalies with very low velocity values (velocity decrease more than 58%).

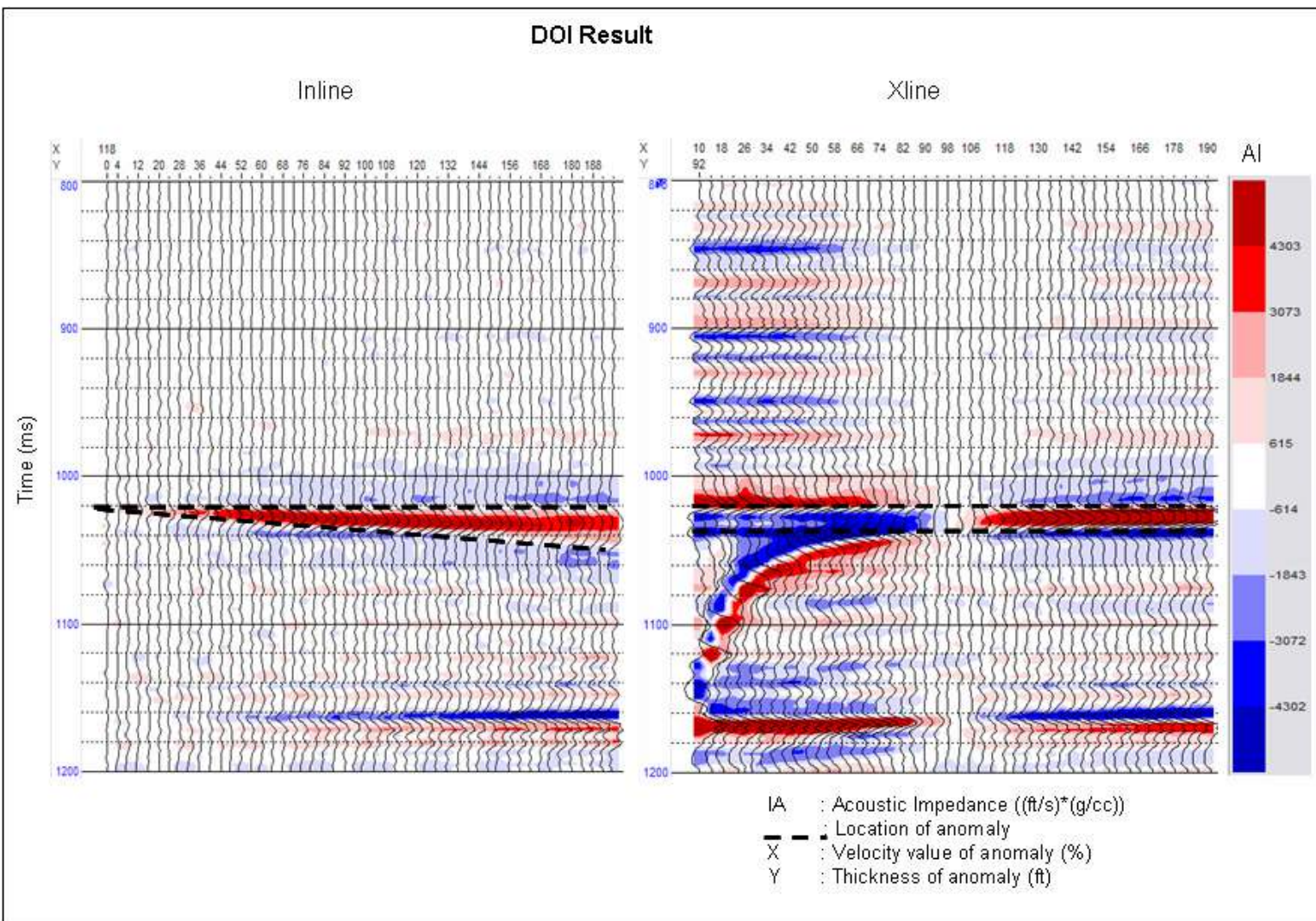


Figure 4.5. Impedance difference from DOI approach.

4.2.2. Inverse of Differences

Time-lapse inversion using Inverse of Differences (IOD) approach is performed to synthetic datasets to generate impedance differences model. IOD is performed by generating amplitude differences between seismic traces. An inversion process is then carried out for this amplitude difference volume to generate an impedance difference model. To generate an impedance difference model distributed around zero value, a constant zero value should be used for initial model. In this study, the inversion process is done using constrained Model Based inversion techniques. Inversion parameter is determined to generate least impedance differences with best correlation of seismic traces. The parameters used in this inversion are: 25% pre-whitening factor (λ); 5 maximum iterations; and 25% impedance constraint.

The first step in this inversion process is to generate amplitude differences volumes. This volume is generated from seismic traces of base data and monitor data. Second important input in the inversion process is initial model. Due to a software limitation, the initial model in inversion process can not be zero value. To overcome this problem, a constant impedance value ($AI = 75000$) is used as the initial impedance model. This value is then extracted from the final inversion result to produce the desired-impedance differences model. Other important input for the inversion process is the seismic wavelet. Seismic wavelet used in this inversion is a wavelet that was extracted from field data (detailed explanation on Chapter 1.6.2.2). The inversion process is then performed using these defined inputs i.e. amplitude differences, initial model and wavelet.

Analysis on the inversion result using IOD approach shows that impedance differences are well distributed around zero values (Figure 4.6). Figure 4.6 also shows comparison of impedance differences value distribution from DOI and IOD approach. This analysis suggests that both approaches have a different type of distribution. The DOI result has a tighter distribution than IOD result. A similar distribution result was also

observed by Galikeev (2002). To analyze time-lapse inversion result, both DOI and IOD result is mapped based on their individual color scale.

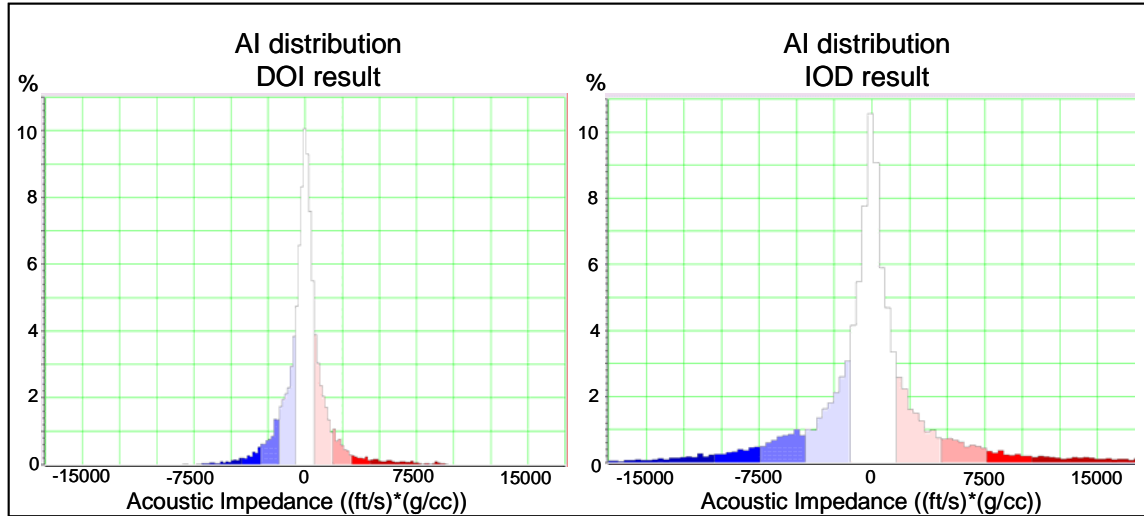


Figure 4.6. Distribution of AI value from inversion result using DOI and IOD approaches.

IOD inversion result is then plotted based on its scale (Figure 4.7). This figure (Figure 4.7) shows that the IOD inversion result has successfully detected time-lapse anomaly with good accuracy. Noise still occurs in this inversion result especially for the low thickness anomalies. This noise can be detected by the occurrence of impedance differences outside anomaly zones. The noise in the IOD inversion can be detected especially in the area of low thickness anomalies and small velocity changes anomalies (Figure 4.7 Inline and Crossline). The noise in the deeper level as suggested by DOI inversion is not detected in the IOD inversion. The inline figure (Figure 4.7. Inline) also shows that this inversion result has been able to detect thickness variations in time-lapse anomalies. An analysis is also performed on crossline figure (Figure 4.7.

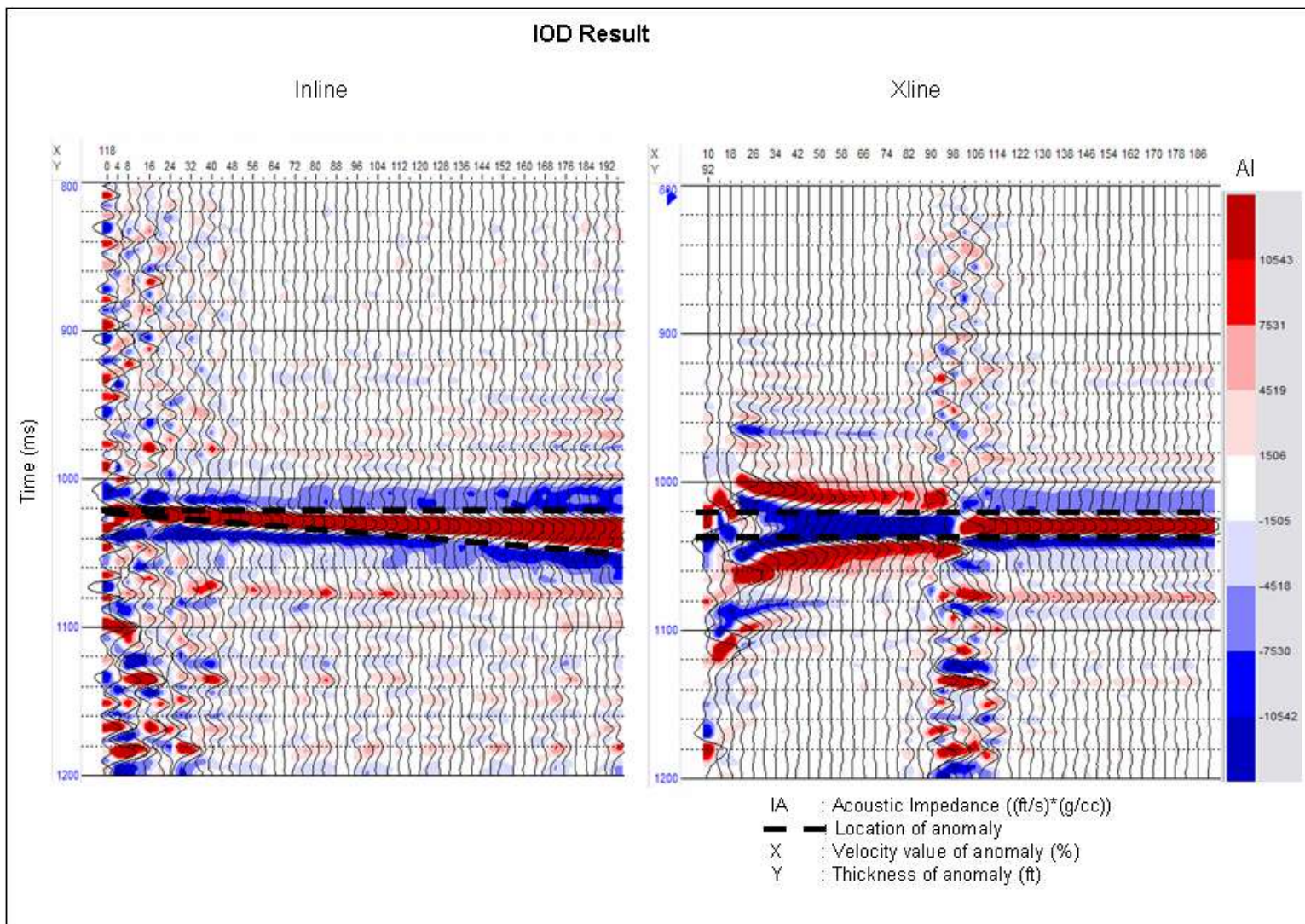


Figure 4.7. Impedance difference from IOD approach.

Crossline). This figure shows that IOD inversion result has been able to detect velocity variation of time-lapse anomaly especially differentiate between negative anomaly (decrease in velocity) and positive anomaly (increase in velocity). In the area of very low velocity, IOD inversion has been able to perform a better job to image the anomaly compare to DOI inversion (Chapter 4.2.1).

Velocity changes are calculated based on impedance difference values. Velocity values are calculated using velocity-impedance correlation (Chapter 1.6.2.1). This velocity-impedance equation is generated based on statistical relation from well data. Using this velocity value, percent velocity change values are calculated. Figure 4.8 shows percent velocity changes from both DOI and IOD approach. This figure (Figure 4.8) indicates that percent velocity changes from the DOI approach have lower values than the actual percent velocity changes. Maximum positive percent changes detected in DOI inversion is only 20% while the actual velocity reaches 70%. The IOD inversion has higher velocity changes estimation than DOI result. But, the distribution of velocity changes from IOD result (Figure 4.8) has failed to predict the true velocity changes value.

Based on this study, the author has been able to analyze the characteristic of IOD inversion. Those characteristics are:

- a) IOD inversion has been able to detect the position of the time-lapse anomalies.
- b) Thickness of time-lapse anomaly has been successfully determined using IOD inversion approach.
- c) Noise in impedance differences model still occurs in IOD inversion. The noise level in the IOD inversion is less than DOI inversion especially in the deeper level. Noise is defined as anomalies outside the known location of time-lapse anomalies.
- d) IOD inversion can detect the time-lapse anomaly for low velocity zones better than DOI inversion.

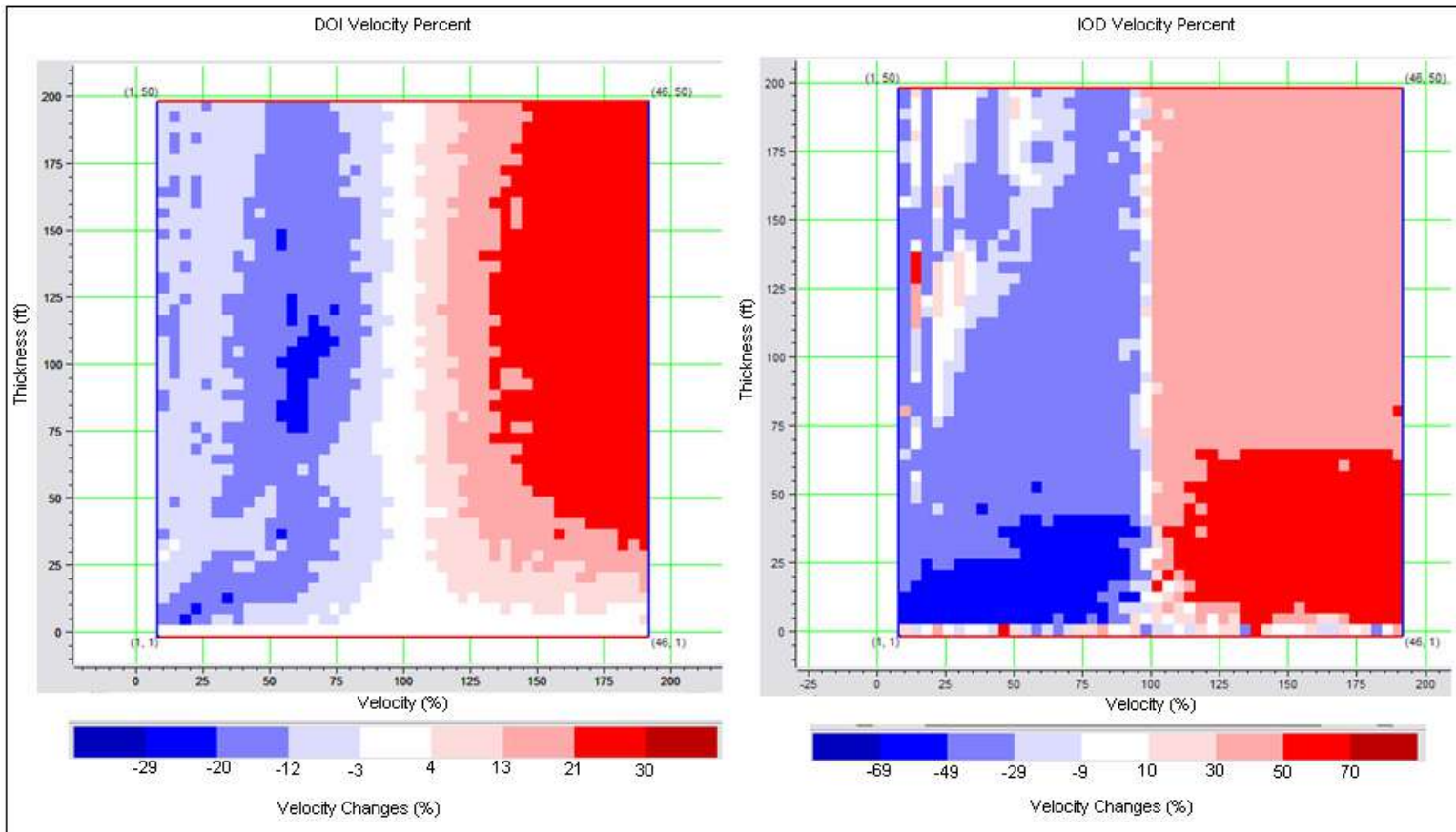


Figure 4.8. Comparison of velocity value (in percent velocity) between DOI and IOD approaches.

- e) IOD inversion result has a different value distribution from DOI inversion. In general, IOD inversion has a higher impedance anomaly value.
- f) Both approaches (DOI and IOD) are unsuccessful to predict accurately the velocity change.

4.3. Application to Rulison Time-lapse Datasets

Time-lapse inversion is applied on Rulison time-lapse datasets to understand more about location, thickness, distribution and other important aspect of time-lapse anomaly in Rulison field. The inversion is performed using both DOI and IOD approach. Using these approaches, the author expects to find consistent figures to determine the dimension, location and other aspects of time-lapse anomaly.

Inversion in both approaches (DOI and IOD) is performed using seismic traces from the cross equalization process (Chapter 2). Inversion process is performed for the whole seismic volumes. Analysis of this inversion result, on the other hand, excludes the edge area. As previously explained in chapter 2, the edge area had low trace repeatability, even after cross equalization process, due to the low trace coverage in this part of the study area. Due to this reason, the inversion result in this edge area is expected to have less reliability. Another important input for inversion process is the seismic wavelet. The seismic wavelet used for the inversion is extracted from the well-to-seismic-tie process (Chapter 1.6.2.2).

A constrained Model Based inversion technique is used as the primary technique for time-lapse inversion in both DOI and IOD approaches. Inversion of the Rulison datasets using this technique will be discussed in detail. Other inversion techniques are also used for the inversion. These inversion techniques are stochastic-model-base and sparse spike inversion for DOI approach; sparse spike and colored inversion for IOD approach. More explanation on these inversion techniques is discussed in the previous

section (Chapter 4.1.1). Inversion results from these techniques will be discussed and compared with the inversion result from constrained-model-base inversion.

To analyze the inversion result, inline and crossline slices are generated from the impedance volumes. These inline and crossline slices are the lines that pass through well Clough 19. Similar lines are also used to analyze time-lapse attributes (Chapter 3). More explanation about location of these lines can be found in chapter 3.3 and Figure 3.10.

4.3.1. Differences of Inversion

Time-lapse inversion is conducted on Rulison datasets using the DOI approach. Base data (1996 survey) and monitor data (2003 survey) are inverted separately using consistent inversion parameters. An impedance difference is then calculated from the inversion results. To generate comparable impedance models, a single initial model is used for inversion of both base and monitor data. This initial model (Figure 4.9) is generated from 4 available wells information (Clough 19, RWF 332-21, RWF and RMV 68-21). More information on these wells is discussed in chapter 1. Impedance information available from all well is from 800-1200 ms. Two wells (RWF and RWF 332-21) has impedance information for deeper zone (up to 1300 ms). All inversion analysis is then performed in the time interval from 800 to 1300 ms.

To perform an analysis on the inversion parameter, a cross-validation process is conducted on base datasets. This process is also called hidden-well-test. The main goal of cross-validation process is to determine an optimum inversion parameter i.e. iteration number, pre-whitening factor and constrained impedance value. This process is conducted for base data inversion, but the resultant-parameters are used for both base

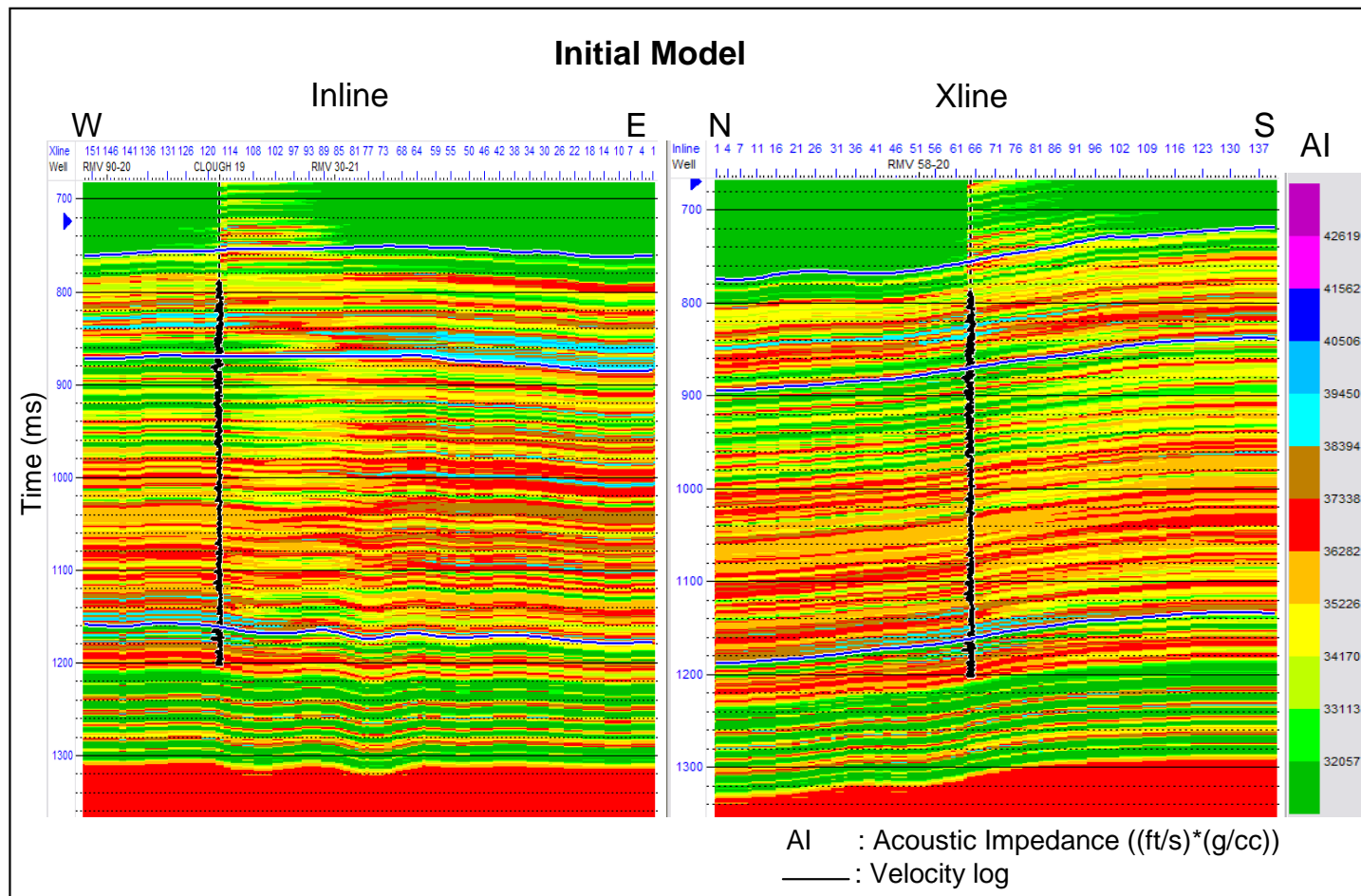


Figure 4.9. Initial AI model for model base inversion.

and monitor data inversion. The cross-validation process is performed by taking the impedance information from one well (“hidden” well) out of the initial impedance model. An inversion process is then conducted using this initial model. The inversion result in the specific location of the “hidden” well is compared with actual impedance value from the well. Correlation value between actual impedance and predicted-impedance from inversion process is used to analyze optimum inversion parameters.

The most important inversion parameter to be determined is the pre-whitening factor (λ). This pre-whitening factor determines the trade off between data misfit and model structure penalty term (detail explanation in Chapter 4.1.1). To analyze an optimum pre-whitening factor, cross-validation process is performed using pre-whitening factor as the objective parameter. Figure 4.10 shows a plot of impedance correlation and seismic trace correlation from cross-validation process. Correlation value in this figure (Figure 4.10) indicates the correlation between actual value from “hidden” well and predicted value from inversion process using specific pre-whitening value. Other inversion parameters are set to be constant in this analysis. This figure (Figure 4.10), in general, shows that impedance correlation increases with the increase of pre-whitening value, while trace correlation decreases with the increase of pre-whitening value. To determine an optimum pre-whitening value, detailed analysis of impedance correlation is performed. Impedance correlation value increases significantly before λ reaches 5%, but the correlation does not increase significantly for higher λ value. In some wells (Clough 19 and RMV 68-21), impedance correlation decreases slightly after this value. Analysis on traces correlation (Figure 4.10) also shows that traces correlation decreased more significantly when λ value is higher than 5%. Based on this analysis, optimum pre-whitening value is determined to be 5%. An interesting feature appears on the trace correlation of RWF well. In this well, synthetic trace correlation increases with the increase of λ . This interesting phenomenon might due to the closeness location between this RWF well with RWF 332-21. Most of the low frequency information in these two wells are similar.

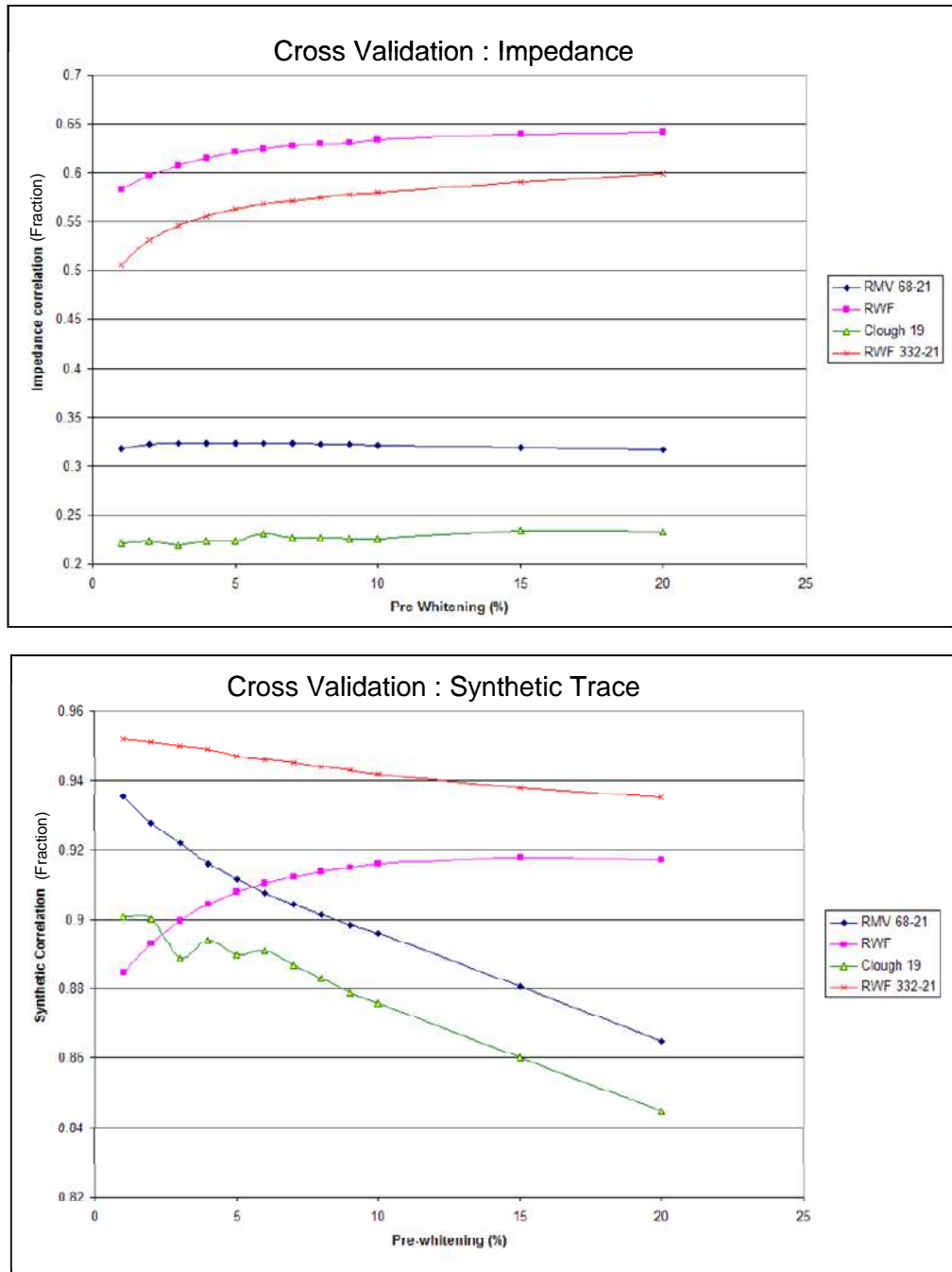


Figure 4.10. Cross validation for determining pre-whitening factor (λ).

Other inversion was set to be constant:

Iteration number = 10; Constrained impedance = 25%.

Using these defined inversion parameters, the inversion process is performed on the base and monitor data. To study the quality of the inversion result, a correlation plot of inversion result is analyzed (Figure 4.11). This figure (Figure 4.11) shows correlation value between actual and predicted value of impedance and seismic traces. Inversion of both base and monitor data shows a similar total correlation value. There is a slight decrease in total impedance correlation in the monitor data compared with baseline data. On the other hand, total trace correlation in the monitor data is slightly higher than the base data. This analysis indicates that inversion process has predicted the impedance model of base and monitor data equally well. But, slight impedance differences might occur between baseline and monitor data.

Figure 4.12 shows impedance distributions of base and monitor data from inversion result. This figure (Figure 4.12) shows that inversion result of base and monitor data generated similar impedance models. There are some areas that have different impedance values especially around 1080 ms and near Cameo horizons. To better delineate time-lapse anomalies, an impedance difference model is generated from impedance model of base and monitor data (Figure 4.13). This DOI result (Figure 4.13) shows very noisy impedance differences. It is difficult to determine time-lapse anomalies from noise in this DOI result. To detect the position of time-lapse anomalies in this DOI result, the result of attributes analysis (chapter 3) is used. Based on attributes analysis (chapter 3), the major time-lapse anomaly is located around 1040-1060 ms. The DOI result indicates a distinct positive impedance anomaly in this time level. To understand this anomaly, a horizon slice along this positive impedance anomaly is generated. This horizon slice is created using the shape of Cameo horizon as a reference. Horizon slice is taken 107 ms above the reference horizon (Cameo horizon) in the middle of the positive impedance anomaly. The result of this horizon slice is shown in Figure 4.14. The horizon slice (Figure 4.14) shows a distinct positive anomaly around well Clough 19 and RWF 332-21. The distribution of this anomaly around Clough 19 is supported by the attribute

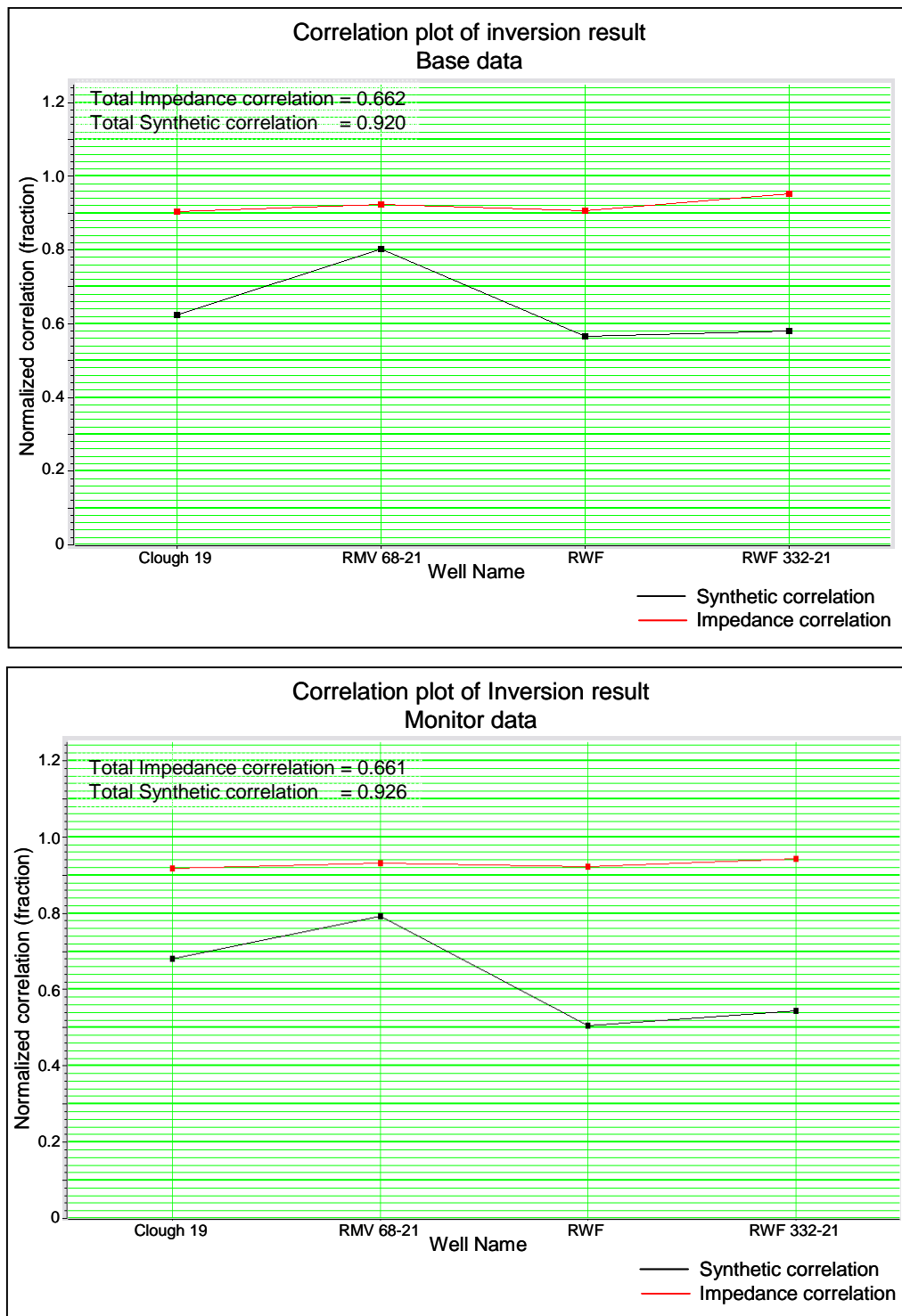


Figure 4.11. Correlation plot of inversion result for base and monitor data.

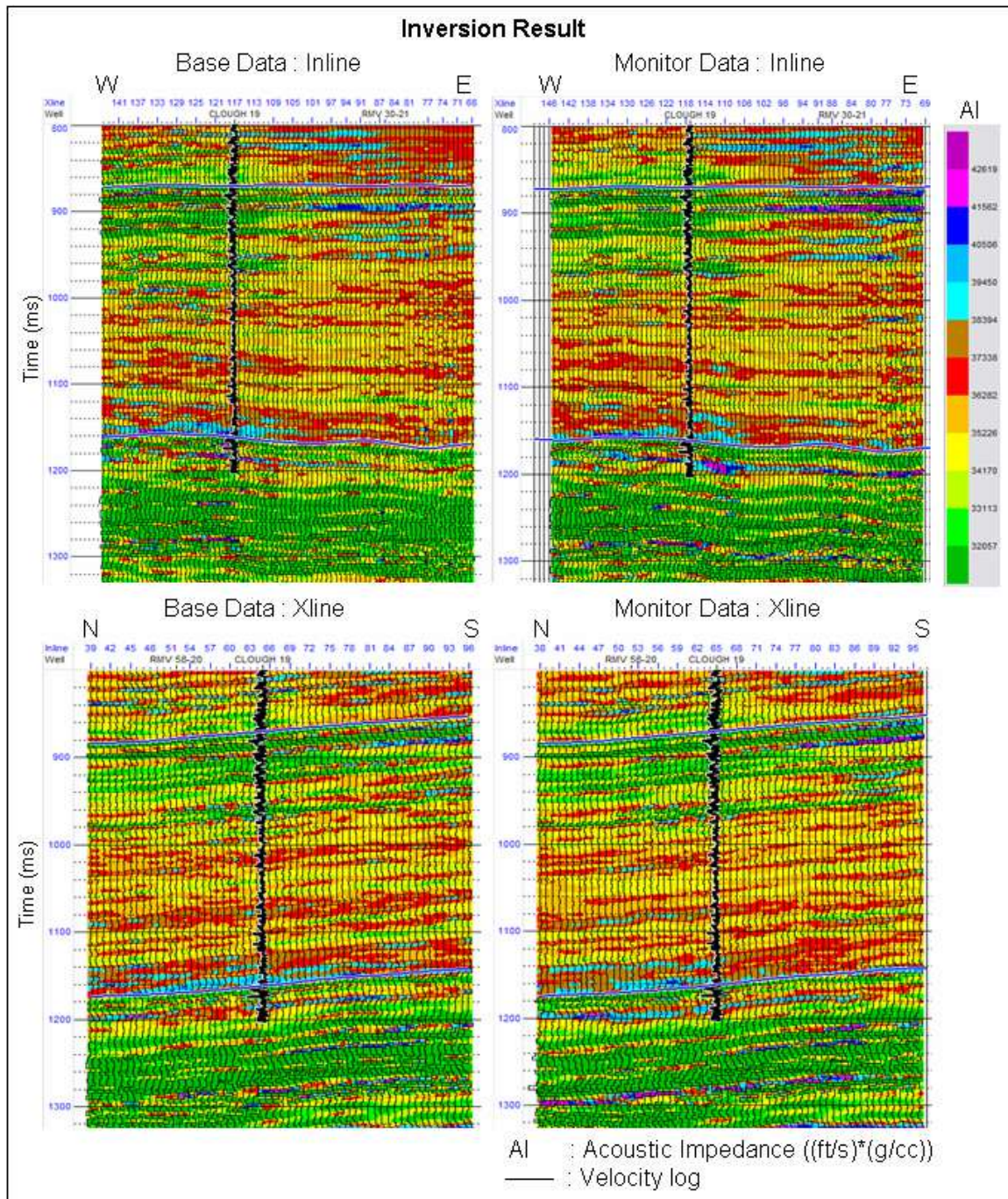


Figure 4.12. Inversion result for base and monitor data.

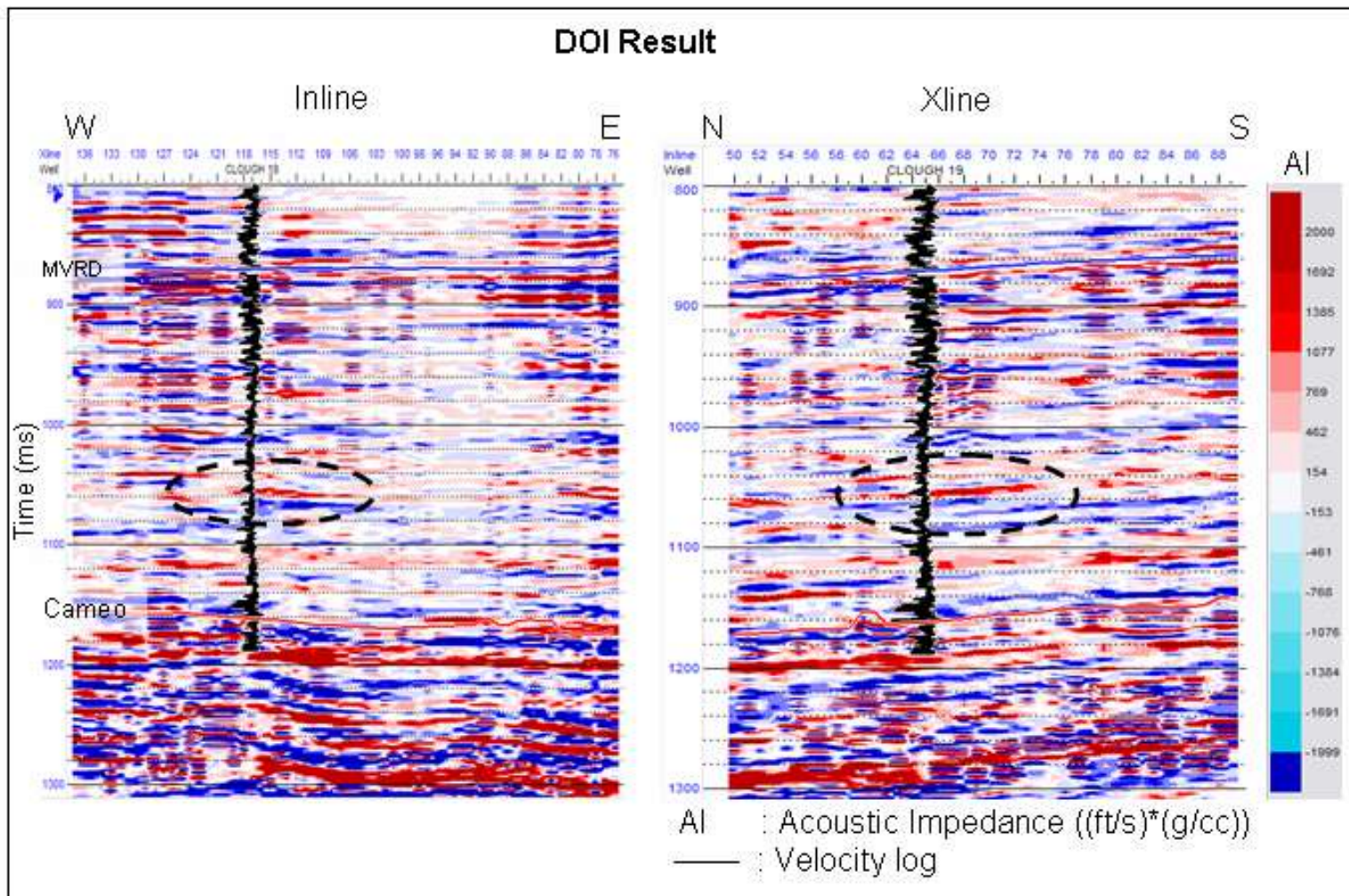


Figure 4.13. Impedance difference value from DOI approach.

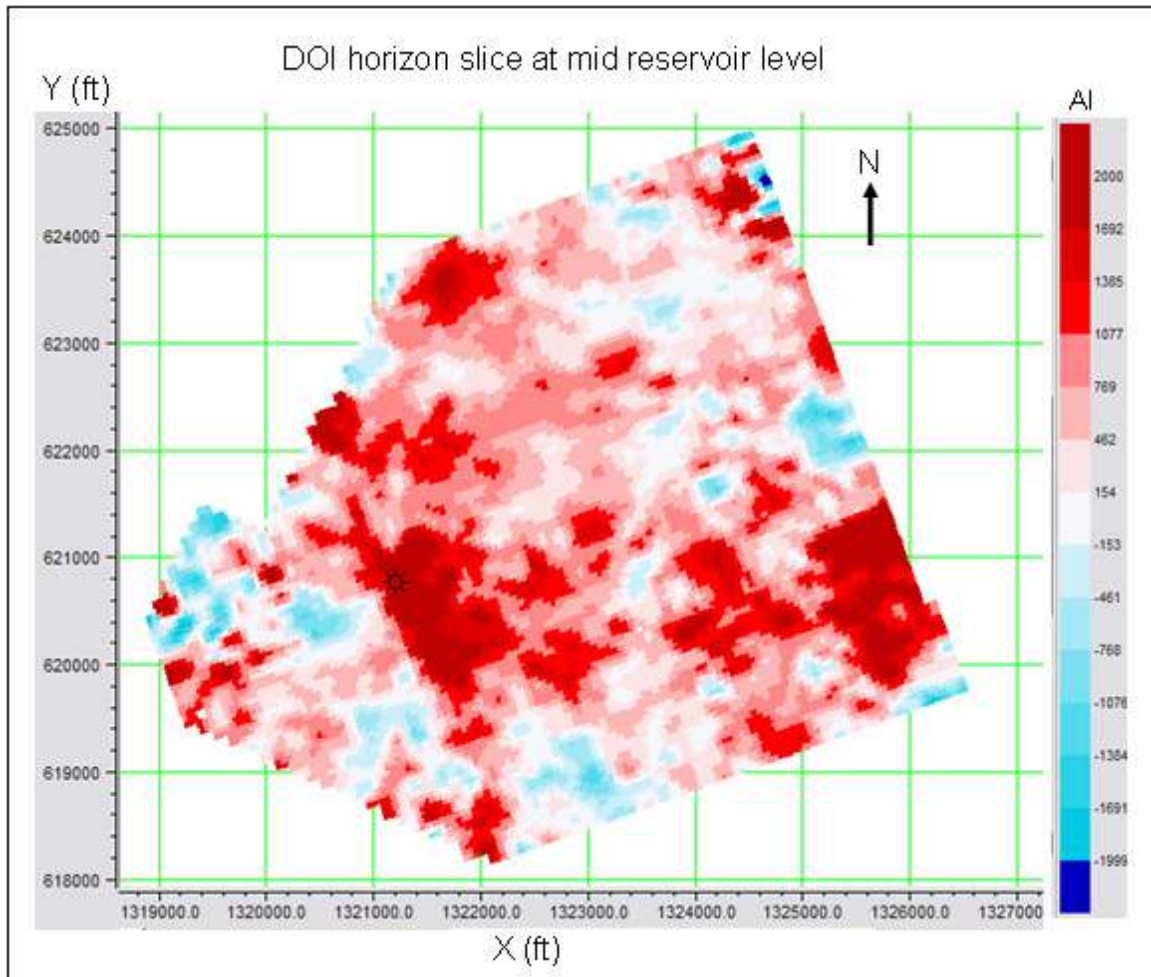


Figure 4.14. Impedance difference horizon slice at mid reservoir level.

This horizon slice was taken from DOI result at 107 ms above Cameo horizon.

analysis result (chapter 3). The positive value of the anomaly also indicates that time-lapse anomaly inside this reservoir is a result of an increase in velocity.

Inversion in this DOI approach is also performed using other inversion techniques i.e. stochastic Model Based and sparse-spike. These other inversion techniques are conducted using the same input parameter and inversion parameter as the constrained Model Based inversion. Horizon slices from each inversion result is then used to compare between inversion techniques (Figure 4.15). These horizon slices are extracted from the same time level as Figure 4.14. Analysis of these inversion results (Figure 4.15) shows that both constrained model based and sparse spike result have detected the time-lapse anomaly around well Clough 19. The result from stochastic Model Based inversion shows very weak time-lapse anomalies in the same location as the other inversion techniques. Analysis on these inversion results strongly supports that impedance anomalies in the reservoir are not an artifact of the inversion process.

4.3.2. Inverse of Differences

Time-lapse inversion using inverse of differences (IOD) approach is conducted on the Rulison datasets. IOD process is started by generating amplitude differences from seismic traces of base and monitor data. Inversion process is then performed in this amplitude difference volume to generate impedance differences model. Due to software limitation to handle zero impedance value ($AI = 0$), constant impedance value ($AI = 75000$) is set to be the initial impedance model. This constant value is then extracted from the inversion result to provide impedance differences that were distributed around zero.

To determine optimum inversion parameters, especially a pre-whitening factor, plots of inversion results using different λ values (Figure 4.16) are generated. These plots are generated from correlation of impedance and traces on the location of the

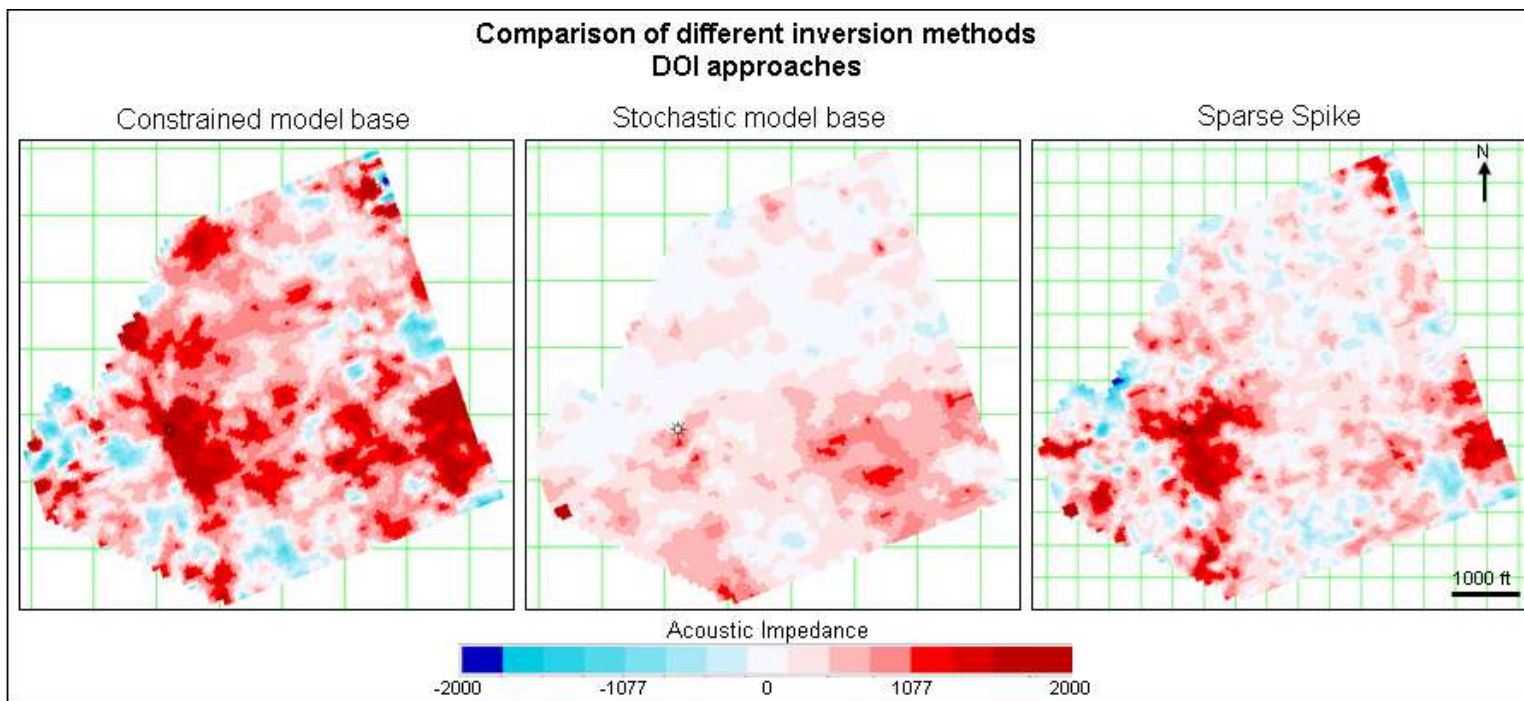


Figure 4.15. Impedance difference horizon slice from different inversion method at the same level as Figure 4.14.

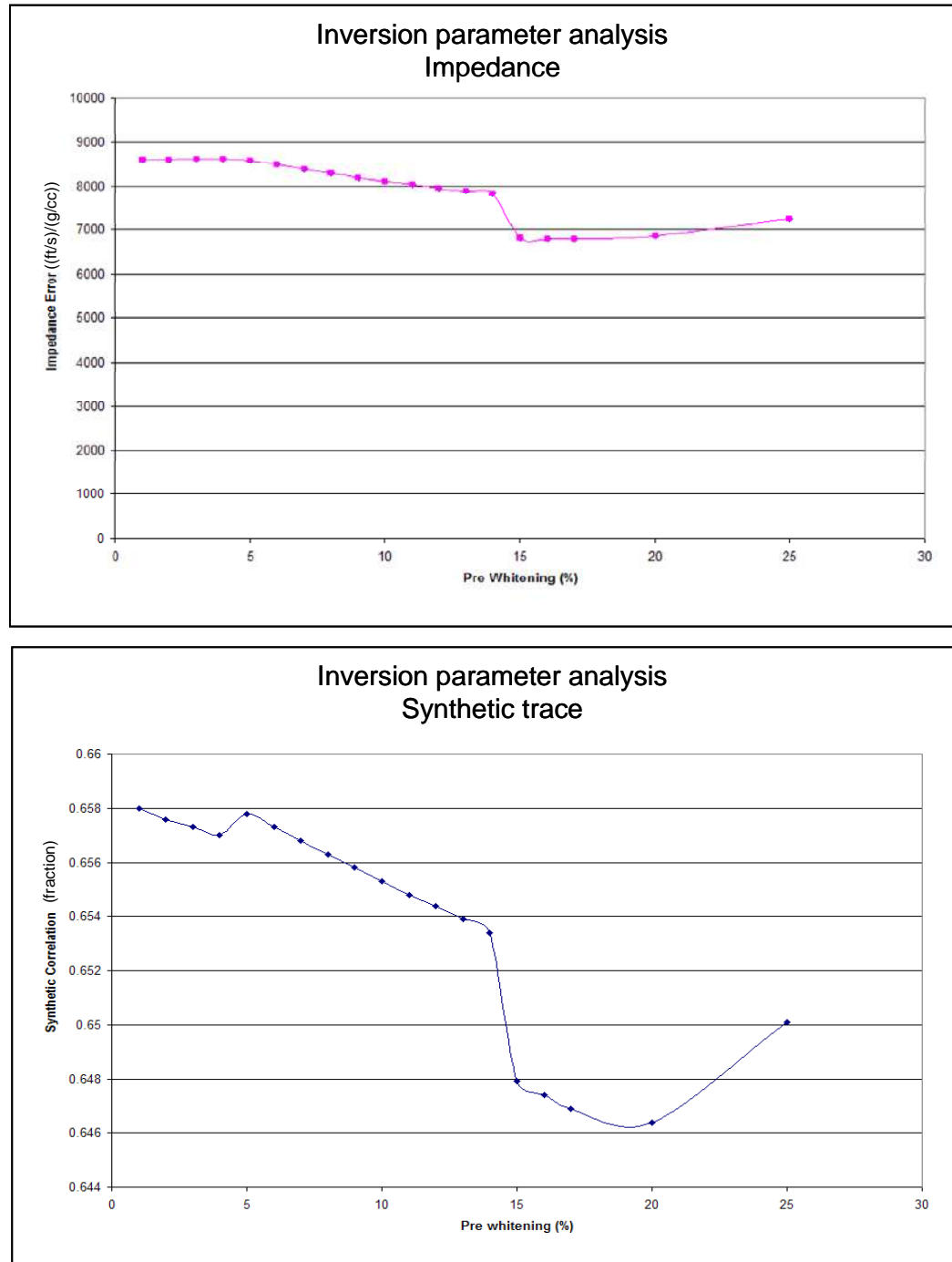


Figure 4.16. Analysis of inversion parameter for IOD approach.

The analysis was performed on the location of well Clough 19.

Clough 19 well. Impedance error values are calculated from total impedance differences between inversion result and initial constant impedance value. Synthetic correlation, on the other hand, is generated based on correlation value of predicted and actual seismic traces in this defined location. To determine the optimum parameter, the author makes an assumption that time-lapse anomalies appear only in a small part of the data. Based on this assumption, the optimum λ value is the one that generates least impedance error while still providing maximum trace correlation. A pre-whitening (λ) value of 15% is then determined to be the optimum parameter, based on these arguments.

Inversion is conducted on the impedance difference volume based on defined inversion parameters. Quality analysis of inversion result is then performed especially for traces near well Clough 19 (Figure 4.17). This figure (Figure 4.17) shows a comparison between predicted and actual traces in this location. Comparison between the impedance model from inversion and initial impedance model indicates that the impedance differences values are larger in the deeper part of the data. Correlation between traces, in other well locations, is also plotted in this figure (Figure 4.17). This correlation plot indicates that the inversion process has predicted seismic traces in these locations equally well.

A plot of impedance differences value (Figure 4.18) is generated to compare IOD results with DOI results. Analysis of this figure (Figure 4.18) suggests that impedances differences from DOI have a tighter distribution than the IOD. Similar results are also observed in the synthetic data study (Figure 4.6). To analyze time-lapse anomalies, IOD result is plotted using its own color scale. The distribution of impedance differences from IOD is shown in Figure 4.19. This figure (Figure 4.19) shows distinct impedance anomalies inside the reservoir level especially around 1060 ms and 1110 ms. Comparison between the IOD result (Figure 4.19) and the DOI result (Figure 4.13) indicates that IOD result has less noisy impedance difference distribution than DOI result.

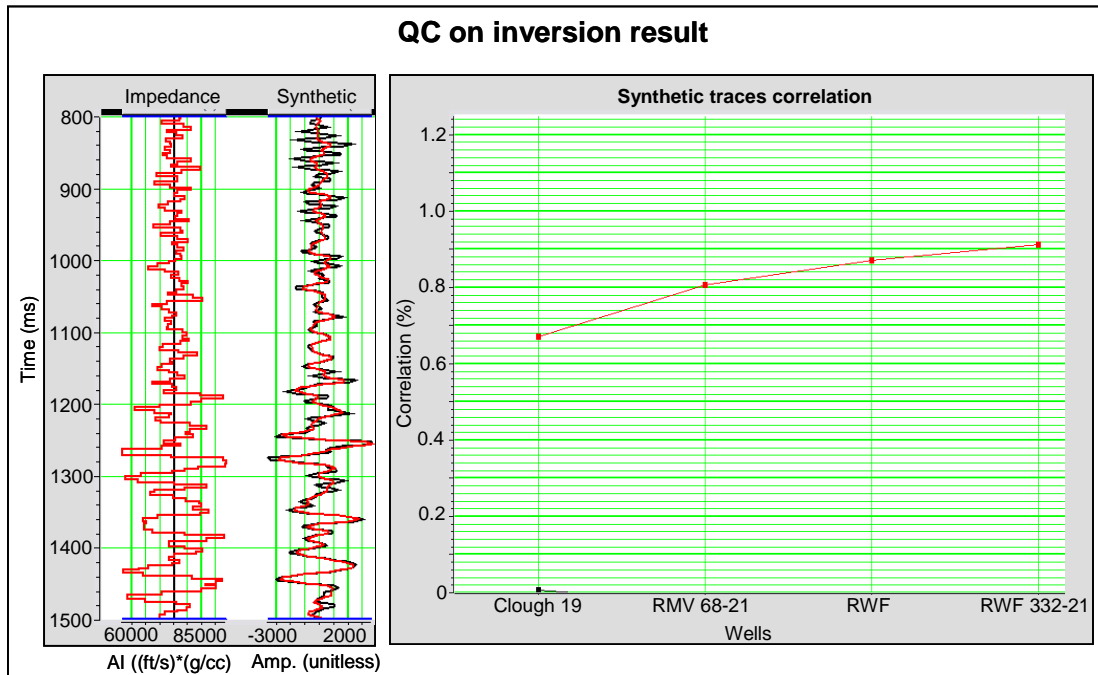


Figure 4.17. QC on inversion result for IOD approach. The left figure indicates impedance and synthetic traces result for well Clough 19. Right figure indicates synthetic correlation from all well in the area.

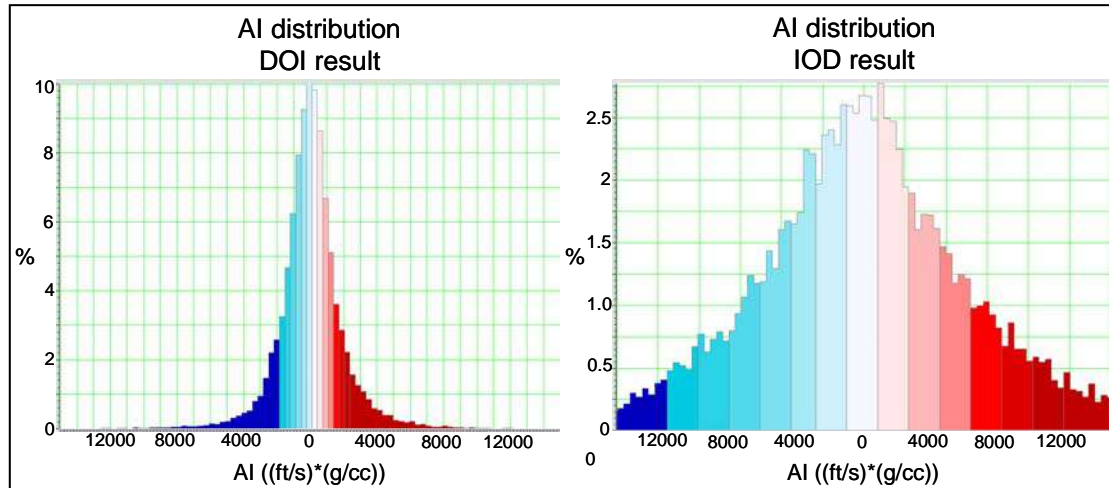


Figure 4.18. Distribution of AI differences value from inversion result using DOI and IOD approaches.

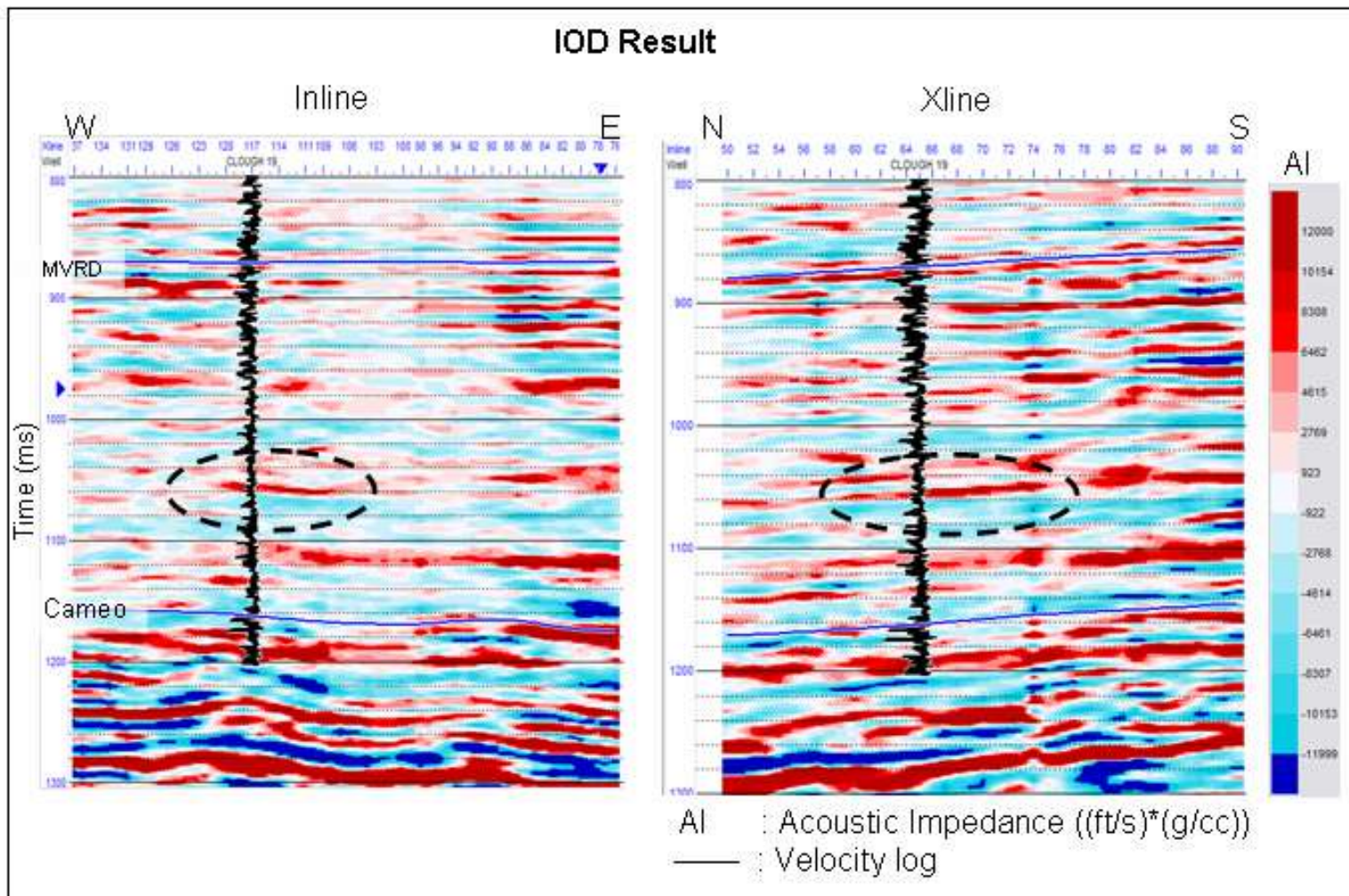


Figure 4.19. Impedance difference value from IOD approach.

To understand the distribution of the impedance anomaly, horizon slice on the anomaly (1060 ms) is generated. This horizon slice (Figure 4.20) is generated using the Cameo as the reference horizon in the same level with DOI horizon slice (Figure 4.14). Figure 4.20 shows the occurrences of distinct impedance anomalies near well Clough 19 and well RWF 332-21. These anomalies occur in similar locations with DOI result. Some impedance also appears at the southern edge of the area. This anomaly is not distinctively detected in the DOI result. The value of impedance anomaly from this IOD approach reaches 12000 which are about 6 times higher than DOI result (Figure 4.14).

Inversion in this IOD approach is also conducted using other inversion techniques i.e. sparse-spike and colored inversion. Input data and inversion parameters in these inversions are set to be similar with constrained Model Based inversion. Inversions are then performed separately for each inversion technique to generate impedance differences volumes. To compare the inversion result of these inversions, horizon slices are extracted from each impedance difference volume and compared with constrained Model Based result (Figure 4.21). Horizon slices is extracted from the same level as Figure 4.20. Analysis on these horizon slices (Figure 4.21) indicates that consistent impedance anomaly is detected near the Clough 19 well. Other anomaly locations are not clearly identified in colored inversion result.

Velocity value of time-lapse anomaly is calculated from impedance changes value of inversion result based on equation 4.3. This equation is derived from statistical relation between rock properties. Log information from available wells (i.e. P-impedance log and P-wave velocity log) is used to determine this equation. Detail explanation on this equation is discussed in chapter 1.6.2.1.

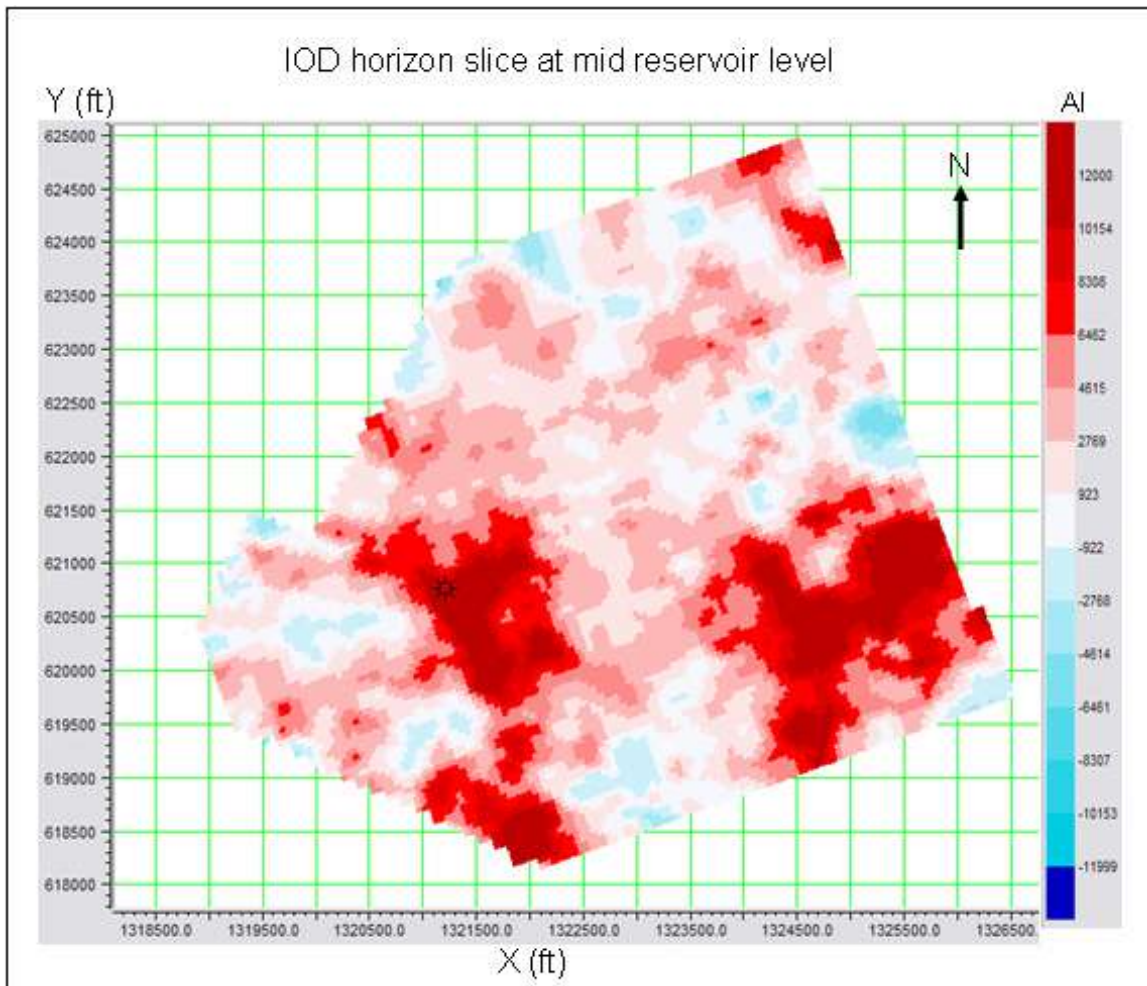


Figure 4.20. Impedance difference horizon slice at mid reservoir level.

This horizon slice was taken from IOD result at 107 ms above Cameo horizon.

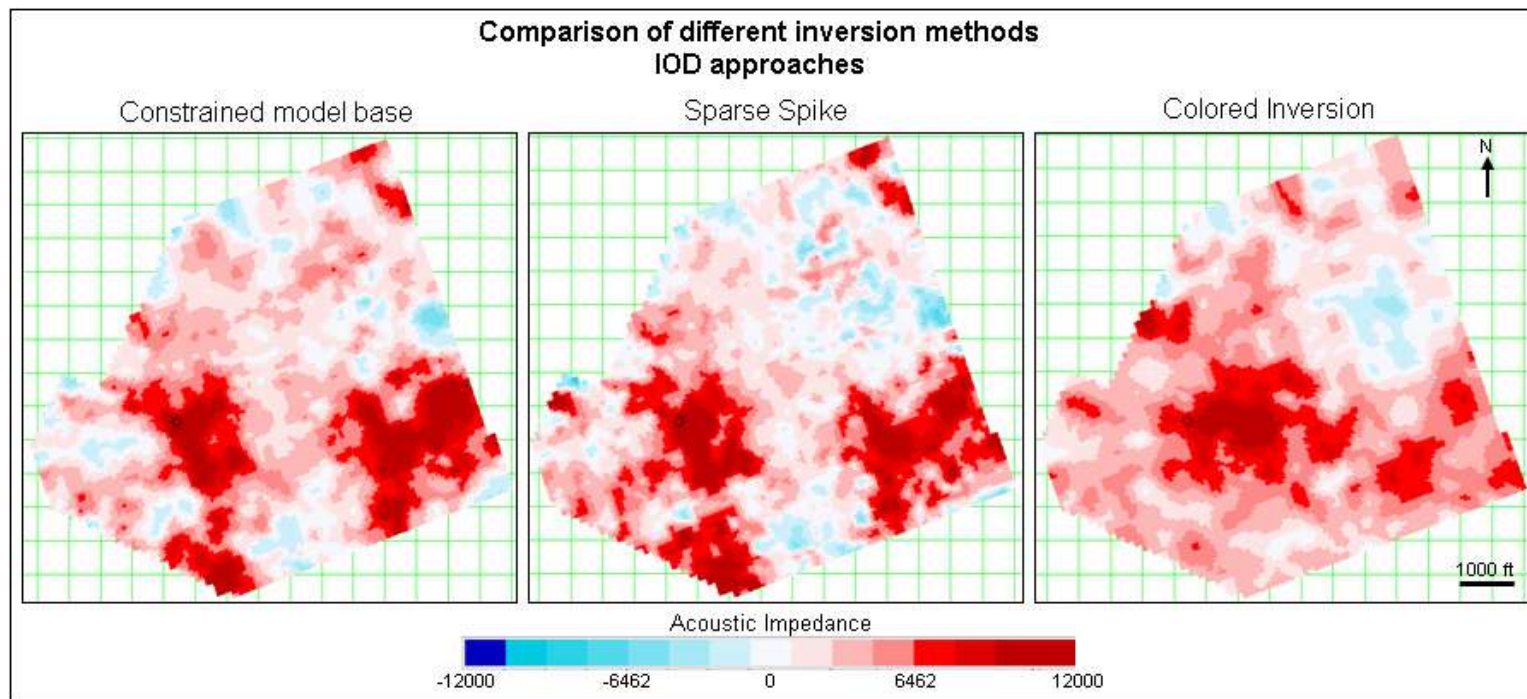


Figure 4.21. Impedance difference horizon slices from different inversion methods at the same level as Figure 4.20.

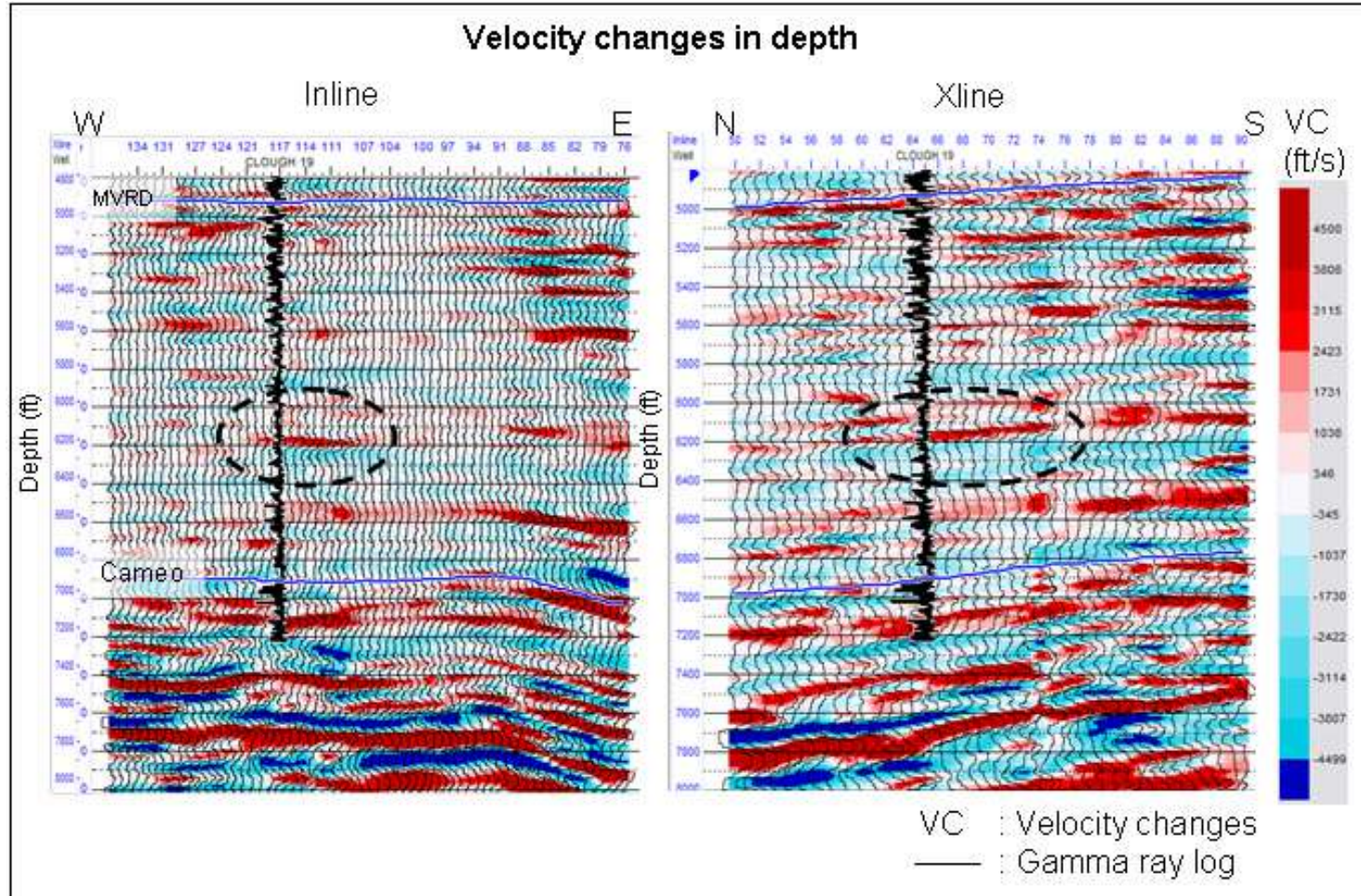


Figure 4.22. Velocity changes distribution after converted from time scale to depth.

The velocity changes value was calculated from IOD inversion result.

Depth conversion was performed using velocity distribution of base data (1996).

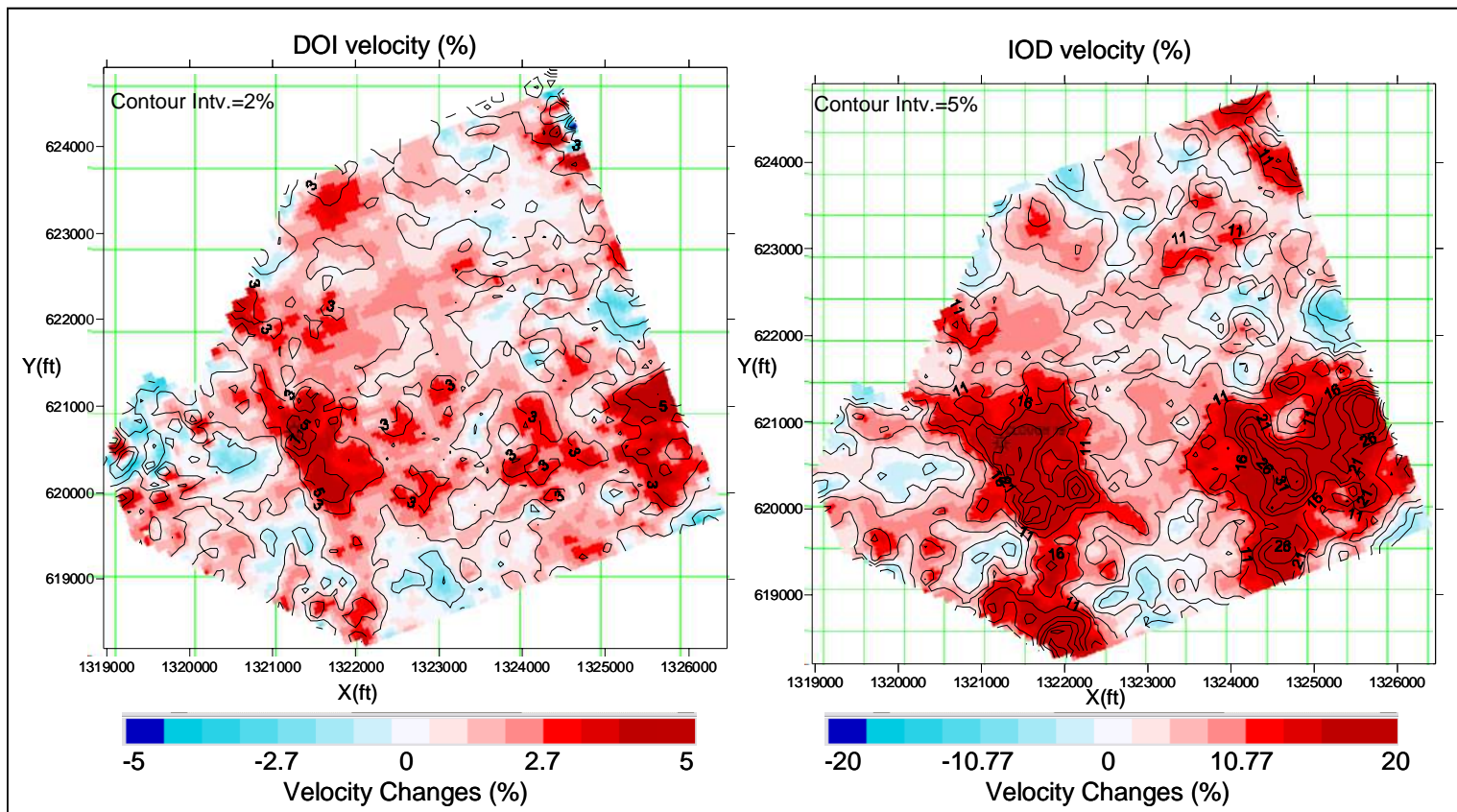


Figure 4.23. Velocity changes prediction from DOI and IOD inversions. Inversion was performed using constrained-model-base method. Horizon slice was extracted 107 ms above Cameo level.

$$AI = 3.284 \text{Vel.} - 10369 \quad \dots \quad (\text{Eq. 4.3.})$$

Where

AI : P-Impedance ((ft/s)*(g/cc))

Vel : P-wave velocity (ft/s)

Using this velocity distribution, time-lapse inversion result is then converted to velocity value. Figure 4.22 shows the distribution of velocity changes value in the depth domain. Depth conversion is performed to provide a direct comparison between time-lapse anomaly and well data.

Percent velocity changes are then calculated based on velocity changes compare with velocity of base data (1996 survey). Percent velocity changes from DOI and IOD inversion is compared to analyze the ability of predicting velocity changes. Figure 4.23 shows horizon slices of percent velocity changes that were predicted using DOI and IOD inversion. These horizon slices is extracted using the Cameo as the reference horizon in the same level with Figure 4.20. Figure 4.23 shows that velocity anomaly value predicted from DOI inversion is about 5-7%. IOD inversion result, on the other hand, predicts velocity anomaly values of more than 20%.

4.4. Comparison of the Approaches

Analysis of time-lapse inversion in previous sections suggested that inversion using different approaches (DOI or IOD) generates different impedance changes results. The main difference in these two approaches is the input seismic traces for the inversion process. In the DOI approach, the input seismic traces are the complete traces which consist of traces from: background impedance, time-lapse anomaly and noises. Generally, the contribution of background impedance to complete traces is much higher than time-lapse anomaly and/or noises. In IOD approach, the input seismic traces are amplitude

difference traces. These input traces are generated by differencing complete traces from baseline and monitor data. Due to this process, the input seismic traces only consist of traces from: time-lapse anomaly and noises. Based on this fact, input traces in the IOD approach have much lower signal-to-noise (S/N) ratio than DOI approach. The S/N ratio of input traces has a significant effect on the stability of inversion. Inversion process is performed much more stable when the input data have higher signal than noise. In this case, DOI inversion is performed much more stable than IOD approach with low S/N ratio input.

One of the advantages of using amplitude difference traces as an input in inversion (IOD approach) is the low coherent noise level. By taking the differences between seismic traces of base and monitor data, coherent noise level in the data is highly reduced. Due to this process, the noise level is reduced and the noise is dominated by random noise. An inversion process can reduce random noise much easier than reduce coherent noise. This analysis provides a possible explanation that the DOI result is noisier than IOD result. Summary of general comparison between DOI and IOD approach is shown in table 4.1.

No	Subject	DOI	IOD
1	S/N Ratio	(+) Higher S/N	(-) Lower S/N
2	Inversion stability	(+) Stable	(-) Unstable
3	Coherent noise	(-) Higher coherent noise	(+) Lower coherent noise

Table 4.1. General comparison between DOI and IOD approach.

Index : (+) Advantages; (-) Disadvantages

Analysis is also performed to compare the DOI and IOD results of Rulison time-lapse datasets. In general, DOI inversion has higher noise levels than the IOD inversion. This result is based on analysis of the impedance differences distribution. Due to high noise levels in the DOI result, it is more difficult to detect time-lapse anomaly in this volume. IOD result, on the other hand, provides clear-detectable time-lapse anomalies. Based on this analysis, IOD inversion result will be used for further study to delineate area of time-lapse anomalies.

One of the weaknesses of IOD result is the velocity value determination. The velocity changes predicted by IOD inversion reach more than 20%. Previous analysis on time shift attribute indicates that, with an average time shift of 4 to 6 ms, velocity changes at Rulison field should be less than 10%. Velocity changes predicted by DOI inversion are about 5 to 7%. These values fall within acceptable ranges of velocity changes based on attribute analysis. Analysis is also performed on the velocity anomaly at mid-lower reservoir level (Figure 4.23). Using velocity changes from IOD inversion, these anomalies (Figure 4.23) should generated time-shift value of 10 ms. This calculated time-shift value is much higher than the observed time-shift value in this area (about 2 ms). Calculation of time-shift is also performed for these anomalies (Figure 4.23) using DOI inversion. With velocity changes of 5 to 7%, the calculated time-shift value is 2 to 3 ms. This calculated time-shift value falls within the range of observed time-shift value of this area. Based on this analysis, velocity change values from DOI inversion will be used for further time-lapse analysis. The comparison between DOI and IOD inversion on Rulison datasets is summarized in table 4.2.

No	Subject	DOI	IOD
1	Anomaly distribution	More noise	Less noise
2	Anomaly detectability	Difficult	Easier
3	Velocity value	within acceptable ranges	Too high

Table 4.2. Comparison between DOI and IOD inversion on Rulison datasets.

4.5. Summary of Time-lapse Seismic Inversion

There are two different time-lapse inversion approaches used in this study i.e. differences of inversion (DOI) and inverse of differences (IOD). The DOI approach is performed by inverting base and monitor separately and then taking the differences from the inversion result. IOD approach, on the other hand, is conducted using by differencing base and monitor traces and then inverting the amplitude differences.

Time-lapse inversion is applied on the synthetic data to study the reliability, sensitivity and error estimation of each inversion result. Synthetic data inversion is performed using DOI and IOD approach. The inversion result from both approaches is then analyzed to study the characteristic, advantages, and disadvantages of each approach. This analysis shows that both DOI inversion and IOD inversion is able to detect the location and thickness of time-lapse anomaly.

Time-lapse inversion using both DOI and IOD approach is performed on the Rulison datasets to generate impedance differences distribution. Analysis on the inversion results from different inversion techniques has strongly supported that impedance anomalies in the reservoir are not some artifact of the inversion process. Further analysis on the inversion result indicates that IOD inversion result has done a better job to delineate the time-lapse anomalies. But, velocity changes predicted from this IOD inversion is much higher (more than 20%) than expected value based on attributes

analysis especially from the time-shift value. Velocity changes predicted from DOI inversion is about 5 to 7%. These velocity change values are within the expected value range. These values will be used for further time-lapse analysis.

Chapter 5

INTEGRATED INTERPRETATION OF TIME-LAPSE SEISMIC

5.1. Integrated Interpretation

Integrated interpretation is performed in Rulison field based on time-lapse seismic, production history, rock physics and structural information. The main goals of this integrated interpretation are:

- a) To verify time-lapse anomalies and their cause.
- b) To analyze effective production area based on time-lapse anomalies
- c) To analyze fault and fractures effect on hydrocarbon depletion based on time-lapse anomalies.

Data for this analysis is time-lapse seismic data. As previously explained, the time-lapse seismic data consists of seismic data from two different surveys (base survey: 1996 and monitor survey: 2003). These seismic datasets have been cross-equalized (chapter 2) to reduce non-repeatable components in the data and to generate more comparable seismic traces. The cross equalization process has successfully reduced non-repeatable components of time-lapse data especially in the southern part of investigation area. Analysis of the seismic volumes after cross equalization indicates that areas along the edge of time-lapse data still have high non-repeatability (chapter 2). These areas are excluded from further time-lapse analysis.

Attribute analysis is performed on these time-lapse data (chapter 3). There are three different attributes used in this analysis i.e. time-shift, cross correlation and percent difference. The result of attribute analysis indicates the appearance of time-lapse anomalies in the William Fork and Cameo levels. This analysis also suggests that time-

lapse anomalies occur due to velocity increase. The biggest anomaly appears near well Clough 19 at time level 1040 ms. Time-lapse inversion is also performed on these datasets (chapter 4). The inversion results support velocity increase anomalies. For the time-lapse anomaly near well Clough 19, velocity change value predicted from inversion is 5-7%. The depth of this specific anomaly is 6150 ft with thickness of 50 ft. Integrated interpretations are conducted using the result of these attribute and inversion analyses.

Other data used in this integrated interpretation is production history. Production data is extracted from 74 active wells in the area. As previously explained in chapter 1, the time-lapse period (1996-2003) was an intensive production period. The number of active wells and cumulative production increased dramatically during this period. The highest producing well during this time period was RMV 33-20 with 1.44 BCF cumulative gas production.

Structural geology of this field is also used in this integrated interpretation. Geology structure information is gathered from previous studies by RCP researchers (Jansen, 2005; Burke, 2005). Important structural geology features in this area are strike-slip faults and step-over faults. These faults generate high fracture density areas. A detailed explanation of geology structure of the area is discussed in chapter 1.

Other important data for this integrated interpretation includes rock property analysis. This rock property information is gathered from previous studies by Rojas (2005) and Burke (2005). Some of the important results of these studies is that the value of porosity and density of sandstone and shale in the reservoir interval is difficult to separate (Rojas, 2005). More explanation on rock properties analysis is discussed in chapter 1.

Production information is used in conjunction with time-lapse seismic data to verify time-lapse anomalies. These data (i.e. production and time-lapse seismic) are also used to analyze the appearances of time-lapse anomalies in certain places and not in other places. Rock properties information is used to explain the cause of time-lapse anomalies. Analysis is also performed using structure data and time-lapse seismic to understand the

effect of faults and fractures on the hydrocarbon movement. Results of these analyses are then combined to generate a comprehensive analysis of Rulison field.

5.2. Production History

Production information is gathered from 74 active wells in the area. These wells are produced with commingled production. Hydrocarbon production from each well is gathered from all perforated zones in reservoir. Until the time that this research is conducted, production logging has not been performed in this area. Therefore, contribution of individual zones to the cumulative well production is unknown.

During the period 1996-2003, this field has been produced intensively. Cumulative gas production from all wells increased from 5 BCF/year in 1996 up to 9 BCF/year in 2002. The number of active wells also increased from 25 in 1996 up to 74 in 2003 (detailed explanation in chapter 1). Contribution of cumulative production from each well is shown in Figure 5.1. This figure (Figure 5.1) shows the distribution of cumulative production from each well during the period 1996-2003. High producing wells with cumulative production more than 1.2 BCF are distributed mostly in the northwestern part of the investigation area (area A). Some areas with relatively low production (0.2 - 0.6 BCF) occur in the northeastern part (area B) and eastern part (area C). Other areas have relatively medium cumulative production (0.8 – 1.2 BCF). The highest producing well RMV 33-20 is located in area A. The lowest producing well RWF 314-16 is located in area B.

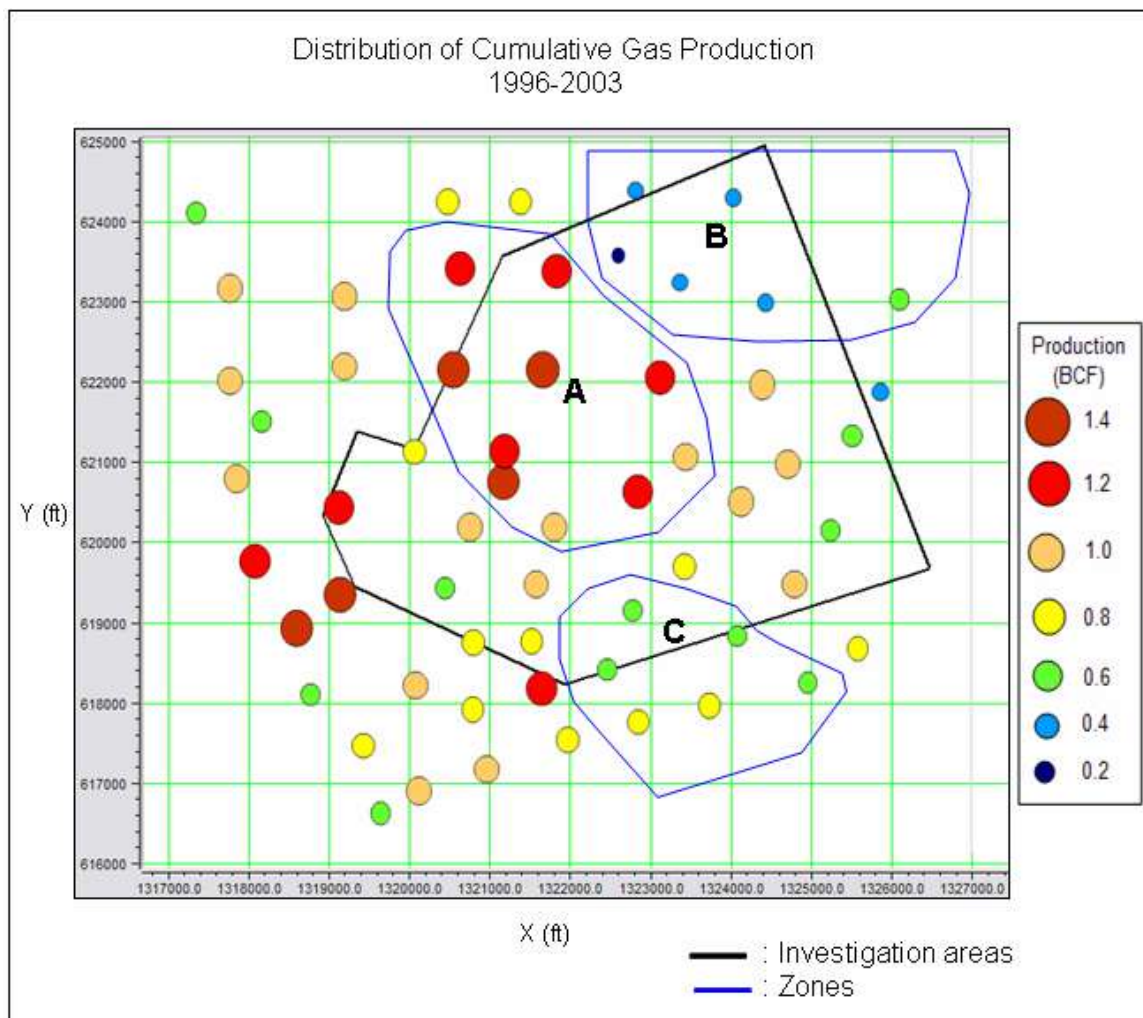


Figure 5.1. Cumulative gas production from years 1996 to 2003 for all production intervals.

Analysis is performed by correlating the cumulative production map with time-shifting attributes (Figure 5.2). This figure (Figure 5.2) shows a correlation pattern between production and time-shift attributes. In high producing areas (area T1), time-shift attributes indicate a significant value of time-lapse (4 – 8 ms). Time shift attributes also show a significant value in the medium producing area (area T3). Meanwhile, in low producing areas (area T2 and T4), time-shift attributes indicates very low values of time-shift (less than 2 ms). This suggests that the dominant factor affecting the time-shift attribute is the production. The time-shift analysis also provides a boundary for possible time-lapse anomaly locations. Any time-lapse anomaly in the reservoir level that is located in the vicinity of area T2 and T4 has a lower possibility to be caused by gas production. This analysis strongly suggests that distribution of time-shift attributes is an indication of average drainage area. Since this attribute is calculated over the entire reservoir interval (William Fork reservoir), time-shift attribute is not a drainage area indicator for individual reservoir interval. Instead, area of high time-shift anomaly indicates high average drainage over the entire William Fork interval (about 2000 ft). Area of low time-shift anomaly might indicate an area with low overall drainage over the reservoir interval or an area that is dominated by production from a specific sand interval.

An interesting feature appears in the vicinity of area T5 (Figure 5.2). Time-shift attribute indicates that area T5 has low time-shift value (less than 2 ms). Based on previous analysis on the correlation between time-shift attributes and production, area T5 should have low cumulative production. In contrast, there is a high producing well (RMV 40-20; cumulative production 1.1 BCF) located within this area. There are several possible explanations of this phenomenon. The first possible explanation is that the time-shift attribute was altered by edge effect in this area. The producing well (RMV 40-20) is located near edge area. There is a possibility that edge effect has made the time-shift

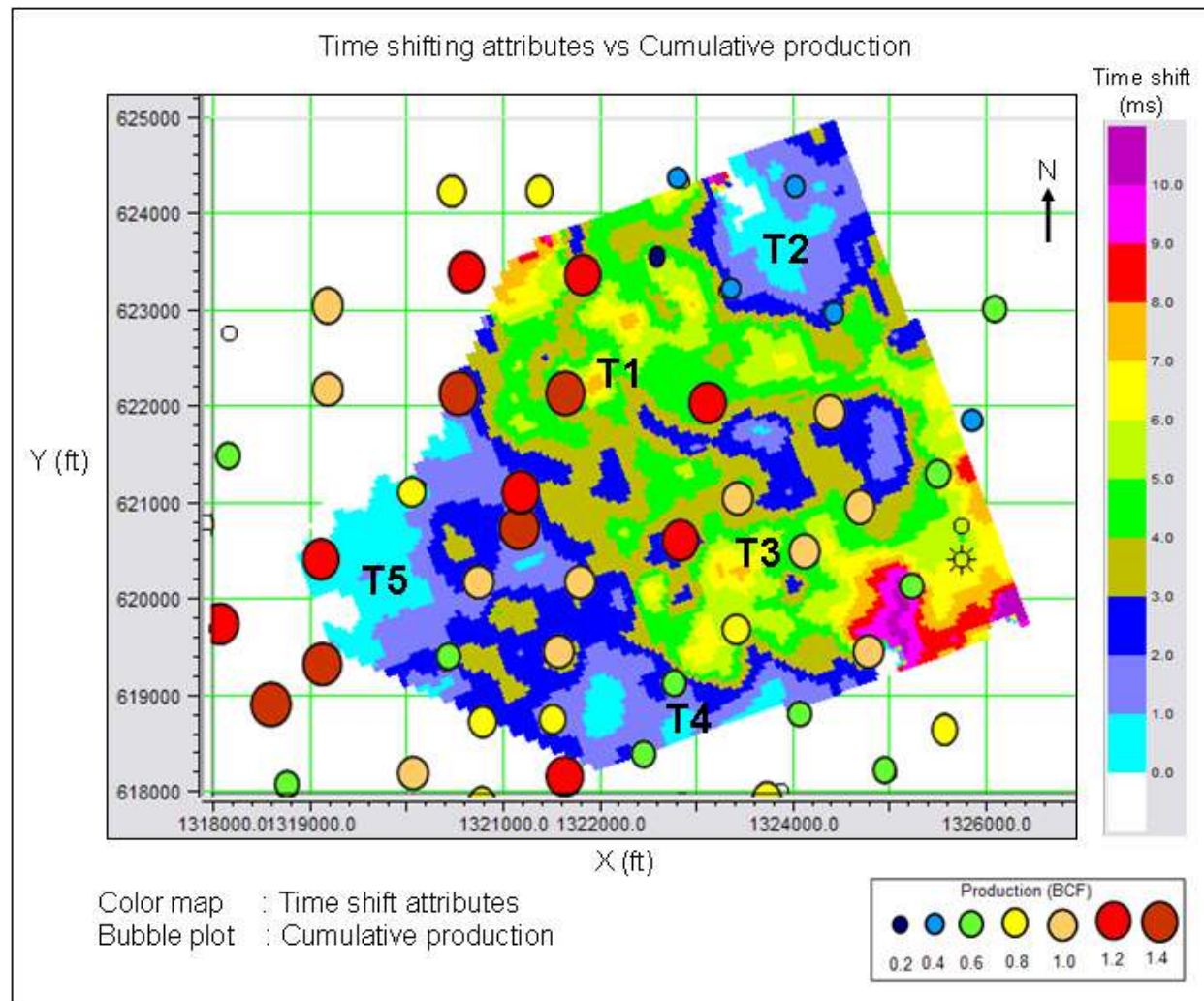


Figure 5.2. Comparison between distribution of cumulative gas production (1996-2003) and time shifting attribute.

anomaly undetected in this area. Another explanation is that this specific well (RMV 40-20) produced from area outside the area of investigation. This possibility might also cause undetectable time-shift attributes.

Analysis is also performed for area in between T1 and T3 for this figure (Figure 5.2). In area between T1 and T3, time-shift attribute shows a low time-shift value. This fact suggests that there is a separation zone between area T1 and T3 that has low average drainage performance. The appearances of relatively high time-shift in the eastern and western part indicate that this zone might not totally separated area T1 from area T3. There are some possible explanations of this separation zone. The first possible explanation is that this zone has low fracture density. The occurrence of fractures as secondary permeability in this field is an important factor for production performance (chapter 1). If this separation zone has lower average fracture density than surrounding areas, most gas will be produced from the surrounding areas. Another possible explanation is sandstone distribution in this separation zone. If this zone has fewer sandstone intervals, cumulative production performance might not be as high as the surrounding area. This factor will affect the time-shift value attribute.

Analysis of time-lapse anomalies inside the reservoir interval of the William Fork is conducted using velocity changes volumes from the inversion result. IOD inversion result is used in this analysis because it has low noise distribution and very distinct time-lapse anomalies (detail explanation in chapter 4). However, the velocity change values from this inversion (IOD inversion) are much higher than predicted values and not used for time-lapse analysis (chapter 4). In mid-upper level of the reservoir, a very distinct time-lapse anomaly distribution is found around 980 ms (about 5600 ft). Figure 5.3 shows a horizon slice at this specific level. This horizon slice is extracted from velocity changes volume using interpreted UMV horizon as base horizon. Distribution of velocity changes in this horizon slice (Figure 5.3) shows three major areas of time-lapse anomaly i.e. area U1, U2 and U3.

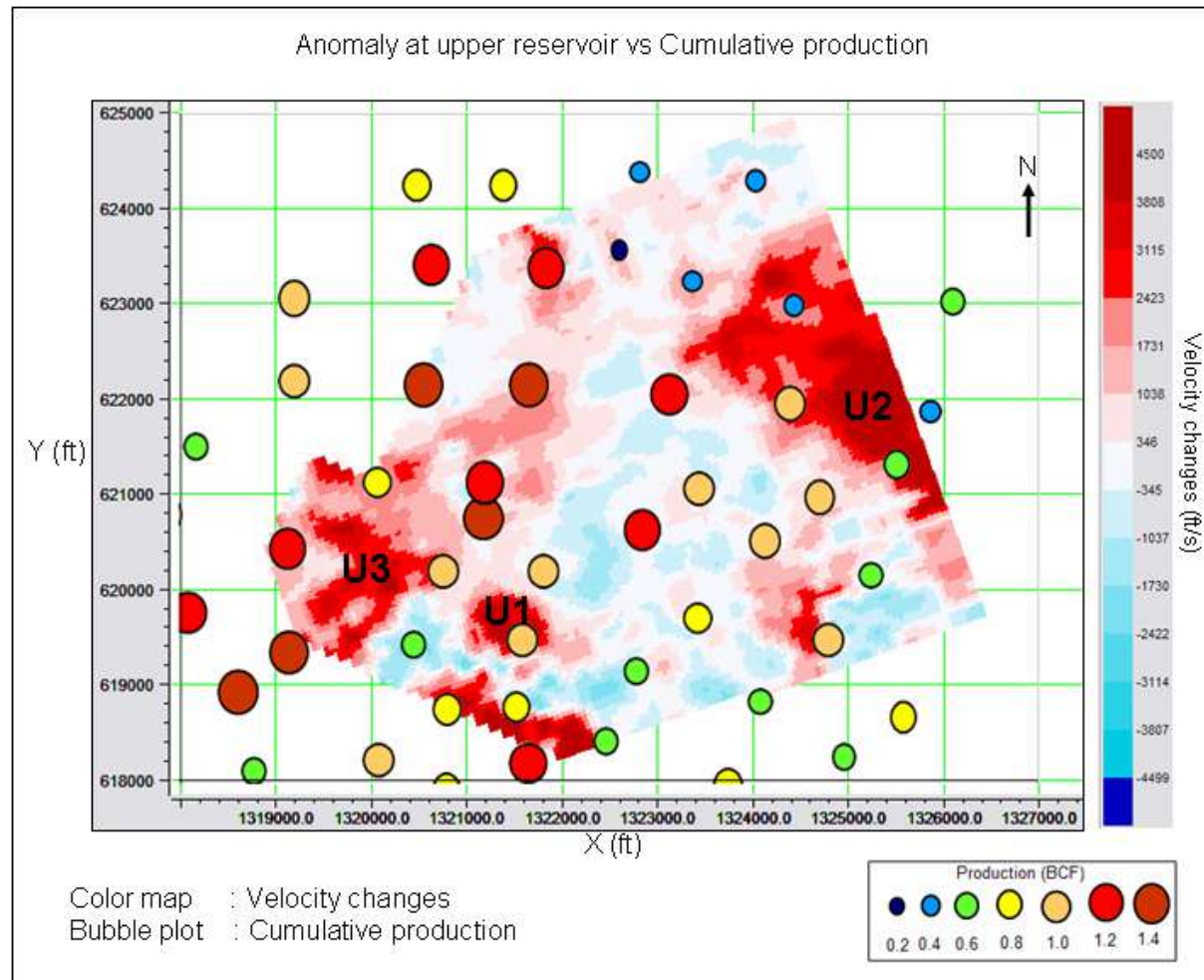


Figure 5.3. Comparison between distribution of cumulative gas production and velocity changes at upper Williams Fork reservoir level. Velocity anomaly was extracted around 980 ms (about 5600 ft).

Note : Time and depth mentioned is an average value.

Time-lapse anomalies at areas U1 and U2 occur near wells with medium gas production (0.6 – 0.9 BCF). Analysis of time-shift attributes (Figure 5.2) supports the occurrence of time-lapse anomaly in these regions (area U1 and U2). The occurrence of time-lapse anomaly in area U3, on the other hand, is opposed by the result of time-shift analysis. Time-shift values in area U3 are very low (less than 2 ms). These low values suggest that any time-lapse that appears in this area may not be due to production effect. Possible explanation is that the velocity anomalies are caused by noise from edge effects. Another explanation of anomalies in area U3 is that the anomalies may be a production effect anomaly, but some negative anomalies below this level have canceled out the effect of the anomaly in time-shift attributes. This explanation is less likely to be true, because analysis on velocity changes volumes has failed to identify any distinctive negative anomalies in the reservoir level.

Analysis is also performed on mid-lower reservoir level. In this mid-lower level, distinct time-lapse anomalies are found around 1060 ms (about 6200 ft). Figure 5.4 shows distribution of velocity changes from a horizon slice around 1060 ms. This horizon slice is extracted from velocity changes volume using the Cameo as the base horizon. Distribution of velocity changes in Figure 5.4 shows three major areas of time-lapse anomaly i.e. M1, M2 and M3.

The velocity anomaly in area M1 is correlated with three high producing wells i.e. Clough 19, RMV 200-20, and RMV 203-20. This figure (Figure 5.4) suggests that there is some connection between these wells in this level (about 6200 ft). Previous analysis on time-shift attribute shows that area M1 shows low time-shift value (2 – 3 ms). The occurrence of significant velocity anomaly in this low time-shift area suggests that gas production in area M1 might be dominated by production from this time level.

In area M2 (Figure 5.4), time-lapse anomalies occur in the vicinity of medium producing wells (0.6 – 1.0 BCF). Distribution of time-lapse anomalies to the north and east parts in area M2 is very limited. This phenomenon suggests that drainage of gas in area M2 is limited somehow to the north and east parts. There are some possible factors

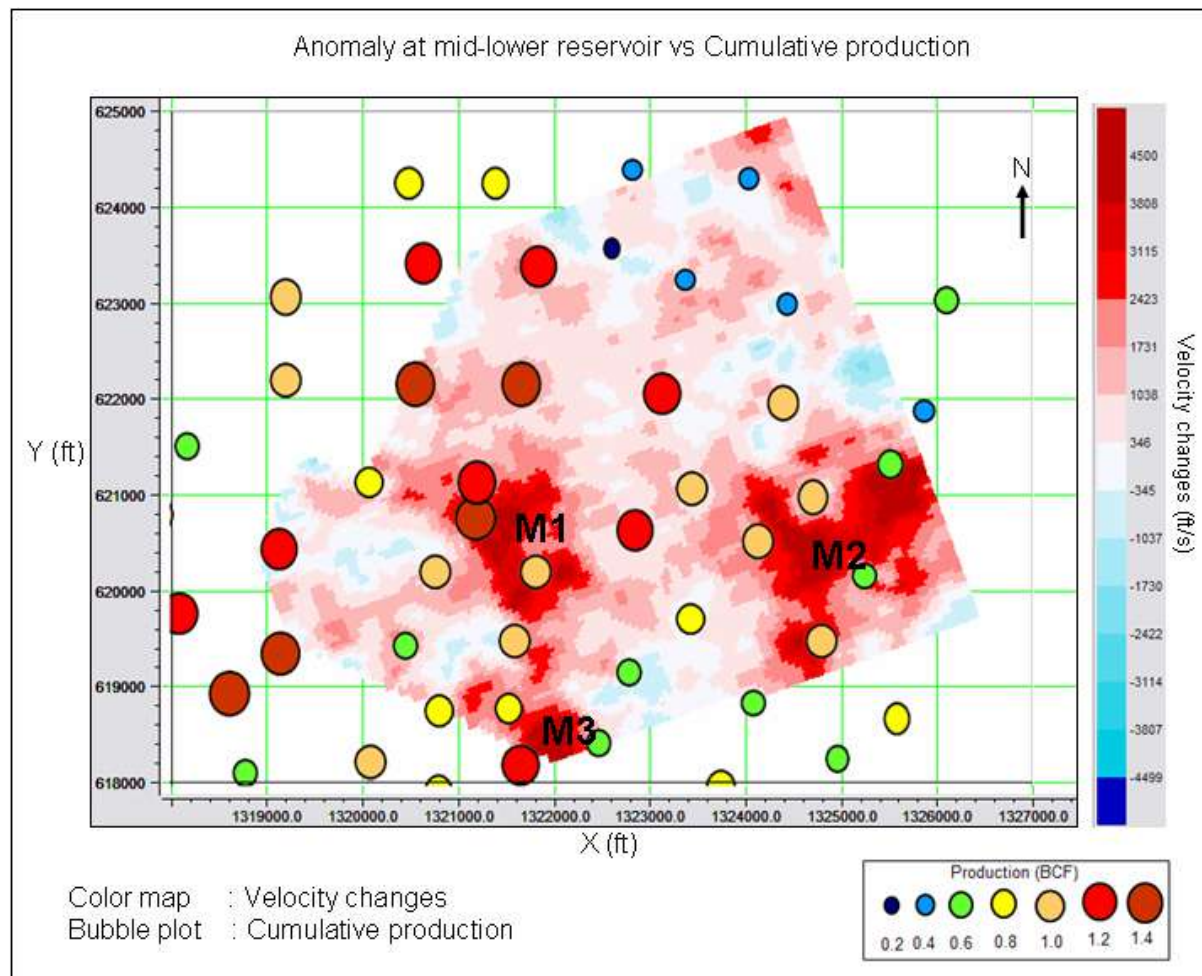


Figure 5.4. Comparison between distribution of cumulative gas production (1996-2003) and velocity changes from inversion result at mid-lower Williams Fork reservoir level. Velocity anomaly was extracted at 1060 ms (about 6200 ft). Note : Time and depth mentioned is an average value.

that might prevent drainage area to extend. The first factor is the sandstone distribution in area M2 in this specific interval. If channel sand distribution in this specific interval is limited in area M2, the extent of gas drainage to other areas is limited. Another factor that limits drainage area is fracture density. The occurrence of natural fracture will increase drainage (chapter 1). If area M2 has high fracture density, while the northern and eastern parts of this area has low fracture density, drainage area might be limited in the northern and eastern parts. To analyze this factor, correlation between time-lapse anomaly and structural geology information is discussed in chapter 5.3.

Velocity change distribution in area M3 (Figure 5.4) indicates positive time-lapse anomalies appear near the edge of the data. Edge effect still has a strong influence on amplitude in this area. Therefore, velocity anomaly in this area might be caused by noise from edge effect. There is also some possibility that velocity anomalies in this area represent real production effects. Analysis on Figure 5.4 shows that this velocity anomaly was located in the vicinity of a high producing well (RMV 3-20) with about 1.1 BCF cumulative production. The production from this well (RMV 3-20) might be the cause of velocity anomaly.

Analysis of time-lapse anomalies is also performed on the lower reservoir level. A distinct time-lapse anomaly in the lower reservoir level occurs near 1180 ms (about 7100 ft). This horizon slice is extracted slightly below the Cameo horizon. Many wells in this area still have perforation intervals in this deeper level. This horizon slice is extracted at about 1180 ms using the Cameo as base horizon. Figure 5.5 shows three distinct areas of time-lapse anomaly i.e. area L1, L2, and L3. In area L1, the velocity anomaly occurs near the highest producing well (RMV 33-20). Most of velocity anomaly appears in the southern part of RMV 33-20 in this level (about 7100 ft). Well information indicates that well RMV 33-20 have active perforation intervals in this depth (7158 and 7246 ft). This information strengthens the hypothesis about the cause of the time-lapse anomalies.

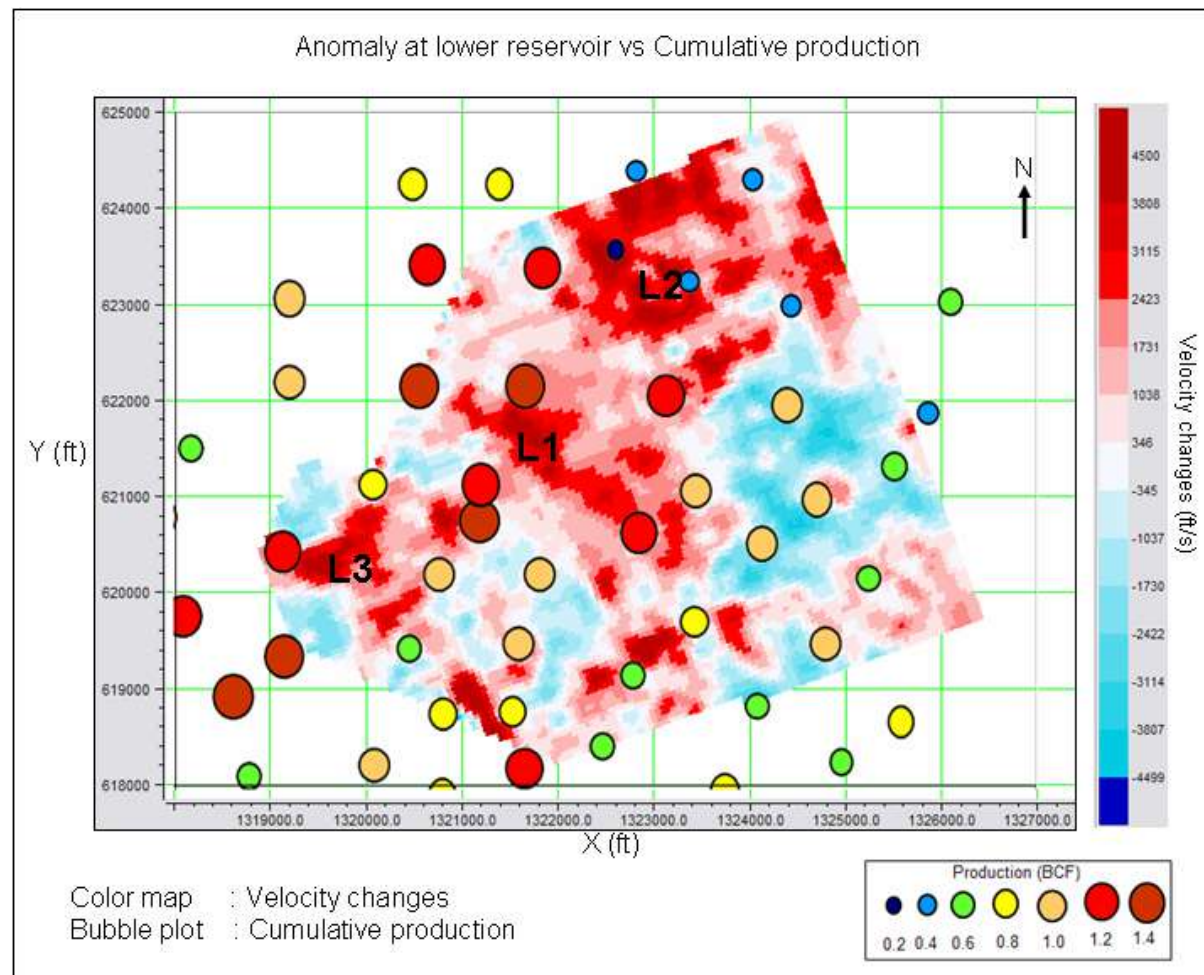


Figure 5.5. Comparison between distribution of cumulative gas production and velocity changes at lower William Fork reservoir level. Velocity anomaly was extracted at 1180 ms (about 7100 ft).

Note : Time and depth mentioned is an average value.

Area L2 (Figure 5.5) also shows a distinctive velocity anomaly. Most active wells in area L2 are low producing wells (0.1 – 0.4 BCF). Appearances of time-lapse anomaly in these low producing wells suggest that these wells produced gas mostly from this specific interval (about 1180 ms or 7100 ft). Velocity anomaly also appears in area L3. Anomaly in area L3 is located near the edge of data. There is a possibility that this anomaly only appears due to edge effect. Analysis on these three reservoir levels (Figure 5.3, 5.4, and 5.5) suggests that most of the gas production came from lower Williams Fork interval (area L1, L2 and L3).

To analyze the cause of time-lapse anomaly, information is gathered from a previous study by Rojas (2005). More explanation on this study is discussed in chapter 1. This study shows that velocity of measured-core increased significantly with the decrease of pore pressure. Pore pressure decrease of 2000 psi can increase velocity about 10-12% in the primary depletion regime. Simulation result by Johnston (2005) also supports this velocity increment (more explanation in chapter 1). All of this simulation (Johnston, 2005) and laboratory study (Rojas, 2005) was conducted using unfractured rock example. The occurrences of fractures in formation can altered the velocity increment value. These previous studies strongly suggested that dominant factor affecting time-lapse anomaly is the pore pressure change. Another possible factor affecting time-lapse is saturation changes. In this dry gas environment, saturation change is not expected.

5.3. Structural Geology and Rock Properties Information

Structural geology information is gathered from previous studies. All interpreted faults used in this analysis are gathered from a study by Jansen (2005). These faults are auto-interpreted using AntTrack software (Jansen, 2005). This study (Jansen, 2005) documented the appearance of strike slip faults and step over faults. There are three major NW-SE faults identified below the Williams Fork Formation. These faults splay

out in reservoir level and generate some NE-SW step-over faults. The appearance of these step-over faults generates high fracture density in surrounding areas.

Analysis is performed to study the connection between fault distribution and time-lapse anomalies. Figure 5.6 shows time-shift attribute and interpreted faults. The fault distribution is extracted from Cameo level (below reservoir). The three major faults are identified in this figure (Figure 5.6) i.e. fault A, B, and C. Analysis on time-shift attributes shows that time-shift anomalies is highly concentrated in the area between fault A and fault B. Further analysis shows that low time-shift values are still detectable between fault A and C. As previously explained, evidence strongly suggests that time-shift anomaly is an indication of high producing area and the distribution of time-shift anomaly indicates average drainage area (chapter 5.2). Analysis on the correlation between time-shift and faults (Figure 5.6) strongly suggests that major faults have behaved as a boundary for areas with different drainage performance. The area bounds by fault A and B has higher drainage performance relative to northeastern and southwestern areas. Analysis of fault distribution for Williams Fork reservoir interval indicates the appearance of NE-SW faults between these two major NW-SE faults (fault A and B). NE-SW faults are not clearly identified to the west of fault A and east of fault B. This analysis strongly suggests a correlation between the appearances of NE-SW faults and drainage performance of the area.

Analysis is also performed to correlate between faults and individual reservoir interval that has a time-lapse anomaly. The faults used in this analysis are the interpreted major NW-SE faults from previous study by Jansen (2005). The first analysis is performed for time-lapse anomaly at mid-upper Williams Fork reservoir level (around 980 ms). This horizon slice (Figure 5.7) is extracted in the same interval as Figure 5.3. Figure 5.7 shows that most of the anomalies in this level were distributed on the west of fault B and the east of fault A. Analysis of this figure (Figure 5.7) also indicates that the anomaly at the area U2 is affected by the fault B. Anomalies at area

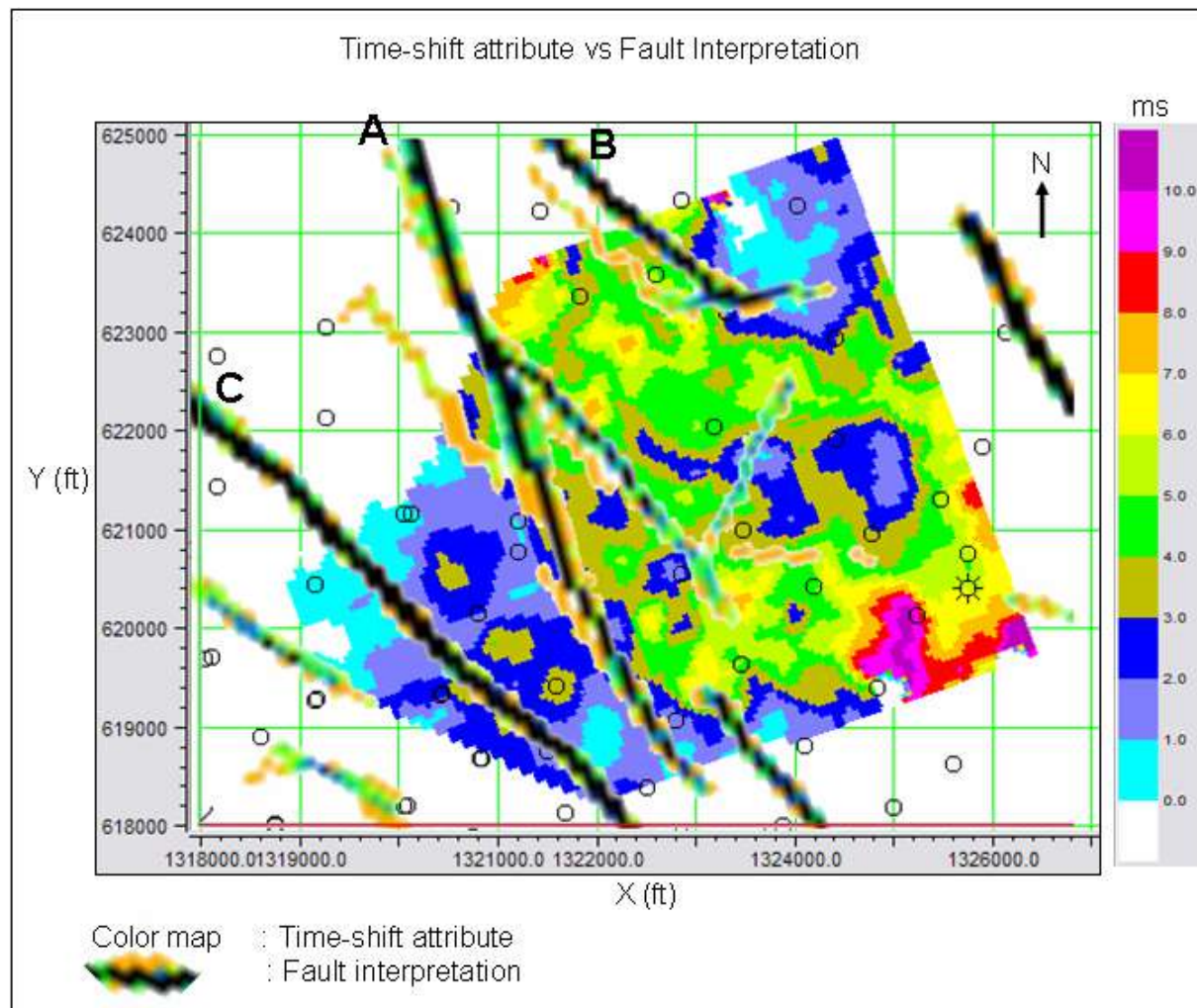


Figure 5.6. Map of time shift attribute and interpreted faults (Jansen, 2005). Faults was extracted at the Cameo level (around 1210 ms)

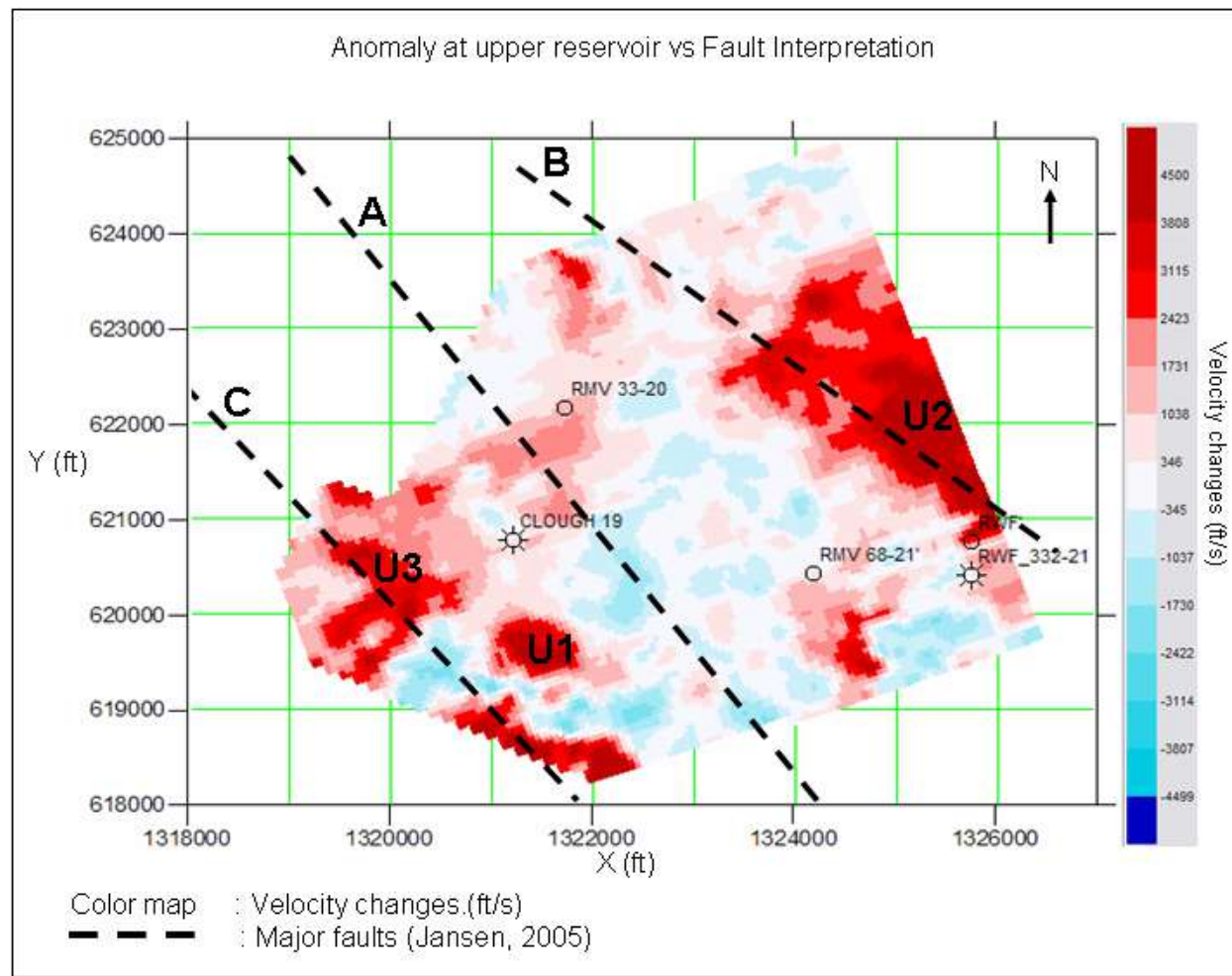


Figure 5.7. Correlation between velocity changes and generalized fault distribution (Jansen, 2005) at upper Williams Fork reservoir level. Velocity anomaly was extracted at 980 ms (about 5600 ft).

Note: Time and depth mentioned is an average value.

U1 and area U3, on the other hand, are not affected significantly by these major NW-SE faults.

In the mid-upper reservoir level, analysis is also performed to correlate time-lapse anomaly and interpreted faults. Figure 5.8 shows horizon slice in mid-upper reservoir level at 1060 ms. There are three areas of time-lapse anomalies that can be identified i.e. area M1, M2, and M3. As previously explained, an interesting phenomenon occurs in area M1. In this specific interval (about 1060 ms), a time-lapse anomaly occurs in the vicinity of area M1. However, time-shift attributes for the entire reservoir interval shows a low time-shift value in area M1 (chapter 5.2). These facts strongly suggest that gas production from area M1 was dominated from this specific interval.

The lower reservoir level is also being analyzed to study the correlation between time-lapse anomaly and fault distribution. Figure 5.9 shows that the distribution of time-lapse anomalies in this interval (area L1, L2, and L3) is highly affected by the distribution of the major faults (fault A, B and C). The distribution of time-lapse anomaly at area L1 to the west is bounded by the fault A.

Analysis is also performed for the deeper interval. Figure 5.10 shows horizon slice of velocity changes at 1260 ms (about 7600 ft). In this figure (Figure 5.10), positive velocity anomalies occur especially near area A. All of the wells near area A are produced from shallower levels. Fault distribution in this interval shows that time-lapse anomalies in area A correlate with the appearance of a major NW-SE fault. The occurrence of velocity anomaly in this deeper interval is an interesting phenomenon. There are some possible explanations for this phenomenon.

The first possible explanation is the re-migration of gas from this deeper interval. As previously explained, the Cameo coal interval is the main source of gas for the Williams Fork reservoir level (chapter 1). There is a possibility that during the production period, the gas inside the fault in the deeper level is re-migrated to the upper level. A study by Haney et al (2005) indicates that the movement of fluid inside fault zones is mainly in the form of fluid pulse. If the same type of fluid movement happens in this

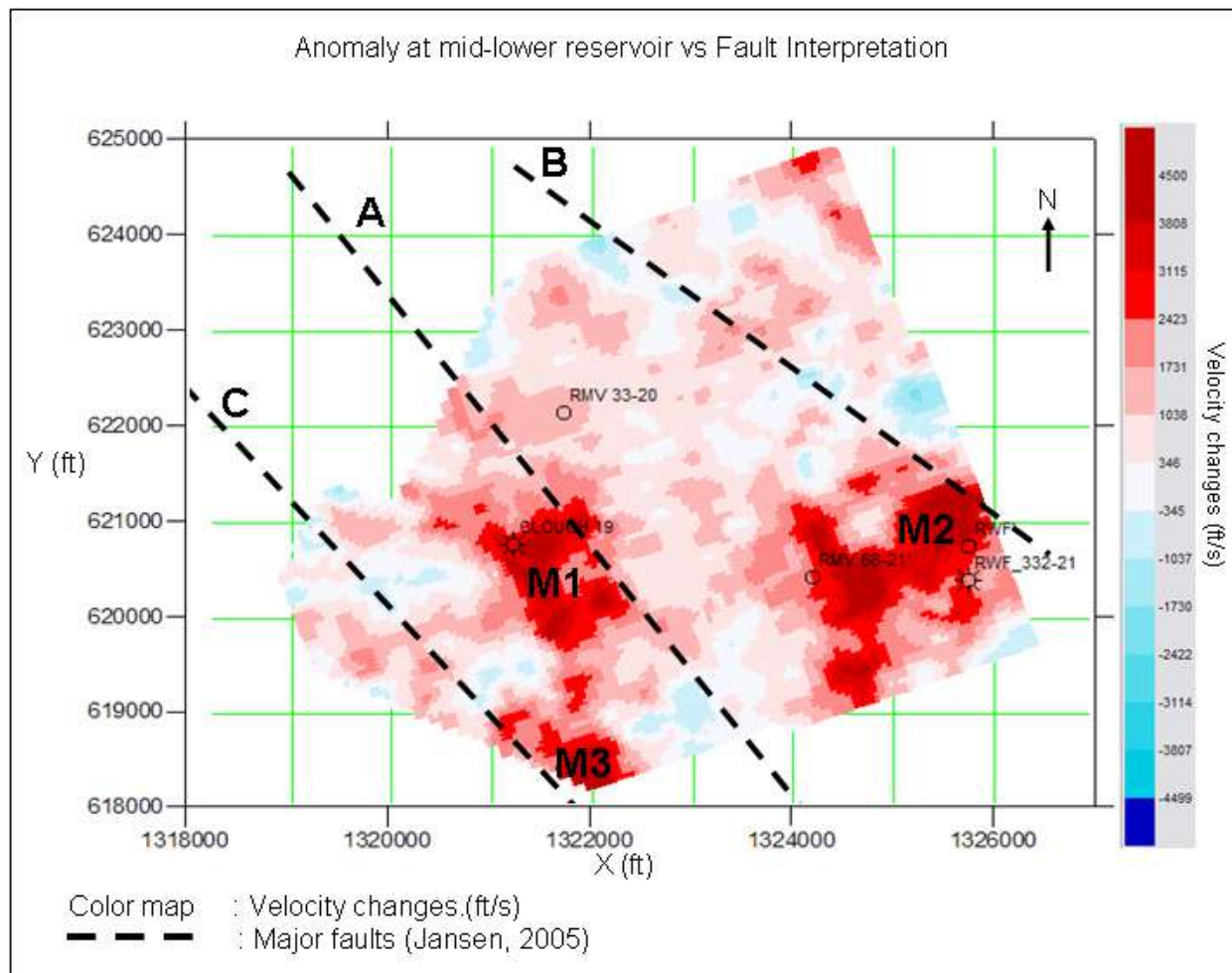


Figure 5.8. Correlation between velocity changes and generalized fault distribution (Jansen, 2005) at mid-lower Williams Fork reservoir level. Velocity anomaly was extracted at 1060 ms (about 6200 ft).

Note : Time and depth mentioned is an average value.

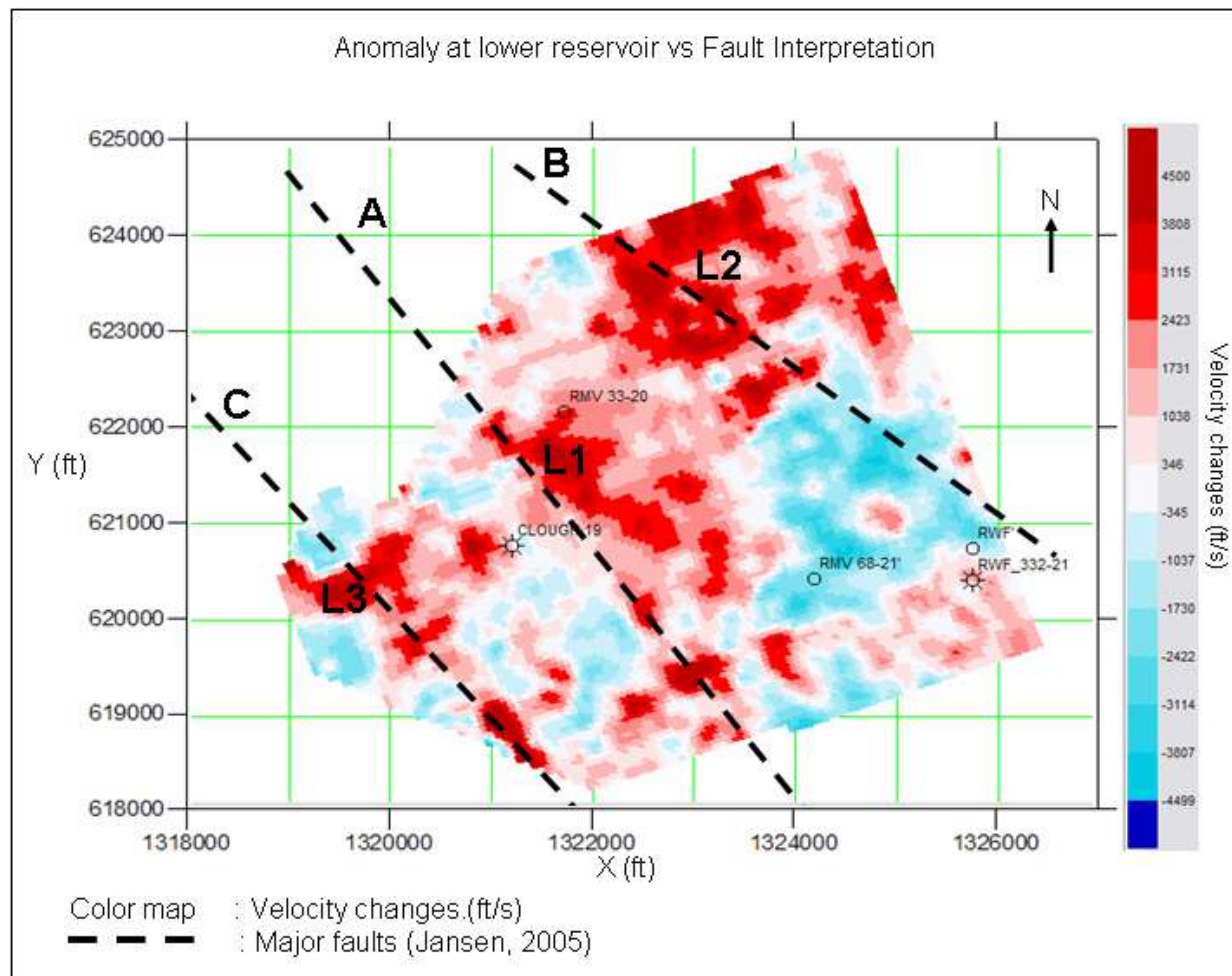


Figure 5.9. Correlation between velocity changes and generalized fault distribution (Jansen, 2005) at lower Williams Fork reservoir level. Velocity anomaly was extracted at 1180 ms (about 7100 ft).

Note : Time and depth mentioned is an average value.

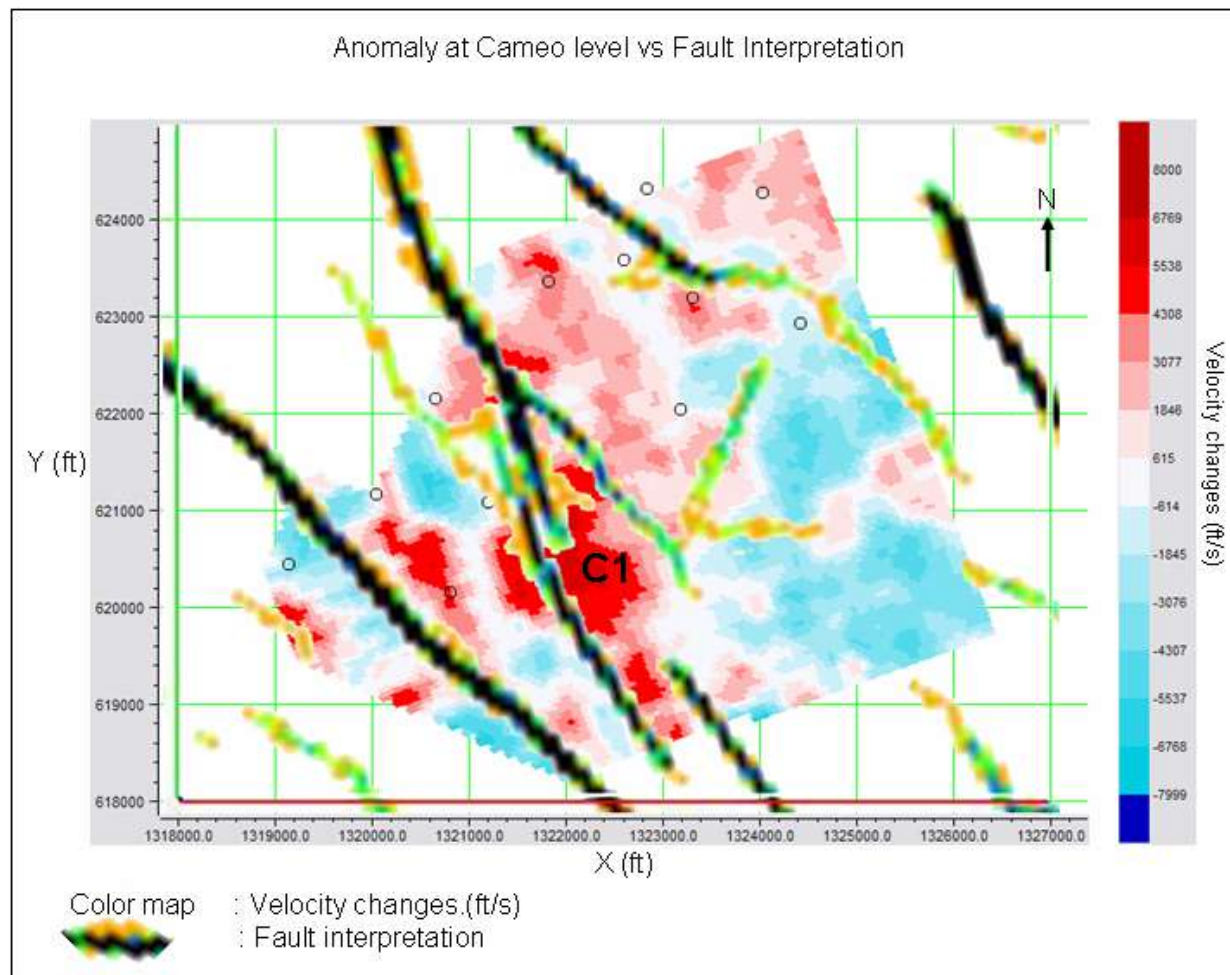


Figure 5.10. Correlation between velocity changes and faults distribution (Jansen, 2005) at Cameo level.

Velocity anomaly was extracted at 1260 ms (about 7600 ft).

Note : Time and depth mentioned is an average value.

field, there will be a high pressure drop area in the deeper interval. A positive time-lapse anomaly in area A might be an indication of this pressure drop zone.

Other possible explanation of this phenomenon is that the anomaly was caused by noise in the data. In this deeper interval, well information (velocity and density) is only available from well RWF 332-21. This well (RWF 332-21) is located in the eastern part of investigation area far from area A. Inversion parameters (wavelet, initial model etc) are mostly extracted using well information from the shallower zone. Inversion result in this interval can be very biased. Other important factor is the difference in acquisition between time-lapse datasets. Most of amplitude differences caused by acquisition have been reduced in the cross equalization process (chapter 2). The different in line orientation between surveys might still affect time-lapse data especially in this deep interval.

Information of sandstone distribution is also used to analyze time-lapse anomaly. Figure 5.11 shows the distribution of gross sand thickness map (courtesy: Williams Production Company) and time-shift attribute. Gross sand thickness value indicates cumulative sand thickness for the entire reservoir level. This map (Figure 5.11) shows a relatively high thickness area in the southern part of the field and relatively low thickness in northern part. In the southeastern part of the field, high time-shift value of area A and low value of area B might be related with the distribution of sandstone in these two areas. Gross sand thickness map shows that area A is a high thickness area (about 700 ft sand thickness) while area B is a low thickness area (about 540 ft sand thickness). Higher time-shift value of area A compare with area B might be caused by the difference in cumulative thickness of sand intervals. This type of correlation is only limited in area A and B. In other areas, sandstone thickness has no correlation with time-shift attribute. In the northwestern part of the field, a low thickness area is located in high time-shift anomaly.

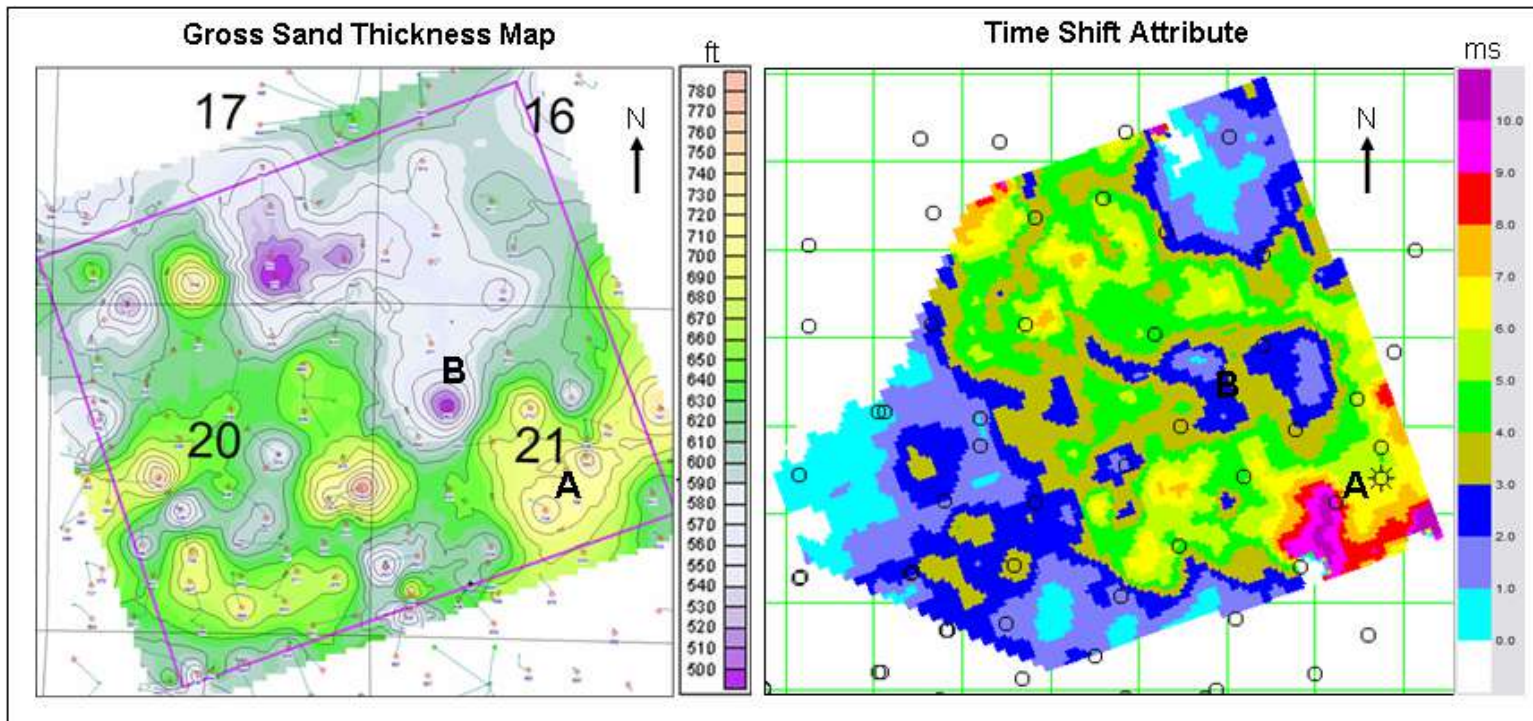


Figure 5.11. Comparison between gross sand thickness map (Courtesy: Williams Production Company) and time-shift attribute.

5.4. Integrated Analysis of Rulison Field

In the previous section (chapter 5.2 and 5.3), analysis is performed to explain the correlation between time-lapse anomaly and other field information (production data, structural geology, sand distribution and rock properties analysis). The results of these analyses are then used to build a comprehensive analysis of the field. This analysis includes study on the cause of time-lapse anomaly, effect of fault on production, and characteristic of separate areas in the field.

Analysis on the cause of time-lapse anomaly was conducted previously in chapter 5.2 and 5.3. Strong correlation between time-shift attribute and production has suggested that this attribute distribution might represent average drainage performance of the area. Analysis on the value of velocity anomaly, time-lapse simulation (Johnston, 2005), and core simulation (Rojas, 2005) has suggested that pore pressure might be the dominant factor affecting time-lapse anomaly (chapter 5.2). Saturation changes might also be an important factor in this time-lapse anomaly. P-wave time-lapse anomaly by itself is not enough to separate the effect of pressure and saturation changes. Thus, combination of this P-wave and S-wave time-lapse analysis is recommended.

Previous analysis of time-lapse data have introduced some areas with high time-shift attributes. Detail analysis also shows the occurrences of velocity anomalies in some areas at certain time intervals. Time-shift attribute is an attribute for the entire reservoir interval. It represents the average value of reservoir changes. The velocity changes anomaly, on the other hand, represents reservoir changes for specific intervals inside the reservoir. Based on these two parameters, there are four types of time-lapse anomalies (table 5.1). Type I is an anomaly with high time-shift value and high velocity anomaly value. This type of anomaly indicates an area where the production is highly dominated by production from certain intervals. Wells located near this type of anomaly have a high cumulative production. Anomaly type II is a time-lapse anomaly with high time-shift value and low velocity anomaly. In this type of anomaly, hydrocarbons are produced in

relatively equal rate from many producing intervals. Wells in this type of area have high cumulative production. Type III anomaly is defined by low time-shift value and high velocity anomaly. In this type of anomaly, cumulative production is dominated by production from several intervals. Wells near this area might have a high cumulative production. Type IV anomaly is identified by low time-shift value and low velocity anomaly. In this type of anomaly, low gas production might occur from many producing intervals. Based on previous analysis (chapter 5.2 and 5.3), time-lapse anomalies in this area are type II and III.

Type of anomaly	Time shift value	Velocity anomaly
I	High	High
II	High	Low
III	Low	High
IV	Low	Low

Table 5.1. Types of time-lapse anomaly.

In chapter 5.3, analysis is performed to study the correlation between the time-lapse anomalies and fault distribution. Information on fault distribution is gathered from the structural study by Jansen (2005). In this area, there are three major NW-SE faults that can be identified. Analysis of time-shift attribute indicates that these major faults separated the area with high drainage performance (indicated by high time-shift value) from other areas (Figure 5.6). Time-shift attribute analysis also shows that NW-SE faults behave as sharp boundaries to the area with high drainage performance. This suggests that, in general, there is only small connectivity across these major faults. However, detail analysis on velocity anomaly especially near well Clough 19 at 1060 ms

(Figure 5.8) suggests that there might be significant connectivity across major NW-SE faults in some producing intervals.

Structure analysis is also performed inside reservoir interval (chapter 5.3). Analysis of velocity anomaly indicates that most of these anomalies are located in the vicinity of intersecting faults (between major NW-SE fault and NE-SW or E-W fault). Jansen (2005) explained the appearances of these NE-SW faults using the Christie-Blick model (Christie-Blick and Biddle, 1985). More explanation on this model is discussed in chapter 1. Based on this model, the occurrence of NE-SW faults can increase fracture density especially in the area of intersecting faults. The increase of fracture density will increase drainage performance of this area and produce areas with high velocity anomalies. Distribution of velocity anomaly near intersecting faults in this time-lapse data supports this model.

Based on integrated data (time-lapse, production, sand distribution, and structure), the area of investigation can be separated into 6 different areas (Figure 5.12). Parameters that are set to analyze and differentiate these areas are cumulative production, gross sand thickness, number of NE-SW or E-W fault, time shift attribute and dominant production interval. Cumulative production value is separated between low (<0.5 BCF), medium (0.5-1.0 BCF) and high (>1.0 BCF) production. Gross sand thickness is defined by low (<600 ft), medium (600-700 ft) and high (>700 ft). Time-shift value is also separated into low (<2 ms), medium (2-5 ms) and high (>5 ms). Another parameter is the number of NE-SW or E-W faults. This parameter is extracted based on fault interpretation at the reservoir level. This parameter is calculated by generating time slices every 2 ms. The number of NE-SW faults can be identified in each time slice is measured for individual area. High number of fault indicates a strong continuous NE-SW or E-W faults in the area. Low number of faults, on the other hand, indicates small discontinuous faults or no identified fault in the area. The last parameter is the velocity anomaly. This parameter is extracted based on the distribution of velocity changes from time-lapse data. A high value of velocity anomaly indicates the appearances of velocity anomalies in two or more time

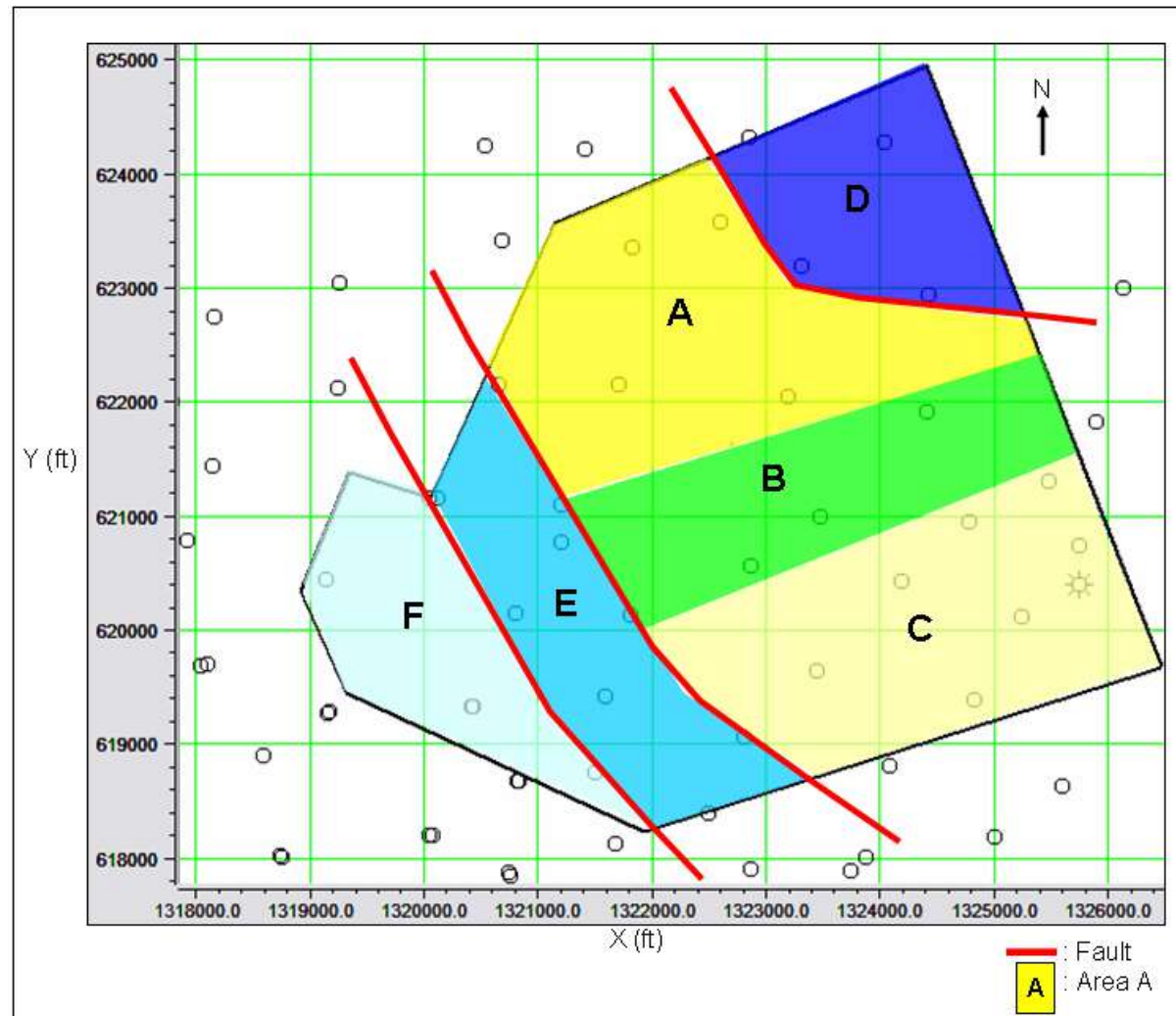


Figure 5.12. Separation between areas based on integrated analysis.

intervals. Medium velocity anomaly indicates the appearances of velocity anomaly in one specific time interval with high velocity changes (>4000 IOD inversion value). Low value of velocity anomaly indicates no identified anomaly in the area or one identified anomaly in specific time interval with low velocity changes (<4000 IOD inversion value).

Zone	Comparison factors				
	Cumulative production	Gross sand thickness	Number of NE-SW or E-W fault	Time shift attribute	Velocity Anomaly
A	High	Low	High	High	Low to medium
B	Medium	Low to Medium	Low	Medium to High	Low
C	Medium	High	Medium to High	High	Low
D	Low	Low	Low	Low	Medium
E	Medium to High	Medium	Low	Medium to Low	Medium
F	Medium	Medium	Low	Low	High

Table 5.2. Comparison between areas in the field.

Based on table 5.2, analysis is then performed to analyze each individual area. First analysis is performed on area A. This area has a high cumulative production area and high number of NE-SW or E-W fault. Time-lapse analysis indicates that this area has high time-shift value and low to medium velocity anomaly. These parameters indicate that area A has high production with relative equal production rate from many producing intervals (type II anomaly). The high occurrences of NE-SW faults suggests that area A is a high fracture density area. The appearances of these faults can generate fracture sets in NE-SW direction and increase average fracture density of this area.

Area B has a medium cumulative production and low number of NE-SW faults. Analysis on time-lapse data indicates that this area has medium to high time-shift and low velocity anomaly (type II anomaly). The decrease in time-shift value in this area compare with area A is an interesting phenomenon. Several possible explanations have been discussed in chapter 5.3. One of those explanations is related with the low number of NE-SW faults. Based on Christie-Blick model (Christie-Blick and Biddle, 1985; Jansen, 2005), area with low (or none) steps over faults might be located in the middle of rotated block (chapter 1). Area in the middle of rotated block will experience less tension forces. The occurrences of fractures due to the rotated block will be less in this area. Due to low fracture density, drainage performance in this area is lower than area A and C. If the drainage performance is low in this area, cumulative production should also be low. Instead, area B has a medium cumulative production. A possible explanation is based on distribution of time-shift attribute in (Figure 5.2). Previous analysis on Figure 5.2 suggests that there is some possibility that most of wells in area B were producing mainly from area A or area C (chapter 5.2). Based on this analysis, most of area B will be low produced.

Area C is characterized by medium cumulative production and medium to high number of NE-SW faults. Time-lapse analysis indicates that area C has high time shift value and low velocity anomaly. These parameters suggest that area C has similar production characteristic with area A (type II anomaly). Medium to high number of NE-SW faults in area C also indicates that most of this area might be located near the edge of rotated block (Christie-Blick model). High tension forces in this area can increase the fracture density and drainage performance. Distribution of high time shift in this area supports this analysis.

Area D is a low cumulative production area. This area also has low number of identified NE-SW faults. Analysis on time-lapse data indicates that area D has low time-shift value and medium velocity anomaly. These parameters indicate that area D has type III anomaly. In this area, gas production is dominated from specific reservoir interval.

Lack of NE-SW fault in this area indicates that this area might not be in rotated block system. Fracture density of this area is predicted to be much lower than area of rotated block system (area A, B and C).

Area E has medium to high cumulative production and medium number of NE-SW faults. Time-lapse data shows that this area has medium to low time-shift value and medium velocity anomaly. Based on time-lapse parameters, this area has type III anomaly. Some dominant production interval can be identified in previous analysis (chapter 5.2 and 5.3). A significant difference between area E and area D is the medium to high cumulative production in area E. One of possible explanation of this cumulative production is based on number of NE-SW fault. The appearances of NE-SW faults in area E can increase the fracture density and total cumulative production.

Characteristic of area F is similar with area E. Separation between these two areas is mostly based on the appearance of major NW-SE faults. Time-shift attribute analysis strongly suggests that NW-SE fault behaved as boundary between these two areas. Further study on production connection across this fault is recommended. Similar with area E, area F also has type III anomaly. Some dominant production interval is also identified in the previous analysis (chapter 5.2 and 5.2).

Analysis is also performed to study anomaly at deep Cameo level. As previously discussed in chapter 5.3, time-lapse anomaly is identified at deep time interval (1260 ms; about 7600 ft). Wells near this anomaly is perforated in the upper interval. These facts suggests that the anomaly might not entirely caused by gas production from well. Several possible explanations of this phenomenon are introduced in chapter 5.3. One of possible explanation is that this anomaly is related with the re-migration of hydrocarbon from Cameo interval. There are some factors that can support this argument. First factor is the alignment of this anomaly with major NW-SE fault. If gas is actively migrated from Cameo level, faults can provide a very good pathway for the migration. Thus, time-lapse anomaly will be aligned with faults. Second factor is the positive velocity changes anomaly at this deep interval. If gas is migrated from this deep interval in the form of

fluid pulse (Haney et al, 2005), pore pressure might decreases significantly in this interval. The decrease in pore pressure increases P-wave velocity and generates a positive velocity anomaly. There are some weaknesses in this explanation. The appearance of pore pressure drop in deep interval should be followed by pore pressure increase in the upper interval. This increase pressure will generate negative velocity anomaly. Analysis on Rulison time-lapse data has failed to identify any significant negative anomaly in the upper interval. To better understand the mechanism of time-lapse anomaly in this deep Cameo interval, other studies need to be conducted in this field.

5.5. Summary of the Integrated Interpretation

Integrated interpretation is performed by combining P-wave time-lapse data with other field data. The other field data used in this analysis includes production history information (Williams Production Co.), gross sand thickness (Williams Production Co.), fault interpretation (Jansen, 2005), rock properties simulation (Rojas, 2005), and time-lapse simulation (Johnston, 2005). Using a combination of these data, analysis is then performed to study the cause of time-lapse anomaly, effect of faults on production, and characteristics of separate areas in the field.

Analysis on time-lapse anomalies indicates that time-shift attribute is a good indication of average drainage performance. Velocity anomalies, on the other hand, are used to detect dominant production intervals. Study of the cause of time-lapse anomalies indicates that pore pressure is the dominant factor for time-lapse changes compared with saturation.

Fault analysis suggests that major NW-SE faults have behaved as a boundary of drainage performance. Connectivity across faults, however, still needs to be studied. The appearance of NE-SW or E-W faults generates areas with high fracture density. The result of this study strongly supports application of the Christie-Blick model in this field.

Analysis is also performed to compare time-lapse anomalies at upper, mid-lower and lower Williams Fork intervals. This analysis indicates that most of the production came from the lower Williams Fork interval.

Based on integrated data, the investigation area is separated into 6 areas. Each area represents different production characteristics. The highest production area is located in the northern part of the study area (area A in Figure 5.12). This area is characterized by high fracture density, small dominant production interval and located in a sheared and rotated block.

Chapter 6

SUMMARIES, CONCLUSIONS AND RECOMENDATIONS

6.1. Summaries

This thesis study is conducted as part of RCP phase X. RCP phase X is conducted to study Rulison field, CO. The purpose of Rulison field study is to improve seismic imaging of reservoir components to increase gas production from the tight gas formation. The focus of this thesis study is the analysis of P-wave time-lapse seismic data in Rulison field. Important processes in this time-lapse study can be summarized as follows:

- a) The Rulison 1996-2003 time-lapse seismic datasets consist of two seismic volumes from two surveys with different acquisition parameter. To reduce the effect of different acquisition parameters and other non-repeatable element of the surveys, both datasets was re-processed and cross-equalized. The re-processing of these datasets was performed by Veritas Geosciences. The cross equalization process has successfully reduced the non-repeatable elements of the surveys. The reduction of non-repeatable element can be identified by the reduction in NRMS value of the static window after cross equalization process. Distribution of high NRMS value can still be identified after cross equalization in the edge area. This high value is mainly caused by high noise levels in the edge of the surveys. This edge area was excluded for further time-lapse analysis.
- b) Based on unique characteristics of Rulison time-lapse data, three time-lapse attributes were chosen and applied to these datasets to analyze time-lapse anomalies. The attributes are time-shifting attributes, correlation coefficient (CC)

attributes and percent differences (PD) attributes. Synthetic datasets were then used to study the reliability, sensitivity, and error estimation of these attributes. The time-lapse attribute analysis using a combination of these attributes has successfully detected time-lapse anomaly at the reservoir level. This attribute analysis also confirmed the time-lapse anomaly at the Cameo level (below the Williams Fork reservoir level).

- c) Two different time-lapse inversion approaches were used in this study i.e. differences of inversion (DOI) and inverse of differences (IOD). Application of these two different approaches on synthetic data was performed to study characteristic advantages and disadvantages of each approach. Inversion of Rulison time-lapse data has successfully delineated time-lapse anomalies.
- d) Integrated interpretation was performed by combining P-wave time-lapse data with other field data. The other field data used in this analysis are production history information, gross sand thickness, faults interpretation, rock properties simulation, and time-lapse simulation. This integrated interpretation was conducted to study the cause of time-lapse anomalies, the effect of faults on production, and characteristics of separate areas in the field.

6.2. Conclusions

- a) Cross equalization has highly reduced non-repeatable noise in most areas of the time-lapse seismic data, with an exception of edge areas.
- b) Time-lapse anomalies inside the reservoir are mainly due to a decrease in pore pressure during gas production.
- c) Application of time-shift attributes to the Rulison datasets defines areas with high average drainage performance.

- d) Inversion results using the IOD approach results in lower noise levels than DOI approach, and better locating and delineating time-lapse anomalies.
- e) The combination of time-shift attribute and amplitude-based inversion has been able to detect dominant production intervals.
- f) Major NW-SE faults performed as boundaries between areas with high drainage performances. The occurrence of NE-SW or E-W faults in the reservoir increases fracture density of specific intervals and increases drainage performance.
- g) The result of this study strongly supports the applicability of the Christie-Blick model in this field as suggested by Jansen (2005).
- h) Based on integrated analysis of the field, the investigation area was separated into 6 different areas. Each area has unique production characteristics.

6.2. Recommendations

- a) A stratigraphic model of the reservoir and detail information of fluvial channels distribution can help to analyze the stratigraphic control on time-lapse anomalies.
- b) To get a better estimation of velocity changes, a full inversion scheme should be developed and applied to the time-lapse datasets. Information of time-shift between seismic datasets should also be included in this inversion.
- c) Production logs should be gathered and analyzed to get a better understanding of pressure decline, production rate, and any dominant production interval. Information from these production logs can also very useful to calibrate velocity changes with pressure or saturation changes.

REFERENCES

- Ansorger, C., and R. Kendall, 2004, Rulison 3D – 1996/2003 time lapse, Fall 2004 RCP Sponsor meeting, Reservoir Characterization Project, Colorado School of Mines.
- Balch, A.H., 1971, Color sonograms – A new dimension in seismic data interpretation: Geophysics, Society of Exploration Geophysics, 36, 1074-1098.
- Benson, R.D., Personal communication, February 2005.
- Blakey, R.C., 2004, Cretaceous paleogeography of the southwestern US, <http://jan.ucc.nau.edu/~rcb7/crepaleo.html>.
- Brown, A.R., 1996, Seismic attributes and their classification, The Leading Edge, October 1996, Society of Exploration Geophysicists.
- Burke, L., 2004, Anisotropy azimuth from RWF 332-21 cross dipole sonic log analysis, Fall 2004 RCP Sponsor meeting, Reservoir Characterization Project, Colorado School of Mines.
- Burke, L., 2005, Anisotropy from RWF 542-20 cross dipole sonic log analysis, Spring 2005 Sponsor Meeting, Reservoir Characterization Project, Colorado School of Mines.
- Calvert, R., 2005, Insights and methods for 4D reservoir monitoring and characterization, Distinguished Instructor Series, Society of Exploration Geophysicists.
- Chen, Q. and S. Sidney, 1997, Seismic attribute technology for reservoir forecasting and monitoring : The Leading Edge, 16, no. 05, Society of Exploration Geophysics.
- Christie-Blick, N., and K.T. Biddle, 1985, Deformation and basin formation along strike-slip faults, in, Biddle, K.T., and N. Christie-Blick: Strike-slip Deformation, basin formation, and sedimentation: Society of Economic Paleontologist and Mineralogists, Special publication no. 37, pp. 1-34.

- Cole, R. and S. Cumella, 2003, Stratigraphic architecture and reservoir characteristics of the Mesaverde Group, southern Piceance Basin, Colorado, *in* K.M. Peterson, T.M. Olsen, and D.S. Anderson, eds., Piceance Basin 2003 guidebook: Rocky Mountain Association of Geologists, 442 p.
- Collins, B.A. 1976. Coal deposits of the Carbondale, Grand Hogback, and Southern Danforth Hills coal fields, Eastern Piceance Basin, Colorado, Colorado School of Mines Quarterly, 71(1).
- Davis, T.L., 2004, Time-lapse seismic analysis, Fall 2004 RCP Sponsor meeting, Reservoir Characterization Project, Colorado School of Mines.
- Duranti, L., 2001, Time-lapse multicomponent seismic analysis of reservoir dynamics, PhD Thesis, Geophysics Department, Colorado School of Mines.
- Galikeev , T., 2004, Application of New Seismic Attributes to Reservoir Monitoring, Phd Thesis, Geophysics Department, Colorado School of Mines.
- Green, C.A., 2004, Hydraulic Fracture Modeling of massively stacked lenticular reservoirs with correlation to production, Rulison Field, Piceance Basin, Colorado, Fall 2004 Sponsor Meeting, Reservoir Characterization Project, Colorado School of Mines.
- Hampson Russell Inc., 1999, Theory of Strata Program, Hampson Russell Software Guide.
- Hampson Russell Inc., 2004, Hampson Russell Software Guide.
- Haney, M.M., R. Snieder, J. Sheiman, S. Losh, 2005, A moving fluid pulse in a fault zone, Nature, Vol. 437, September 2005.
- Herawati, I., 2002, The use of Time-Lapse P-wave Impedance Inversion to Monitor a CO₂ Flood at Weyburn Field, Saskatchewan, MS. Thesis, Geophysics Department, Colorado School of Mines.
- Hintze, L.F., 1988, Geologic history of Utah: Brigham Young University Geology Studies Special Publication 7, 202 p.

Jack, I., 1998, Time-Lapse Seismic in Reservoir Management, Distinguished Instructor Short Course notes, Society of Exploration Geophysicist.

Jansen, K., 2005, Seismic Investigation of wrench faulting and fracturing at Rulison Field, Colorado, MS Thesis, Geophysics Department, Colorado School of Mines.

Jenkins, S.D., M.W. Waite, and M.F. Bee, 1997, Time-lapse monitoring of the Duri steamflood: A pilot and case study, Leading Edge, September 1997, Society of Exploration Geophysicist.

Johnson, R. C., 1989. Geologic history and hydrocarbon potential of Late Cretaceous-age, low-permeability reservoirs, Piceance Basin western Colorado: U. S. Geological Survey Bulletin 1787-E, 51 p.

Johnson, R. C., and V.F. Nuccio, 1986. Structural and Thermal history of the Piceance Creek Basin, western Colorado, in relation to hydrocarbon occurrence in the Mesaverde Group: in Spencer, C. W., and Mast, R. F., eds., Geology of Tight Gas Reservoirs: American Association of Petroleum Geologists Studies in Geology No. 24, p. 165-205.

Johnson, R.C., and D.D. Rice, 1990, Occurrence and geochemistry of natural gases, Piceance basin, northwest Colorado; American Association of Petroleum Geologists Buletin, v. 74, p. 805-829.

Johnston, D., 2005, Simulation of Rulison field 4D effect, Reservoir Characterization Project, Internal report, Colorado School of Mines.

Karaman, A., and P.J. Carpenter, 1997, Fracture density estimates in glaciogenic deposits from P-wave velocity reductions: Geophysics, Volumes 62, pp. 138-148 (January-February 1997), Society of Exploration Geophysicist.

Kragh, E., and P. Christie, 2002, Seismic repeatability, normalized rms, and predictability, The Leading Edge July 2002, Society of Exploration Geophysicists.

Kuuskraa, V.A., and J.P. Brashear, 1978, Enhanced Recovery of Unconventional Gas : The Program-Volume II, U.S. Department of Energy.

- Kuuskraa, V.A., T. Barrett, R. Mueller, and J. Hansen, 1997, Reservoir characterization for development of Mesaverde Group sandstones of the Piceance Basin, Colorado, Innovative Applications of Petroleum Technology Guidebook: Rocky Mountain Association of Geologists, Denver, Colorado.
- Landes, K.K., 1951, Petroleum Geology, John Wiley & Sons Inc., pp. 207-325.
- Landro, M., and J. Stammeijer, 2004, Quantitative estimation of compaction and velocity changes using 4D impedance and traveltimes changes, *Geophysics*, Vol. 69, No. 4, Society of Exploration Geophysicist.
- Latimer, R.B., R. Davison, and P. van Riel, 2000, An interpreter's guide to understanding and working with seismic-derived acoustic impedance data, *The Leading Edge*, 19, No. 3, 242-256, Society of Exploration Geophysicist.
- Lilis, P. G., A. Warden, D. King, 2003, Petroleum Systems of the Uinta and Piceance Basins – Geochemical Characteristics of Oil Types, USGS Digital Data Series DDS-69-B.
- Madiba, G.B., 2003, Seismic impedance inversion and interpretation of a gas carbonate reservoir in the Alberta Foothills, Western Canada: *Geophysics*, Volume 68, pp. 1460-1469, Society of Exploration Geophysicist.
- Magoon L.B., and J.W. Schmoker, 2000, The total petroleum system; the natural fluid network that constrains the assessment unit, U.S. Geological Survey Digital Data Series, Report: DDS-0060, 31 pp.
- Magoon, L.B., 1988, The petroleum system – A classification scheme for research, exploration, and resource assessment: U.S. Geological Survey Bulletin, p. 319-320.
- Magoon, L.B., and W.G. Dow, 1994, The petroleum system – From source to trap: American Association of Petroleum Geologists Memoir 60, p. 3-24.
- McFall, K.S., D.E. Wicks, V.A. Kuuskraa, and K.B. Sedwick, 1986. A geologic assessment of natural gas from coal seams in the Piceance Basin, Colorado. Gas Research Institute, Topical Report. GRI-87/0060 (September 1985-September 1986), 76 p.

Mukerji, T., A. Jorstad, P. Avseth, G. Mavko, and J.R. Granli, 2001, Mapping lithofacies and pore-fluid probabilities in a North Sea reservoir: Seismic inversions and statistical rock physics: Geophysics, Volume 66, pp. 988-1001 (July-August 2001), Society of Exploration Geophysicist.

Partyka, G.A., J.A. Lopez, N.L. Haskell, and S.E. Nissen, 1997, Identification of deltaic facies with 3-D seismic coherency and the spectral decomposition cube. Page 191 of : Int. Geoph. Conf. & Exposition, Istanbul '97, Abstracts, Society of Exploration Geophysicist.

Peyton, L., R. Bottjer, and G. Partyka, 1998, Interpretation of incised valleys using new 3-D seismic techniques : A case history using spectral decomposition and coherency, The Leading Edge, 17(9), 1294-1298, Society of Exploration Geophysicist.

Reading, H., 1983, Sedimentary environments and facies, Reading, H. ed., 569 p.

Rickett, J.E., and D.E. Lumley, 2001, Cross-equalization data processing for time-lapse seismic reservoir monitoring: A case study from the Gulf of Mexico, Geophysics, 66, 1015-1025.

Robinson, G., 2001, Stochastic Seismic Inversion applied to reservoir characterization, CSEG Recorder, January 2001.

Rojas, E., 2005, Elastic rock properties of tight gas sandstones for reservoir characterization at Rulison Field Colorado, MS thesis, Geophysics Department, Colorado School of Mines.

Ross, C.P., G.B Cunningham, D.P. Weber, 1996, Inside the Crossequalization Black Box, The Leading Edge, Society of Exploration Geophysicist.

Russell, B., 2005, Introduction to Seismic Inversion, Short Course Notes, Hampson Russell.

Russell, B., 2005, Seismic Inversion Theory, Short Course Notes, Hampson Russell.

Sarkar, D., W.P. Gouveia, and D.H. Johnston, 2003, On the inversion of time-lapse data, Pages 1489-1492 of: 73rd Annual International Meeting, Society of Exploration Geophysicist.

Satriana, M., 1980, Unconventional Natural Gas : Resources, Potential and Technology, Energy Technology Review No. 56.

Scales, J.A., M.L. Smith, and S. Treitel, 1997, Introductory Geophysical Inverse Theory, Samizdat Press, Colorado.

Sterner, R., 1995, Color landform atlas of the United States, John Hopkins University, Applied Physic Laboratory, <http://fermi.jhuapl.edu/states/states.html>

Taner, M.T., 2001, Seismic Attributes, CSEG Recorder September 2001.

Taner, M.T., F. Koehler, and R.E. Sheriff, 1979, Complex Seismic trace analysis, *Geophysics*, 44, 1041-1063.

Tremain, Carol M. and Tyler, R. 1997. Cleat, fracture, and stress patterns in the Piceance Basin, Colorado: Controls on coalbed methane producibility. Rocky Mountain Association of Geologists, Fractured Reservoirs: Characterizations and Modeling Guidebook.

Tyler, R., A.R. Scott, W.R. Kaiser, H.S. Nance, R.G. McMurry, C.M. Tremain, and M.J. Mavor, 1996, Geologic and hydrologic controls critical to coalbed methane producibility and resource assessment: Williams Fork Formation, Piceance Basin, Northwest Colorado. The University of Texas at Austin, Bureau of Economic Geology, topical report prepared for the Gas Research Institute, GRI-95/0532, 398 p.

Vasco, D.W., A.D. Gupta, R. Behrens, P. Condon, and J. Rickett, 2004, Seismic imaging of reservoir flow properties : Time-lapse amplitude changes; *Geophysics* Vol. 69, No. 6, Society of Exploration Geophysicist.

Vasco, D.W., J.E. Peterson Jr., and E.L. Majer, 1996, A simultaneous inversion of seismic traveltimes and amplitudes for velocity and attenuation, *Geophysics*, Volumes 61, pp. 1738-1757 (November-December 1996), Society of Exploration Geophysicist.

Waite, M.W., and R. Sigit, 1997, Seismic monitoring of the Duri steamflood: application to reservoir management, *Leading Edge*, September 1997, Society of Exploration Geophysicist.

Winarsky, R., and R. Kendall, 2004, RCP 9C Processing Review, Fall 2004 RCP Sponsor meeting, Reservoir Characterization Project, Colorado School of Mines.

www.edge.ou.edu/seismic-interpretation/vol-1d.htm

Yilmaz, O., 1987, Seismic Data Processing, Society of Exploration Geophysicist.

Yilmaz, O., 2001, Seismic data analysis: Processing, Inversion, and Interpretation of Seismic Data, Society of Exploration Geophysicist.